

**Efficient Creation of Ultracold Ground State ${}^6\text{Li}{}^{40}\text{K}$ Polar
Molecules**

CANMING HE

(Bachelor of Physics, Sichuan University)

**A THESIS SUBMITTED
FOR THE DEGREE OF DOCTOR OF PHILOSOPHY
CENTRE FOR QUANTUM TECHNOLOGIES
NATIONAL UNIVERSITY OF SINGAPORE**

2025

Thesis Advisor:

Associate Professor Kai Dieckmann

Examiners:

Associate Professor XX

Assistant Professor XX

Professor XX

Declaration

I hereby declare that this thesis is my original work and it has been written by me in its entirety. I have duly acknowledged all the sources of information which have been used in the thesis.

This thesis has also not been submitted for any degree in any university previously.

Canming He

CANMING HE

Jan, 2025

Acknowledgments

The beginning of my PhD journey in 2020 was marked by extraordinary challenges due to the onset of the global pandemic. Navigating through lockdowns and various restrictions, our group faced significant hurdles in progressing with our experiments. Despite these difficulties, we persevered and made remarkable progress, enabling me to successfully complete my PhD project.

I would like to express my deepest gratitude to everyone who supported and assisted me throughout this journey.

First and foremost, I extend my heartfelt thanks to my advisor, Professor Kai Dieckmann, at the Centre for Quantum Technologies (CQT), National University of Singapore (NUS). His insightful guidance and constructive suggestions have been pivotal to my research and personal growth. His foresight and intuition regarding experimental challenges were instrumental in advancing our work. Under his mentorship, I gained invaluable experimental skills and developed a deeper understanding of complex physics problems, for which I am profoundly grateful.

I am also deeply appreciative of the support and expertise provided by Dr. Anbang Yang, Dr. Sofia Botsi, and Dr. Sunil Kumar. Their technical skills and theoretical insights were crucial in bringing the experimental system back to operational status during a challenging period. I owe special thanks to Dr. Anbang Yang, who later became our postdoctoral researcher and played a vital role in the lab with his extensive knowledge of our experiments.

My sincere gratitude also extends to my colleagues Victor Andre Avalos Pinillos and Xiaoyu Nie, who contributed immensely to creating a productive and collaborative work environment. Together, we achieved the efficient creation of ground state LiK in the lab. Victor, who joined the lab at the same time as me, took on various lab duties and demonstrated exceptional expertise in electronics. Xi-

aoyu, who joined a year later, brought profound insights into physics problems and consistently provided fresh inspiration to our work.

I would also like to thank Athira Krishnan Sreedevi, Rishav Koirala, and Haotian Song from another lab in our group. The time spent traveling and dining out with them brought much-needed joy and camaraderie to my PhD life.

Additionally, I am grateful to the Physics Department and the CQT at NUS for providing me with the opportunity to pursue my studies and for the financial support that enabled me to focus on my research.

Finally, my deepest thanks go to my family, especially my parents, for their unwavering support and encouragement. Their belief in me has been a constant source of strength during the many challenges I faced along the way.

Contents

Summary	ix
List of Tables	xi
List of Figures	xiii
1. Introduction	1
1.1. Dipole-Dipole Interaction in Ultracold Gases	2
1.2. Creation of Ground State Molecules	3
1.3. Optical Lattice	5
1.4. Thesis Outline	6
2. Theoretical Background	9
2.1. STIRAP Process	9
2.1.1. Three-Level System	10
2.1.2. STIRAP Process	12
2.1.3. Singlet Pathway	13
2.1.4. Extend to Multi-Level System with Decoherence	16
2.2. Optically Plugged Trap	19
2.2.1. Optical dipole potentials	19
2.2.2. Plugged Trapping Potential	20
2.3. Optical Lattice	22
2.3.1. Lattice Potential	22
2.3.2. Band Structure	25
3. Experimental Apparatus and Procedures	28
3.1. Overview of Fermi-Fermi Mixture Platform	28
3.2. Improved Raman Laser System	31
3.2.1. Updated Pump and Stokes Setup	32
3.2.2. Phase Noise Measurement	35
3.2.3. Pound-Drever-Hall Locking	37
3.2.4. Frequency Control with Frequency Comb	39
3.2.5. Summary of Setting and Stabilization of Laser Frequencies	42
3.3. Removal of Residual Atoms	44
3.3.1. Atom Cleaning with High Field imaging Light	45
3.3.2. Imaging Calibration	47

3.4. Free Space Optical Lattice	48
3.4.1. Lattice Setup	48
3.4.2. Avoiding Undesired Interference	49
3.5. Optically Plugged Trap	52
3.5.1. Plugged Beam Setup	52
3.5.2. Plug Beam Alignment	53
3.5.3. Rb Evaporative Cooling	56
3.5.3.1. RF Evaporation	56
3.5.3.2. MW Evaporation	58
3.5.4. OPT with Li and K	62
4. Creation of Ground State Molecules	66
4.1. Ground State Spectroscopy	66
4.1.1. Single-Photon Spectroscopy	67
4.1.2. Dark Resonance Spectroscopy	67
4.1.3. AC Stark Shift from Stokes Light	70
4.2. Off-Resonance Raman Process	72
4.2.1. Two-Photon Detuning and Raman Oscillation	72
4.2.2. Rabi Frequency Calibration and Dephasing Analysis	73
4.3. STIRAP	75
4.3.1. STIRAP Procedures	75
4.3.2. STIRAP Results	78
4.3.3. Background Detection	79
4.3.4. Evolution Fitting	80
4.4. Efficiency Analysis	81
4.4.1. Non-adiabatic Loss	82
4.4.2. Fast Laser Phase Noise Loss	82
4.4.3. Phase Noise Improvement	84
4.4.4. Loss Probability	89
4.4.5. Detuning Conditions	92
4.4.6. Magnetic Field Around Feshbach Resonance	98
5. Properties of Ground State ${}^6\text{Li}{}^{40}\text{K}$ Molecules	101
5.1. Temperature Measurements	101
5.2. Lifetime Measurement	103
5.3. Two-body Loss Rate Constant	105
5.4. Stark Shift Spectroscopy	106
5.4.1. Permanent Dipole Moment from Stark Shift Measurement	106
5.4.2. Simulation of Electric Field	108
5.5. MW Transition	109
5.5.1. Molecular Hamiltonian	111
5.5.2. Prediction of N=1 Transition Frequency	112

5.5.3. MW Spectroscopy	113
5.5.4. Discussion	115
5.5.5. Outlook	118
6. Exploration of a 3D Lattice	120
6.1. 3D Lattice Implementation	120
6.2. Kapitza-Dirac Scattering	125
6.3. Creation of Molecules in the Lattice	130
7. Conclusions and Outlook	133
7.1. Outlook	135
A. Fundamental Physical Constants	184
B. STIRAP Summary Table	186

Summary

This thesis reports on the experimental design and preparation for realizing high efficient creation of ultracold rovibrational ground state ${}^6\text{Li}{}^{40}\text{K}$ molecules, and the experimental investigation towards implementing quantum simulation in 3D optical lattices with long-range dipolar interactions.

The primary goal of this work is to achieve a high transfer efficiency from the Feshbach state to the ground state. To facilitate this, a singlet pathway is employed, involving singlet-to singlet optical transitions, which avoids addressing the unresolved hyperfine structure. The detrimental effects of fast phase noise on the STIRAP efficiency are mitigated by suppressing the phase noise of the Stokes and Pump lasers by 73% and 71%, respectively. This is achieved by replacing high quality laser diodes and extending the external cavity of the ECDL structure from 3 cm to 20 cm. Non-adiabatic loss is reduced by increasing the Rabi frequency, and a 10 MHz single-photon detuning is implemented to prevent off-resonance excitation to undesired hyperfine fine states caused by Raman laser polarization impurities. A four-level system with decoherence is developed to describe the STIRAP process. As a result, a one-way STIRAP transfer efficiency of up to 96(4)% is achieved, representing one of the highest efficiencies among bi-alkali species.

With the successful creation of ground state ${}^6\text{Li}{}^{40}\text{K}$ molecules, the properties are investigated. The temperature of the ground state sample is estimated to be $0.91(7)\,\mu\text{K}$, inferred from measurements of the Feshbach state. The lifetime is measured to be $5.0(3)\,\text{ms}$ after cleaning the remaining atoms, consistent with expectations for chemically reactive molecules. The decay rate constant is calculated to be $3.8(1.9)\times 10^{-10}\,\text{cm}^3\text{s}^{-1}$, in close agreement with theoretical predictions. The high dipole moment of the ground state ${}^6\text{Li}{}^{40}\text{K}$ is revealed through Stark shift spectroscopy in an external electric field, showing a maximum dipole moment of 3.1(3) D. Furthermore, rotational spectroscopy is performed to locate the transition frequency of the first rotational excited state, which is found to be around 17.4795 GHz. However, the coherence time for those transitions are found to be very short (on the order of a few microseconds), attributed to differences in the ac polarizability of the states involved.

In addition, an optically plugged trap is tested with the aim of accelerating the experimental sequence. And three-dimensional optical lattice is also constructed, verified by observing phase transition between superfluid and Mott-insulator, band mapping of the 1st Brillouin zone, and calibrated using the Kapitza-Dirac scattering.

List of Tables

1.1. Summary of the STIRAP results from different groups	5
3.1. EOM frequency and beat value sign relation	43
4.1. Phase noise of the Setups	89
5.1. Coupling constants in the molecular Hamiltonian	112
B.1. Summary of the STIRAP results from different groups	187

List of Figures

2.1.	Three-level system	10
2.2.	Adiabatic potential energy curves	14
2.3.	Four level scheme with spontaneous decay	17
2.4.	OPT potential	21
2.5.	Band structure	26
3.1.	The experimental platform of MOT and UHV chamber with transfer coils . .	29
3.2.	The Raman setup for Pump laser	32
3.3.	The Raman setup of Stokes laser	34
3.4.	The Raman setup near UHV chamber	35
3.5.	The phase noise setup	36
3.6.	Phase noise measurements for Pump laser	37
3.7.	PDH setup	38
3.8.	Error signal	40
3.9.	Optical setup of beat measurement	41
3.10.	Frequency correction	44
3.11.	Cleaning setup	46
3.12.	Imaging calibration	47
3.13.	Free space optical lattice setup	50
3.14.	Undesired interference	51
3.15.	Optically plugged trap setup	53
3.16.	Trapping potentials for different beam waist and power	54
3.17.	Effect of the aligned plug beam	56
3.18.	Evaporative cooling process of ^{87}Rb : Temperature vs number	58
3.19.	Evaporative cooling process of ^{87}Rb : PSD vs number	59
3.20.	Evaporative cooling process of ^{87}Rb by MW	61
3.21.	OPT with undesired interference	63
3.22.	OPT potential with different species	64
4.1.	Precision spectroscopy of $\text{A}^1\Sigma^+ v' = 23, J' = 1\rangle$	68
4.2.	Two-photon resonance	69
4.3.	Observation of dark resonance in ${}^6\text{Li}{}^{40}\text{K}$ molecules and fit to an analytical model. .	70
4.4.	ac Stark shift from Stokes light	71
4.5.	Raman resonance	73
4.6.	Dephasing of Raman oscillation	74
4.7.	Spectroscopy beam alignment	76

4.8. STIRAP sequence	77
4.9. STIRAP results	78
4.10. Phase noise measurement with old setup	83
4.11. Phase noise measurement with old setup	85
4.12. Long cavity ECDL	87
4.13. Phase noise measurement with new setup	88
4.14. Phase noise with intra-cavity EOM	89
4.15. Loss probability	90
4.16. 2D density plot loss for loss probability	91
4.17. Single-photon and two-photon detuning with balanced impure polarization .	93
4.18. Linewidth of two-photon detuning	94
4.19. Efficiency based on single-photon detuning	95
4.20. Efficiency based on ζ_s and ζ_s/ζ_p	97
4.21. Single-photon and two-photon detuning with imbalanced impure polarization	98
4.22. Background detection	99
5.1. TOF measurement	102
5.2. Lifetime of the ground state molecules	104
5.3. Stark shift of the ro-vibrational ground state	108
5.4. High-voltage electrode setup	109
5.5. Simulation of E field	110
5.6. Simulation of E field gradient	110
5.7. Two-photon ground state spectroscopy including the rotationally excited state	113
5.8. MW schematic and the transition illustration	114
5.9. MW spectroscopy	115
5.10. Population transfer between $N'' = 0$ and $N'' = 1$	116
5.11. Level schematic of MW shielding	119
6.1. Lattice beam alignment	121
6.2. Superfluid in 1D and 2D lattice	123
6.3. Brillouin zone for Rb and K	124
6.4. Procedure for measuring KD scattering	127
6.5. KD scattering patterns	128
6.6. Simulation results for KD scattering	128
6.7. Lattice trap depth versus laser power	129
6.8. Band structures with maximum lattice power.	130
6.9. Feshbach association in optical lattice	132
6.10. Feshbach association in optical lattice with Pump excitation	132

1. Introduction

In the past few decades, ultracold quantum gases have provided an optimal platform for investigating a wide range of topics in fundamental physics. Routinely produced using laser cooling (Aspect et al., 1988; Chu et al., 1985; Lett et al., 1988; Wineland et al., 1978) and evaporative cooling (Davis et al., 1995; Ketterle and Druten, 1996) technologies, these quantum gases reach temperatures in the nanokelvin regime, enabling the exploration of exotic quantum states. Notable achievements include the generation of Bose-Einstein condensation (BEC) (Anderson et al., 1995; Bradley et al., 1995; Davis et al., 1995) and the production of degenerate Fermi gases (DeMarco and Jin, 1999). By utilizing the magnetically tunable Feshbach resonance (FRs) (Courteille et al., 1998; Inouye et al., 1998; Stwalley, 1976), short-range interaction can be precisely controlled. Significant breakthroughs have been made by manipulating the FRs, including the observation of the BCS-BEC crossover in degenerate Fermi gases (Bartenstein et al., 2004; Bourdel et al., 2004; Regal et al., 2004), the controlled collapse of a BEC (Roberts et al., 2001), the investigation of universal Efimov physics (Kraemer et al., 2006; Pollack et al., 2009b; Zaccanti et al., 2009), the observation of long lifetime fermionic near FRs (Dieckmann et al., 2002), and the creation of weakly-bound molecules from atom pairs (Chin et al., 2003; Donley et al., 2002; Dürr et al., 2004b; Herbig et al., 2003). In addition, homonuclear molecular BECs have been created from atomic pairs (Greiner et al., 2003; Jochim et al., 2003b; Regal et al., 2003; Zwierlein et al., 2003) and the first dipolar molecular BEC has been achieved recently (Bigagli et al., 2024).

Furthermore, the application of optical lattice technologies has enabled the investigation of landmark phenomena in these quantum systems, including the phase transition between superfluid and Mott insulator (Greiner et al., 2002; Stöferle et al., 2004), confinement-induced FRs (Bergeman et al., 2003; Haller et al., 2010; Lamporesi et al., 2010; Moritz et al., 2005; Olshanii, 1998), and strongly correlated systems (Greif et al., 2013; Mazurenko et al., 2017; Simon et al., 2011).

1.1. Dipole-Dipole Interaction in Ultracold Gases

Interest in studying long-range interaction in ultracold quantum gases has grown significantly in experimental researches. A prominent example is the dipole-dipole interaction (DDI), which is long-range and anisotropic. The interaction energy between two dipoles can be expressed to be ([Lahaye et al., 2009](#))

$$U_{dd}(r) = \frac{C_{dd}}{4\pi} \frac{(\mathbf{e}_1 \cdot \mathbf{e}_2)r^2 - 3(\mathbf{e}_1 \cdot \mathbf{r})(\mathbf{e}_2 \cdot \mathbf{r})}{r^5} , \quad (1.1)$$

where C_{dd} represents the coupling constant, which can be either magnetic dipole moments $\mu^2\mu_0$ or electric dipole moments d^2/ϵ (μ_0 and ϵ are vacuum permeability and vacuum permittivity). \mathbf{e}_1 and \mathbf{e}_2 represent the position of the dipoles, and \mathbf{r} is the relative position vector between dipoles with modulus r . If dipoles are polarized along same direction with an angle θ relative to \mathbf{r} , the interaction energy is simplified to the angular dependent form of

$$U_{dd}(r) = \frac{C_{dd}}{4\pi} \frac{1 - 3\cos^2\theta}{r^3} . \quad (1.2)$$

The long-range interaction follows the $\sim 1/r^3$ relation, and the spatial anisotropy is governed by θ . Specifically, the interaction is repulsive when $\theta > 54.7^\circ$ and attractive when $\theta < 54.7^\circ$.

The DDI can be investigated using ultracold gas in several systems. Relatively large magnetic dipole moment has been achieved with ^{52}Cr ($6\mu_B$), ^{164}Dy ($10\mu_B$), and ^{168}Er ($7\mu_B$) ([Aikawa et al., 2012](#); [Griesmaier et al., 2005](#); [Lu et al., 2011](#)), Gigantic electric dipole moments can be realized with Rydberg atoms ([Gallagher, 2023](#); [Saffman et al., 2010](#)), and also the electric dipole moments can be produced with polar molecules. ([Bohn et al., 2017](#)).

Special attention has been devoted to ultracold heteronuclear dipolar molecules, which are predicted with large permanent electric dipole moment (on the order of Debye) in their vibrational ground state ([Aymar and Dulieu, 2005](#)). Combined with their rich internal state, including electronic, vibrational, rotational, and hyperfine structures, ultracold heteronuclear dipolar molecules provide an exceptional platform for a variety of applications.

The creation of ultracold dipolar molecules offers exciting opportunities to explore atom-molecule and molecule-molecules collisions ([Hu et al., 2019](#); [Hudson et al., 2008](#); [Ulmanis et al., 2012](#); [Yang et al., 2019, 2022a,b](#)). At ultracold temperatures, reaction dynamics change significantly, offering an entry into ultracold chemistry ([Guo et al., 2018a](#); [Ospelkaus et al.,](#)

2010b). Furthermore, collisional dynamics can be precisely controlled using external conditions such as dc electric fields and optical confinement (de Miranda et al., 2011; Gregory et al., 2020; Ni et al., 2010). Additionally, dipolar molecules also hold great potential for studying many-body physics. By controlling their rotational states and employing optical lattice confinement, quantum simulations of lattice-spin models can be realized. (DeMille, 2002; Li et al., 2023a; Yan et al., 2013). Moreover, leveraging the rich internal structure of molecules, dipolar molecules serve as promising candidates for quantum information processing. Full control over nuclear spin states enables the creation of storage qubits (Gregory et al., 2021). Additionally, their sensitivity to energy shifts in rotational levels makes them an ideal platform for precision measurements, such as determining the electron electric dipole moment (ACME collaboration et al., 2014; Andreev et al., 2018; Cairncross et al., 2017; DeMille et al., 2008; Roussy et al., 2023).

1.2. Creation of Ground State Molecules

There are two main methods to create ultracold ground state molecules. The first involves direct cooling of molecules using techniques such as laser cooling (Anderegg et al., 2017; Augenbraun et al., 2023; Fitch and Tarbutt, 2021; Shuman et al., 2010), Stark deceleration (Bethlem et al., 1999, 2000), or cryogenic buffer-gas cooling (Weinstein et al., 1998). These approaches typically cool molecules to submillikelvin temperatures. The second, and more widely adopted protocol for producing ultracold polar molecules, which can be achieved with high phase-space density later, is a two-step coherent transfer process. In the two-step method, the pre-cooled bi-alkali atomic mixtures are first associated into the weakly-bound Feshbach molecules via magneto-association (Köhler et al., 2006; Takekoshi et al., 2012; Wang et al., 2015; Wu et al., 2012; Zirbel et al., 2008). Then, these molecules in the Feshbach state are coherently transferred to the rovibrational ground state using a two-photon Raman process. This approach was first demonstrated by Ni et al. (2008) with $^{40}\text{K}^{87}\text{Rb}$ molecules. Subsequently, following same procedures, rovibrational ground state molecules of various species, including $^{23}\text{Na}^{40}\text{K}$, $^{23}\text{Na}^{39}\text{K}$, $^{87}\text{Rb}^{137}\text{Cs}$, $^{23}\text{Na}^{87}\text{Rb}$, $^{23}\text{Na}^{137}\text{Cs}$, $^{23}\text{Na}^6\text{Li}$ have also been successfully created. (Cairncross et al., 2021; Guo et al., 2016; Liu et al., 2019; Molony et al., 2014; Park et al., 2015a; Rvachov et al., 2017; Seeßelberg et al., 2018a; Stevenson et al., 2023; Takekoshi et al., 2014; Voges et al., 2020b). Recently, we demonstrated the creation of

ground state ${}^6\text{Li}{}^{40}\text{K}$ (He et al., 2024). Notably, since both the association and transfer processes are adiabatic, the temperature of molecules remains consistent with the temperature of the atomic mixture. By applying evaporative cooling to molecular samples, it allows the achievement of the first degenerate quantum gas of ${}^{40}\text{K}{}^{87}\text{Rb}$ (Valtolina et al., 2020) and first polar molecular BEC of ${}^{23}\text{Na}{}^{137}\text{Cs}$ (Bigagli et al., 2024).

A key focus is how to efficiently generate ground state molecules. In the two-step process, the overall efficiency is limited by each individual step. In the first step the efficiency of Feshbach molecule formation is typically below 50% in optical traps (Heo et al., 2012; Köppinger et al., 2014; Ospelkaus et al., 2006; Takekoshi et al., 2014; Wang et al., 2015; Weber et al., 2008; Wu et al., 2012), meaning that less than half of the atomic mixture is converted into molecules. The remaining atoms can introduce undesired atom-molecule collisions, leading fast decay of the molecular sample. To improve the association efficiency, a bichromatic optical trap (Duda et al., 2023) or an optical lattice (Covey et al., 2016) can be employed to enhance the density overlap of the atomic mixture. These methods can increase the association efficiency to $80 \sim 100\%$.

The second step is constrained by the STIRAP transfer efficiency (η), which has been reported to range between 50-93% (Bause et al., 2021; Guo et al., 2018a; Li et al., 2023b). As proposed by Yatsenko et al. (2014), the phase noise of the Raman laser has a detrimental effect on the transfer efficiency, particularly when the intermediate state used in the STIRAP process has a large linewidth. By suppressing the phase noise using a long external cavity ECDL design (Riehle, 2003) or a feedforward noise cancellation system (Chao et al., 2024; Li et al., 2022), the STIRAP efficiency can be improved to $96 \sim 99\%$ (He et al., 2024; Maddox et al., 2024). The results of the STIRAP efficiency are presented in Table 1.1, demonstrating that one of the highest STIRAP transfer efficiencies among bialkali species has been achieved in this work.

Studying quantum phenomena in degenerate molecular samples not only requires efficient production, but also sufficient sample lifetimes. One of the main challenges with dipolar molecules is their rapid decay. For some bi-alkali species chemically reactive two-body collisions (Żuchowski and Hutson, 2010) lead to significant losses (Ni et al., 2010). Even for chemically stable bi-alkali species, collisional losses can occur due to so-called *sticky* collisions. In this process, two molecules can be excited by the optical trapping light and form a

Species	Excited State	η	reference
${}^6\text{Li}{}^{40}\text{K}$	$\text{A}^1\Sigma$	96(4)%	This work
${}^{23}\text{Na}{}^{40}\text{K}$	$\text{c}^3\Sigma^+ \sim \text{B}^1\Pi$	75 – 80%	Bause et al. (2021) ; Liu et al. (2019) ; Park et al. (2015a)
${}^{23}\text{Na}{}^{40}\text{K}$	$\text{d}^3\Pi \sim \text{D}^1\Pi$	50%	Seeßelberg et al. (2018a)
${}^{23}\text{Na}{}^{39}\text{K}$	$\text{c}^3\Sigma^+ \sim \text{B}^1\Pi$	70%	Voges et al. (2020b)
${}^{23}\text{Na}{}^{87}\text{Rb}$	$\text{A}^1\Sigma^+ \sim \text{b}^3\Pi$	93%	Guo et al. (2016) ; Ye et al. (2018)
${}^{23}\text{Na}{}^{133}\text{Cs}$	$\text{B}^1\Pi$	55(3)%	Stevenson et al. (2023)
${}^{40}\text{K}{}^{87}\text{Rb}$	$\text{2}^3\Sigma^+ \sim \text{1}^1\Pi$	89(4)%	Ni et al. (2008)
${}^{87}\text{Rb}{}^{133}\text{Cs}$	$\text{A}^1\Sigma^+ \sim \text{b}^3\Pi$	98.7(1)%	Maddox et al. (2024) ; Molony et al. (2014) ; Takekoshi et al. (2014)
${}^{23}\text{Na}{}^6\text{Li}$	$\text{c}^3\Sigma^+$	86%	Rvachov et al. (2017)

Table 1.1.: A collection of the STIRAP efficiency (η) achieved for different molecular species is presented. This work has achieved one of the highest efficiencies among all species. More details are shown in Table B.1.

long-lived collisional complex ([Christianen et al., 2019](#); [Gersema et al., 2021](#); [Gregory et al., 2020](#); [Mayle et al., 2012, 2013](#)). Detrimental effects due to those inelastic collisional loss can be mitigated in several ways. When molecules are trapped in a deep optical lattice or an optical tweezer array, two-body collisions are prevented by the suppression of tunneling ([Yan et al., 2013](#)). Also, by controlling the dipole-dipole interactions with static electric fields ([Matsuda et al., 2020](#)), or microwave fields ([Anderegg et al., 2021](#); [Bigagli et al., 2023a](#); [Karman and Hutson, 2018, 2019](#); [Lin et al., 2023](#)), the inelastic collisions can also be significantly suppressed, which based on the formation of a repulsive potential between two dressed molecules induced by the external field. The shielding method requires a coherent control of the hyperfine structures of the ground state ([Will et al., 2016](#)), and dipolar collisions of molecules induced by MW signals have been observed with ${}^{23}\text{Na}{}^{40}\text{K}$ and ${}^{23}\text{Na}{}^{87}\text{Rb}$ ([He et al., 2021](#); [Yan et al., 2020](#)).

1.3. Optical Lattice

Optical lattices provide precise control over trapping potentials and enable the creation of periodic potentials that closely resemble those in crystalline condensed matter systems ([Kimura and Itikawa, 2000](#)). Additionally, optical lattices serve as a versatile toolbox for quantum simulations ([Schr et al., 2020](#)), where lattice-spin model simulations have already been demon-

strated and successfully implemented. (Barnett et al., 2006; Micheli et al., 2006; Yan et al., 2013). With sufficiently deep lattices, the lifetime of molecules can be significantly extended by suppressing two-body collisions. In this case, understanding loading strategies and interspecies interactions within optical lattices become critical. The creation of doubly-occupied lattice sites (doublons) has been extensively studied in ultracold Bose-Fermi mixtures (e.g., $^{40}\text{K} - ^{87}\text{Rb}$) (Covey et al., 2016; Safavi-Naini et al., 2015), Bose-Bose mixtures (e.g., $^{87}\text{Rb} - ^{23}\text{Na}$ and $^{87}\text{Rb} - ^{87}\text{Rb}$) using the Bose-Hubbard model (Lin et al., 2022; Winkler et al., 2006), and Fermi-Fermi mixtures (e.g., $^{40}\text{K} - ^{40}\text{K}$ and $^6\text{Li} - ^6\text{Li}$) within the Fermi-Hubbard model (Jordens et al., 2008; Parsons et al., 2016; Sensarma et al., 2010). Notably, previous studies on Fermi-Fermi mixtures have primarily investigated doublons formed by fermions of the same species in a spin mixed states. In contrast, our experiment focuses on the ^6Li and ^{40}K mixture, which uniquely forms doublons from two different fermion species with imbalanced mass properties. Also, the $^6\text{Li} - ^{40}\text{K}$ offers the prospect of achieving a high lattice filling factor by starting the conversion to Feshbach molecules from a dual fermionic band insulator (Hackermüller et al., 2010; Schneider et al., 2008), without the need to achieve a Mott insulator phase (Sugawa et al., 2011).

Additionally, by tuning the optical trap to a wavelength where the polarizabilities of the target states are identical, so called "magic-wavelength" trapping conditions can be achieved. Under these conditions, second-scale coherence between hyperfine states has been observed (Gregory et al., 2021; Lin et al., 2022; Park et al., 2017). Furthermore, rotational coherence time has been extended to the order of seconds for ground state molecules such as $^{87}\text{Rb}^{137}\text{Cs}$ (Gregory et al., 2024). This magic-wavelength technique can also be applied to optical lattice, offering enhanced control and stability for molecular systems (Christakis et al., 2023; Lin et al., 2022).

1.4. Thesis Outline

$^6\text{Li}^{40}\text{K}$ is predicted with a large electric dipole moment of 3.6 Debye in the rovibrational ground state, making it an excellent candidate for studying many-body physics involving DDI. In addition, when $^6\text{Li}^{40}\text{K}$ is loaded into an optical lattice with 532 nm spacing, the corresponding dipole interaction energy is approximately $k_{\text{B}} \times 600 \text{ nK}$, which is comparable to the temperature of the atomic mixture after evaporative cooling.

Based on the previous work of exploring a singlet pathway from the Feshbach state to the ground state (Sofia, 2022; Yang, 2021b), this thesis focuses on the creation of the ground state ${}^6\text{Li}{}^{40}\text{K}$ molecules via a STIRAP process with high transfer efficiency. Leveraging the precision laser spectroscopy results for the molecular structure and the Raman laser setups for generating STIRAP pulses, a high one-way transfer efficiency up to 96(4)% is achieved. During the efficiency analysis, it is demonstrated that the phase noise of the Raman lasers has a detrimental effect on the STIRAP process, primarily due to the large linewidth of the intermediate state. To address this, modifications to the laser system are implemented to suppress phase noise and improve transfer performance. Also, the properties of the ground stated ${}^6\text{Li}{}^{40}\text{K}$ are investigated, including the lifetime, permanent dipole moment, and the rotational spectroscopy. A 3D optical lattice is also constructed during this PhD period, laying the groundwork for future studies into dipolar systems and quantum many-body physics.

In Chapter 2, the necessary theoretical background for understanding the experiments is presented. The basics of the three-level system utilizing STIRAP are introduced, followed by a discussion on the selection of the singlet pathway. An extension of the three-level system to a multi-level system with decoherence is also described. Additionally, the foundational concepts of an optically plugged trap and optical lattice are explained.

In Chapter 3, the updates made to the experimental apparatus and procedures to facilitate the efficient creation of ground state ${}^6\text{Li}{}^{40}\text{K}$ molecules are detailed. The setups for the optically plugged trap and the free-space 3D optical lattice are also included.

In Chapter 4, the process of creating ground state ${}^6\text{Li}{}^{40}\text{K}$ with high efficiency is described. Starting with the calibration of transition frequencies and strengths, the STIRAP process is used to achieve a one-way transfer efficiency of 96(4)%. The factors influencing the transfer efficiency, such as adiabatic conditions, laser phase noise, frequency detuning, laser polarization impurities, and magnetic fields for Feshbach association, are analyzed.

In Chapter 5, the properties of the ground state molecules are discussed. The temperature and lifetime measurements are used to extract the decay rate constant of the ground state ${}^6\text{Li}{}^{40}\text{K}$, which is comparable to the theoretically predicted universal rate. Also, the permanent dipole moment is extracted from ac Stark shift measurements in an external electric field.

Additionally, the rotational spectroscopy of the vibrational ground state is scanned in the ODT to estimate the transition frequency, and the reasons for short coherence time are proposed.

In Chapter 6, the initial construction of a 3D optical lattice is shown. The challenges in overlapping the lattice beams are discussed. The existence of the optical lattice is verified through the observation of superfluidity and band mapping. Kapitza-Dirac scattering is measured to calibrate the lattice trap depth, and then the Feshbach association of the molecules within the lattice is explored.

In Chapter 7, the conclusion of this work and an outlook on future studies are provided. The implementation of MW shielding and deep optical lattice in future experiments is expected to suppress inelastic collisions and extend the lifetime of ground state molecules.

In this thesis, the work for the efficient creation of ground state ${}^6\text{Li}{}^{40}\text{K}$ molecules has been published in "Efficient Creation of Ultracold Ground State ${}^6\text{Li}{}^{40}\text{K}$ Polar Molecules.", He, C., Nie, X., Avalos, V., Botsi, S., Kumar, S., Yang, A., Dieckmann, K. *Physical Review Letters*, **132**(24), 243401(2024) ([He et al., 2024](#)).

Further details on improving STIRAP efficiency will be published in: "Improving STIRAP Efficiency for Ultracold Ground State ${}^6\text{Li}{}^{40}\text{K}$ Molecules.", Yang, A., He, C., Nie, X., Avalos, V., Botsi, S., Kumar, S., Dieckmann, K. *preprint* (2025) ([Yang et al., 2025](#)).

Additionally, the phase noise measurement in this thesis has contributed to the publication: "Field-programmable-gate-array-based digital frequency stabilization of low-phase-noise diode lasers.", Avalos, V., Nie, X., Yang, A., He, C., Kumar, S., Dieckmann, K. *Review of Scientific Instruments*, **94**(6), (2023) ([Avalos et al., 2023](#)).

2. Theoretical Background

This chapter introduces the basic theories for our experiments with ultracold ${}^6\text{Li}{}^{40}\text{K}$ molecules. Firstly, the STIRAP process in a three-level system is explained. A singlet pathway method is applied to locate the three-level system. This is followed by a discussion on the extension to a multi-level system with spontaneous decay. Next, the optically plugged trap is discussed, which is designed to reduce the time required for each experimental cycle. The potential of a plugged trap and its trapping frequencies are reviewed in detail. Finally, a brief overview of an optical lattice is provided. The ${}^6\text{Li}{}^{40}\text{K}$ molecules are expected to be loaded into a 3D optical lattice to prevent chemical loss. The trapping potential and band structures of an optical lattice are also included in the discussion.

2.1. STIRAP Process

As discussed in the introduction, two-photon Raman processes including STIRAP and off-resonance Raman transfer are adapted to produce ultracold polar molecules with high phase-space density ([Bergmann et al., 2019](#); [Vitanov et al., 2017](#)). The two coherent methods offer several advantages: the transfer is state-selective, efficient, and can remove energy difference via state transfer (from weakly-bound molecular state to deeply bound molecular state). To discuss the transfer process, a three-level system is considered first. The reason is that the direct transition from the Feshbach molecular state to the ro-vibrational ground state is forbidden mainly due to electric dipole selection rule. Hence, an intermediate state is selected to facilitate the coupling between the Feshbach state and ground state, thus forming a three-level system. In this section, I first discuss the typical three-level system, and the coherent STIRAP transfer process. This is followed by an illustration of the singlet pathway method and the development of a four-level system with decoherence.

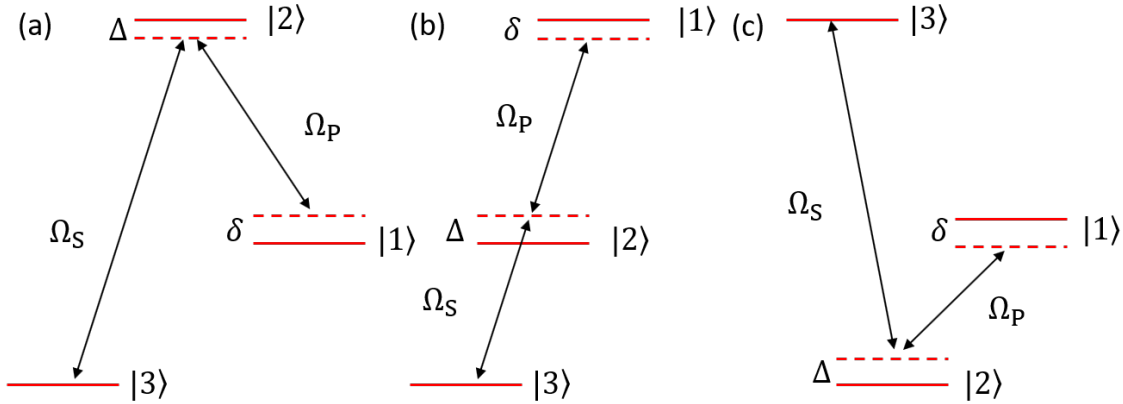


Figure 2.1.: Scheme of three-level system in different configurations. (a) Λ -type three-level system. (b) Ladder-type three level system. (c) V -type three level system. The δ and Δ represent the two-photon detuning and single-photon detuning of the three-level systems. Ω_p and Ω_s are the Rabi frequencies of external laser fields

2.1.1. Three-Level System

The basic three-level systems involves electric dipole couplings between three quantum states. As illustrated in Fig. 2.1, there are three possible configurations of the three-level systems: Λ -type, Ladder-type, and V -type. The figure also depicts the two-photon detuning δ and single-photon detuning Δ , along with the two external coherent laser fields labeled as Pump and Stokes. The following section focuses on the Λ -type system, which is used in our experiments.

Fig. 2.1 (a) shows the Λ -type three-level system. The states $|1\rangle$ and $|3\rangle$ represent the initial Feshbach state and rovibrational ground state, while $|2\rangle$ serves as the intermediate state. The energy differences between these states result from variations in the electronic states as well as the vibrational and rotational levels of the molecule. For the transition between $|1\rangle$ and $|2\rangle$, the energy difference is denoted as $\hbar\omega_{12}$. Similarly, for the transition between $|3\rangle$ and $|2\rangle$, the energy difference is denoted as $\hbar\omega_{23}$. Two lasers, named as Pump and Stokes, couple the state $|1\rangle$ to $|2\rangle$ with frequency ω_p and state $|3\rangle$ to $|2\rangle$ with frequency ω_s . Using the Rotating-Wave Approximation (RWA) (Shore, 1991), the Hamiltonian of this three-level system can be expressed as (Shore, 2013)

$$H(t) = \hbar \begin{pmatrix} 0 & \frac{1}{2}\Omega_p(t) & 0 \\ \frac{1}{2}\Omega_p(t) & \Delta & \frac{1}{2}\Omega_s(t) \\ 0 & \frac{1}{2}\Omega_s(t) & \delta \end{pmatrix}, \quad (2.1)$$

where $\Omega_p(t)$ and $\Omega_s(t)$ are the Rabi frequencies of Pump and Stokes laser varying with time t . The laser detunings for Pump laser is defined as $\Delta_p \equiv \omega_p - \omega_{12}$ and for the Stokes laser it is $\Delta_s \equiv \omega_s - \omega_{23}$. The two-photon detuning $\delta = \Delta_p - \Delta_s$ is typically set to zero for STIRAP and off-resonance Raman processes. Consequently, the single-photon detuning Δ is defined as $\Delta \equiv \Delta_p \equiv \Delta_s$.

Within the RWA, the rapid oscillation carrier frequencies $\omega_{p,s}$ are eliminated from the Pump and Stokes electric fields ($\mathbf{E}_{p,s} = \text{Re}(\mathbf{e}\epsilon_{p,s}(t)e^{-i\omega_{p,s}t+i\phi_{p,s}})$, where \mathbf{e} is the unit vector and $\phi_{p,s}$ is the phase), leaving only the slowly varying electric field amplitudes $\epsilon_{p,s}(t)$ that do not vanish. Then the time varying Rabi frequencies $\Omega_p(t)$ and $\Omega_s(t)$ are given by

$$\begin{aligned} \hbar\Omega_p(t) &= -d_{12}\epsilon_p(t) & , \\ \hbar\Omega_s(t) &= -d_{23}\epsilon_s(t) & . \end{aligned} \quad (2.2)$$

where d_{12} and d_{23} are the elements of transition dipole moment for the $1 \leftrightarrow 2$ and $2 \leftrightarrow 3$ transitions.

When the $\delta = 0$ condition is applied, the eigenstates of Hamiltonian Eqn. (2.1) are expressed as

$$|+\rangle = \sin \theta \sin \phi |1\rangle + \cos \phi |2\rangle + \cos \theta \sin \phi |3\rangle \quad (2.3)$$

$$|\psi_{\text{dark}}\rangle = \cos \theta |1\rangle - \sin \theta |3\rangle \quad (2.4)$$

$$|-\rangle = \sin \theta \cos \phi |1\rangle - \cos \phi |2\rangle + \cos \theta \sin \phi |3\rangle . \quad (2.5)$$

Here, θ and ϕ are the mixing angles, which can be defined as

$$\tan \theta(t) = \frac{\Omega_p(t)}{\Omega_s(t)} \quad (2.6)$$

$$\tan 2\phi(t) = \frac{\sqrt{\Omega_p(t)^2 + \Omega_s(t)^2}}{\Delta} \quad . \quad (2.7)$$

It is noteworthy that one of the eigenstate, $|\psi_{\text{dark}}\rangle$, of the Hamiltonian is a superposition of the two ground state $|1\rangle$ and $|3\rangle$, which is free from light scattering. The excited state $|2\rangle$, acting as intermediate state, typically has a lifetime in nanosecond or microsecond scale. Due to the rich internal molecular energy levels, the decay from the excited state can cause population to drop out of the three-level system entirely. Any population in the excited state $|2\rangle$ could lead to the loss of molecules from the system. By adjusting the ratio of the Rabi frequencies Ω_p and Ω_s , the mixing angle θ can be controlled to coherently transfer the population of molecules between $|1\rangle$ and $|3\rangle$ through the dark state, without populating the state $|2\rangle$.

The application of the dark state relies on the resonance condition where two-photon detuning $\delta = 0$. Any deviation from this resonance leads to populating the excited state $|2\rangle$, resulting in decoherence of the system. For the single-photon detuning Δ , there is no strict resonance requirement in the ideal three-level system. The off-resonance condition for Δ will be discussed in later section.

2.1.2. STIRAP Process

To transfer population between two quantum states $|1\rangle$ and $|3\rangle$, which is dipole-forbidden for direction coupling, STIRAP is applied. STIRAP achieves the transfer via a two-photon process involving two lasers, Pump and Stokes. The dipole coupling between $|1\rangle$ and $|3\rangle$ is mediated via an intermediate state $|2\rangle$. As mentioned in the last section, the application of dark state ensures that no population occupies the intermediate state $|2\rangle$, thereby avoiding spontaneous emission losses or other decay processes. Based on Eqn. (2.6), the mixing angle θ can be manipulated by adjusting the powers of the Pump and Stokes lasers. Starting with zero Pump power and nonzero Stokes power ($\theta = 0$), the dark state $|\psi_{\text{dark}}\rangle$ is initially in the pure state $|1\rangle$. By adiabatically increasing the Pump power while simultaneously decreasing the Stokes power, $|\psi_{\text{dark}}\rangle$ evolves into a coherent superposition of $|1\rangle$ and $|3\rangle$. Finally, by

reducing the Stokes power to zero while keeping the Pump power nonzero, $|\psi_{\text{dark}}\rangle$ transitions to the pure state $|3\rangle$ with $\theta = \pi/2$. The adiabatic process avoids system heating and prevents the population from leaving the dark state. To satisfy the adiabatic criteria for STIRAP, the rate of change of the mixing angle θ must adhere to a local adiabatic condition, as provided by (Kuklinski et al., 1989)

$$\Omega_{\text{rms}}(t) \gg |\dot{\theta}(t)| = \frac{|\Omega_s(t)\dot{\Omega}_p(t) - \Omega_p(t)\dot{\Omega}_s(t)|}{\Omega_p^2 + \Omega_s^2} , \quad (2.8)$$

where the root-mean squared Rabi frequency $\Omega_{\text{rms}}(t) = \sqrt{\Omega_p(t)^2 + \Omega_s(t)^2}$. With the satisfaction of the criteria, the population transfer is robust against the fluctuations of experimental conditions, such as pulse duration and spatial and time difference of laser intensity. With $\int_{-\infty}^{\infty} |\dot{\theta}(t)| dt = \frac{\pi}{2}$, the global adiabatic criteria is then given by

$$\Omega_{\text{peak}}T \geq \int_{-\infty}^{\infty} \Omega_{\text{rms}}(t) dt = \int_{-\infty}^{\infty} \sqrt{\Omega_p(t)^2 + \Omega_s(t)^2} dt \gg \frac{\pi}{2} . \quad (2.9)$$

In STIRAP, Ω_{peak} represents the maximum Rabi frequency during the process, and T is the duration of STIRAP pulse. The global adiabatic criteria depends on the pulse shape and indicates that achieving efficient transfer requires a long pulse duration and high laser intensities. In practice, $\Omega_{\text{peak}}T \geq 3\pi$ is utilized to ensure more than 95% population transfer efficiency (Vitanov et al., 2017). Further discussions on the violation of adiabaticity and its effect on transfer efficiency are provided in Section 4.4.

2.1.3. Singlet Pathway

Achieving high transfer efficiency in STIRAP relies on carefully selecting the initial and intermediate states for the three-level system, which requires studying the molecular structure and identifying a suitable electronically excited state. Typically, an excited state with a mixture of singlet and triplet character is utilized. This strategy, first implemented by Ni et al. (2008) for KRb, has been adopted in most subsequent experiments. It enables coherent transfer from a triplet character Feshbach state to the singlet ground state. To fully control the molecular state, it is crucial to identify the spectroscopically resolved hyperfine components of the excited state. Otherwise, the undesired coupling to unresolved hyperfine components can significantly reduce STIRAP efficiency (Vitanov and Stenholm, 1999). Locating an excited

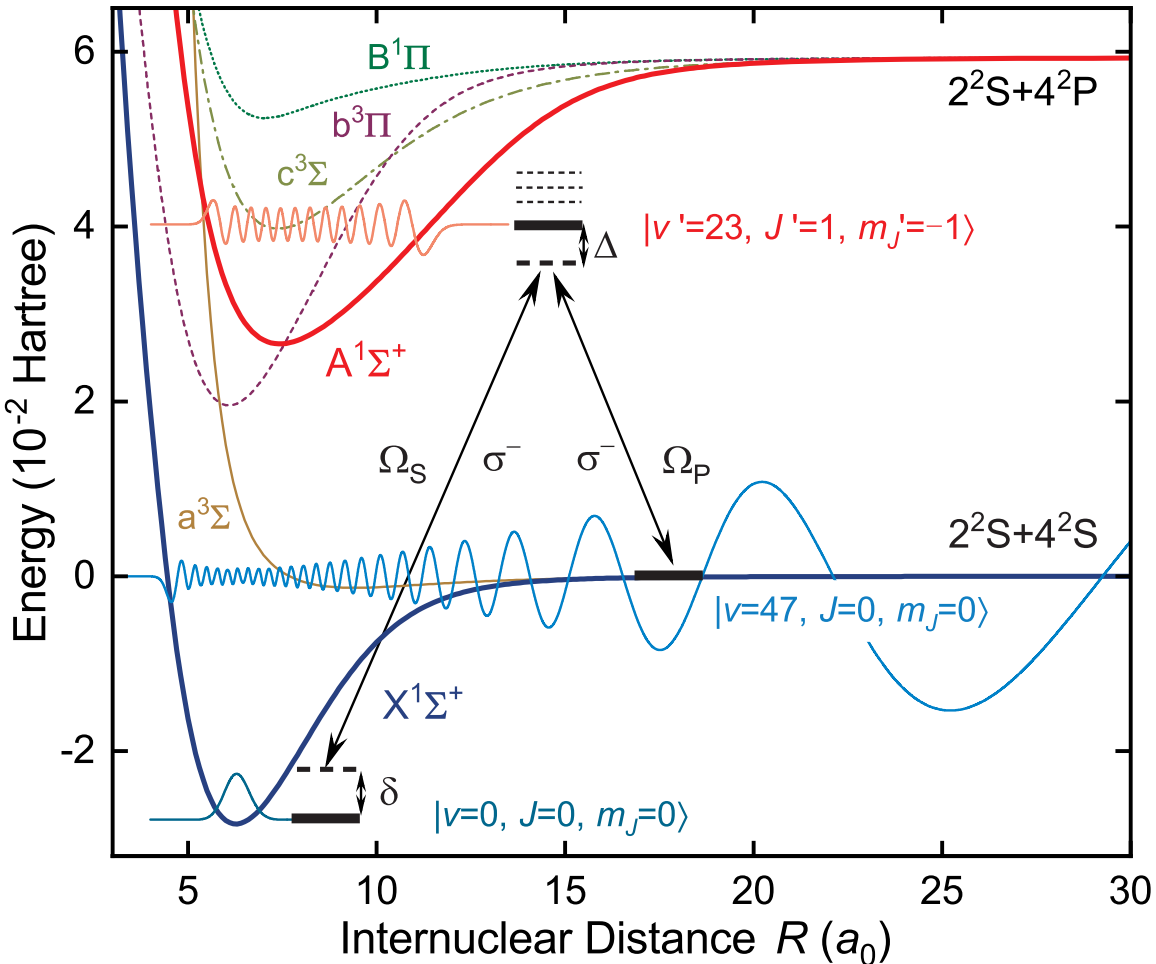


Figure 2.2.: Adiabatic potential energy curves of ${}^6\text{Li}{}^{40}\text{K}$. By employing STIRAP with the singlet pathway, the Feshbach molecules are transferred to the ro-vibrational ground state of the $\text{X}^1\Sigma^+$ potential via the $\text{A}^1\Sigma^+$ potential. The parameters relevant for STIRAP are the Rabi frequencies of Pump and Stokes laser denoted by Ω_p and Ω_s and the one-photon and two-photon detunings Δ and δ . Polarizations of the Raman laser beams are relative to the quantization axis of the magnetic field, which is σ^- . Figure is taken from [He et al. \(2024\)](#)

state where triplet admixture results in substantial hyperfine splitting and singlet admixture is sufficiently strong to couple to the ground state involves extra efforts in resolving the spectroscopy ([Debatin et al., 2011](#); [Guo, 2017](#); [Kotochigova et al., 2009](#); [Park et al., 2015b](#); [Rvachov et al., 2018b](#); [Zabawa et al., 2011](#)). Moreover, even with fully resolved hyperfine structure, off-resonance coupling to the hyperfine components of the excited state can lead to an undesired superposition of hyperfine components in the ground state ([Liu et al., 2019](#)).

In our experiments, a singlet pathway method ([Yang et al., 2020](#)) is proposed to avoid the need for spectroscopically resolving mixed hyperfine components. The singlet pathway relies on singlet-to-singlet transitions from both the Feshbach state and the ground state to the excited state. The relevant potential curves are shown in Fig. 2.2. For achieving the

desired Feshbach state, the ${}^6\text{Li}$ and ${}^{40}\text{K}$ atoms are prepared in $|F_{\text{Li}} = 1/2, m_{F,\text{Li}} = -1/2\rangle$ and $|F_{\text{K}} = 9/2, m_{F,\text{K}} = -9/2\rangle$ states, where F and m_F denote the hyperfine quantum number and its projection. The Feshbach state is then associated at the resonance of 215.6 G. For this narrow Feshbach resonance, closed-channel dominated molecules are created with a total projection quantum number of $M = -5$. This Feshbach state shows a strong singlet character (52%), which is contributed by only one hyperfine component $(|J = 0, m_J = 0, S = 0, m_S = 0, N = 0, m_N = 0, m_{I,\text{Li}} = -1, m_{I,\text{K}} = -4\rangle)$ with fully-stretched nuclear spins ($I_{\text{Li}} = 1$ and $I_{\text{K}} = 4$). Here, J and m_J are the total angular momentum and its magnetic quantum numbers, S and m_s are the spin quantum number of electron and its projection; N and m_N represent the molecular rotation angular momentum and its projection on the magnetic guiding field axis, and $m_{I,\text{Li}}$ ($m_{I,\text{K}}$) is the projection of the Li (K) nuclear spin. This Feshbach state $\text{X}^1\Sigma^+ |v = 47, J = 0, m_J = 0, m_{I,\text{Li}} = -1, m_{I,\text{K}} = -4\rangle$ serves as an excellent starting point for identifying the intermediate state in the $\text{A}^1\Sigma^+$ potential (v is the vibrational quantum number).

Next, a excited state in $\text{A}^1\Sigma^+$ potential is chosen as the intermediate state. Start with $M = -5$ for the initial Feshbach state, M' of the excited intermediate state can take the values of -4 , -5 , and -6 depending on the Pump laser polarization (σ^+ , π , and σ^-). According to the selection rule for total angular momentum J , $\Delta J = 0, \pm 1$, except for $J = 0 \rightarrow J' = 0$ in a dipole transition. Therefore $J' = 1$ is selected with m_J taking values of $0, \pm 1$. Since $M' = m'_J + m'_{I,\text{Li}} + m'_{I,\text{K}}$, there are six combinations of the hyperfine components for $M' = -4$ with σ^+ polarized light three combinations for $M' = -5$ with π polarized light, and only one fully-stretched hyperfine component for $M' = -6$ with σ^- polarized light: $|J' = 1, m'_J = -1, m_{I,\text{Li}} = -1, m_{I,\text{K}} = -4\rangle$. By using σ^- -polarized light for the Pump transition from the Feshbach to the excited state we ensure that only this fully-stretched hyperfine component ($|1, -1, -1, -4\rangle$) is addressed. This choice prevents coupling to other unresolved hyperfine states. Additionally, the singlet component of the Feshbach state imposes the condition $\Delta S = 0$ for the intermediate state, making the rotationally excited state $N' = J' = 1$ the only viable candidate, where $m'_N = m'_J = -1$.

A similar analysis applies to the rovibrational ground state at $\text{X}^1\Sigma^+$ potential. The total projection quantum number for the ground state is given by $M'' = m''_J + m_{I,\text{Li}} + m_{I,\text{K}}$. Considering $M' = -6$ for intermediate state, M'' must be -5 for the ground state. With

condition $J'' = 0$ and $m_J'' = 0$, the only possible combination for $M'' = -5$ is the fully-stretched state $|J = 0, m_J = 0, m_{I,\text{Li}} = -1, m_{I,\text{K}} = -4\rangle$. Therefore, σ^- -polarized Stokes light is applied to drive the transition from the ground state to the excited state.

The next step is to determine the vibrational level v' of the excited state. The Franck-Condon Factors (FCFs) are calculated for Pump and Stokes transitions for different v' . Details and results can be found in [Yang \(2021b\)](#) or [Yang et al. \(2022a\)](#), where $v' = 23$ is chosen as the target intermediate state. Also in experiments, the normalized Rabi frequency for Pump and Stokes transitions are measured and fitted from single-photon spectroscopy and dark resonance spectroscopy. The values are further verified by the off-Resonance Raman oscillation results. The results are shown in Section [4.1](#).

In summary, three fully-stretched states, $X^1\Sigma^+ |v = 47, J = 0, m_J = 0, m_{I,\text{Li}} = -1, m_{I,\text{K}} = -4\rangle$ for Feshbach state, $A^1\Sigma^+ |v' = 23, J' = 1, m_J' = -1, m_{I,\text{Li}} = -1, m_{I,\text{K}} = -4\rangle$ for excited state, and $X^1\Sigma^+ |v'' = 0, J'' = 0, m_J'' = 0, m_{I,\text{Li}} = -1, m_{I,\text{K}} = -4\rangle$ for ground state are selected to achieve an ideal three-level system. σ^- polarized Pump and Stokes light are employed to maintain the fully-stretched states during the transfer process. With the singlet pathway method, this configuration is expected to yield high transfer efficiency.

2.1.4. Extend to Multi-Level System with Decoherence

The transfer scheme for the ground state molecules can be regard as an ideal three-level system based on the selection of the singlet pathway, as discussed in previous section. However, in actual experiments it is challenging to fully satisfy the requirements of an ideal three-level system. For instance, achieving the transition between the full-stretched states requires the application of purely σ^- -polarized. Despite careful polarization control of the Raman beams, the power in the undesired polarization component can still amount to approximately 2% of the total laser power. This results in an undesired coupling strength of $\sim 0.1\Omega_{s/p}(t)$ to the wrong hyperfine components of the excited state. Due to the weak hyperfine interactions of the $A^1\Sigma^+$ potential ([Yang et al., 2020](#)), the hyperfine splitting of the excited state is not spectroscopically resolved. Consequently, when the single-photon detuning Δ is near 0, the undesired laser polarization component cause weak but resonant driving from the ground state to the wrong excited state. The population of this excited state introduces decoherence into the system.

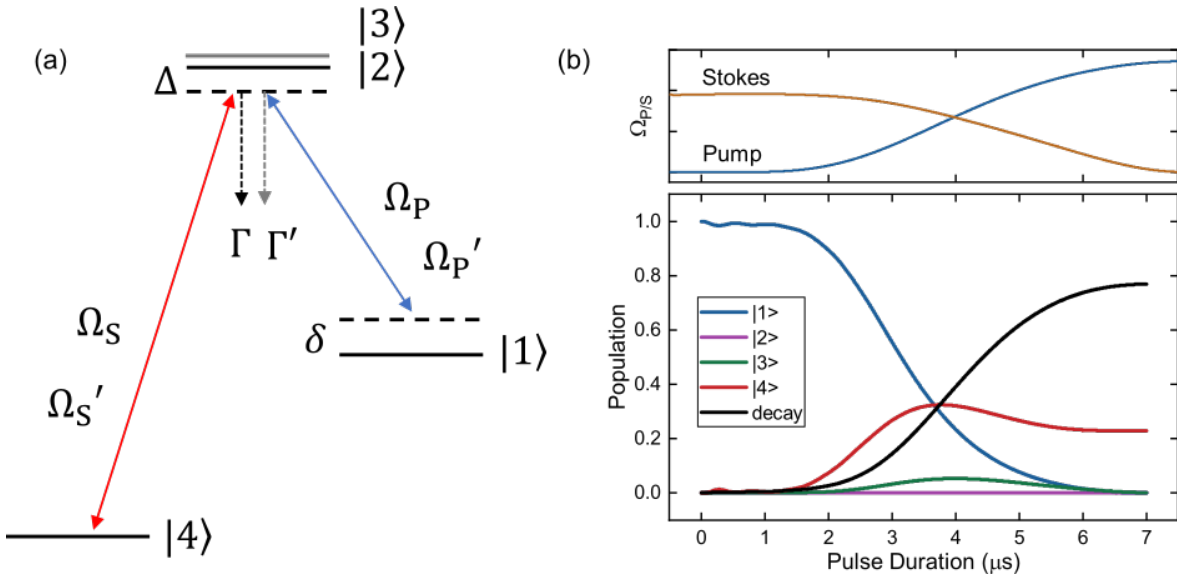


Figure 2.3.: (a) The four-level scheme with spontaneous decay. The decay rates from state \$|2\rangle\$ and \$|3\rangle\$ are labeled as \$\Gamma\$ and \$\Gamma'\$. (b) Population for state \$|1\rangle\$ to state \$|4\rangle\$ during a STIRAP process. The population decay out of the system is presented in solid black line. The pulse shapes of Pump and Stokes are shown above. The parameters are specially manipulated to show a much clear signal for population transfer between different states. The single-photon detuning is set to 0 MHz, the decay rate is set to 1 MHz, \$\Omega'_p = 0.2\Omega_p\$, and \$\Omega'_s = 0.1\Omega_s\$.

To describe the multi-level system with decoherence, a simplified model is presented in Fig. 2.3 (a), illustrating an extended four-level system based on our experiments. This four-level system consists of two closely separated excited state, \$|2\rangle\$ and \$|3\rangle\$, the initial Feshbach state \$|1\rangle\$, and the ground state \$|4\rangle\$. Two external fields Pumps and Stokes couple the ground state and Feshbach state to the excited states. And the decoherence effects are accounted by the optical Bloch equation (OBE) ([Arecchi and Bonifacio, 1965](#))

$$\dot{\rho} = -\frac{i}{\hbar}[H, \rho] + \Gamma(\rho) \quad , \quad (2.10)$$

where \$H\$ is the Hamiltonian of the four-level system, \$\rho\$ is the density matrix describe the population and coherence of the system, and \$\Gamma(\rho)\$ represents the decoherence of the involved energy levels. Similar to the three-level system, the Hamiltonian is written as

$$\mathbf{H}(t) = \frac{\hbar}{2} \begin{bmatrix} 2\delta & \Omega_p(t) & \Omega'_p(t) & 0 \\ \Omega_p(t) & 2\Delta & 0 & \Omega_s(t) \\ \Omega'_p(t) & 0 & 2\Delta_1 & \Omega'_s(t) \\ 0 & \Omega_s(t) & \Omega'_s(t) & 0 \end{bmatrix} . \quad (2.11)$$

The $\Omega'_p(t)$ and $\Omega'_s(t)$ is the time varying Rabi frequency for the second excited state. The Δ_1 is the single-photon detuning when coupling to the second excited state. $\Gamma(\rho)$ describes the effect of decoherence due to spontaneous emission from the population in excited states $|2\rangle$ and $|3\rangle$

$$\Gamma(\rho) = \begin{bmatrix} 0 & -\frac{\Gamma}{2}\rho_{12} & -\frac{\Gamma'}{2}\rho_{13} & 0 \\ -\frac{\Gamma}{2}\rho_{21} & -\Gamma\rho_{22} & 0 & -\frac{\Gamma}{2}\rho_{24} \\ -\frac{\Gamma'}{2}\rho_{31} & 0 & -\Gamma'\rho_{33} & -\frac{\Gamma'}{2}\rho_{34} \\ 0 & -\frac{\Gamma}{2}\rho_{42} & -\frac{\Gamma'}{2}\rho_{43} & 0 \end{bmatrix}. \quad (2.12)$$

ρ_{ij} are the matrix elements of the density matrix ρ . Γ and Γ' are the spontaneous decay rates for $|2\rangle$ and $|3\rangle$, which are assumed to have same value due to their close separation. The spontaneous decay leads to population loss in the system. By numerically solving Eqn. (2.10), we can simulate the transfer process. Fig. 2.3 (b) shows a population transfer for the four-level system via STIRAP process with specially designed parameters. Based on the parameter obtained from the experiments, the fit results agrees well with the measurement results in Section 4.3.2

Also, the system could be extended to N-level case with Hamiltonian ([Vitanov and Stenholm, 1999](#))

$$\mathbf{H} = \hbar \begin{bmatrix} \delta & \Omega_{p,1} & \Omega_{p,2} & \dots & \Omega_{p,N-1} & \Omega_{p,N} & 0 \\ \Omega_{p,1} & \Delta_1 & 0 & \dots & 0 & 0 & \Omega_{s,1} \\ \Omega_{p,2} & 0 & \Delta_2 & \dots & 0 & 0 & \Omega_{s,2} \\ \vdots & \vdots & \vdots & \ddots & \vdots & \vdots & \vdots \\ \Omega_{p,N-1} & 0 & 0 & \dots & \Delta_{N-1} & 0 & \Omega_{s,N-1} \\ \Omega_{p,N} & 0 & 0 & \dots & 0 & \Delta_N & \Omega_{s,N} \\ 0 & \Omega_{s,1} & \Omega_{s,2} & \dots & \Omega_{s,N-1} & \Omega_{s,N} & 0 \end{bmatrix}. \quad (2.13)$$

The index i from 1 to N indicates the i th state, with correspond Rabi frequency $\Omega_{s,i}$ and $\Omega_{p,i}$ and single-photon detuning Δ_i . The multi-level system is used to analysis the detuning effects in Section 4.4.5.

2.2. Optically Plugged Trap

An optically plugged trap (OPT) combines a quadrupole magnetic trap with a blue-detuned optical plug beam to prevent Majorana losses near the center of the trap. This setup enables tight confinement of neutral atoms, particularly at ultracold temperatures. In the following sections, the basic concepts of the trap and the calculation of the trapping potentials are presented.

2.2.1. Optical dipole potentials

Atoms exposed to a laser field experience a modification in their potential energy, the phenomenon is known as the ac Stark shift ([Foot, 2005](#)). For a two-level system, the potential generated by the laser beam varies spatially and is expressed as:

$$U_{dip} = -\frac{3\pi c^2}{2\omega_0^3} \left(\frac{\Gamma}{\omega_0 - \omega} + \frac{\Gamma}{\omega_0 + \omega} \right) I(\vec{r}) , \quad (2.14)$$

where ω_0 is the resonant atomic transition frequency, ω is the laser frequency, $I(\vec{r})$ represents the intensity of laser, and Γ is the natural linewidth of the excited state. For our experiments, all three species (${}^6\text{Li}$, ${}^{40}\text{K}$, and ${}^{87}\text{Rb}$) are alkali atoms. In this case, both the D_1 and the D_2 must be taken into account ([Grimm et al., 2000a](#)). The resulting dipole potential is expressed as

$$U_{dip} = -\frac{\pi c^2 \Gamma}{2\omega_0^3} \left(\frac{2 + \mathcal{P} g_F m_F}{\Delta_{2,F}} + \frac{1 - \mathcal{P} g_F m_F}{\Delta_{1,F}} \right) I(\vec{r}) . \quad (2.15)$$

Here, \mathcal{P} represents the polarization of the laser (linear polarization for $\mathcal{P} = 0$ and σ^\pm) polarization for $\mathcal{P} = \pm$) and $\Delta_{2,F} = \omega_{2,0} - \omega$ and $\Delta_{1,F} = \omega_{1,0} - \omega$ are the laser detuning for D_2 and D_1 transitions, respectively. Note that the Eq. 2.15 applies when $\Delta \ll \omega_0$, otherwise the counter-rotating term ($\omega_0 + \omega$) need to be considered like Eq. 2.14.

In the experimental setup, the beam follows a Gaussian profile and propagates along the x-direction, the electric field of the beam can be expressed as:

$$\vec{E}_{+x} \approx \frac{\sqrt{2P}}{\sqrt{\pi} w_0} \frac{1}{\sqrt{1 + (x/Z_x)^2}} e^{-\frac{(y^2 + z^2)}{w_0^2} \frac{1}{1 + (x/Z_x)^2}} e^{-ikx} , \quad (2.16)$$

where $k = 2\pi/\lambda$ is the wave number. Then the intensity of the Gaussian beam is given by

$$I(x, y, z) = \left| \vec{E}_{+x} \right|^2 , \quad (2.17)$$

which gives the intensity profile as:

$$I(\vec{r}) = I(x, y, z) = \frac{2P}{\pi w_0^2} \frac{1}{1 + (x/Z_x)^2} \exp^{-\frac{2(y^2+z^2)}{w_0^2} \frac{1}{1+(x/Z_x)^2}} , \quad (2.18)$$

where P represents the laser power, w is the beam waist, and $Z_x = \frac{\pi w_0^2}{\lambda}$ is the Rayleigh length.

Whether atoms are attracted to or repelled from the laser beam depends on the value of the laser frequency ω . For $\omega > \omega_0$, the laser frequency is blue-detuned, and atoms are repelled from the high intensity region of the beam. If $\omega < \omega_0$, the laser frequency is red-detuned, and atoms are attracted to the high intensity region. To prevent Majorana losses in a quadrupole magnetic trap, a blue-detuned beam is shinned on the central of the trap. This creates a "plug" effect, efficiently pushing the atoms away from the loss region.

2.2.2. Plugged Trapping Potential

The OPT combines a quadrupole magnetic trap and an optical plug beam, so the total potential of the trap is the combination of the magnetic potential $U_B(\vec{r})$ generated by the quadrupole coils, the dipole potential $U_{dip}(\vec{r})$ generated by the plug beam, and the gravitational potential mgy . Thus, the total potential is expressed as:

$$U_{OPT}(\vec{r}) = U_B(\vec{r}) + U_{dip}(\vec{r}) + mgy . \quad (2.19)$$

In the lab configuration (Fig. 3.15), the symmetry axis of the coils is aligned with y-direction, while the plug beam propagates along x-direction, following a Gaussian profile as described in Eq. 2.18. With the alkali atoms ^{87}Rb , ^{40}K and ^6Li loaded into the trap, the total potential is written as:

$$\begin{aligned} U_{OPT}(x, y, z) = & \mu b' \sqrt{\frac{x^2 + z^2}{4} + y^2} - \left(\frac{3\pi c^2}{2} \left(\frac{\Gamma_1}{3\omega_1^3} \left(\frac{1}{(\omega_1 - \omega)} + \frac{1}{(\omega_1 + \omega)} \right) \right. \right. \\ & \left. \left. + \frac{2\Gamma_2}{3\omega_2^3} \left(\frac{1}{(\omega_2 - \omega)} + \frac{1}{(\omega_2 + \omega)} \right) \right) \right) I(y, z, x) - mgy , \end{aligned} \quad (2.20)$$

where $\mu = m_F g_F \mu_B$ represents the magnetic moment, and b' is the axial magnetic field gradient. The two terms in the dipole trapping potential, with natural linewidth Γ_i and

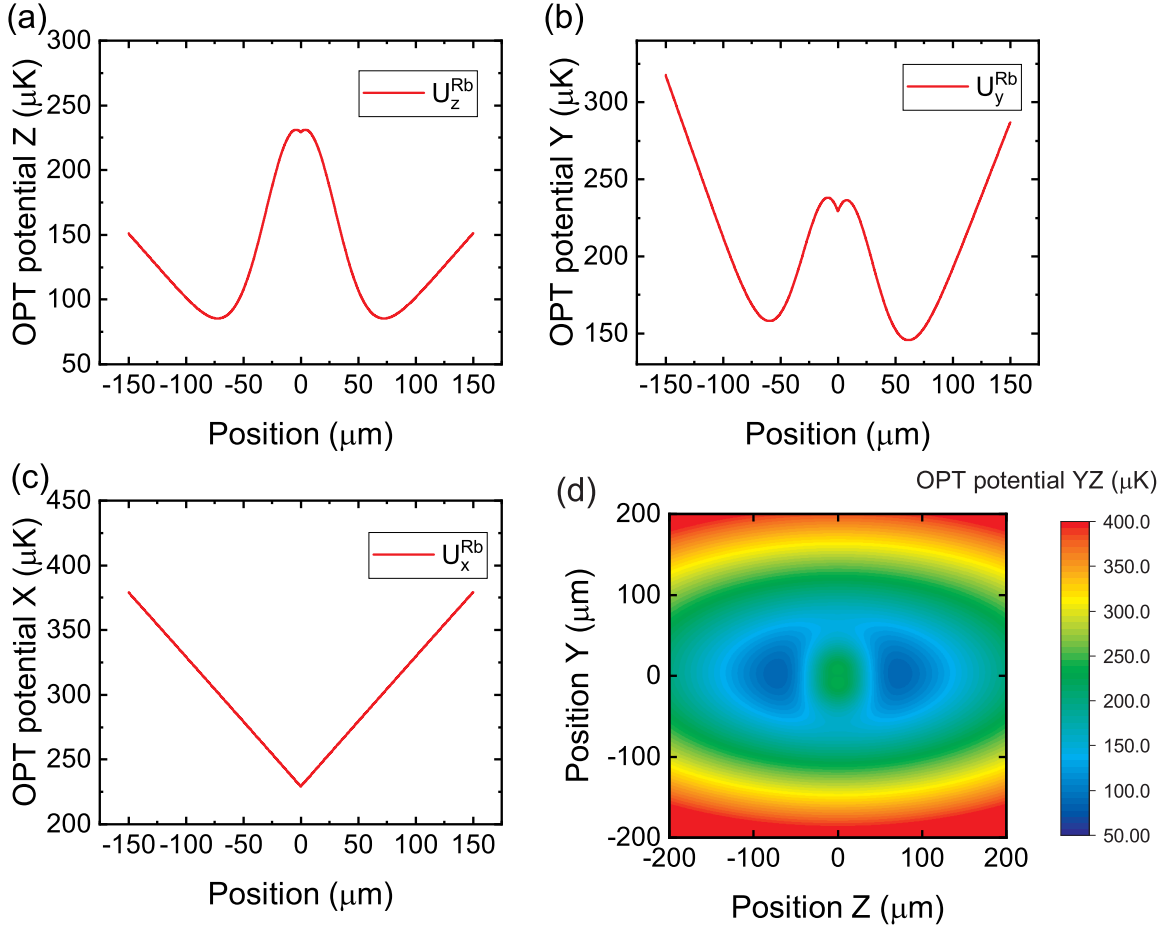


Figure 2.4.: OPT potential along x-, y-, and z-directions and in the y-z plane for ^{87}Rb . The potential curve along each direction is plotted when the other two directions are fixed at the 0 position. The minimum potential along the z-direction is located at $z_{\min} = 72.3 \mu\text{m}$ away from the central barrier.

resonant atomic transition frequency ω_i ($i = 1, 2$) represent the contributions of the D_1 and the D_2 lines to the total dipole potential for alkali atoms. Moreover, various configurations of the OPT have been discussed in the literature. For example, in some setups, the plug beam propagates along the same direction as the symmetry axis of the quadrupole coils (the x-direction) (Dubessy et al., 2012; Naik and Raman, 2005). Additionally the plug beam may not have a perfect Gaussian profile, particularly in the wings, where it can shape an elliptical shape, creating a double well potential (Naik and Raman, 2005). Also, a slightly misaligned plug beam from the central of the magnetic trap can produce a single well potential (Heo et al., 2011). Thus the formation of the trapping potential depends on specific configuration of the OPT. Here, I focus on the configuration used in our lab, as described above.

Fig. 2.4 shows the potential curves along the x-, y-, and z-directions, as well as in the y-z plane, based on Eq. 2.20. The parameters of a magnetic gradient $b' = 300 \text{ G/cm}$, plug beam

power $P = 22 \text{ W}$, beam waist $w = 60 \mu\text{m}$, and laser wavelength $\lambda_{\text{plug}} = 532 \text{ nm}$ are adopted. The asymmetry of the potential along the y -direction is due to the effect of gravity. The trap depth along z -direction is deeper than along y -direction because of the different magnetic gradient along y - and z -directions. From the combined y - z potential, the atoms are trapped in the deep blue region with the minimum potential point located at $z_{\min} = 72.3 \mu\text{m}$ along z axis. The trapping frequencies at this minimum position are expressed as:

$$\begin{aligned}\omega_z &= \sqrt{\frac{\mu b'}{2mz_{\min}}} \\ \omega_x &= \omega_z \sqrt{\frac{4z_{\min}^2}{w^2} - 1} \\ \omega_y &= \omega_z \sqrt{3} \quad ,\end{aligned}\tag{2.21}$$

With the parameters given in Fig. 2.1, the trapping frequencies for ^{87}Rb are

$$\omega_z = 2\pi \times 184 \text{ Hz}, \omega_x = 2\pi \times 403 \text{ Hz}, \omega_y = 2\pi \times 318 \text{ Hz} \quad .\tag{2.22}$$

Similarly, the trapping frequency for ^{40}K are

$$\omega_z = 2\pi \times 271 \text{ Hz}, \omega_x = 2\pi \times 595 \text{ Hz}, \omega_y = 2\pi \times 469 \text{ Hz} \quad .\tag{2.23}$$

And for ^6Li are

$$\omega_z = 2\pi \times 696 \text{ Hz}, \omega_x = 2\pi \times 1544 \text{ Hz}, \omega_y = 2\pi \times 1205 \text{ Hz} \quad .\tag{2.24}$$

2.3. Optical Lattice

A 3D optical lattice, formed by three forward Gaussian beams with their retroreflections, has been implemented in the lab. For our experiments, one practical purpose of this lattice is to do simulation of lattice-spin model. In this section, the relevant aspects of the optical lattice physics are introduced to provide a fundamental understanding of lattice technologies.

2.3.1. Lattice Potential

The optical dipole potentials have been discussed in Section 2.2.1. For the optical lattice, the potential and trapping frequency can be calculated once the spatial distribution of the light

intensity $I(x, y, z)$ is known. The forward and retroreflected beams form standing waves, and the interference between the standing waves is avoided in our setup (Section 3.4.1), resulting in a simple-cubic (sc) optical lattice. Without interference between different standing waves, the total light intensity $I_{\text{total}}(x, y, z)$ is simply the sum of the standing wave intensities in three directions ($I_x(x, y, z)$, $I_y(x, y, z)$, and $I_z(x, y, z)$). For simplicity, the case of a 1D lattice is first considered.

A Gaussian light field along x-direction is applied to form a 1D optical lattice. The electric field and intensity for a single forward light follows Eq. 2.16 and Eq. 2.18. Assuming that the reflected beam has the same size and power and it perfectly overlaps with the forward beam, the intensity of the standing wave formed by the Gaussian light field can be expressed as

$$I_x(x, y, z) = \left| \vec{E}_{+x} + \vec{E}_{-x} \right|^2 = \frac{8P}{\pi w_0^2} \frac{1}{1 + (x/Z_x)^2} e^{-\frac{2(y^2+z^2)}{w_0^2} \frac{1}{1+(x/Z_x)^2}} \cos^2(kx) . \quad (2.25)$$

The term $\cos^2(kx)$ represents the effects of the standing wave. The trapping potential of the 1D optical lattice can be calculate by inserting Eq. 2.25 into Eq. 2.15 for any given position. Here the $U_0 \equiv U_{1D,x}(x = 0, y = 0, z = 0)$ is defined as

$$U_0 \equiv U_{1D,x}(x = 0, y = 0, z = 0) = -\frac{4Pc^2\Gamma}{\omega_0^3 w_0^2} \left(\frac{2 + \mathcal{P}g_F m_F}{\Delta_{2,F}} + \frac{1 - \mathcal{P}g_F m_F}{\Delta_{1,F}} \right) , \quad (2.26)$$

which means the 1D optical potential can be expressed as

$$U_{1D,x}(x, y, z) = \frac{U_0}{1 + (x/Z_x)^2} e^{-\frac{2(y^2+z^2)}{w_0^2} \frac{1}{1+(x/Z_x)^2}} \cos^2(kx) . \quad (2.27)$$

However, in actually experiments, the optics along the light path can attenuate the power of the reflected beam, which lead to lower intensity compared to the forward beam. Now taking the imbalance of forward beam and retroreflected beam into consideration, a factor f ($f \leq 1$) is introduced to represent the attenuation of the intensity, which corresponds to a \sqrt{f} effect on the amplitude of \vec{E}_{-x} . As a result, the intensity $I_x(x, y, z)$ is rewritten as

$$I_x(x, y, z) = \left| \vec{E}_{+x} + \sqrt{f} \vec{E}_{-x} \right|^2 , \quad (2.28)$$

and the trapping potential $U_{1D,x}(x, y, z)$ is given by

$$\begin{aligned} U_{1D,x}(x, y, z) &= \left| e^{-ikx} + \sqrt{f} e^{+ikx} \right|^2 \frac{U_0/4}{1 + (x/Z_x)^2} \exp\left[-\frac{2(y^2 + z^2)}{w_0^2} \frac{1}{1 + (x/Z_x)^2}\right] \\ &= (1 + f + \sqrt{f}(e^{+2ikx} + e^{-2ikx})) \frac{U_0/4}{1 + (x/Z_x)^2} \exp\left[-\frac{2(y^2 + z^2)}{w_0^2} \frac{1}{1 + (x/Z_x)^2}\right] \\ &= ((1 - \sqrt{f})^2 + 4\sqrt{f} \cos^2(kx)) \frac{U_0/4}{1 + (x/Z_x)^2} \exp\left[-\frac{2(y^2 + z^2)}{w_0^2} \frac{1}{1 + (x/Z_x)^2}\right] . \end{aligned} \quad (2.29)$$

Commonly, a dimensionless parameter s is used to describe the trap depth, which is defined as

$$s \equiv \frac{U_0}{E_r} , \quad (2.30)$$

where $E_r = \frac{\hbar^2 k^2}{2m}$ is the recoil energies of atoms with mass m .

Then the trapping frequency is calculated by taking the second order term of the Taylor expansion of Eq. 2.29 at $(0, 0, 0)$ and shown as

$$\omega_{y,z} = \frac{1 + \sqrt{f}}{2} \sqrt{\frac{4U_0}{mw_0^2}} , \quad (2.31)$$

and

$$\omega_x = f^{1/4} \sqrt{\frac{2k^2 U_0}{m}} . \quad (2.32)$$

With the attenuation factor f , we could observe from Eq. 2.29 that the potential has two forms. With term $(1 - \sqrt{f})^2$ the potential only provide a dipole trap effect, while only with the term $4\sqrt{f} \cos^2(kx)$ the potential works as an optical lattice with $a = \pi/k = \lambda/2$ spacing. In that case, to obtain a lattice trap with trap depth s_0 , a factor \sqrt{f} of power for the lattice beams need to be increased compared to the case of without attenuation ($f = 1$). Correspondingly, the trapping frequency $\omega_{y,z}$ would increase a factor of $\frac{1+\sqrt{f}}{2f^{1/4}}$ when reach to the same trap depth. More discussion for the attenuation effects are presented in Section 3.4 and Section 3.5.

Then for a 3D optical lattice, the potential can be simply calculated by summing up the potential of 1D optical lattice from three directions

$$U_{3D} = U_{1D,x} + U_{1D,y} + U_{1D,z} , \quad (2.33)$$

and the maximum trap depth is $3U_0$. The trapping frequencies for 3D optical lattice are

$$\omega_{3D} = f^{1/4} \sqrt{\frac{2k^2 U_0}{m}} . \quad (2.34)$$

for all three directions.

2.3.2. Band Structure

In solid state physics, the Bloch theorem (Bohm, 1949) is employed to characterize the eigenstates of electrons traversing a periodic potential generated by the ions in metals or crystals. This formalism is similarly applicable to ultracold atoms in an optical potential that shows a periodic structure. When we only consider the central area of the optical lattice, and ignore spatial variation of the Gaussian beams, the optical lattice potential in one direction (x-direction) is simplified as $U_{1D,x} \approx U_0 \cos^2(kx) = sE_r \cos^2(kx)$, which possesses discrete translational symmetry $U(x) = U(x + a)$. Therefore, the time independent Schrödinger equation

$$-\frac{1}{k^2} \frac{d^2\psi_{n,q}(x)}{dx^2} + s \cos^2(kx) \psi_{n,q}(x) = \epsilon_{n,q} \psi_{n,q}(x) , \quad (2.35)$$

can be solved based on Bloch's theorem. Here, n is referred as band index and q is the quasi-momentum. The eigenstate of the equation is given by Bloch wave function, which has the form of plane waves $e^{iqx/\hbar}$ times a function $u_{n,q}$ with same periodicity $u_{n,q}(x) = u_{n,q}(x + a)$

$$\psi_{n,q}(x) = e^{iqx/\hbar} u_{n,q} . \quad (2.36)$$

Also, the $u_{n,q}$ can be written as a Fourier sum $u_{n,q} = c_{l,n,q} e^{i2klx}$, where l denotes the momentum order. By inserting the Bloch wave function $\psi_{n,q} = c_{l,n,q} e^{i(2kl+q/\hbar)x}$ into Eq. 2.35, we can numerically solve it to obtain the eigenenergies $\epsilon_{n,q}$ and eigenvectors $c_{l,n,q}$, which represent the energy and the coefficients of the plane wave for the Bloch wave function $\psi_{n,q}$ in the n -th band of the lattice with quasi-momentum $\hbar q$. Fig. 2.5 illustrate the band structure of an optical lattice at varying lattice depths s . From this plot we could obtain that the band width decreases while the gap between different bands becomes larger when increasing the lattice depth.

Commonly, for shallow lattices, Bloch functions serve as a useful basis due to their delocalization across the entire lattice. Conversely, in the case of deep lattices, the Wannier functions

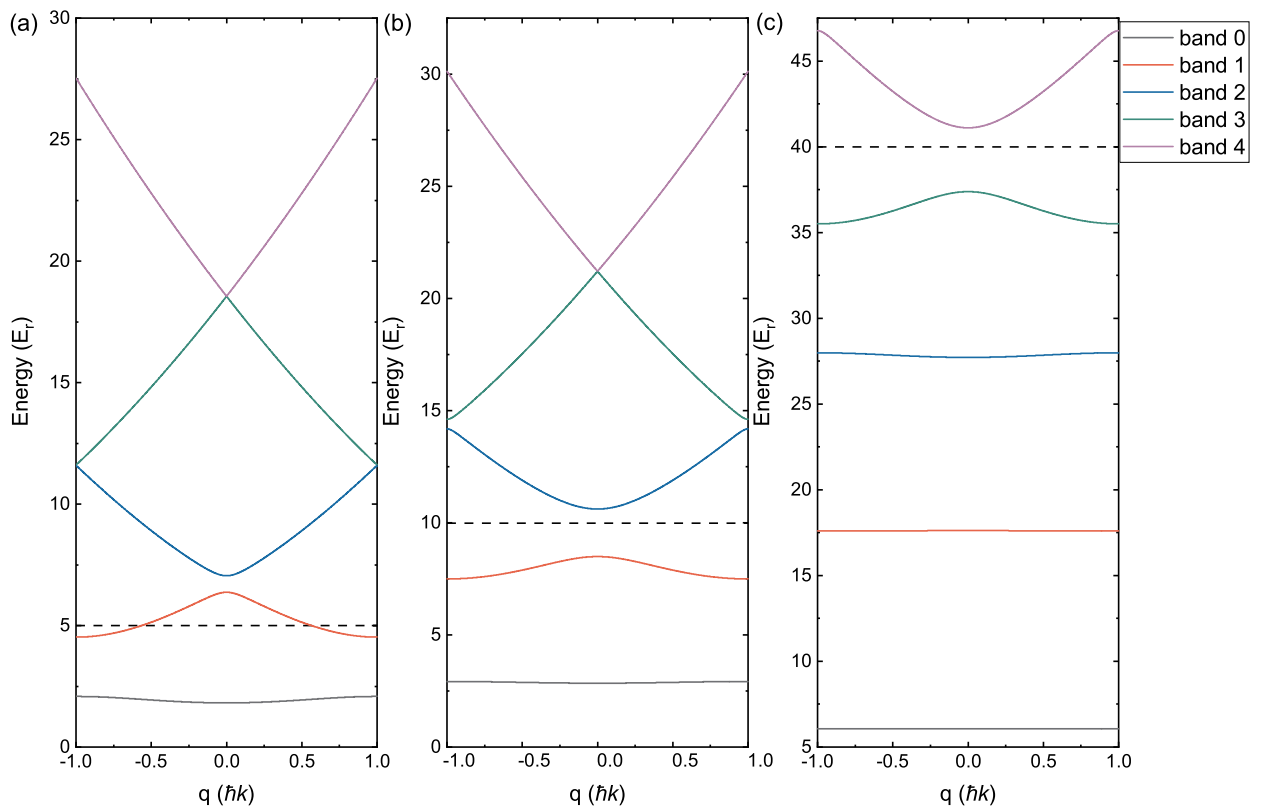


Figure 2.5.: Band structure for an optical lattice with different trap depths (a) $s = 5$, (b) $s = 10$, and (c) $s = 40$. The bands are plotted with eigenenergies $\epsilon_{n,q}$ for different bands number n at different quasi-momentum q in the first Brillouin zone. The first five bands are shown in the plots. The dashed black lines represent the trap depths of each plot. Note that all the atoms with energy higher than s are out of the lattice trap.

are more advantageous. The Wannier functions have the form (Kittel and McEuen, 2018)

$$w_n(x - x_i) = \frac{1}{\sqrt{N}} e^{-iqx_j/\hbar} \psi_{n,q}(x) , \quad (2.37)$$

where x_i is the centered site and N is the normalization factor. In our case, a deep lattice is anticipated to mitigate the chemical loss for ${}^6\text{Li}{}^{40}\text{K}$ molecules. However, for the initial calibration of the lattice, we will concentrate on loading the atoms into a shallow lattice. Consequently, most calculations in the later sections will be based on Bloch functions.

3. Experimental Apparatus and Procedures

This chapter outlines the setup and advancements made to the experimental apparatus and procedures used for creating ultracold $^6\text{Li} - ^{40}\text{K}$ ground state molecules. It also covers the setup for loading the molecules into optical lattice. It begins in Section 3.1 with an overview of the experimental platform for producing ultracold $^6\text{Li} - ^{40}\text{K}$ Fermi mixtures and Feshbach molecules. Section 3.2 details the upgraded Raman laser system for molecular spectroscopy and ground state transfer, presenting setup of measuring phase noise. In Section 3.3, the preparation and detection of pure ground state molecular samples is depicted. Section 3.4 illustrates the free-space optical setup for realizing a 3D optical lattice. Finally, Section 3.5 describes the development of an optically plugged trap for expediting experimental cycles.

3.1. Overview of Fermi-Fermi Mixture Platform

The platform for creating the $^6\text{Li} - ^{40}\text{K}$ Fermi-Fermi mixture has been extensively detailed in previous publications and theses by former lab members ([Brachmann, 2012a](#); [Costa, 2011](#); [Eigenwillig, 2007](#); [Lam, 2016](#); [Pal, 2016](#); [Sofia, 2022](#); [Taglieber, 2008](#); [Voigt, 2009](#); [Wieser, 2006](#); [Yang, 2021b](#)). In this section, a brief overview of the essential components and sequences required to generate $^6\text{Li}^{40}\text{K}$ Feshbach molecules is provided.

Our experiments start with simultaneously loading of three species of atoms into a Magneto-Optical trap (MOT) inside a high vacuum chamber. The ^{87}Rb , and ^{40}K atomic vapor loaded into MOT is generated by atomic vapor dispensers ([DeMarco and Jin, 1999](#)). The ^6Li atoms are loaded from an oven and captured by the MOT using a spin-flip Zeeman slower ([Barrett et al., 1991](#)) to decelerate them. The total loading time for all species is 15 s, which ensures the loading of ^6Li is saturated. Subsequently, the density of the atomic cloud is increased by loading ^6Li and ^{87}Rb into a compressed MOT (cMOT) ([Petrich et al., 1994](#)) and switching on a dark MOT(dMOT) ([Townsend et al., 1995](#)) and optical molasses ([Ungar et al., 1989](#);

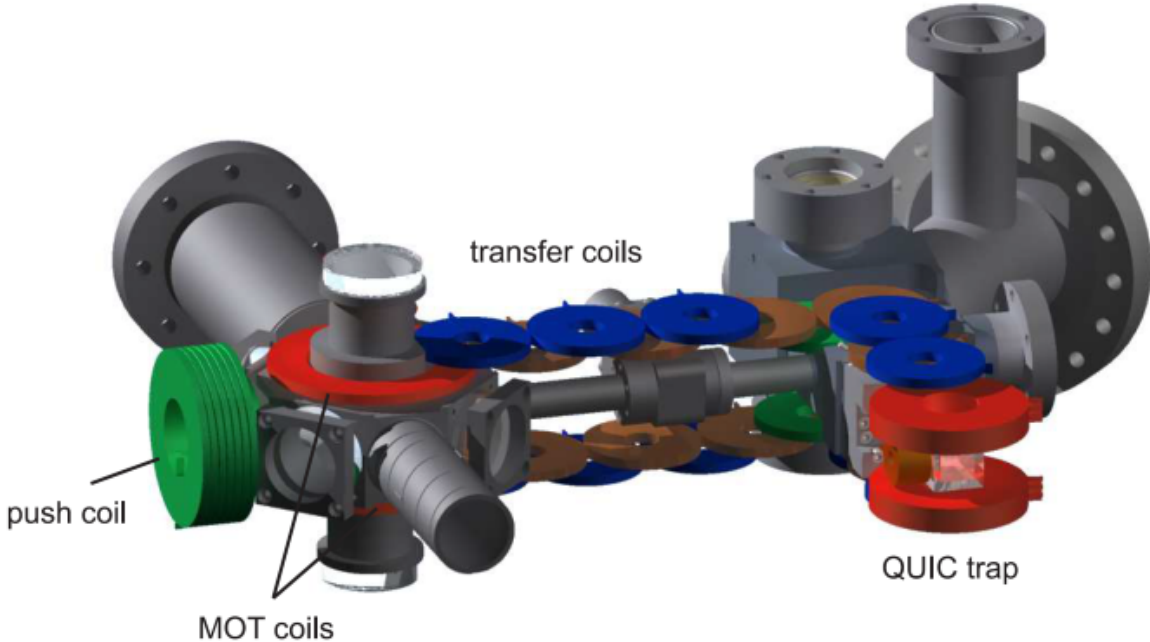


Figure 3.1.: The experimental platform involves capturing ^{87}Rb , ^{40}K and ^6Li atoms in a MOT chamber, transferring the atoms from the MOT to an Ultra-High Vacuum (UHV) chamber using transfer coils, evaporating the atoms into quantum degenerate gases, and associating ^{40}K and ^6Li atoms into Feshbach states.

Weiss et al., 1989) for ^{87}Rb . The cMOT and dMOT stages hold for 30 ms and are followed by 1.5 ms of optical molasses. After the MOT process, three species are in a mixed hyperfine states. To prevent the loss and heating due to spin-exchange collisions, ^{87}Rb , ^{40}K and ^6Li are prepared in $|F = 2, m_F = 2\rangle_{\text{Rb}}$, $|9/2, 9/2\rangle_{\text{K}}$ and $|3/2, 3/2\rangle_{\text{Li}}$ states using optical pumping. The spin-polarized atoms are recaptured by a quadrupole magnetic field generated by the MOT coils. The atoms are then magnetically transferred to the UHV chamber. By controlling the current flow through 13 pairs of transfer coils, the atoms are transported through a differential pumping tube over a distance of 26 cm and turned 90° at the corner to enter the UHV chamber (Greiner et al., 2001). The transfer efficiency from the MOT chamber to the UHV chamber is 10% – 20%. In the UHV chamber the quadrupole trap is adiabatically transformed to a Quadrupole-Ioffe-configuration trap (QUIC trap) (Esslinger et al., 1998) to suppress atom losses due to Majorana spin-flip (Majorana, 1932) during the later evaporative cooling process. The evaporative cooling for ^{87}Rb is achieved by transferring the high energy atoms to the anti-trapping $|1, 1\rangle$ state with microwave (MW) signals at 6.8 GHz in 60 s. The ^{40}K and ^6Li atoms are sympathetically cooled by elastic collisions with ^{87}Rb atoms during the evaporative cooling process. Part of the high energy ^6Li atoms are removed from the

trap by driving the hyperfine transition $|3/2, 3/2\rangle \rightarrow |1/2, 1/2\rangle$, ramping the RF signal from 320 MHz to 234.451 MHz. The lengthy cooling process is primarily due to the small scattering cross-section $\alpha_{\text{Li},\text{Rb}}$ between ^{87}Rb and ^6Li . Moreover, the prolonged cooling process heats up the QUIC coils, which also take around 40 s to cool down before the next experimental cycle. One idea to accelerate the cooling process and reduce waiting time is to use an optically-plugged magnetic trap (Davis et al., 1995) instead of a QUIC, which will be discussed in Section 3.5. At the end of MW evaporative cooling the ^{87}Rb atoms can reach Bose-Einstein condensation (BEC), and quantum degenerate gases of ^{40}K (150 nK, $0.12T_F$, $N_K \approx 1 \times 10^5$) and ^6Li (500 nK, $0.25T_F$, $N_{\text{Li}} \approx 3 \times 10^4$) are obtained. These numbers reflect typical conditions achieved during the period of this thesis work. After evaporative cooling, the remaining ^{87}Rb atoms are removed by further ramping down the MW frequency until it cuts below the trap bottom. The remaining fermionic ^{40}K and ^6Li atoms are then loaded into a crossed optical dipole trap (ODT). In the ODT, a homogeneous magnetic field, generated by Helmholtz configuration coils (Feshbach coils), serves as the guiding field for imaging and addressing the Feshbach resonance. The current in the Feshbach coils is regulated and stabilized through slow regulation of the power supply for long-term stability, and a current by-pass parallel to the coils for short-term control (Pal, 2016; Voigt, 2009). The magnetic field is initially ramped up from 3 G to 20 G in 10 ms for state preparation. ^6Li atoms are transferred from $|F = 3/2, m_F = 3/2\rangle \rightarrow |1/2, 1/2\rangle$ using RF adiabatic rapid passage (ARP), sweeping the frequency from 270 MHz to 269.4 MHz in 735 ns. Simultaneously, ^{40}K atoms are transferred from $|F = 9/2, m_F = 9/2\rangle \rightarrow |9/2, -9/2\rangle$ by sweeping the RF frequency from 8.4 MHz to 4.475 MHz over 2 ms. Next, the magnetic field strength is ramped up to 216 G in 56 ms. At the end of the ramping, a second state preparation occurs, transferring ^6Li atoms to the $|1/2, -1/2\rangle$ state by sweeping the RF frequency from 72 MHz to 71.5 MHz in 3 ms. The Feshbach field is then adiabatically ramped down across the interspecies Feshbach resonance at 215.6 G (Pal, 2016), approximately 9 ms for associating weakly-bound $^6\text{Li}^{40}\text{K}$ dimers. The association efficiency can vary a lot in the daily experiments due to the loading condition, up to 50% efficiency can be achieved as reported (Costa et al., 2010). At this point, weakly bound $^6\text{Li}^{40}\text{K}$ Feshbach molecules are formed, along with residual ^6Li atoms in the $|1/2, -1/2\rangle$ state and ^{40}K atoms in the $|9/2, -9/2\rangle$ state. The remaining ^6Li atoms are then transferred to the $|1/2, 1/2\rangle$ state by an RF π pulse at 71.74 MHz with duration of 45 μs . This pulse

shelve the uncombined ^6Li into the state which the imaging light is not at resonance for later detection of Feshbach molecules. This RF pulse is applied at the Feshbach resonance, which needs to be calibrated daily by adjusting the magnetic field ramping time at a fixed ramping rate. This is because the narrow s-wave resonance (Wille et al., 2008) is comparable to the drifting of magnetic field. The ending point of the ramp is selected to maximize the number of Feshbach molecules. However, the procedure changes slightly when STIRAP transfer is activated, as discussed in Section 4.4.6. The Feshbach molecules can be detected by the same imaging light used for detecting ^6Li atoms in the $|1/2, -1/2\rangle$ state and ^{40}K atoms in the $|9/2, -9/2\rangle$ state. This is possible due to the R^{-6} behavior of heteronuclear molecular potentials at long range and the small binding energy of $^6\text{Li}^{40}\text{K}$ Feshbach molecules (Zirbel et al., 2008). By following this approach, the detection background can be decreased to a magnitude of thousands. The entire detection process, including background reduction using an RF pulse, has been further improved for detecting ground state molecules, as discussed in Section 3.3 and Section 4.3.3. Both residual ^{40}K and ^6Li atoms are kicked out of ODT trap instead of being shelved to other hyperfine state. After these improvements, both ^{40}K and ^6Li imaging light can be used to detect Feshbach molecules, further reducing the detection background to the level of hundreds.

3.2. Improved Raman Laser System

To achieve the STIRAP transfer described in Section 2.1.2 with high efficiency, certain requirements must be met in terms of phase noise, laser power, and frequency stability for the laser system. Section 3.2.1 presents the setup of our new Raman laser system, which employs two diode lasers combined with tapered amplifiers. The phase noise measurement setup is introduced in Section 3.2.2. Section 3.2.3 describes the setup for Pound-Drever-Hall (PDH) frequency stabilization. In Section 3.2.4, the utilization of a frequency comb for the measurement and stabilization of the Raman laser frequency through the analysis of beat signals is discussed. Finally, Section 3.2.5 summarizes the process for correctly determining and stabilizing the Raman laser frequency using the PDH lock and frequency comb. The impact of these parameters on the STIRAP transfer is discussed in detail in Section 4.4.

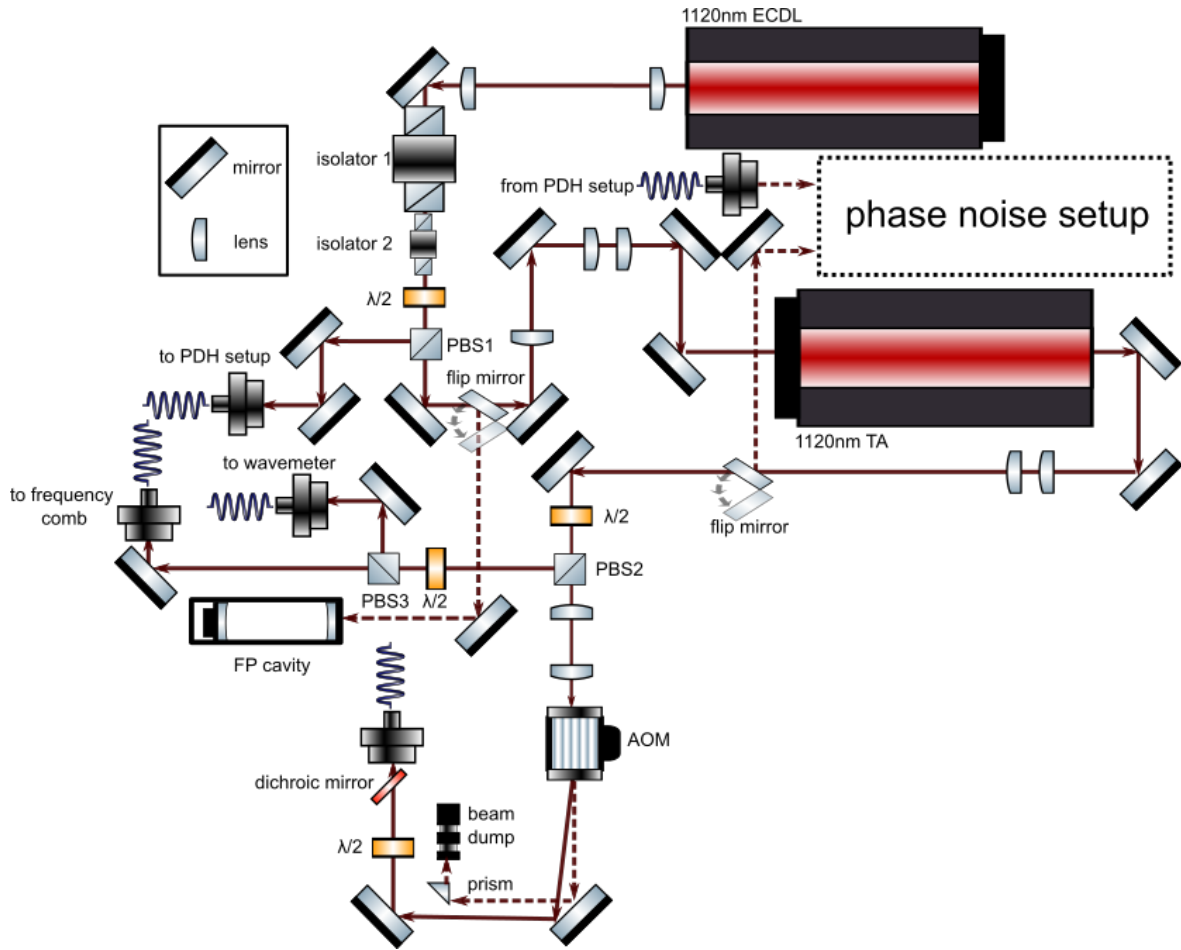


Figure 3.2.: Raman setup for Pump laser. The Pump transition is driven by a commercial laser with an anti-reflection coated laser diode from Optical AG. The laser output is amplified by a tapered amplifier (TA) chip and the power is distributed to various applications. An acoustic-optical-modulators (AOM) is used for fast beam switching. The dash box represents the phase noise setup, which will be detailed in Fig. 3.5

3.2.1. Updated Pump and Stokes Setup

To explore molecular spectroscopy and achieve the ground state transfer, a stable Raman laser system with both Pump and Stokes lasers must be carefully prepared. The initial setup for molecular spectroscopy is described in [Pal \(2016\)](#). Further attempts to improve the setup for molecular spectroscopy and STIRAP transfer are discussed in [Sofia \(2022\)](#); [Yang \(2021b\)](#). Based on the previous apparatus, the most recent updated version is shown in Fig. 3.2 (Pump) and Fig. 3.3 (Stokes).

An anti-reflection (AR) coated laser diode (Toptica AG, LD-1120-AR2) is used for the infrared Pump laser in an external cavity diode laser (ECDL) configuration. The diode operates at approximately 1120 nm, producing an output power of 63 mW. The beam first passes through two single-stage Faraday isolators, providing more than 60 dB of reflection isolation.

Next, a polarizing beam splitter (PBS) along with a half-wave plate (HWP) controls the power distribution of the reflected and transmitted beams. The reflected beam of approximately 9 mW is sent to the PDH setup, which is used for both PDH locking and phase noise measurements (discussed in Section 3.2.2 and Section 3.2.3). The transmitted beam, at 42 mW, is sent to seed a TA (Innolume, TA-1120-50-CM-3W). After amplification, the output power reaches 500 mW, and the amplified beam is once again split using a PBS and HWP. Approximately 20 mW of the reflected beam is distributed to a home-built wavemeter (2.5 mW) and a frequency comb (13.5 mW). The transmitted beam (450 mW) then passes through a 110 MHz AOM (Goush&Housego, 3110-197), where the +1st order beam is used. The 0th order beam is diverted by a prism and absorbed by a beam dump, while the deflected +1st order beam (350 mW) is sent through a fiber to the molecules on the MOT table. Additionally, two flipper mirrors are used for beam routing. The first mirror is placed after the PBS1, directs the beam to a Fabry-Pérot (FP) cavity for single mode monitoring. The second flipper is positioned in front of TA, sending the beam to the phase noise measurement setup.

The visible Stokes laser operates around 665 nm and uses the same diode (Mitsubishi, ML101-J29) as in our ${}^6\text{Li}$ MOT laser setup. Similar to the Pump laser, the output beam (62 mW) first passes through a two-stage 60 dB Faraday isolator. Afterwards, the beam (47 mW) is split by a PBS, with an HWP controlling power distribution. The reflected beam (6.5 mW) is sent to the PDH setup, while the transmitted beam (20.5 mW) is sent to a TA (Eagleyard, EYP-TPA-0650). The amplified output (130 mW) from TA is then split by another PBS and again controlled by an HWP. The reflected beam (30 mW) is sent to the wavemeter and frequency comb, while the transmitted light (90 mW) is sent to a 80 MHz AOM (Goush&Housego, 3080-125) with +1st order efficiency of 70%. The 0th order beam is deflected by a prism and absorbed by a beam dump, while the +1st order beam (70 mW) is sent through the same fiber as Pump laser to reach the molecules on the MOT table. One beam sampler (BS) is set after the first PBS diverts a small portion of the beam (0.3 mW) to a FP-cavity for single mode monitoring. Additionally, a flipper mirror after the second PBS can send the beam to the phase noise measurement setup.

Both the Pump and Stokes beams are combined using a dichroic mirror and then coupled into a single mode fiber. A shared polarizer with two independent HWPs for each beam is

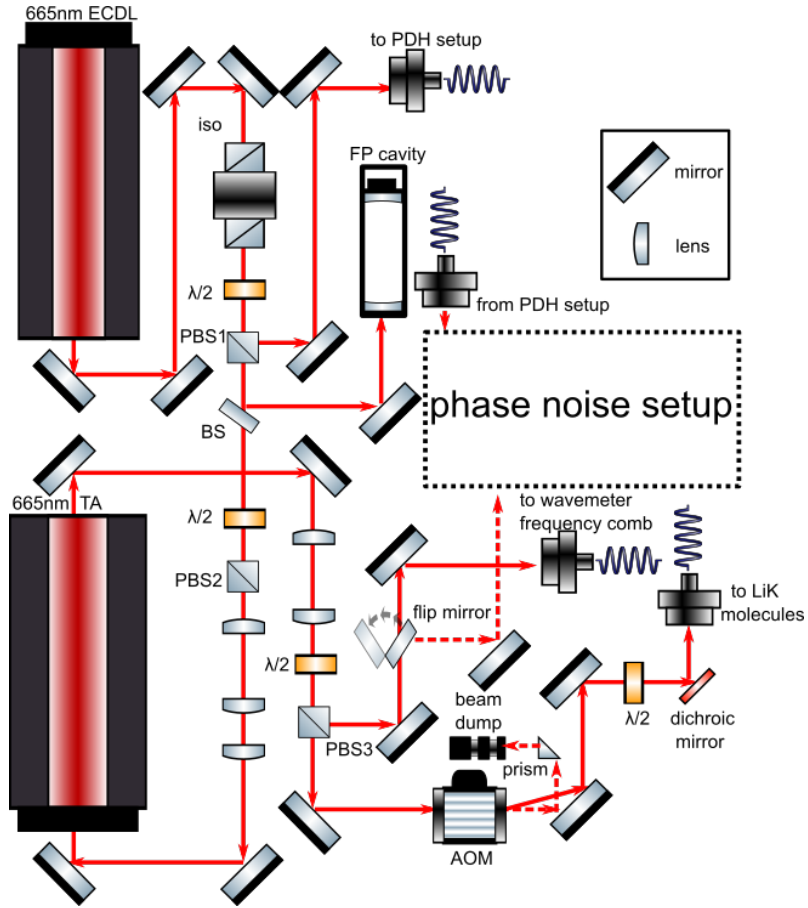


Figure 3.3.: Raman setup for Stokes laser. The Stokes transition is driven by a Fabry-Pérot Mitsubishi diode. Similar to the Pump setup, the Stokes beam is amplified by a TA, and its power is distributed via different PBS for various applications. A fast beam switch is controlled using an AOM. The Stokes beam is then combined with Pump beam using a dichroic mirror and coupled to a fiber, which sends beams to the MOT table. The dash box represents the phase noise setup.

used to control the polarization before coupling into the fiber. Fig. 3.4 illustrates the optical setup on the MOT table for the Raman laser. A dichroic mirror separates the combined Pump (110 mW) and Stokes (12 mW) beams into two paths for polarization adjustment. The polarization of each beam is individually controlled by a HWP, a QWP, and a polarizer. The polarization is selected to σ^- for spectroscopy measurements and ground state transfer, meaning that both Pump and Stokes beams are left-handed circular polarized and propagate parallel to the magnetic field direction (z-direction). A prism is used to combine the pump (60 mW) and Stokes (7 mW) beams to prevent obstruction of the optical dipole trap (ODT), lattice, and imaging beams. Two homemade polarization analyzers are used to measure the polarization of both beams. After the prism, the analyzers measure σ^+ polarization (right-handed circular) for both beams and the dielectric coated mirror flips the polarization to σ^- (left-handed circular). Also from the measurement, undesired polarization is detected to be

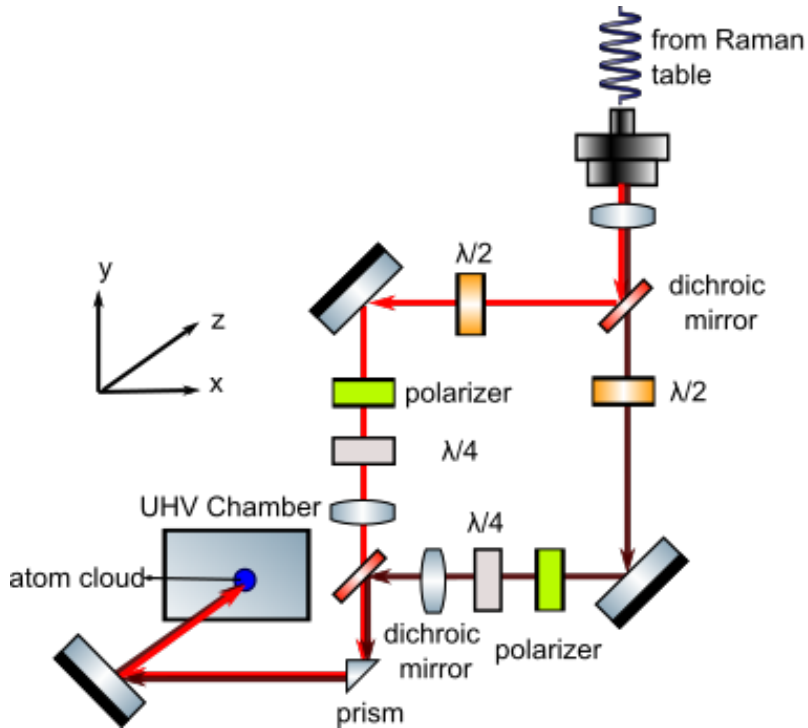


Figure 3.4.: The Raman setup near UHV chamber. The Pump and Stokes beams are first combined on the Raman table and then separated after an optical fiber using a dichroic mirror. After separation, the polarization of each beam is readjusted individually using a HWP, a quart-Waveplate(QWP), and a polarizer. The pump and Stokes beams are then recombined on another dichroic mirror and directed toward the atomic cloud using a prism and a dielectric mirror.

less than 2% ratio of the total beam power. All the laser power mentioned above represents the max power can be utilized in the experiments. The actual power is based on certain experiments , which would be shown in correspond sections.

The main modification of the Raman setup is the newly added TAs which are utilized to achieve high power for Pump and Stokes laser. In that case, the higher Rabi frequency is expected in the experiments, which would benefit the search for high ground state transfer efficiency.

3.2.2. Phase Noise Measurement

The method for measuring phase noise in our experiments, as proposed and demonstrated by Schmid et al. (2019), involves comparing the frequency of measured laser with frequency of a reference laser, which has superior frequency stability. In this approach, a high finesse cavity acts as a low-pass filter, filtering the spectrum of the transmitted beam at half-width-half-maximum (HWHM) of the cavity resonance, which is typically on the order of a few tens of kHz. The beat signal of two laser is measured and the transmitted light through the high

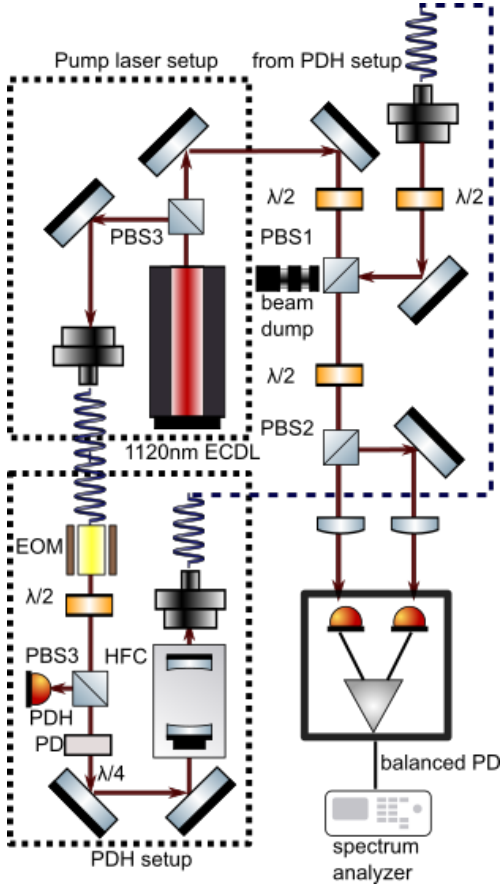


Figure 3.5.: The phase noise setup on Raman table. The dashed boxes represent Pump laser and PDH setups, and the details be found in Fig. 3.2 and Fig. 3.7. The Pump beam overlaps with reference beam on PBS1, and both beams are then redistributed by PBS2 to a balanced photodiode. The beat signal is sent to a spectrum analyzer to display the single-sideband phase noise results.

finesse cavity serves as a good candidate for the reference laser.

Fig. 3.5 shows the setup for phase noise measurement, using Pump laser as an example. The setup for the Stokes laser is similar. Based on the Raman laser setup described in Section 3.2.1, part of the beam is diverted for phase noise measurement. The flipper mirror shown in Fig. 3.2 can alternatively send the beam to PBS1, with a HWP controlling the power to 10 mW. PBS1 combines the measured Pump beam with the transmitted light (10 μ W) from the PDH setup of the high finesse cavity. After PBS1, another pair of PBS and HWP is used to distribute the laser power to a balanced photodiode (THORLABS, PDB465C-AC). The beat signal output from the balanced photodiode is sent to a spectrum analyzer (ROHDE&SCHWARZ, FPL1026). To achieve a better signal-to-noise ratio, the power sent to each side of the balanced photodiode should be approximately equal. The phase noise results for Pump laser are shown in Fig. 3.6 as an example.

The blue curve and red curve represent the single-sideband (SSB) phase noise measured

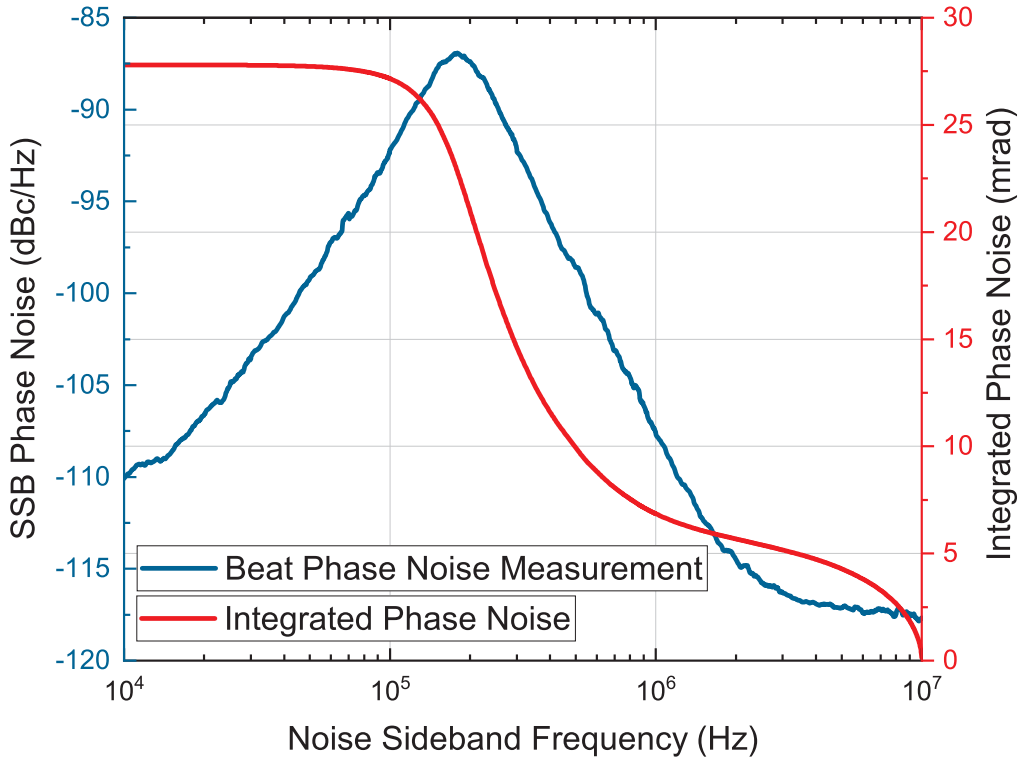


Figure 3.6.: Phase noise measurements of the Pump laser with an AR coated diode after amplification by the TA. The measurement is performed using the optical beat method. The blue curve represents the single-sideband phase noise measured by the spectrum analyzer, while the red curve shows the integrated phase noise, integrated from 10 MHz to 10 KHz. The measurements take average of 100 repeats.

from spectrum analyzer and calculated integrated phase noise from 10 MHz to 10 KHz. The integrated phase noise for the pump laser is approximately 28 mrad. The phase noise is specific to a particular mode of the laser and is unaffected after amplification by the TA. As to be described in details in Section 4.4.3, lower phase noise contributes to the achievement of high transfer efficiency of ground state molecules. Therefore, the phase noise should be checked whenever there is any suspicion of degradation. Readjusting the feedback of the laser can shift it to different modes, allowing for the selection of a mode at the required wavelength with low phase noise.

3.2.3. Pound-Drever-Hall Locking

To create the prerequisite phase coherence between the two largely detuned lasers, the Pound-Drever-Hall (PDH) locking scheme (Drever et al., 1983) is used. This method simultaneously stabilizes the two-laser systems and narrow the laser linewidth to sub-kHz level. The goal is to lock the laser to the peak of a high-finesse FP cavity resonance using a feedback control system.

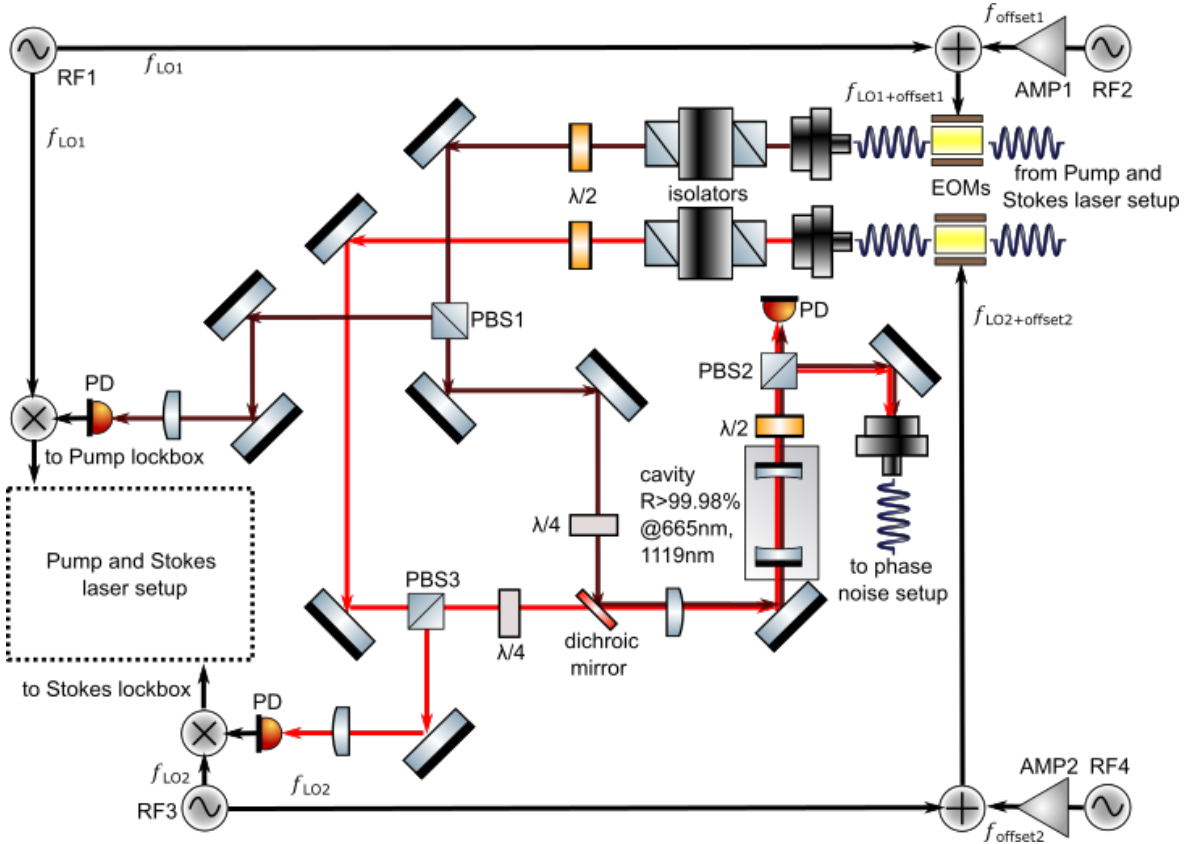


Figure 3.7.: The schematic of PDH setup for locking and stabilizing the Raman laser to a high finesse cavity with a feedback control system. Two fiberized electro-optic modulators (EOM) are used for frequency sidebands generation, each driven by an independent RF signal generator. The Pump and stokes beams overlap on the dichroic mirror and then go through the cavity. The reflected beams from the cavity are detect by two photodiodes, and the photodiode signals are mixed with the RF signals to generate error signal required to stabilize the Raman laser. The transmitted beams from the cavity are sent to phase noise measurement setup.

The basic techniques and working principles have been introduced by a elegant review ([Black, 2001](#)). The setup and properties of the high-finesse cavity situated in a vacuum chamber have been introduced in ([Sofia, 2022](#); [Yang, 2021b](#)), which will not be discussed further here.

The locking scheme and optical setup are illustrated in Fig. 3.7. The Pump and Stokes beams, each approximately 1.5 mW, are sent from the Raman laser setup discussed in Section 3.2.1. Each beam is modulated by an independent broadband EOM (PM635&PM1060, Jenoptik). The EOMs are driven by two RF signals ($f_{LO} + f_{offset}$) generated by FlexDDS signal generator units (Wieserlabs). The f_{offset} enhances the laser power in the sidebands, and f_{LO} creates sidebands around f_{offset} and laser carrier frequency. The two RF signals are combined and sent to the EOM to modulate the laser frequency. For the Pump (Stokes) laser, the $f_{offset1}$ ($f_{offset2}$) is set to 368 MHz (357 MHz), and then amplified by a RF amplifier (ZHL-5W, Mini-circuits). The local oscillator frequency f_{LO1} (f_{LO2}) is set to 18.6 MHz (28 MHz).

After each fiber coupler, an isolator with 30 dB isolation is placed to reduce etalon effects between the cavity mirror and fiber tip. A HWP after each isolator is used to clean up the polarization and maximize the transmitted light through PBS1 (for Pump) and PBS3 (for Stokes). Next, a QWP is placed after PBS1 (PBS3), rotating the polarization of reflected beam from cavity by 90° with respect to the forward beam. This allows the reflected beam to be reflected by PBS1 (PBS3) and directed to the photodiode. The forward beams after the QWP are combined by a dichroic mirror and then sent into the cavity. With the free spectroscopy range (FSR) of 1.3 GHz, the cavity finesse is calculated to be 15500 for Stokes beam and 56700 for Pump beam by measuring the cavity ring-down spectroscopy (CRDS) ([Berden et al., 2000](#)). After passing through the cavity, the transmitted beams are sent to a HWP and PBS2, which distribute the power to a monitor photodiode connected to an oscilloscope and a fiber port. The power spectrum of transmitted beam is filtered by the cavity resonance, with a width in the range of tens of kHz, making it a good reference source for phase noise measurements. The reflected light from the cavity is split by dichroic mirror and sent to the photodiode. To generate the error signal, the photodiode signal is mixed with local oscillator frequency f_{LO} , with the phase of the RF signal delayed by a coaxial cable to achieve phase matching. Fig. 3.8(a) shows the error signal and the transmission signal from high finesse cavity as the laser frequency is scanned. For both curves, the central peak correspond to the offset frequency f_{offset} , while the sidebands around are generated by phase modulation with f_{LO} . Fig. 3.8(b) shows most power is distributed to the offset sidebands instead of the carrier peak. Finally the error signal is sent to a PID controller, which generates feedback signal to lock the Pump and Stokes lasers by controlling the laser current.

3.2.4. Frequency Control with Frequency Comb

To investigate the high-resolution spectroscopy of molecular structure for the ground state transfer, the frequency of the laser used to drive the transitions must be measured with a precision of a few tens of kHz level. This requirement is based on the two-photon detuning analysis in Section 4.4.5. Additionally, stabilizing the laser frequency in our day-to-day operations is crucial due to the fast drifting and high precision requirement. Fortunately, our lab is equipped with a commercial frequency comb (FC) system (Menlo Systems, FC1500-250), which provides high precision measurements down to the sub-kHz level and offers a method



Figure 3.8.: The error signal for PDH locking with feedback loop open. The blue curves represent the PDH error signal, and red curves show the transmission signal from the high finesse cavity. (a) The central peak corresponds to the offset frequency, while the sidebands are generated by phase modulation. (b) Most power is distributed to the upper sidebands on the right side, while the carrier peak on the left side is almost undetectable.

for stabilizing the Raman laser.

The frequency measurement is based on a two-step process: coarse frequency scanning using a homemade Michelson interferometer ([Schuckert, 2014](#)), followed by fine frequency calculating using the frequency comb. The working principles are detailed in previous works ([Pal et al., 2016](#); [Pal, 2016](#); [Sofia, 2022](#); [Yang, 2021b](#)), which will not be repeated here. However, the key concept of how the frequency is calculated is outlined below, along with a schematic of the optical setup for beat measurement, which is essential for explaining the method of checking our laser frequency on a daily basis.

The frequency comb generates light with discrete frequency components, equally spaced by a fixed repetition frequency f_{rep} , and a carrier-envelope offset frequency f_{ceo} . The frequency of spectroscopy laser beats with the nearest comb line, the "needle" of comb, and the beat frequency f_{beat} is recorded. The spectroscopy laser frequency f_{spec} is calculated as:

$$f_{\text{spec}} = N f_{\text{rep}} + f_{\text{ceo}} \pm f_{\text{beat}} , \quad (3.1)$$

where N is the number of comb needle that the beat covers. The sign of the beat frequency $\pm f_{\text{beat}}$ depends on whether the spectroscopy frequency f_{spec} is higher or lower than the closest needle. The repetition frequency f_{rep} is set to 250 MHz, which means the beat frequency f_{beat} must be less than 125 MHz. The number N is determined by the following formula:

$$N = \text{int}[(f_{\text{wm}} \pm f_{\text{beat}} - m f_{\text{ceo}})/f_{\text{rep}}] , \quad (3.2)$$

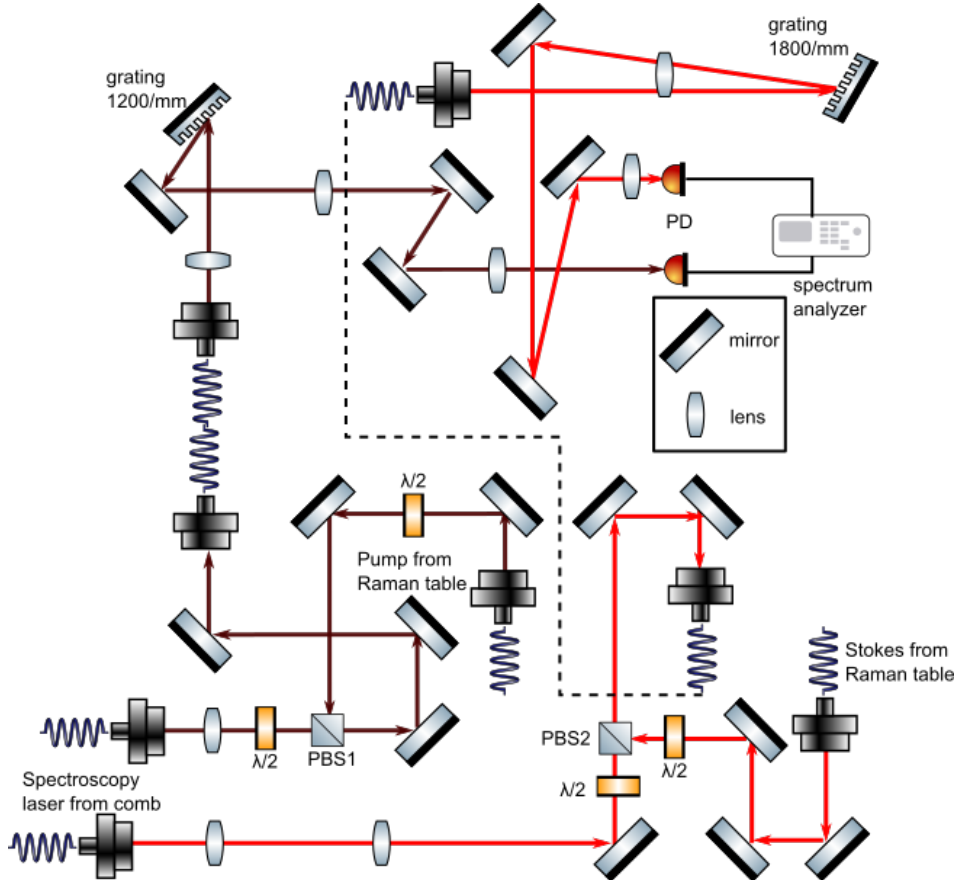


Figure 3.9.: Optical setup of beat measurement between the Raman laser and frequency comb. The red line represents the Stokes (665 nm) light with its corresponding comb needle and brown line represents the Pump (1120 nm) light with its corresponding comb needle. The SNR is improved by extending the light path and using a telescope to expand the beam. The fibers are used to spatial overlap between Raman comb beams.

where the int function rounds the value to the nearest integer. Here, f_{wm} is the laser frequency coarsely measured using the homemade wavemeter, and $m = 1$ or 2 is determined based on whether the comb light used for the beat measurement is at the fundamental or frequency-doubled frequency. The comb system is referenced to a 10 MHz reference generator (Timetech, Refgen 10491), which was later switched to a hydrogen maser (HM) reference from the neighbouring optical metrology lab of Prof. Murray Barrett. The former reference provides a specified relative frequency stability of $\leq 10^{-13}$ for averaging times longer than than 1 s (Allan, 1966).

Fig. 3.9 shows the setup for the beat measurement, optimized for a high signal-to-noise ratio (SRN). Both Pump and Stokes laser, each with approximately 1.5 mW, are transmitted from the Raman table through fibers. They are then combined with different comb light using PBS1 and PBS2, with a HWP controlling the polarization. Afterward, both beams

are coupled into separate fibers to ensure optimal spatial overlap between the Raman and frequency comb (FC) beams. Then, the overlapped beams are sent to a diffraction grating, which disperses the comb light and filters out unnecessary spectral components to prevent saturation of the beat photodiodes (Thorlabs, PDA10CF-EC for 1119 nm and PDA10A-EC for 665 nm). To enhance this process, the light path is extended by reflecting the beams across multiple mirrors, and a lens is used to expand the beam. This setup ensures that a large number of grating lines are covered, achieving greater dispersion. Finally the signals are detected by the beat photodiodes and sent to a spectrum analyzer. The SNR for both Raman lasers is around 30 dB.

3.2.5. Summary of Setting and Stabilization of Laser Frequencies

In daily operations, a key task is to quickly identify and stabilize the desired laser frequency. The following outlines the detailed procedure to achieve this. The coarse frequency is measured using the homemade wavemeter. The Raman beams are sent to the wavemeter, with a reference frequency corresponding to the transition $|\frac{9}{2}, -\frac{9}{2}\rangle \rightarrow |\frac{11}{2}, -\frac{11}{2}\rangle$ for K imaging. By scanning the piezo, current, and temperature a rough reading should be obtained. For the desired STIRAP transfer frequency, the expected readings are approximately 267842.6(1) GHz for the Pump laser and 450841.0(1) GHz for the Stokes laser. For off-resonance Raman transfer the value should be around 267842.0(1) GHz for the Pump and 450840.5(1) for the Stokes. Once those values are reached, the PDH error signal should be visible on the oscilloscope, as shown in Fig. 3.8, if the RF signal f_{offset} and f_{LO} are properly updated. The next step is to carefully recognize the sidebands of the error signal and determine the sign of the beat with the frequency comb to ensure the correct frequency is acquired.

The first step is to confirm the sidebands of the error signal from the PDH setup. The side of the sidebands is determined by tuning the EOM frequency with f_{offset} . If increasing f_{offset} shifts the error signal to the right, the sidebands is on the upper side. Conversely, if the error signal shifts to the left, the sidebands is on the lower side. Once the sidebands is identified, the laser can be locked using current control. Also, the piezo is used to adjust the laser frequency to maintain resonance with the high finesse cavity. This means that if the sidebands frequency increases, the piezo reduces the carrier laser frequency to keep the laser locked to the cavity. The same principle applies when the sidebands frequency decreases – the piezo compensates

process	STIRAP			Raman		
	EOM frequency	beat value	sign of beat	EOM frequency	beat value	sign of beat
Pump	↑	↓	blue	↑	↑	red
Stokes	↑	↓	blue	↑	↑	red

Table 3.1.: The relation between EOM frequency and beat sign. ↑ indicates an increase in the EOM frequency or the beat value increase. ↓ indicates a decrease. The beat sign determines whether the beat signal is a red beat or a blue beat, with the sidebands always selected as the upper sidebands.

by increasing the laser carrier frequency. Next, the focus shifts to the frequency comb. The sign of the beat between the Raman laser and the needle is determined by tuning the laser frequency. If increasing the laser frequency causes the beat value to increase, the beat is on the right side of the needle (blue beat). If the beat value decreases, the beat is on the left side of the needle (red beat). With this understanding, one can establish the relationship between the EOM frequency and the sign of the beat, using the laser frequency as a bridge. Table 3.1 shows the current relationship between the EOM frequency and the sign of beat. Usually, the upper sidebands is used to lock the laser. For the STIRAP process, when increasing the EOM frequency, the beat value should decrease, indicating a blue beat for both lasers. For the Raman process, increasing the EOM frequency causes the beat value to increase, corresponding to a red beat. This relationship is crucial because even if the beat value is correct, the laser frequency can still be wrong if the beat sign and sidebands direction are not selected properly. With the correct beat sign and sidebands, the beat value for the STIRAP process is selected as 83.7 MHz for Pump laser, and 20.8 MHz for Stokes laser, corresponding to an 11 MHz single-photon detuning. And for Raman process, the Pump beat is set to 8.8 MHz and Stokes beat is set to 71.3 MHz, corresponding to a 580 MHz single-photon detuning.

One important note here is the frequency of the carrier envelope may drift by several MHz for unknown reasons. Therefore, it is advisable to confirm the frequency by performing the single-photon spectroscopy mentioned in Section 4.1.1.

After the laser frequency is acquired, the next step is to stabilize the frequency for the experiments. Even with PDH locking, the laser frequency can still fluctuate because the resonance frequency of the cavity shifts due to the temperature fluctuations. The recommended room temperature setting is 23°C, which helps mitigate cavity drifts. To further stabilize the laser, a frequency locking program developed by Prof. Kai Dieckmann using LabVIEW software, is employed. This program adjusts the EOM frequency by tuning f_{offset} , compen-

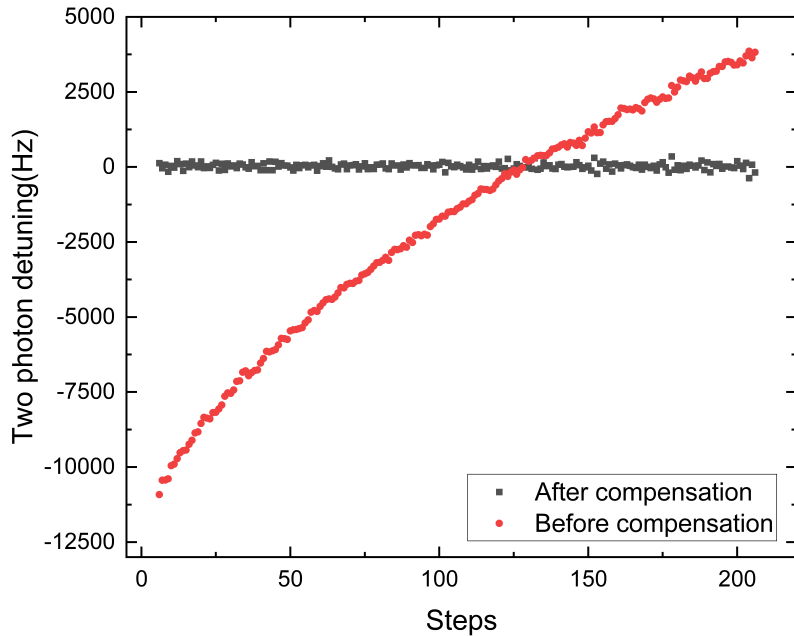


Figure 3.10.: Frequency stabilization is managed using a LabVIEW program. The red points in the data represent the frequency shift without the program active, while the black points show the frequency shift with the program engaged. Each steps take around 1 s and a two-photon detuning of 0 Hz corresponds to the desired frequency for the STIRAP process.

sating for the resonance point drift caused by the thermal expansion of the high finesse cavity. Fig. 3.10 presents the changes in laser frequency with and without compensation at a room temperature of 25° C. Each step takes approximately 1 s. The results indicate that without frequency correction, the laser frequency can shift by about 11 kHz over 2 minutes. By activating the locking program, the frequency is stabilized at 0 Hz two-photon detuning with a root mean square (RMS) noise of 188.7 Hz. This noise level is significantly smaller than the linewidth of the two-photon detuning for STIRAP (580 kHz at 16 μ s pulse duration, see Section 4.4.5). Therefore, it is highly recommended to keep the program running to prevent frequency drifts.

3.3. Removal of Residual Atoms

After Feshbach association (magneto-association), the Feshbach molecules coexist with unassociated atoms. This section discusses the purpose and method for removing the remaining atoms, as outlined in Section 3.3.1. To implement the atom cleaning system, adjustments are made to the imaging system. The new imaging calibration with modification of the integrated setup is presented in Section 3.3.2.

3.3.1. Atom Cleaning with High Field imaging Light

There are two main reasons for removing the unassociated atoms. Firstly, when both atoms and molecules are trapped, the effects of atom-atom collisions, atom-molecule collisions, and molecule-molecule collisions are intertwined, making it challenging to study the system. Removing the unassociated atoms simplifies the system by isolating molecule-molecule collisions, allowing for a more straightforward and focused experiment. Secondly, to accurately count the number of ground state molecules, it is necessary to remove unassociated atoms and residual Feshbach molecules from the counting process. To accomplish this, a system for atom removal is built using an imaging setup designed to operate under a high magnetic field. The design and working principle of the high field imaging system are described in detail by [Pal \(2016\)](#). Absorption imaging of ${}^6\text{Li}$ and ${}^{40}\text{K}$ atoms is carried out under a 216 G magnetic field. For Feshbach molecules, they are first dissociated into atoms, and then absorption imaging of ${}^6\text{Li}$ atoms is performed.

To distinguish between unassociated ${}^6\text{Li}$ atoms and disassociated atoms from Feshbach state, RF-shelving is applied before disassociation to flip the ${}^6\text{Li}$ state from $|\frac{1}{2}, -\frac{1}{2}\rangle \rightarrow |\frac{1}{2}, \frac{1}{2}\rangle$. However, this only hides the ${}^6\text{Li}$ atoms in another hyperfine state, and ${}^{40}\text{K}$ atoms still remain in the ODT, potentially leading to atom-molecule collisions. Accurately counting the number of ground state molecules also requires additional attention. Direct imaging of ground state molecules has not yet been fully developed in our lab. This project will be detailed in the thesis of our group member Victor ([Pinillos, Expected 2025](#)). Currently, counting ground state molecules involves transferring them back to the Feshbach state and then imaging the Feshbach molecules using the same laser beam as for the absorption imaging for ${}^6\text{Li}$. However, the transfer efficiency is not 100%, meaning that some Feshbach state molecules remain throughout the process, potentially leading to over-counting or high background number. To address this, an atoms-cleaning system is proposed to reduce the influence of residual atoms or non-transferred Feshbach molecules and enable imaging with ${}^{40}\text{K}$.

The cleaning method involves cycling transitions with σ^- light for $|\frac{1}{2}, -\frac{1}{2}\rangle \rightarrow |\frac{3}{2}, -\frac{3}{2}\rangle$ (${}^6\text{Li}$) and $|\frac{9}{2}, -\frac{9}{2}\rangle \rightarrow |\frac{11}{2}, -\frac{11}{2}\rangle$ (${}^{40}\text{K}$), same as the high field imaging. Initially, the cleaning pulse followed the same light path as the imaging pulse. After the first STIRAP trip, the cleaning pulse is applied for $500\ \mu\text{s}$ to remove both ${}^6\text{Li}$ and ${}^{40}\text{K}$ atoms. A new cleaning setup has since been implemented from a different direction, reducing the cleaning duration to $20\ \mu\text{s}$.

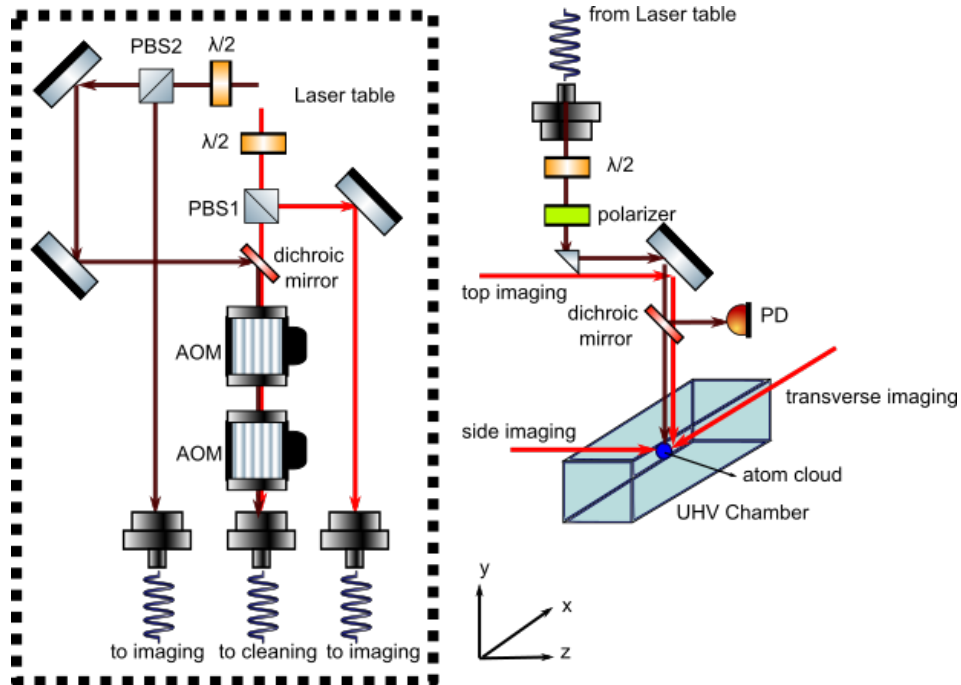


Figure 3.11.: Atoms cleaning set up on laser table and MOT table. The cleaning light for ${}^6\text{Li}$ and ${}^{40}\text{K}$ is separated from their respective high field imaging light. Using HWP and PBS, most of the power is sent to the fiber used for cleaning. The cleaning beam is sent to the atom cloud from the top imaging direction. A photodiode is used to detect the cleaning beam, ensuring that it switches on and off at the desired times. In this scheme, the z-direction corresponds to the Feshbach field direction, which also serves as the guiding field for imaging.

Fig. 3.11 shows the setup of new atom-cleaning system. Instead of using the same light path as side imaging, a new path has been built up from the laser table. Using PBS1 and PBS2, the imaging beams for ${}^6\text{Li}$ and ${}^{40}\text{K}$ are split into two part. One part is still used for imaging system (20%), while the other is combined using a dichroic mirror, passing through a tandem AOM for fast switching, and sent to a new fiber coupler. Two HWPs are used to control the power distribution for the imaging and cleaning light of both ${}^6\text{Li}$ and ${}^{40}\text{K}$. The cleaning beams are then sent through the top imaging direction to perform the atom cleaning. After the fiber, a HWP and a polarizer are used to create circularly polarized light.

A crucial detail is the polarization of the cleaning beams. The traveling of the cleaning light follows wave function $\psi(r, t) = A \cos(k \cdot r - \omega t + \phi)$, where A is the amplitude of the wave, k is the wave vector, ω is angular frequency, and ϕ is the phase offset. When the k vector of cleaning beams are parallel to the magnetic field (the Feshbach field in z-direction), pure left-handed circular polarized light is generated, enabling a σ^- cycling transition. When the k vector is perpendicular to the magnetic field, and circularly polarized light is applied, transition for σ^- , σ^+ , and π are theoretically possible. However, under our conditions, σ^+

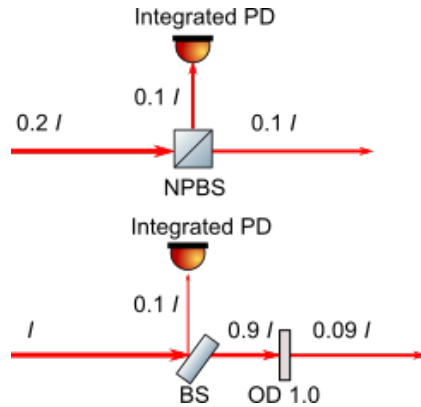


Figure 3.12.: Imaging calibration with integrated photodiode. The upper path in the diagram illustrates the modifications made to the imaging system after distributing the power to the cleaning path, while the lower path shows the original setup without the cleaning path. In the new setup, the BS has been replaced with a NPBS, and the OD 1 filter has been removed. The goal is to maintain the new imaging system as close as possible to the old one in terms of performance. In both setups, I represents the intensity of the light normalized to the initial intensity of the imaging light. The integrated PD is used to control the duration of the light pulse.

and π transitions do not occur. At the high magnetic field of 216 G, the transition frequencies for σ^- , σ^+ , and π are separated by hundreds of MHz because the quantum numbers F and m_F are no longer good quantum numbers at such high magnetic fields. Instead, the actual quantum numbers are total angular momentum and its projection J and m_J . Therefore, with a specific laser frequency, only the σ^- transition occurs, maintaining the cycling transition condition. The advantage of separating the imaging and cleaning light is that both process can be manipulate independently. Compared to the RF-shelving method, this setup allows the detection of ground state molecules with either ${}^6\text{Li}$ or ${}^{40}\text{K}$. And the consideration is simplified by only focusing on molecule-molecule collisions.

3.3.2. Imaging Calibration

The imaging setup needs to be readjusted due to the additional cleaning setup. As show in Fig. 3.12, in the old design, a beam sampler was used to split 10% of the power into the integrated photodiode, while the remaining 90% went for imaging. On the imaging path, an OD 1 filter attenuated 90% of the power, meaning that 10% of the original power reached the integrated photodiode, and 10% was used for imaging. In the new setup, 80% power is distributed to atom cleaning, leaving only 20% for imaging. To maintain the same conditions as in the old setup, a NPBS with 50% reflection rate is used to split the remaining light between the integrated photodiode and the imaging path. Additionally, the OD filter has

been removed. In this new configuration, 10% of the original light goes to the integrated photodiode, and 10% is used for imaging. With the modification, the new setup effectively restore the same balance as before.

3.4. Free Space Optical Lattice

Studying quantum phenomena in degenerate molecular samples not only requires efficient production, but also sufficient sample lifetimes. For ${}^6\text{Li}{}^{40}\text{K}$ chemical reactive two-body collisions ([Żuchowski and Hutson, 2010](#)) lead to rapid decay. Even for those bi-alkali species that are chemically stable in the ground state, loss occurs due to so-called *sticky* collisions of two molecules forming a long-lived collisional complex ([Christianen et al., 2019](#); [Gersema et al., 2021](#); [Gregory et al., 2020](#); [Mayle et al., 2012, 2013](#)), which can be excited by the optical trapping light. One approach to mitigate these losses is to construct a deep optical lattice with single-site molecular occupancy. The setup of such an optical lattice is shown in Section 3.4.1 for future research on the ground state molecules in an optical lattice. An undesired interference phenomenon encountered during the lattice setup is also discussed in Section 3.4.2.

3.4.1. Lattice Setup

The optical lattice is formed by three orthogonal retro-reflected laser beams at a wavelength of 1064nm. Fig. 3.13 shows the schematic of a free-space 3D optical lattice. A Mephisto MOPA laser (1064 nm) is used, which can deliver 30 W output power with a narrow linewidth of 3 kHz. The narrow linewidth ensures a long coherence length, preventing fluctuations in trap depth, while the high power allows the generation of a deep lattice. An optical isolator is placed after the laser output to protect it from the retro-reflection. Combinations of HWPs and PBSs are used to divide the output into three beams, with fully-controllable power for each beam. These beams form the lattice in three directions: the side (z-direction), combined with the ODT side beam; the top (y-direction), combined with the ODT top beam; and the transverse (x-direction), combined with the optical plug beam. Each beam is modulated by an AOM enabling fast switching of the lattice. The AOMs are set to different frequencies (+80 MHz, -80 MHz, and 200 MHz) to prevent unwanted interference between standing waves from different directions. Beam dumps with prisms are used to capture excess power, while

beam samplers reflect 1% of the light into photodiodes. The photodiode signals are sent to fast feedback loops to stabilize the light intensity, ensuring that power drifts from the laser and AOM do not affect the experiment. After the samplers, dichroic mirrors are used to combine another laser system (950 nm) with the lattice setup for a magic lattice project. This project will be detailed in the thesis of our group member Xiaoyu ([Xiaoyu, Expected 2026](#)). Several lenses are used to shape the beam waist and focus the beams on the atomic cloud (not fully shown in the schematic). The beams waists on the atomic cloud are measured to be approximately $110\ \mu\text{m}$, with power reaching up to 5 W in all three directions. After passing through the UHV chamber, the beams are reflected by retro-mirrors to form standing waves.

To align the lattice beams properly, alignment fibers are introduced into the system to help ensure that the lattice beams are focused on the atomic cloud and the retro-reflected beams overlap precisely with the forward beams. Proper alignment is crucial, as misaligned beams or imperfect overlap can create potential gradients, negatively impacting experimental results. Fine alignment and overlapping will be further optimized through superfluidity measurements, as will be discussed in Section [6.1](#). Additionally, spatial filtering and fiber alignment for the beams are proposed, with further details available in [Xiaoyu \(Expected 2026\)](#). The free-space lattice is currently being used to verify lattice parameters and achieve an understanding of how to align the lattice.

3.4.2. Avoiding Undesired Interference

When aligning the lattice, unwanted interference has been observed, which can impact the experiments for different optical traps including the optical lattice trap. A similar issue has been discussed by [Moses \(2016\)](#). Fig. [3.14\(a\)](#) shows the formation of this interference. The main issue is the small incident angle of the beams on a glass cell, which doesn't have an anti-reflection coating for the inner surface. Without the coating, the reflection rate at the inner surface is 4% and a small incident angle can be set at θ with respect to the normal. When both forward and retro-reflection beams pass through the glass cell, four reflected beams are generated, each with 4% power the primary incident light (not considering the loss for the retro beam). These reflected beams interfere with the primary light. If the beams are exactly normal to the glass surface, i.e., $\theta = 0^\circ$, the result is a standing wave pattern with 532 nm spacing, typical of the optical lattice. Given that the pixel resolution

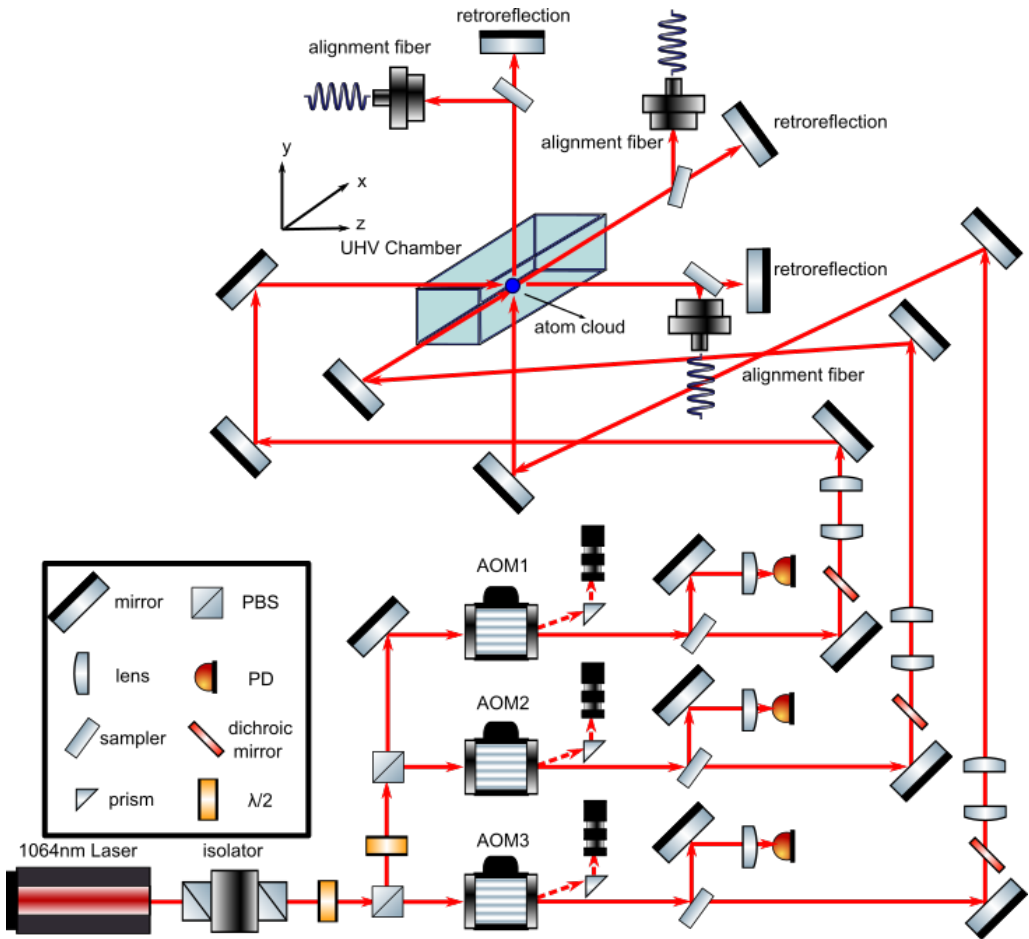


Figure 3.13.: Free space optical lattice setup. The setup consists of three separate beams, each with its own retro-reflection, used to generate standing waves. Three AOMs are used to independently and quickly switch the lattice beams on and off, allowing the formation of 1D, 2D, or 3D lattice. Three dichroic mirrors are used to combine another laser system into the lattice setup, enabling lattice formed by different laser sources. Additionally, three alignment fibers are utilized as spatial references, making beam alignment and overlapping significantly easier. The lenses used to collimate and focus the beams are simplified in the schematic.

of our imaging system corresponds to $3.11\ \mu\text{m}$. This means no interference fringes should be detected by the camera under these conditions. However, when the incident angle is small, assume $\theta \approx 1^\circ$, the distance between interference fringes becomes $d = \frac{\lambda}{2\sin\theta} = 30.49\ \mu\text{m}$ which can be clearly observed by our imaging system. Fig. 3.14(b) shows the slits in a ^{87}Rb atomic cloud, created by the interference fringes with incident angle $\theta \approx 0.82^\circ$. The interference is problematic because the interference potential scales as $\sqrt{I_{\text{in}}I_r}$, where I_{in} is the intensity of the incident beams and I_r is the intensity of the reflected beams. A 4% reflection can create a trapping potential with 20% of the strength of the original lattice. The issue is more serious when considering the ODT potential. The potential of the optical trap is calculated using Equation 2.29($[(1 - \sqrt{f})^2 + 4\sqrt{f} \cos^2(kx)] \frac{U_0/4}{1+(x/Z_x)^2} \exp[-\frac{2(y^2+z^2)}{w_0^2} \frac{1}{1+(x/Z_x)^2}]$). The first term in

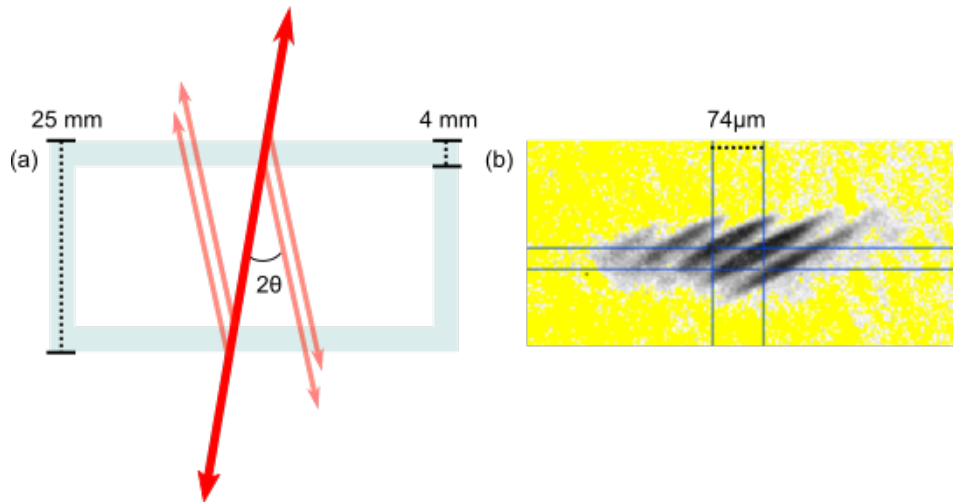


Figure 3.14.: The formation of undesired interference pattern with uncoated inner surface of the glass cell. (a) The diagram shows the primary lattice beams (red arrows) and the reflected beams from the uncoated inner surface of the glass cell (light red arrows). The incident angle of the primary lattice beams is θ . The thickness of the glass cell walls is 4 mm, and the total width of the glass cell from the side direction is 25 mm. (b) The effect of the interference pattern with incident angle $\theta \approx 0.82^\circ$. The interference causes the ^{87}Rb atomic cloud to be segmented into pieces with approximately $37 \mu\text{m}$ spacing.

$[(1 - \sqrt{f})^2 + 4\sqrt{f} \cos^2(kx)]$ represents the ODT, and the second term corresponds the optical lattice, where f is attenuation factor and k is the wave number. When there is no reflected light from the inner surface of the glass cell, $f = 0$, which effectively cancels out the second term, leaving only the first term to represent the ODT potential. However, with 4% reflected light, $f = 0.04$ and the potential formula becomes $0.64 + 0.8 \cos^2(kx)$, indicating that the trapping potential of the lattice is comparable to that of the ODT. Consequently, minimizing unwanted reflections is essential to maintaining a pure ODT trap.

To avoid the formation of unwanted interference, the angle of the incident beam needs to be carefully chosen. With a sufficiently large incident angle, the reflected light wouldn't overlap with the primary incident light. As the waist of lattice beams $\omega_0 = 110 \mu\text{m}$, the Rayleigh range is calculated as $Z_R = \frac{\pi\omega_0^2}{\lambda} = 35.7 \text{ mm}$, which is larger than the width of glass cell, so the beams are colimated inside the glass cell. To prevent interference, the separation between the primary incident beams and the reflected beams should be approximately 3 – 4 beam waists apart. This promises that the trap potential of the undesired lattice is $\ll 1\%$ of the potential of the ODT, which requires the incident angle $\theta > 1.5^\circ$. In experiments, the θ is set to 3° to ensure sufficient separation.

3.5. Optically Plugged Trap

The optically plugged quadrupole trap (OPT) was first demonstrated by Ketterle's group ([Davis et al., 1995](#)). The optically plugged magnetic quadrupole (OPT) trap offers several advantages, as demonstrated by various research groups ([Dubessy et al., 2012](#); [Heo et al., 2011](#); [Naik and Raman, 2005](#); [Wu et al., 2011](#)). The key advantage relevant to our lab is the tight trap confinement, which allows for a faster evaporative cooling process and provides a large trapping volume to hold atoms. As discussed in Section 3.1, the evaporation process for Rb, K, and Li is time-consuming due to the application of the QUIC trap. The long evaporation period (~ 60 s) in the QUIC trap causes significant heating of the magnetic coils, necessitating an additional cooling period of more than 30 s for the coils in each experimental cycle. To accelerate this process, the optically plugged trap method is proposed as a replacement for the QUIC trap. Also, the atom cloud is positioned exactly at the center of the chamber, ensuring optimal optical access for later experiments, such as optical dipole traps or optical lattice setups. In this section, the setup for the OPT is presented.

3.5.1. Plugged Beam Setup

Fig. 3.15 shows the setup of the plug beam. The maximum output power of the laser (IPG, GLR-30) can reach up to 30 W at a wavelength of 532 nm. In experiments the power is set to 28 W. The output laser is first sent into an AOM with 80% 1st-order efficiency, which serves as a fast switch to control the plug on and off. The 0th-order beam is sent to beam dump 1 and the 1st-order beam passes through a telescope is used to adjust the beam waist. The beam is then combined with the transverse imaging beam through dichroic mirror 1 and sent into the UHV chamber along the x-direction. The lens before the chamber is used to focus the beam at the atomic cloud position. The telescope and focusing lens are used to control the beam waist, which is set to be $60 \mu\text{m}$ in recent experiments. The laser power is measured as 22 W before entering the chamber and 18 W after passing through the chamber, with the loss mainly due to reflections from the chamber window. Dichroic mirror 2 sends the plug beam into dump 2 to absorb the remaining light, allowing the transverse imaging beam to pass through to the camera. The magnetic field is provided by the coils used in the quadrupole trap.

One critical issue to address is the formation of interference patterns, as discussed in Sec-

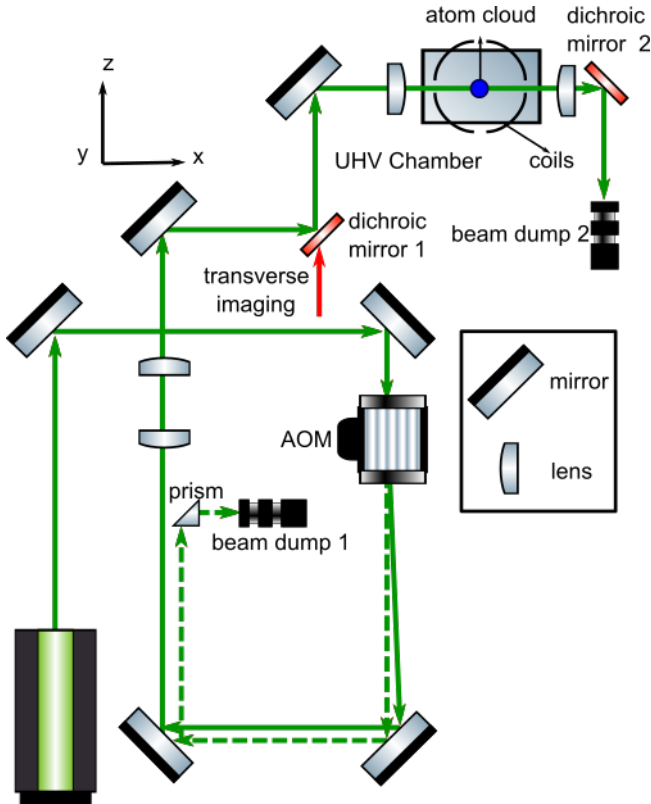


Figure 3.15.: Optically plugged trap setup. The Plug beam is sent from the transverse imaging direction (x-direction) and focused at the position of atomic cloud. Due to the high power of the plug beam, the remaining beam after chamber must be sent to an optical dump to avoid damaging the camera. The black circle presents the quadrupole coils used in OPT.

tion 3.4.2. Reflected beams from both the uncoated inner surface of the glass cell and the chamber window can interfere with the incident plug beam, forming an interference lattice if the incident angle is too small. This situation can be even more problematic than the interference from the lattice and ODT beams mentioned earlier, as the reflection from the chamber window is much stronger. The general approaches would be to break the coherence of the laser with an EOM and tilt the incident angle to a relatively large value (3° e.g.). Unfortunately, the plug beam setup was implemented before we realized the issue of interference, and neither of these solutions has been applied yet. However, these are proposed as potential improvements for future upgrades to the system.

3.5.2. Plug Beam Alignment

When building up the OPT, the beam waist and power need to be determined first. Two primary considerations are involved. Firstly, the potential minimum position z_{\min} should be located sufficiently far from the center of the trap. One reason for this is that the atoms

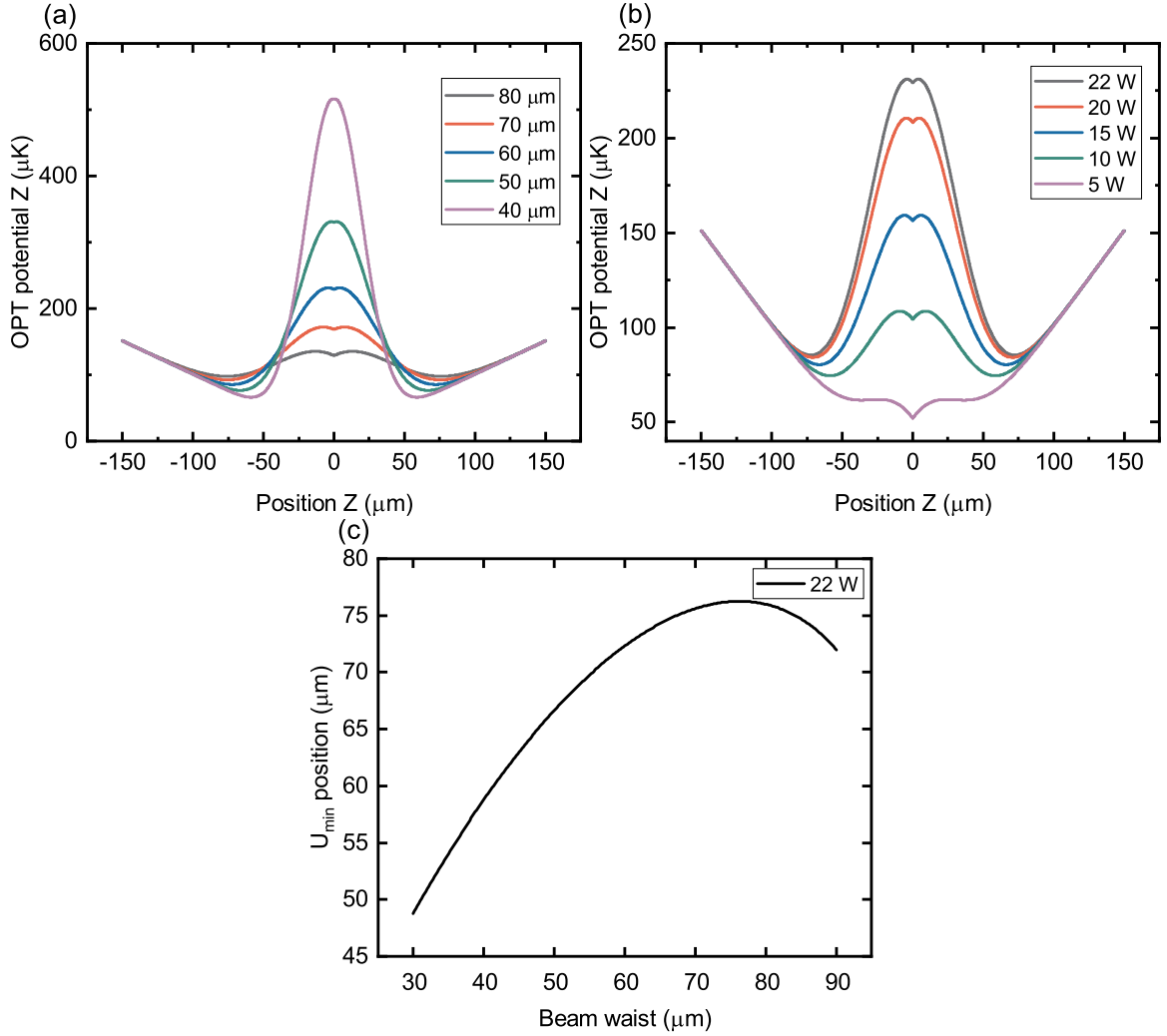


Figure 3.16.: Trapping potentials along z -direction for different beam waist (a) and power (b). (a) The power is set to 22 W while varying the beam waist. (b) The beam waist is set to 60 μm while varying the power. The magnetic field gradient is set to 300 G/cm and remains consistent throughout unless otherwise specified. (c) The position of the minimum potential, z_{\min} , as a function of beam waist at 22 W.

are confined at z_{\min} , which should be located away from the Majorana loss region. Another reason is that the magnetic field at z_{\min} needs to be strong enough to separate hyperfine states of ^{87}Rb between the $|F = 2, m_F = 2\rangle$ and $|2, 1\rangle$ states, as discussed in Section 3.5.3. Secondly, the potential difference between the central barrier and the minimum potential at z_{\min} should be large enough to prevent atoms from tunneling through the central barrier. The fundamental requirement is to set the beam waist $w > \rho_{\text{Maj}}$, where $\rho_{\text{Maj}} = \sqrt{\frac{\hbar v}{\pi \mu b'}}$ is the effective size of Majorana loss region (Ketterle et al., 1999). Here, v is the velocity of atoms and the size of the region is typically on the micrometer scale.

Fig. 3.16 illustrates the potentials of the trap as a function of power and beam waist,

using ^{87}Rb as an example. In Fig. 3.16 (a), with the power fixed at 22 W, varying the beam waist significantly alters the potential curvature. In general, a smaller beam waist results in a greater difference between the central barrier and the minimum potential, which is the desired scenario. However, within a specific range, a decreased beam waist could cause the minimum potential position z_{\min} to shift to the trap center, which should be avoided. The relation between the minimum potential position and beam waist is also demonstrated in Fig. 3.16 (c). The position z_{\min} increases with the beam waist until it reaches $75 \mu\text{m}$, necessitating careful selection of the beam waist. In the experimental setup to achieve a ^{87}Rb BEC, the beam is chosen to be $60 \mu\text{m}$. In Fig. 3.16 (b), with the beam waist fixed at $60 \mu\text{m}$, varying the laser power alters the potential curvature. A similar analysis to that conducted with beam waist reveals that increasing the power not only enhances the difference between the central barrier and the minimum potential but also shifts the minimum potential position z_{\min} farther from the central position which is precisely the desired outcome. Thus the OPT benefits from higher power, consequently, the power is set to the maximum available value of 22 W in the experiment.

The next step is to align the plug beam. Firstly, the center of the quadrupole trap is located by analyzing images captured by a CCD camera that displays ^{87}Rb cloud. An image of ^{87}Rb cloud is taken with only the quadrupole trap active, utilizing 0 time of flight (TOF) to achieve an inter-trap imaging. The cloud is evaporatively cooled to around 2 MHz (the process of RF evaporation, which will be discussed in next section) to create a small cloud that marks the center of the quadrupole trap. A weak leakage of the plug beam is then directed from dichroic mirror 2 to the CCD camera, creating a bright spot. (The leakage power needs to be further attenuated with a filter to avoid saturating the camera.). Dichroic mirror 1 is adjusted to overlap this bright spot with the marked position of the atomic cloud. This completes the coarse alignment. Once the plug beam is roughly aligned, it should overlap with the atomic cloud, which can be verified visually. As shown in Fig. 3.17, when RF frequency for evaporative cooling is gradually swept down from 4 MHz to 1.2 MHz, a hole appears on the atomic cloud and eventually splits it into two distinct pieces. The alignment is optimized if the hole is precisely at the center of the cloud and the two separated parts of the cloud are roughly equal in size.

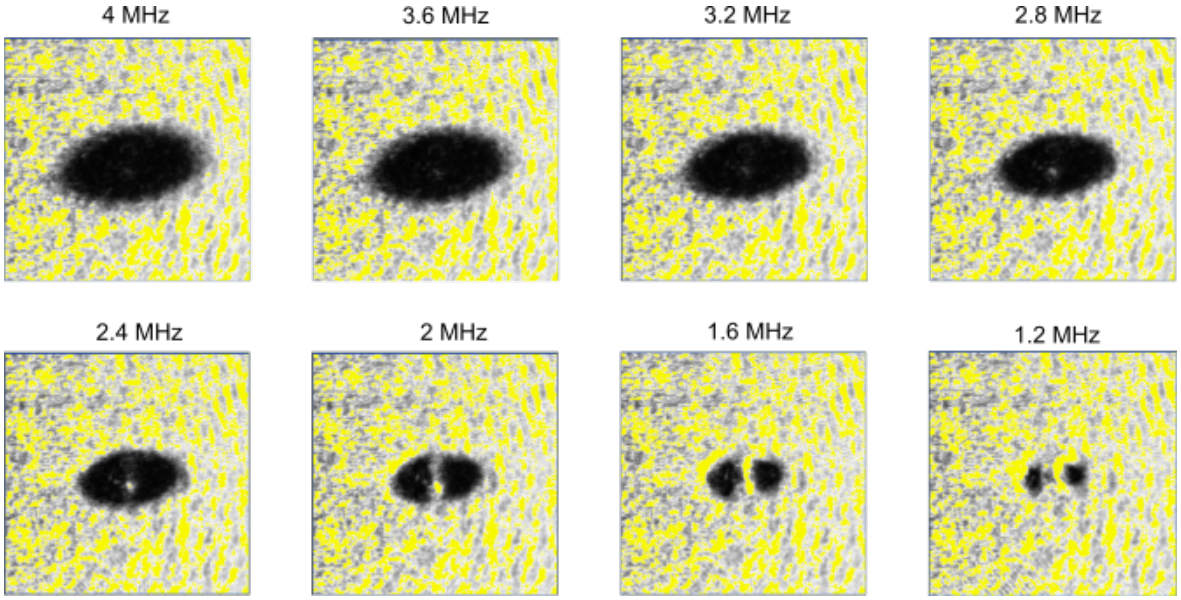


Figure 3.17.: Image of the effect of the aligned plug beam on the ^{87}Rb atoms cloud. When RF frequency is gradually ramping down from 4 MHz to 1.2 MHz, the temperature of the cloud decreases simultaneously from $40 \mu\text{K}$ to $10 \mu\text{K}$. Additionally, the effect of the plug beam gradually becomes apparent. A hole at the center of the atoms cloud can be observed at beginning and then the cloud is separated into to two parts.

3.5.3. Rb Evaporative Cooling

To verify the OPT, the evaporative cooling of ^{87}Rb is first tested using both RF and MW evaporation methods. The evaporation process follows the existing design used in the QUIC trap, as detailed introduced in [Taglieber \(2008\)](#); [Taglieber et al. \(2008\)](#). In this section, only the essential part will be discussed to aid understanding of the process.

3.5.3.1. RF Evaporation

Evaporative cooling relies on the selective removal of atoms with the highest energy from the trap. The remaining atoms subsequently rethermalize to a lower temperature through elastic collisions within the atomic ensemble. To remove atoms with energy higher than a truncation energy, ϵ_t , a RF field is applied to couple the trapped and untrapped Zeeman states. The angular frequency of the RF field satisfies the resonance condition

$$\mu_B g_F |B(\vec{r})| = \hbar \omega_{\text{rf}} \quad . \quad (3.3)$$

and the relation between the truncation energy ϵ_t and the frequency of the applied RF signal is

$$\epsilon_t = m_F \hbar (\omega_{\text{rf}} - \omega_{\text{min}}) \quad . \quad (3.4)$$

where $\omega_{\text{min}} = \mu_B g_F |B(z_{\text{min}})|/\hbar$ is the resonance frequency at the potential minimum of the trap.

In general, the initial RF frequency in the evaporation process is selected based on the temperature of the cloud transferred to the trap with relation $k_B T = \epsilon_t$. In our OPT experiment, the initial temperature of the cloud is measured to be $380 \mu\text{K}$, and the starting frequency is set to 50 MHz . By progressively sweeping down the RF frequency, atomic density increases as the temperature decreases, despite the loss of atoms during this process. The efficiency of the cooling process is characterized by monitoring the number of atoms N and temperature T . The preference is to achieve a lower temperature with minimal atom loss. Consequently, an efficiency parameter is defined as

$$\alpha_{\text{ev}} = \frac{d(\ln T)}{d(\ln N)} = \frac{\dot{T}/T}{\dot{N}/N} \quad , \quad (3.5)$$

which is a quantity that describes the temperature decrease per lost particle ([Ketterle and Druten, 1996](#)). The temperature and number of atoms are measured at the beginning and the end of each cooling period. The evaporative cooling process is optimized in each period to achieve a lower temperature with minimal atom loss. The measured results are shown in the Fig. [3.18](#), presenting the temperature and atom number during the evaporative cooling process. From the data, the efficiency parameter is fitted to be $\alpha_{\text{ev}} = 0.98(5)$, indicating that the temperature decreases by approximately one order of magnitude for each order of magnitude reduction in atom number. Notably, α_{ev} remains almost constant until the end of evaporation process (as seen in the last data point).

In addition, the phase-space density (PSD) $\rho_{\text{PSD}} = n \lambda_{\text{DB}}^3$ is also used to evaluate the cooling efficiency, where λ_{DB} is the de Broglie wavelength. The cooling efficiency related to PSD is defined by

$$\chi = - \frac{d(\ln \rho_{\text{PSD}})}{d(\ln N)} \quad , \quad (3.6)$$

which represents the relative increase in ρ_{PSD} per relative loss in atoms number N . Fig. [3.19](#) shows the measured results based on the same cooling process as in Fig. [3.18](#). From the data

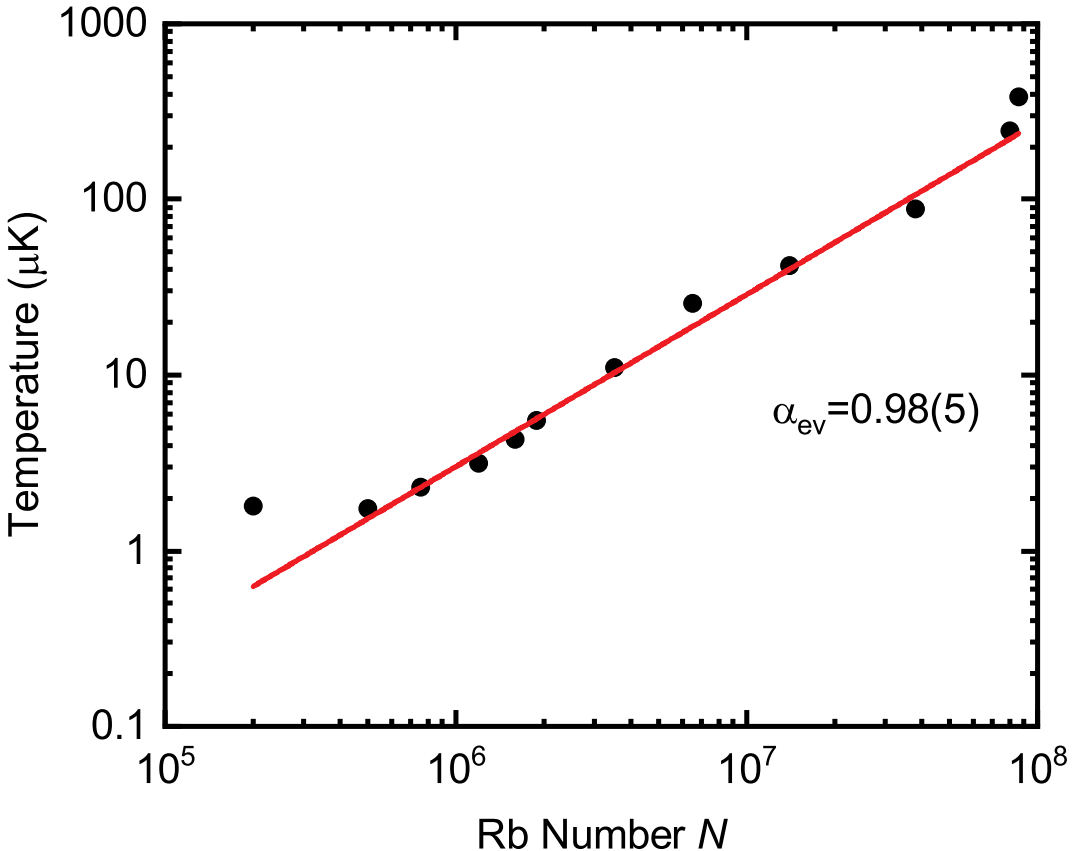


Figure 3.18.: Evaporative cooling process of ^{87}Rb by RF evaporation. The black circles represent the measured atom number and temperature during the evaporative cooling. The red line is a fit to the data, yielding an efficiency parameter $\alpha_{\text{ev}} = 0.98(5)$.

and fitting, $\chi = 1.97(9)$, indicating an increase in degeneracy by two orders of magnitude for each order of magnitude reduction in atom number.

In the experiments, we did not observe a clear BEC signature with RF evaporative cooling in the OPT, which shows lower efficiency compared to evaporation in the QUIC trap. Possible explanations for this will be discussed later. In Section 3.5.3.2, I present the MW evaporation method for ^{87}Rb , which would be used for achieving triple degeneracy ^{87}Rb - ^{6}Li - ^{40}K in future experiments. This discussion is based on preliminary experimental results and theoretical calculations.

3.5.3.2. MW Evaporation

To achieve quantum degeneracy of ^{6}Li and ^{40}K MW evaporative cooling for ^{87}Rb need to be adapted instead of RF evaporation. The main reason is that RF evaporation is not perfectly species-selective. For ^{6}Li in state $|F = 3/2, m_F = 3/2\rangle$, the truncation energy is calculated as

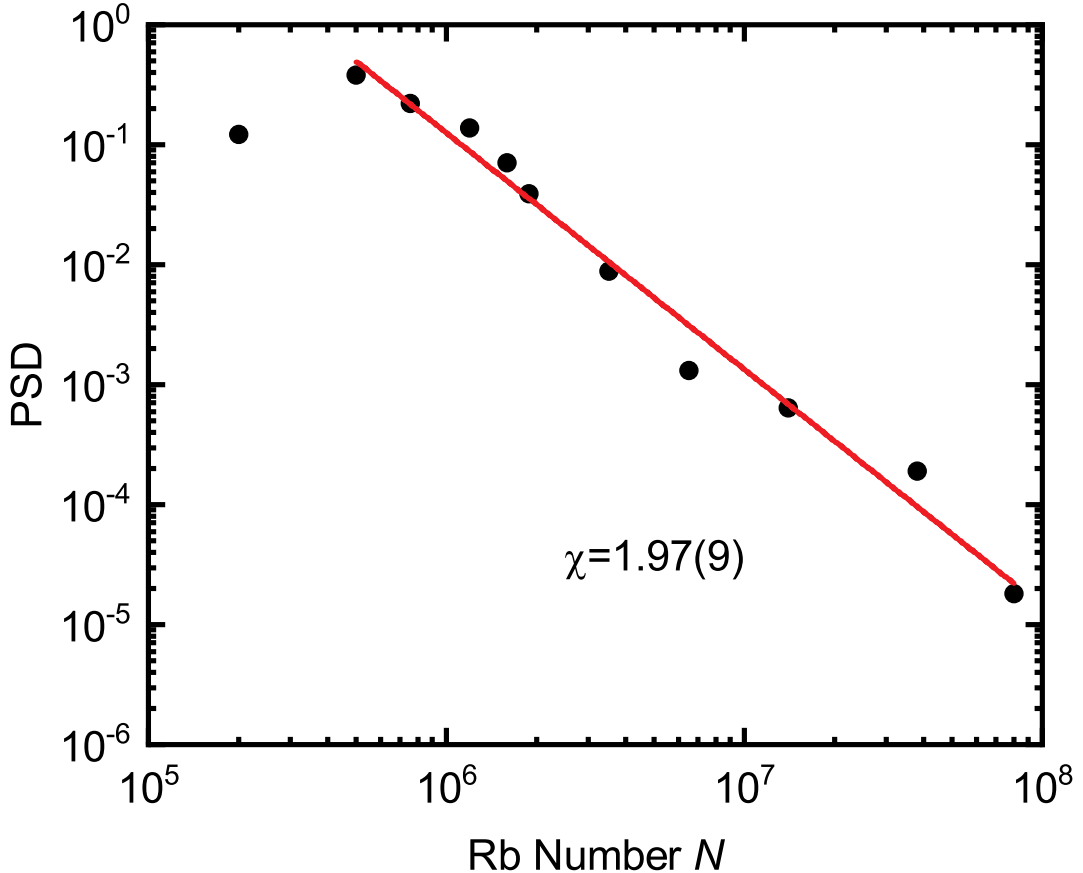


Figure 3.19.: Evaporative cooling process of ^{87}Rb by RF evaporation. The black circles indicate the measured atom numbers and PSD during the evaporative cooling. The red line is fit to the data, giving a degeneracy parameter $\chi = 1.97(9)$.

$\epsilon_{t,\text{Li}} = \frac{3}{2}\hbar\omega_{\text{rf}} - \mu_{\text{B}}B_{\min,\text{Li}}$. Comparing this with the truncation energy for ^{87}Rb atoms in $|2, 2\rangle$ states, $\epsilon_{t,\text{Rb}} = 2\hbar\omega_{\text{rf}} - \mu_{\text{B}}B_{\min,\text{Rb}}$, the RF evaporation targeting ^{87}Rb atoms also undesirably removes ^6Li atoms at a lower energy region. Here, B_{\min} represents the magnetic field at the potential minimum position z_{\min} for different species. It will be shown in Section 3.5.4 that $B_{\min,\text{Rb}} \approx B_{\min,\text{Li}}$.

For MW evaporative cooling, the processes differs slightly between the QUIC trap and the OPT, even when using only ^{87}Rb . In the QUIC trap, evaporative cooling of ^{87}Rb involves three MW signals (as shown in Fig. 3.20) to drive different transitions. One signal (solid red line) couples the trapped state $|F = 2, m_F = 2\rangle$ to the untrapped state $|1, 1\rangle$ for removing atoms above ϵ_t . Two other signals are used to remove undesired trapped states: $|2, 1\rangle \rightarrow |1, 0\rangle$ (solid blue line) and $|1, -1\rangle \rightarrow |2, 0\rangle$ (solid yellow line). The atoms in the $|1, -1\rangle$ state are remnants from the MOT and are not produced during the cooling process. The atoms in $|2, 1\rangle$ state, however, are reproduced during the cooling process mainly due to the resonant

transition $|1, 1\rangle \rightarrow |2, 1\rangle$ induced by the same MW signal used for $|2, 2\rangle \rightarrow |1, 1\rangle$ transition at different magnetic field (dashed red line). Additionally, the $|2, 1\rangle$ state can be generated by dipolar relaxation of atoms in $|2, 2\rangle$ state at a lower rate ($10^{-15} \text{ cm}^3 \text{s}^{-1}$) (Boesten et al., 1996; Mies et al., 1996; Moerdijk and Verhaar, 1996). The slow repopulation of the $|2, 1\rangle$ state has been observed and is discussed in Section 6.1.5 of Taglieber (2008). This effect becomes noticeable only after holding the Rb cloud in the magnetic trap at $1.5 \mu\text{K}$ for 20 s. In contrast to the fast repopulation of the $|2, 1\rangle$ state caused by MW transitions, dipolar relaxation is not a significant factor during the cooling process.

The cleaning MW frequency (solid blue line) is effective due to a 3 G offset at the bottom of the QUIC trap. This offset creates a Zeeman splitting between $|2, 2\rangle$ and $|2, 1\rangle$ (also between $|1, -1\rangle$ and $|1, 0\rangle$) with $\omega_{\text{rf}} = \mu_B g_F |B| / \hbar = 2\pi \cdot 2.1 \text{ MHz}$. This splitting prevents the $|2, 2\rangle \rightarrow |1, 1\rangle$ transition from occurring at the same MW frequency (solid blue line) used for cleaning. The same principle applies for cleaning $|1, -1\rangle$ state.

Cleaning out undesired hyperfine states is essential because spin-exchange collisions can lead to heating of atomic ensemble and atoms loss. Specifically, the only stable combination of magnetically trappable atomic states for ^{87}Rb , ^{40}K , and ^6Li is

$$^{87}\text{Rb} |2, 2\rangle \& {}^{40}\text{K} |9/2, 9/2\rangle \& {}^6\text{Li} |3/2, 3/2\rangle$$

from the spin-exchange condition (Tiesinga et al., 1993).

The discussion returns to the topic of evaporative cooling within the OPT. In this setup, the methods employed to eliminate undesired hyperfine states have proven ineffective at the beginning of evaporation. As illustrated in Fig. 3.20, there is a lack of magnetic field offset at the center of the OPT. This means that the MW signal used to clean the $|2, 1\rangle$ state (solid blue line) could also drive the transition $|2, 2\rangle \rightarrow |1, 1\rangle$ in regions of low magnetic field (dashed blue line). This undesired transition results in the removal of low energy atoms located near the potential minimum position z_{min} . Therefore, the MW evaporative cooling process fails due to the continuous loss of low energy atoms while attempting to clean the $|2, 1\rangle$ state.

To address this, instead of cleaning the undesired $|2, 1\rangle$ state, a method is proposed to prevent the $|1, 1\rangle \rightarrow |2, 1\rangle$ transition (dashed red line) from occurring, which avoids the generation of $|2, 1\rangle$ state. This is achieved by applying two RF signals during the cooling process, as shown in the right part of Fig. 3.20. After ^{87}Rb atoms are transferred from $|2, 2\rangle \rightarrow$

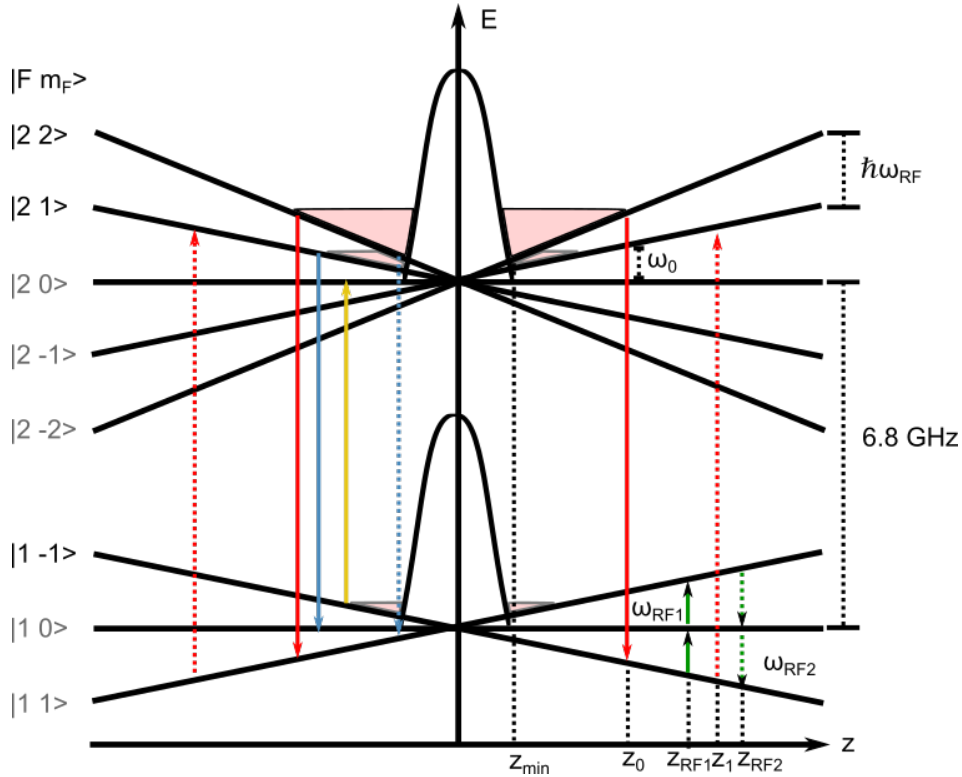


Figure 3.20.: Schematic level scheme for MW evaporative cooling in the OPT with relevant transitions. The MW signals used in QUIC trap configuration is also included for comparison. ^{87}Rb atoms are transferred from $|2, 2\rangle \rightarrow |1, -1\rangle$ by a MW signal (solid red line). Since the state is anti-trapped, the atoms in this state are accelerated away from the trap center towards regions of higher magnetic field. At a certain magnetic field strength, the same MW signal becomes resonant with $|1, -1\rangle \rightarrow |2, 1\rangle$ transition (dashed red line), causing atoms to be transferred into the undesired trapped state $|2, 1\rangle$. In the QUIC trap, population in this state $|2, 1\rangle$ is continually removed by a second MW signal (solid blue line). While in OPT, the second MW signal also drives the $|2, 2\rangle \rightarrow |1, -1\rangle$ transition (dashed blue line) in regions of low magnetic field, inadvertently removing atoms in the low temperature $|2, 2\rangle$ state. To avoid this issue, two RF signals (solid and dashed green lines) are applied to bypass the $|1, -1\rangle \rightarrow |2, 1\rangle$ transition at higher magnetic fields. Additionally, a third MW pulse (solid yellow line) is applied at the beginning of the cooling process to remove atoms in the $|1, -1\rangle$ states. The position z on the z axis indicates the magnetic field position corresponding to certain MW or RF frequency during the cooling process.

$|1, 1\rangle$, RF1 signal (solid green line) is applied to transfer atoms from $|1, 1\rangle \rightarrow |1, -1\rangle$ before they are accelerated away from the trap center and reach position z_1 , where the undesired transition (dashed red line) would otherwise occur. The atoms continue moving away from the trap center due to inertia. Once the atoms cross z_1 , RF2 signal (dashed green line) is applied to transfer the atoms back to the $|1, 1\rangle$ state. Thus, the unwanted transition (dashed red line) can be avoided by implementing two RF signals.

There are several restrictions for selecting $\omega_{\text{RF}1}$ and $\omega_{\text{RF}2}$ when the MW signals (solid red line) couple the transition at position z_0 . Firstly, the frequency $\omega_{\text{RF}1}$ should be high enough to couple to the resonance frequency of $|1, 1\rangle \rightarrow |1, -1\rangle$ transition beyond position z_0 . This

requires $\omega_{\text{RF1}} > \omega_0$, where ω_0 is the resonance frequency coupling neighboring hyperfine state at position z_0 . Secondly, the transition driven by ω_{RF1} should occur before the undesired repumping transition (dashed red line) happens. This means that $z_{\text{RF1}} < z_1$, which implies $\omega_{\text{RF1}} < \frac{3}{2}\omega_0$. Similarly, ω_{RF2} should drive the transition after the position, where undesired repumping transition occurs, which requires $\omega_{\text{RF2}} > \frac{3}{2}\omega_0$. Also, the distance $z_{\text{RF1}} - z_0$ should be larger than $z_{\text{RF2}} - z_{\text{RF1}}$ to ensure that the atoms have been accelerated enough to reach z_{RF2} before being transferred back to $|1, 1\rangle$ state. This imposes an additional frequency constraint: $2\omega_{\text{RF1}} > \omega_0 + \omega_{\text{RF2}}$. Additionally, when considering the loading of ^6Li atoms at a later stage, the ω_{RF1} should guarantee that the truncation energy for ^6Li atoms is higher than that for ^{87}Rb . This requires $\omega_{\text{RF1}} > \frac{4}{3}\omega_0$. In conclusion, the ω_{RF1} and ω_{RF2} must satisfy the following conditions

$$\frac{4}{3}\omega_0 < \omega_{\text{RF1}} < \frac{3}{2}\omega_0 , \quad (3.7)$$

$$\frac{3}{2}\omega_0 < \omega_{\text{RF2}} , \quad (3.8)$$

$$2\omega_{\text{RF1}} > \omega_0 + \omega_{\text{RF2}} . \quad (3.9)$$

This method has been tested experimentally, unfortunately, the atoms could not be cooled down to achieve BEC, even with the two RF signals. One possible issue could be the undesired interference encountered during the construction of the lattice. If the incident angle of the plug beam is close to normal with respect to the glass cell and chamber windows, interference could occur, weakening the central barrier created by the plug beam. This effect is illustrated in Fig. 3.21. The reflection rate from the chamber is assumed to be 10%. The incident angle of the plug beam is set to 1° . Compared to the potential without the interference depicted in Fig. 2.1, the atoms can tunnel to the center of the trap. In this situation, the plug beam fails to prevent Majorana losses at the central region.

3.5.4. OPT with Li and K

In future experiments, ^6Li and ^{40}K atoms will be loaded into the OPT for sympathetic cooling with ^{87}Rb . The main focus is to achieve spatial (density) overlap of the three species, as the quality of this overlap affects the cooling efficiency. Fig. 3.22 (a) and (b) present the OPT potential curves for three species. The potentials for ^6Li atoms are elevated due to the higher

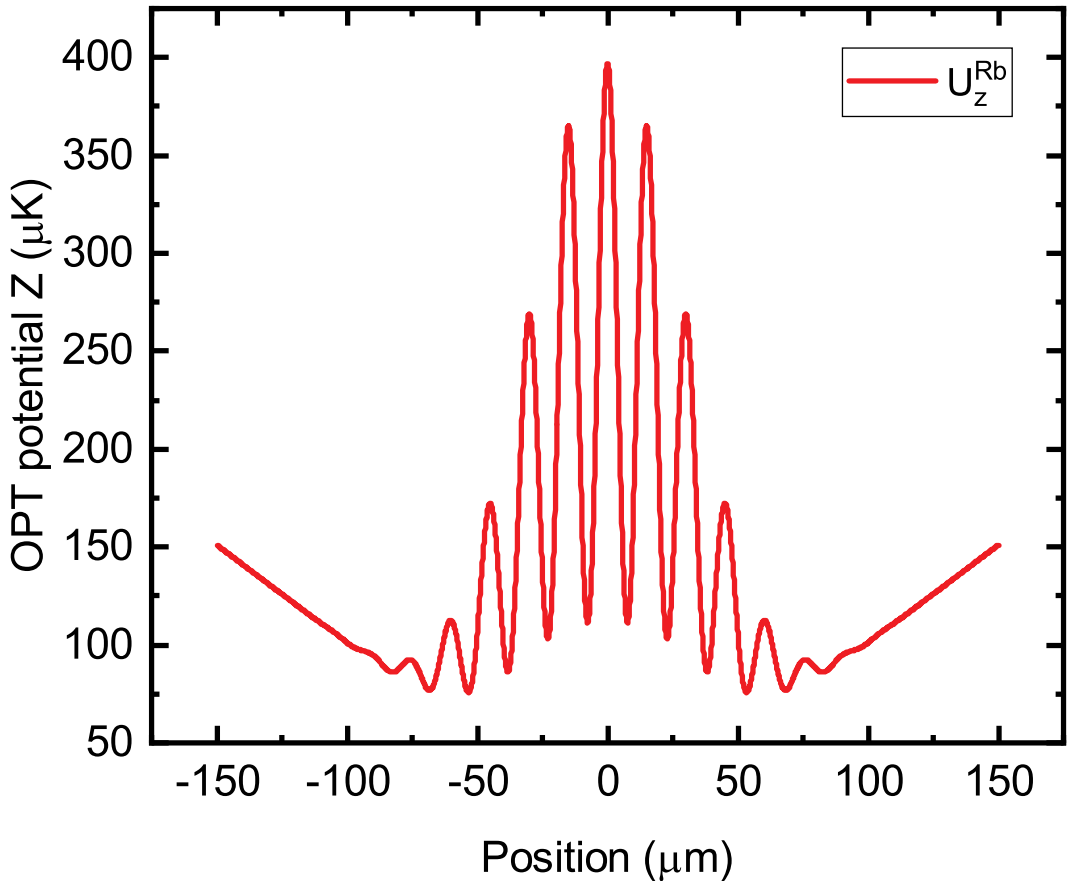


Figure 3.21.: OPT with undesired interference. The potential curve represent the optical along z-direction with undesired interference. The reflection rate from the chamber is assumed to be 10%. The incident angle of the plug beam is set to 1°

transition frequency of the D line. Additionally, the potential minima for three species are slightly offset. For ^{87}Rb , the minimum is located at $72.3\ \mu\text{m}$ away from the center along z axis, while for ^6Li and ^{40}K , the minima are at $73.0\ \mu\text{m}$ and $72.4\ \mu\text{m}$, respectively. The displacement between ^{87}Rb and ^6Li is only $0.7\ \mu\text{m}$. When considering a magnetic gradient with $300\ \text{G/cm}$ the $B_{\min,\text{Rb}} \approx B_{\min,\text{Li}}$ can be verified. The small offset is due to the plug beam wavelength being close to a "magic wavelength". As shown in Fig. 3.22 (c) and (d), when the plug beam wavelength is at $518\ \text{nm}$, the potential minima for three species are nearly coincide along the z-direction. The wavelength of our plug beam is $532\ \text{nm}$, which is quiet close to this "magic" wavelength. Along the y axis, the displacement between ^{87}Rb and ^6Li is primarily due to gravity and is approximately $2.3\ \mu\text{m}$ at a wavelength of $532\ \text{nm}$. This displacement remains consistent as the wavelength varies. The total offset between ^{87}Rb and ^6Li is $2.32\ \mu\text{m}$ (the minimum positions along x axis are always at 0). This level of overlap is relatively acceptable compared to the radial size of the atomic cloud, which is around $10\ \mu\text{m}$ at a temperature

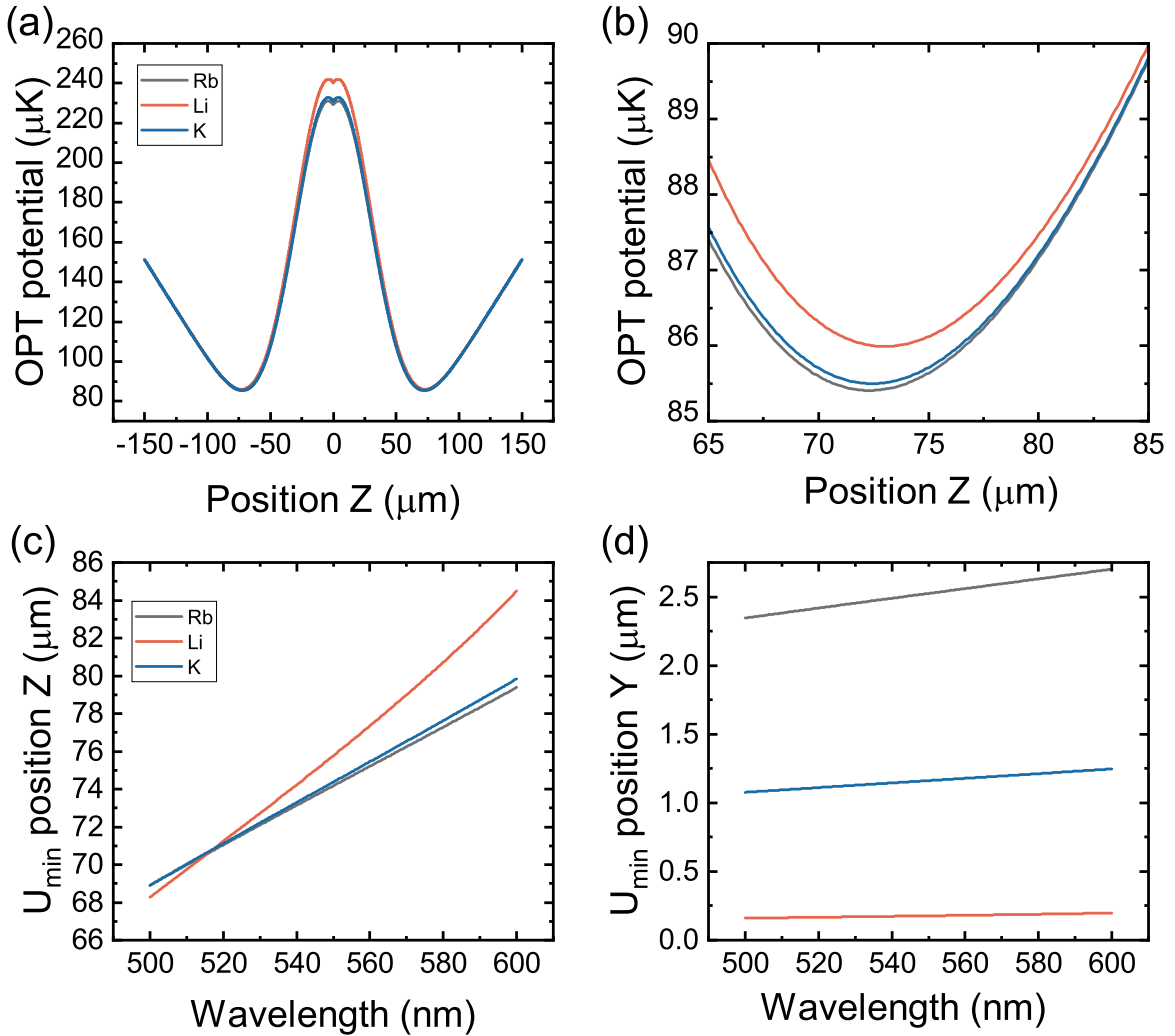


Figure 3.22.: (a) The OPT potential along z axis for ^{87}Rb , ^6Li , and ^{40}K . **(b)** A zoomed in view of the potential minimum positions, highlighting the slight differences in minima for the three species. **(c)** The potential minimum position along z axis as a function of the plug beam wavelength for the three species. There is a crossover point around 518 nm, where the potential minima for all three species coincide at z-direction. **(d)** The potential minimum positions along y axis, indicating that the relative distances between the three species remain nearly constant as the wavelength varies.

of 500 nm ([Taglieber, 2008](#)). The current selection of the plug beam wavelength is already sufficient to achieve the necessary density overlap for sympathetic cooling, allowing all three species to be effectively cooled in the OPT.

4. Creation of Ground State Molecules

This chapter discusses the creation of ${}^6\text{Li}{}^{40}\text{K}$ ground state molecules with high efficiency. Single-photon spectroscopy and dark resonance spectroscopy are employed to determine and calculate the transition frequencies and strengths, which are shown in Section 4.1. Then, a pulsed Raman scheme is applied to suppress scattering losses from the excited state, with the results introduced in Section 4.2. The main results of creation of ground state molecules via STIRAP are presented in Section 4.3. Finally, a detailed analysis of achieving high transfer efficiency is provided in Section 4.4.

Part of the content of this chapter is published in: "Efficient Creation of Ultracold Ground State ${}^6\text{Li}{}^{40}\text{K}$ Polar Molecules.", He, C., Nie, X., Avalos, V., Botsi, S., Kumar, S., Yang, A., Dieckmann, K. *Physical Review Letters*, **132**(24), 243401(2024).

Further details on improving STIRAP efficiency will be published in: "Improving STIRAP Efficiency for Ultracold Ground State ${}^6\text{Li}{}^{40}\text{K}$ Molecules.", Yang, A., He, C., Nie, X., Avalos, V., Botsi, S., Kumar, S., Dieckmann, K. *preprint* (2025)

4.1. Ground State Spectroscopy

The implementation of the singlet pathway for the ground state transfer (Section 2.1.3) requires the identification and location of both intermediate and rovibrational ground states (Yang et al., 2020). Building on our previous measurement results Sofia (2022); Yang (2021b), this section presents the relevant spectroscopic investigations for the singlet pathway. Firstly, the precision spectroscopy for the $\text{A}^1\Sigma^+ |v' = 23, J' = 1\rangle$ intermediate state is shown with single-photon spectroscopy. Subsequently, dark resonance spectroscopy for the $\text{X}^1\Sigma^+ |v'' = 0, J'' = 0\rangle$ is performed to locate the rovibrational ground state and calibrate the coupling strengths between the intermediate and the rovibrational ground state. Moreover, the ac Stark shift induced by Stokes laser is discussed.

4.1.1. Single-Photon Spectroscopy

To locate the required Pump laser frequency for the ground state transfer, a fine spectroscopy for $A^1\Sigma^+ |v' = 23, J' = 1\rangle$ intermediate state is scanned and depicted in Fig. 4.1. Starting with 10^4 Feshbach molecules, the Pump laser power and pulse duration are adjusted to deplete all the molecules when the laser is on resonance. The σ^- polarized Pump light is scanned over a 160 MHz board spectroscopy range first to exclude any contributions from hyperfine components of the $b^3\Pi$ bound state. The results are shown in Fig. 4.1(a). And the resonance frequency is measured to be 267842.704(2) GHz with Pump power set to 0.86 mW, pulse duration set to $12\ \mu s$, and beam waist measured as $46\ \mu m$. The low energy pulse can avoid power broadening of the transition and results are presented in Fig. 4.1(b). Then in Fig. 4.1(c), the Pump laser frequency is fixed at resonance. By varying the pulse duration t_{irr} , the number of molecules shows an exponential decay , which can be fitted using the formula (Debatin et al., 2011)

$$N_{\text{mol}} = N_{\text{off}} + N_0 \exp\left(-t_{\text{irr}} \Omega_P^2 \frac{\Gamma}{\Gamma^2 + 4\delta_P^2}\right) \quad , \quad (4.1)$$

where N_{off} is the offset of the molecular number counting, N_0 is the initial number of Feshbach molecules, Ω_P is the Pump Rabi frequency, Γ is the excited state linewidth, and Δ_P is the Pump laser detuning. Within Fig. 4.1(c) case, the $\delta_P = 0$. From fit the Pump Rabi frequency $\Omega_P = 2\pi \times 373(25)$ kHz is extracted together with the excited state linewidth $\Gamma = 2\pi \times 6.6(1.3)$ MHz.

The single-photon process can be used to calibrate the frequency of the comb laser. As mentioned in Section 3.2.5, the beat value between the measured laser and the frequency comb may drift by several MHz. The fixed molecular transition serves as a stable reference to correct this drift.

4.1.2. Dark Resonance Spectroscopy

The existence of a dark state and thus the efficiency of STIRAP transfer depends strongly on the two-photon resonance ($\delta = 0$), the linewidth of which is often found to be on the order of 100 kHz (Ni et al., 2008; Park et al., 2015a; Takekoshi et al., 2012; Voges et al., 2020b). In our previous work (Yang et al., 2020), the Pump and Stokes transition frequencies were both determined with MHz precision. To coherently transfer the population from Feshbach

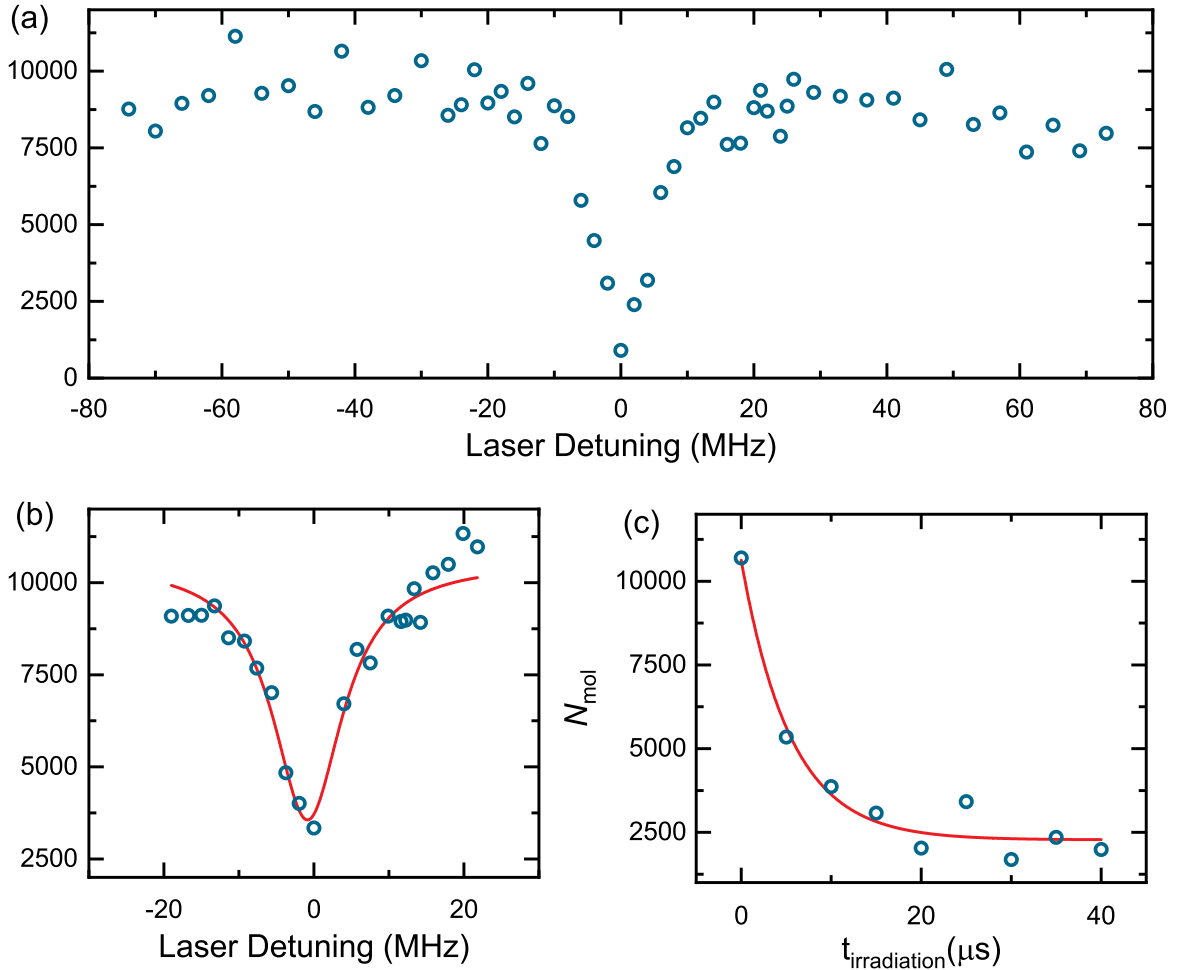


Figure 4.1.: Precision spectroscopy of $A^1\Sigma^+ |v' = 23, J' = 1\rangle$. (a) Loss spectrum with a ± 80 MHz board range scan. (b) Fine scan around the resonance point. The power is reduced compared with (a) to avoid power boarding. (c) Molecular decay data for resonant irradiation. The figure is taken from Yang (2021b).

molecule state to the target singlet rovibrational ground state, the two-photon resonance must be located with high precision. Here, we perform dark resonance spectroscopy with the narrow-linewidth Raman lasers to determine the two-photon resonance with improved precision of approximately 200 kHz.

The level scheme and laser pulse sequences for the dark resonance spectroscopy are shown in Fig. 4.2. Here, $|F.B.\rangle$ represents the initial Feshbach state, $|e\rangle$ represents the intermediate state $A^1\Sigma^+ |v' = 23, J' = 1\rangle$, and $|G.S.\rangle$ represents the target ground state $X^1\Sigma^+ |v'' = 0, J'' = 0\rangle$. In this spectroscopy, the single-photon detuning is set to zero. And the dark resonance process is controlled with two squared pulses from Pump and Stokes lasers. The pulse amplitude and duration are implemented by modulating the power of RF signals (FlexDDS, Wieserlabs), which are used to drive AOMs as shown in Fig. 3.2 and Fig. 3.3. It is important to note that

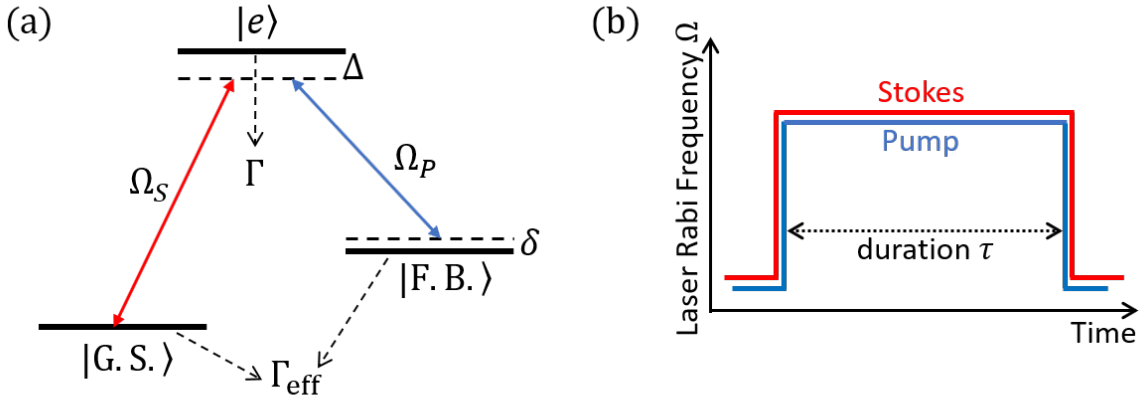


Figure 4.2.: Dark resonance process with single-photon detuning of $\Delta = 0$ MHz. (a) Level scheme for performing dark resonance spectroscopy. (b) Pulses sequence for the dark resonance process. Stokes light is switched on earlier than Pump and switched off later than Pump. The value of Rabi frequency doesn't indicate the actual value used in experiments

the Stokes light is switched on slightly earlier and switched off slightly later than the Pump light to prevent decoherence caused by residual Pump light leakage.

The results of the dark resonance spectroscopy are shown in Fig. 4.3. The power of Pump laser is set to 0.03 mW and beam waist measured as $44.7 \mu\text{m}$, while the Stokes laser is set to 2.6 mW and beam waist measured as $37.3 \mu\text{m}$. With a fixed Stokes laser frequency at resonance (450840.970(2) GHz), the Pump laser frequency is scanned in 500 kHz steps over a 20 MHz range. Both lasers use square pulse profiles, with the Stokes laser switched on $2 \mu\text{s}$ earlier off $2 \mu\text{s}$ later than Pump laser. And the pulse duration is set to $t_{\text{irr}} = 100 \mu\text{s}$ for Pump laser. The data is fitted using the analytic solution for the lambda-type three-level system with formula (Debatin et al., 2011; Fleischhauer et al., 2005)

$$N_{\text{mol}} = N_{\text{off}} + N_0 \exp\left(-t_{\text{irr}} \Omega_P^2 \frac{4\Gamma\delta^2 + \Gamma_{\text{eff}}(\Gamma_{\text{eff}}\Gamma + \Omega_S^2)}{|\Omega_S^2 + (\Gamma + 2i\delta)(\Gamma_{\text{eff}} + 2i\delta)|}\right) , \quad (4.2)$$

in the region of $\Omega_P \ll \Omega_S$. Here, Γ_{eff} is the effective decay rate that characterizes the decoherence process of the dark state, which can for example be caused by laser phase fluctuations or magnetic field noise as shown in Fig. 4.2(a). In this fitting, Γ_{eff} is neglected due to the pulse duration $t_{\text{irr}} = 100 \mu\text{s}$ is much shorter than the lifetime of both Feshbach and ground states. The two-photon resonance detuning δ coincides with Pump laser detuning $\delta = \delta_P$

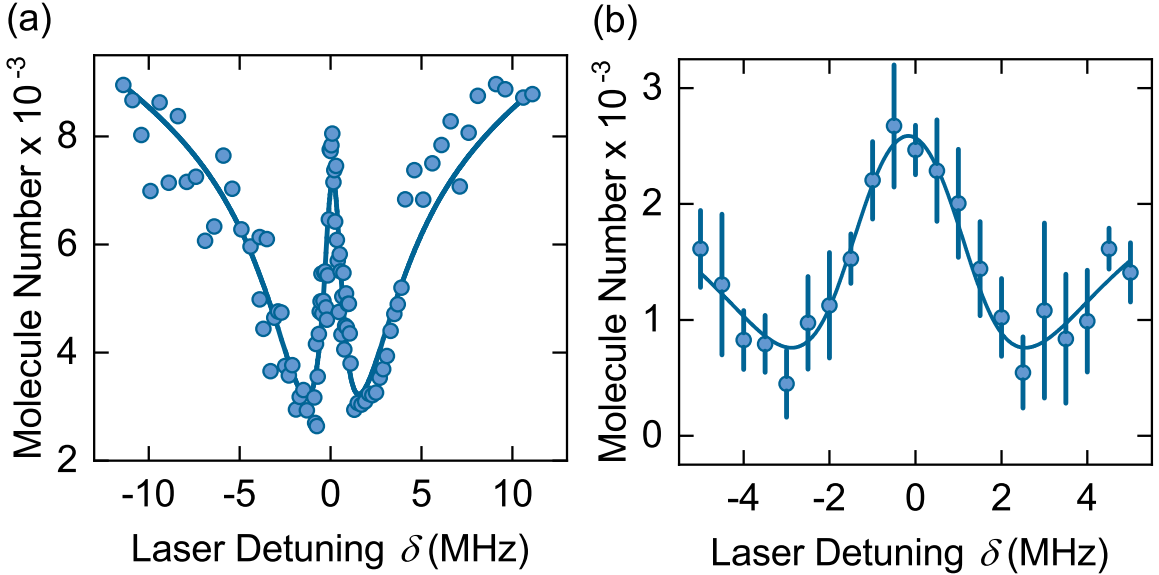


Figure 4.3.: Observation of dark resonance in ${}^6\text{Li}{}^{40}\text{K}$ molecules and fit to an analytical model. (a) Dark resonance spectroscopy at 30 MHz range. Driving the Pump transition with a $100\ \mu\text{s}$ pulse leads to a broad loss signal in the number of Feshbach molecules. The signal is recovered in the center, where the narrow dark resonance occurs. (b) Spectroscopy with focus on the central peak. Error bars are the standard deviation coming from four different experimental runs. Figures are taken from [He et al. \(2024\)](#).

in this measurement. The excited state linewidth Γ obtained from the single-photon spectroscopy is fixed at $2\pi \times 6.6$ MHz for this fit. From the fit, the Rabi frequencies are extracted as $\Omega_P = 2\pi \times 0.113(4)$ MHz and $\Omega_S = 2\pi \times 5.43(20)$ MHz. A significant feature of the spectroscopy is that frequency splitting between the two minima corresponds to the Stokes Rabi frequency Ω_S . Then the normalized Rabi frequencies are calculated using the formula $\tilde{\Omega} = \Omega / \sqrt{\frac{2P}{\pi w^2}}$, giving $\tilde{\Omega}_P = 2\pi \times 3.68(15)$ kHz/ $\sqrt{\text{mW/cm}^2}$ and $\tilde{\Omega}_S = 2\pi \times 15.8(6)$ kHz/ $\sqrt{\text{mW/cm}^2}$.

4.1.3. AC Stark Shift from Stokes Light

The 665 nm wavelength of the Stokes laser is close to the atomic D-line transition of ${}^6\text{Li}$. As a result, an ac Stark shift of the Pump transition induced by the Stokes light might occur, which can diminish the efficiency of STIRAP ([Vitanov et al., 2017](#)). To investigate this effect, we perform the dark state spectroscopy at different intensities of the Stokes laser. The spectroscopy is taken at different Stokes Rabi frequencies: $\Omega_{S1} = 2\pi \times 3.26(15)$ MHz and $\Omega_{S2} = 2\pi \times 5.43(20)$ MHz. The results are shown in Fig. 4.4.

Assume a coefficient α that represents the effect of polarizability, α quantifies the frequency shift per square of Rabi frequency (considering the Ω is proportional to \sqrt{I} , where I is the

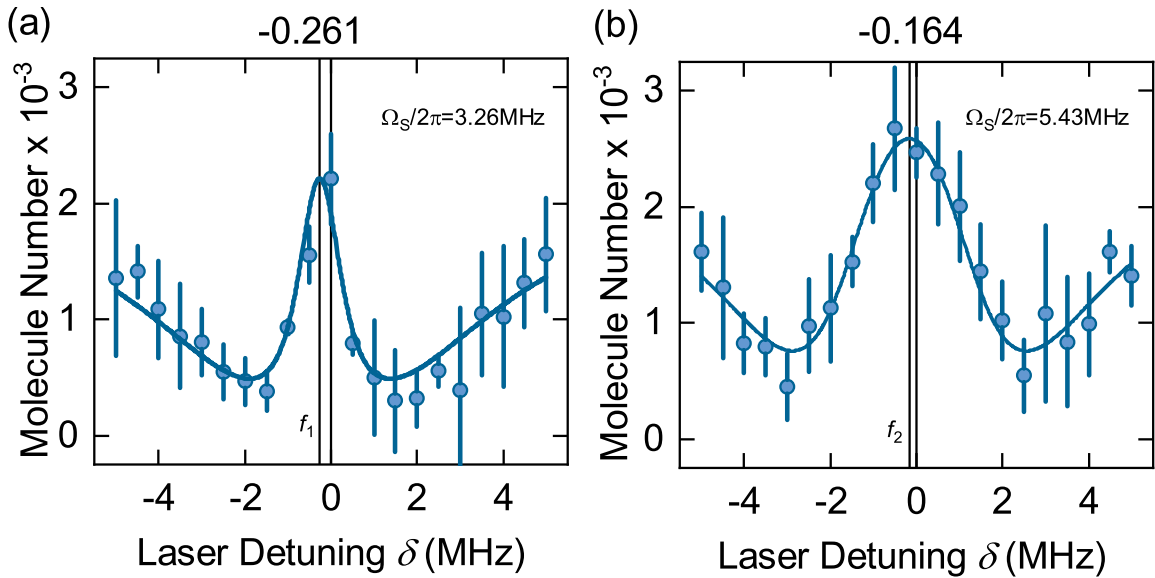


Figure 4.4.: The ac Stark shift of Pump transition from Stokes light. (a) Dark resonance spectroscopy with $\Omega_{S1} = 2\pi \times 3.25$ MHz. (b) Dark resonance spectroscopy with $\Omega_{S2} = 2\pi \times 5.43$ MHz. The two solid black lines in each plot represent the shift frequency f_1 and f_2 compared with 0 MHz detuning of Pump frequency. Error bars are the standard deviation coming from four different experimental runs.

light intensity). Then the coefficient is given by

$$\alpha = \frac{\Delta f}{\Omega_{S1}^2 - \Omega_{S2}^2} , \quad (4.3)$$

where $\Delta f = f_1 - f_2$ is the frequency shift due to different value of Ω_S . The frequency shift $\Delta f = 0.097$ MHz is extracted from the fit and the coefficient is calculated as $\alpha = 5.14$ kHz/MHz². From this we infer that an ac Stark shift of $\delta f > 90$ kHz can be excluded for the $\Omega_S < 2\pi \times 4$ MHz applied in the STIRAP measurements.

To summarize, the single-photon spectroscopy and dark resonance spectroscopy measurements have confirmed the transition frequencies and strengths. The next step involves transferring molecules to the ground state using STIRAP pulses. However, during these experiments, the program controlling the STIRAP pulse envelope encountered persistent bugs that could not be easily resolved. As a workaround, a pulsed Raman scheme was tested first, as it simplifies the generation of the pulse envelope by using square pulses.

4.2. Off-Resonance Raman Process

In this section, a pulsed Raman scheme is applied first and discussed. The two-photon resonance is resolved with higher precision of 50 kHz under the Raman scheme. And the off-resonance Raman transfer is performed with a single-photon detuning of $\Delta = 2\pi \times 580$ MHz, achieving a relevant high one-way efficiency up to 92%. Additionally, the Rabi frequencies of the Pump and Stokes lasers are calibrated, which are consistent with the values obtained from dark resonance spectroscopy.

4.2.1. Two-Photon Detuning and Raman Oscillation

The level scheme and pulse sequence of the off-resonance Raman process are similar to those used in the dark resonance spectroscopy as shown in Fig. 4.2. A single-photon detuning of $\Delta = 2\pi \times 580$ MHz is selected to suppress scattering losses from the excited state. Furthermore, the pulse sequence shows same behavior, with the Stokes pulse being activated and deactivated slightly earlier and later than the Pump pulse, respectively. The identification of the laser frequency used in Raman process can refer to Section 3.2.5.

The Raman resonance is shown in Fig. 4.5 (a). Using 43.7 mW Pump power and 11.6 mW Stokes power, an 8 μ s square pulse of Raman beam is applied to measured the resonance. The two-photon detuning of the Pump laser is scanned in 30 kHz steps. The results are fitted with the following formula ([Cairncross et al., 2021](#))

$$N_{\text{mol}} = N_{\text{off}} + N_0 e^{-R_{\text{sc}}\tau} \left[1 - \frac{\Omega_{\text{R}}^2}{2\Omega_{\text{eff}}^2} (1 - e^{\gamma\tau} \cos(\Omega_{\text{eff}}\tau)) \right] , \quad (4.4)$$

where R_{sc} is the scattering rate, Ω_{R} is the Raman Rabi frequency, $\Omega_{\text{eff}} = \sqrt{\Omega_{\text{R}}^2 + \delta^2}$ is the effective Rabi frequency, γ^{-1} is the dephasing time, and τ is the pulse duration. With 8 μ s pulse duration, the formula is simplified to

$$N_{\text{mol}} = N_{\text{off}} + N'_0 \left[1 - \frac{\Omega_{\text{R}}^2}{\Omega_{\text{eff}}^2} \sin^2(\Omega_{\text{eff}}\tau/2) \right] , \quad (4.5)$$

where the scattering and dephasing terms are absorbed into the initial molecule number N'_0 . From the fit, a two-photon resonance with a precision of 50 kHz is determined.

By fixing the Pump and Stokes laser frequencies to $\delta = 0$ and varying the pulse duration, we observe a damped Rabi oscillation as shown in Fig. 4.5 (b). The fit is also based on

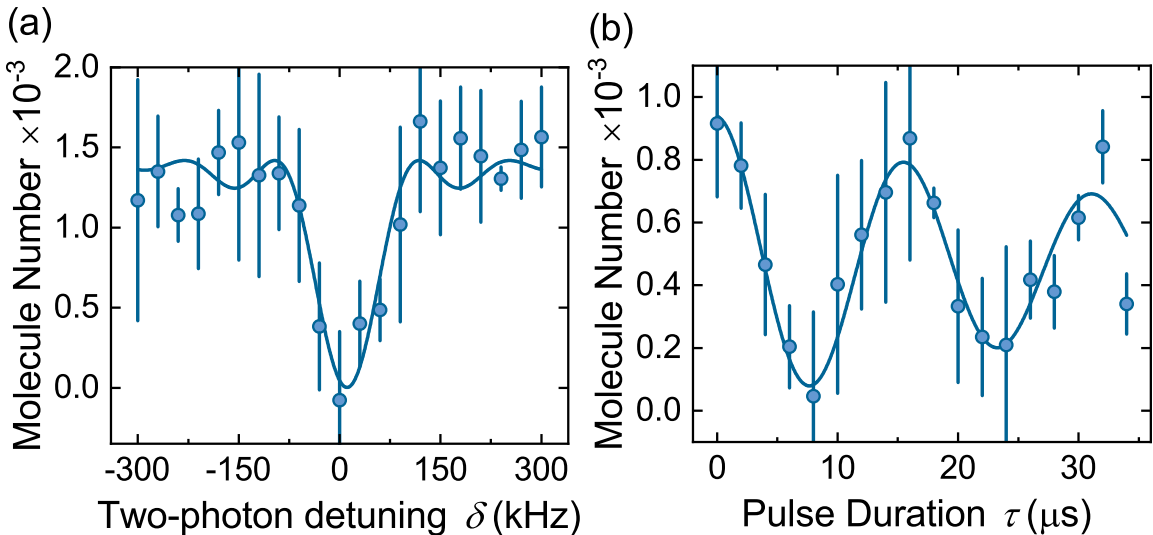


Figure 4.5.: (a) Raman resonance and (b) Raman Rabi oscillation between the Feshbach state and the ro-vibrational ground state of ${}^6\text{Li}{}^{40}\text{K}$. The blue curve represents a fit to a line shape model for square Raman pulses and dephasing. The counting background N_{off} has been subtracted from those plot. Error bars are the standard deviation coming from four repeated experimental runs. Figures are taken from He et al. (2024).

Equation 4.4. The scattering rate R_{sc} is set to 0, considering the milliseconds scale lifetime of the molecules, and $\Omega_{\text{eff}} = \Omega_{\text{R}}$ due to $\delta = 0$. Under these conditions, the fitting formula simplifies to

$$N_{\text{mol}} = N_{\text{off}} + N_0 \left[1 - \frac{1}{2} (1 - e^{\gamma\tau} \cos(\Omega_{\text{R}}\tau)) \right] . \quad (4.6)$$

The observed Raman Rabi frequency is $\Omega_{\text{R}} = 64.3(8)$ kHz and the dephasing time is extracted as $\gamma^{-1} = 42(1)$ μs . Then, a one-way Raman transfer efficiency of $\eta_{\text{R}} = \sqrt{N_{2\pi}/N_0} = 92(2)\%$ is inferred by comparing the initial molecule number (N_0) to the molecule number after one period ($N_{2\pi}$).

4.2.2. Rabi Frequency Calibration and Dephasing Analysis

The measured results of the Raman Rabi oscillation are used to verify the normalized Rabi frequencies extracted from dark resonance spectroscopy. The Rabi frequency for Pump and Stokes are $\Omega_{\text{P}} = 2\pi \times 6.35(25)$ MHz and $\Omega_{\text{S}} = 2\pi \times 11.47(42)$ MHz, calculated based on the Pump power of 43.7 mW, Stokes power of 11.6 mW, and the normalized Rabi frequencies $\tilde{\Omega}_{\text{P}} = 2\pi \times 3.68(15)$ kHz/ $\sqrt{\text{mW/cm}^2}$ and $\tilde{\Omega}_{\text{S}} = 2\pi \times 15.8(6)$ kHz/ $\sqrt{\text{mW/cm}^2}$. The Raman Rabi frequency is then calculated to be $\Omega_{\text{Rc}} = \frac{\Omega_{\text{P}}\Omega_{\text{S}}}{2\Delta} = 2\pi \times 63(3)$ kHz. This calculated value

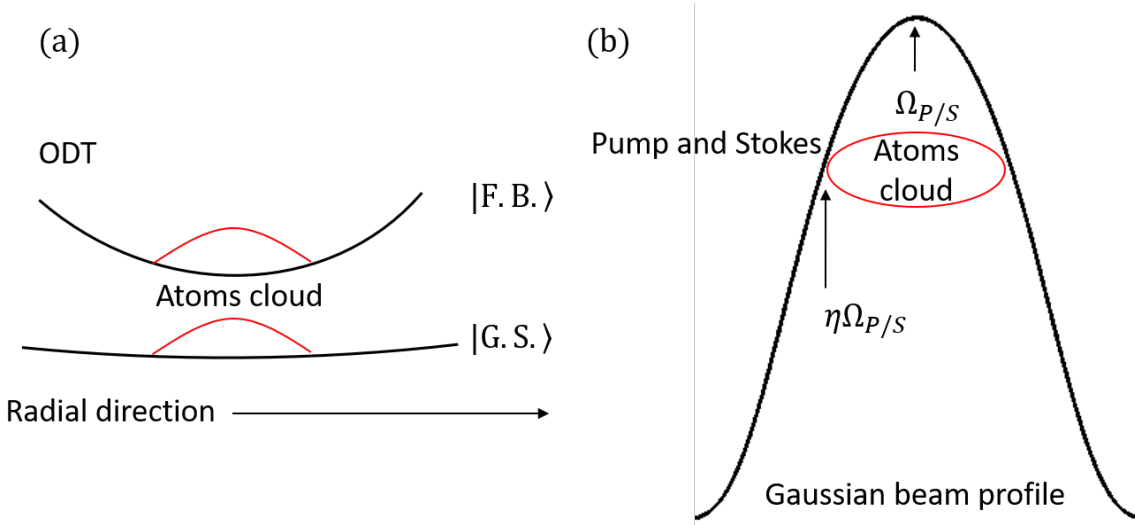


Figure 4.6.: (a) A sketch of the optical dipole potentials for the $|G.S.\rangle$ state and $|F.B.\rangle$. The black curve represents the ODT potential. The two states experience different optical trapping potential due to their differential polarizability. An arrow indicates the Radial direction. (b) Dephasing of Raman oscillation due to the Gaussian intensity distribution of Pump and Stokes laser. The red curve indicates the size and position of molecular cloud.

is in agreement with the observed Raman Rabi frequency from the fit, $\Omega_R = 2\pi \times 64.3(8)$ kHz, confirming the high precision of the normalized Rabi frequency determination.

The dephasing time of the Rabi oscillation is fitted to be $\gamma^{-1} = 42(1)$ μ s. Since the laser coherence time is expected to be much longer, the short dephasing time is attributed to two main factors, as shown in Fig. 4.6. The first factor is the difference in trapping potentials experienced by the Feshbach state $|F.B.\rangle$ and rovibrational ground state $|G.S.\rangle$. This arises from their differential polarizability, resulting in distinct trapping frequencies. Similar effects have been reported in [Bause et al. \(2020\)](#); [Cairncross et al. \(2021\)](#); [Leung et al. \(2021\)](#); [Vexiau et al. \(2017\)](#). Furthermore, the optical trapping potential varies spatially due to the inhomogeneous intensity distribution of the ODT light. The difference in trapping frequencies causes a wavefunction mismatch, which projects part of the population onto undesired excited states, leading to decoherence and the observed short dephasing time. A more detailed explanation of this effect is provided in rotational transition of Section 5.5.4

Another factor is the Gaussian intensity distribution of the spectroscopy laser beams across the molecular cloud, resulting in spatially varying Raman Rabi frequencies. As shown in Fig. 4.6 (b), molecules at the center of the cloud experience Rabi frequencies $\Omega_{P/S}$, while molecules located at the edge of the cloud experience the Rabi frequency of $\eta_{P/S}\Omega_{P/S}$, where $0 < \eta_{P/S} < 1$. This creates a factor of $\eta_{P/S}$ difference in Raman Rabi frequencies between

the center and edge of the cloud. Consequently, the Rabi oscillation period varies by a factor of $1/\eta_P\eta_S$ across the molecular cloud. Given that the cloud size is approximately $10\ \mu\text{m}$, comparable to the beam waists of the spectroscopy beams ($44.7\ \mu\text{m}$ for Pump and $37.3\ \mu\text{m}$ for Stokes), the $\eta_P\eta_S$ is approximately 0.88, which significantly contributes to the short dephasing time.

The short dephasing time is expected to be improved in the case of STIRAP, as detrimental effects due to the Gaussian profile of the spectroscopy beams are mitigated. The population transfer between $|\text{F.B.}\rangle$ and $|\text{G.S.}\rangle$ relies on the mixing angle θ ($\tan \theta(t) = \Omega_P(t)/\Omega_S(t)$, Section 2.1), which is governed by the ratio of Ω_P and Ω_S rather than their absolute amplitudes.

4.3. STIRAP

The successful implementation of the off-resonant Raman process has enabled us to produce ${}^6\text{Li}{}^{40}\text{K}$ in the rovibrational ground state. To further enhance the transfer efficiency, STIRAP is tested and implemented due to its fast speed and robustness against fluctuations in pulse energies (Vitanov et al., 2017). Initial attempts at STIRAP were unsuccessful, as the process either could not be distinguished from background detection fluctuations or exhibited lower efficiency compared to the off-resonance Raman process. To address these issues, several methods were employed to troubleshoot and improve the process, ultimately achieving high efficiency STIRAP. These improvements will be detailed in the analysis of STIRAP efficiency. Here, we provide a comprehensive discussion of the sequence used to achieve the STIRAP .

4.3.1. STIRAP Procedures

The Raman laser setups used for STIRAP are illustrated in Fig. 3.2 and Fig. 3.3. As described in Section 4.1.2, the pulse amplitude and duration are controlled by modulating the power of RF signals that drive the AOMs. Unlike the simple on-off switching of the RF source used to generate square pulses for spectroscopy measurements and the off-resonant Raman process, STIRAP requires carefully designed pulses shapes to satisfy the adiabatic condition (Section 2.1.2). Typically, these pulse shapes are Gaussian or Sine-like profile. To achieve the desired pulse shapes for the Pump and Stokes beams, two arbitrary waveform generators (AWG) (33220A, Agilent) are used. The waveforms sent to the AWGs are programmed in the time sequence by General-Purpose Interface Bus (GPIB) commands. In this case, pulse

switching can be achieved in two ways: either by sending a trigger to active the AWGs at specific times or by directly modifying the waveform sent to the AWGs. However, the timing precision of the trigger method is limited to approximately $1\ \mu\text{s}$. Therefore any modulation within $1\ \mu\text{s}$ timescale must be accomplished by pre-programming the waveform sent to the AWGs.

The alignment of Pump and Stokes beams is also critical, as it directly affects the actual Rabi frequency discussed in Section 4.4. The coarse alignment follows a method similar to Plug beam alignment discussed in Section 3.5.3. The position of the atomic cloud on the camera is used to roughly locate the beam positions. The Stokes beam is initially aligned to the cloud using a prism (see Fig. 3.4), while the Pump beam is aligned using a dichroic mirror. However, due to the chromatic aberration of the optics, the displacement between the spectroscopy beams and atomic cloud can reach tens of micrometers, which may cause the atomic cloud to move completely out of the beam waist region. To address this, fine alignment is performed by observing the ODT effect with the Pump beam and the Plug effect with the Stokes beam, as shown in Fig. 4.7. Considering the relatively low power of the Pump beam (60 mW) compared with the ODT beam used in the experiments (670 mW), a single Pump beam alone cannot create an ODT trap strong enough to hold the atoms. To assist in this alignment, the forward lattice beam along the x-direction (described in detail in Section 6.1) is switched on to create a bar-shaped atomic cloud. When the Pump beam is turned on, the atoms concentrate at the crossing point of the Pump beam and the lattice forward beam. The Pump beam is aligned by adjusting it until the crossing point overlaps with the original position of the atomic cloud. For the Stokes beam, the opposite behavior is observed due to its Plug effect, which repels the atomic cloud away from the crossing point of the two beams.

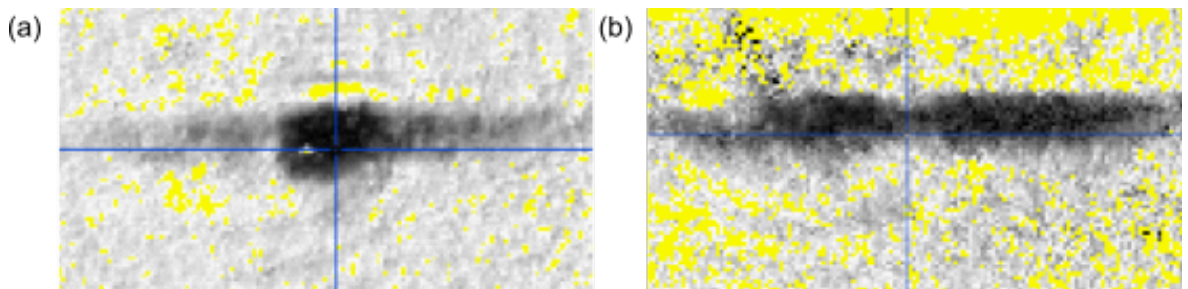


Figure 4.7.: (a) The ODT effect of Pump beam. The atoms are concentrated at the cross point of two beams. (b) The Plug effect of Stokes beam. The atoms are repelled from the cross point of two beams. The cross point of the blue cursors represents the original position of the atomic cloud.

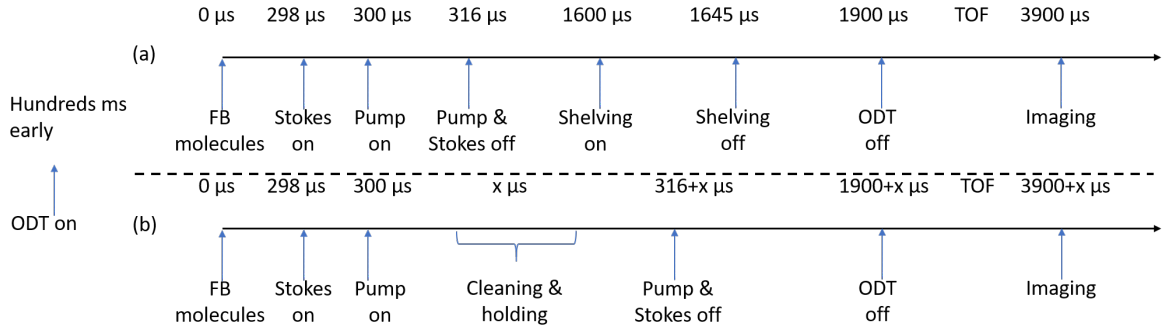


Figure 4.8.: The STIRAP procedure with (a) RF π pulse shelving and (b) ${}^6\text{Li}$ and ${}^{40}\text{K}$ cleaning or an extra holding time x (x depends on certain experimental purpose) for the ground state molecules.

The Stokes beam is also aligned in the same method to ensure that the crossing point of the Pump and Stokes beams overlaps with the atomic cloud.

After successfully manipulating the Pump and Stokes intensities and precisely aligning the beams on the atomic cloud, we start our experiments to perform the STIRAP transfer. The procedure leading up to the generation of ${}^6\text{Li}{}^{40}\text{K}$ Feshbach state has been briefly introduced in Section 3.1. The detailed STIRAP sequence is described below and also illustrated in Fig. 4.8. The sequence begins with the association of Feshbach molecules. The Stokes laser is switched on first, followed $2\ \mu\text{s}$ later by the Pump. The $2\ \mu\text{s}$ delay ensures that the state vector of dark state initially points to the Feshbach state (ensuring mixing angle $\theta = 0$). Depending on whether the molecules are held in their ground state, the STIRAP procedure follows slightly different paths, as shown in Fig. 4.8. In Fig. 4.8 (a), the molecules are immediately transferred back to the Feshbach state after reaching the ground state. An RF π pulse shelving is applied to hide the remaining ${}^6\text{Li}$ atoms. Then the ODT trap is switched off and after 2 ms time-of-flight (TOF) the molecular cloud is imaged to count the molecule number. In Fig. 4.8 (b), the molecules are held in the ground state for a certain period, and the cleaning light (discussed in Section 3.3) is applied to remove any residual atoms and Feshbach molecules. Afterward, the molecules are transferred back to the Feshbach state, following the same procedure as described above. For future experiments, a 3D optical lattice will replace the ODT trap, and a 0 ms TOF is expected to be used. All the other procedures should remain valid.

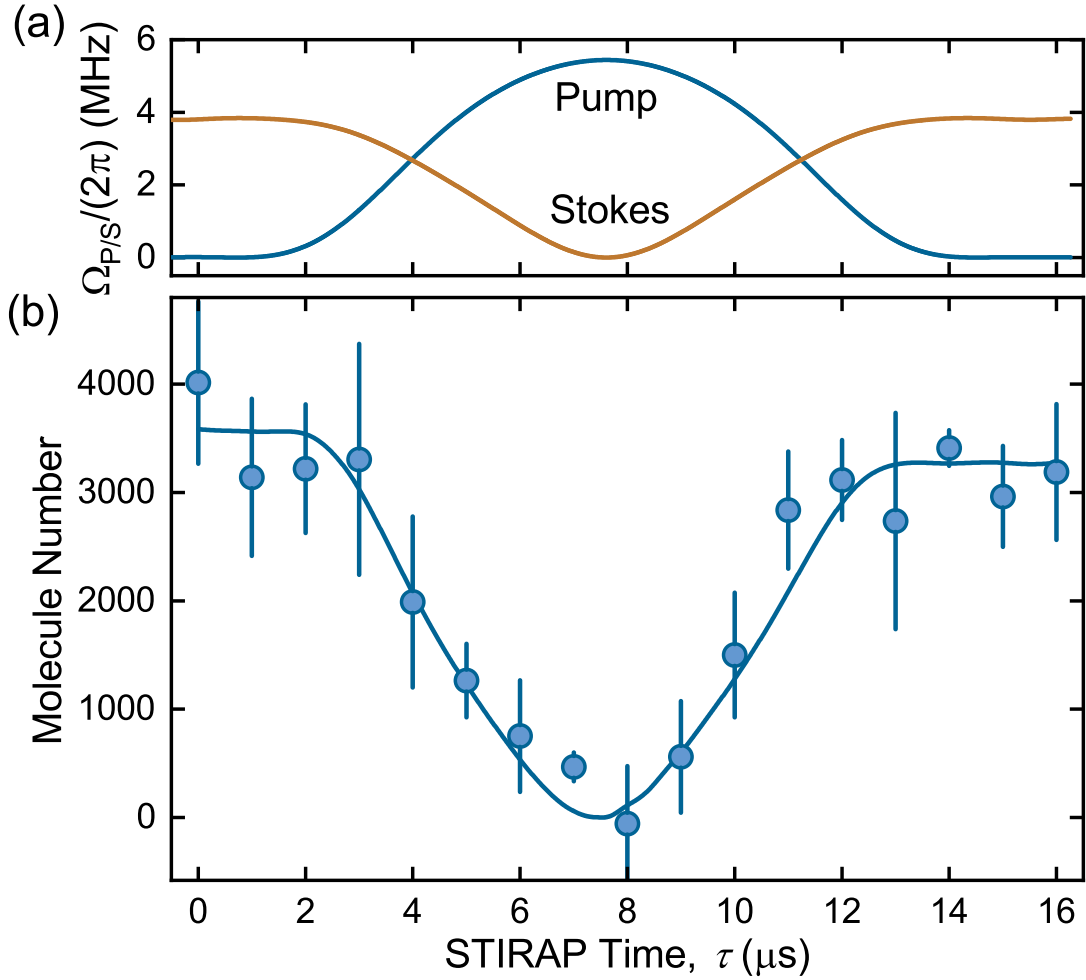


Figure 4.9.: STIRAP process for the ground state transfer of ${}^6\text{Li}{}^{40}\text{K}$ molecules. (a) Sweep of the Rabi frequencies of Pump and Stokes lasers for STIRAP transfer to the ground state and its reversal. (b) Evolution of molecular population in the $|\text{FB}\rangle$ state. The blue circles are data points for the measured Feshbach molecule numbers, accompanied with error bars representing the standard deviation of a 4-time average. The blue curve is a fit to the data by numerically solving the master equation for a four-level system. The number of atoms that remain in the trap due to incomplete Feshbach molecule association is measured independently and subtracted from the count to infer the molecule number. Figures are taken from [He et al. \(2024\)](#).

4.3.2. STIRAP Results

The STIRAP process achieved with high efficiency is shown in Fig. 4.9. Starting with maximum (minimum) Stokes (Pump) laser intensity, the counter-intuitive sweep of the intensities are implemented, as shown in Fig. 4.9 (a). At $\Delta = 2\pi \times 10$ MHz a sweep time of approximately $T = 7.5 \mu$ s is sufficiently long to adiabatically transfer the molecules to the ground state as the mixing angle θ approaches $\pi/2$. Subsequently, the sequence is reversed to transfer the molecules back to the Feshbach state. The number of Feshbach molecules after this sequence is then detected after 2 ms TOF. While the full sequence lasts 16μ s, Fig. 4.9 (b) shows the

number of detected Feshbach molecules, if the sequence is truncated at earlier times. This shows that a large fraction of the molecules is successfully transferred to the ground state and back. The one-way STRAP efficiency can be inferred from the ratio of final to initial molecules number as $\eta = \sqrt{N_f/N_i}$. From a fit to the data a efficiency up to $\eta = 96(4)\%$ is obtained.

One concern is the reliability of the high efficiency measurement, as it may be affected by the association of Feshbach molecules during the STIRAP process. Given the limitations in the stability of the current used to control the magnetic field (Pal, 2016), fluctuations in the magnetic field near the resonance point could lead to the association of Feshbach molecules. This issue is particularly relevant considering that ${}^6\text{Li}{}^{40}\text{K}$ has a narrow s-wave resonance at 215.6,G (Wille et al., 2008). However, this concern is mitigated by the way the experimental sequence is executed. In our experiment, truncating the STIRAP sequence does not actually shorten the overall duration of the sequence. As shown in Fig. 4.8, the STIRAP sequence in case (a) applies a truncation where Pump and Stokes lasers are switched off early, at $308\,\mu\text{s}$, for example. However, the active timing for switching on the RF π pulse shelving remains unchanged at $1600\,\mu\text{s}$. Thus, with the same total duration, the effect on the measurement process remains consistent. The number of Feshbach molecules associated after the STIRAP process would be counted equally as background, regardless of the truncation timing.

4.3.3. Background Detection

Despite the efficiency of the transfer process, the precise quantification of ground state molecules is crucial for revealing their properties. To accurately determine the number of ground state molecules, it is necessary to reverse the sequence and transfer the molecules back to the Feshbach state. Subsequently, the number of Feshbach molecules is detected using imaging light for ${}^6\text{Li}$ and ${}^{40}\text{K}$, which serves as a proxy for the quantity of ground state molecules. However, the counting obtained does not reflect the actual number of ground state molecules, as the detection background must be subtracted. This background primarily arises from two sources: residual atoms resulting from incomplete Feshbach molecule association and remaining Feshbach molecules. Two distinct methods are employed to subtract the detection background, utilizing different experimental sequences. In the sequence depicted in Fig. 4.8 (a), no holding time is introduced for the ground state molecules. The molecules

are directly transferred back to the Feshbach states. To mitigate the detection of residual atoms, atoms are transferred to undetectable $|1/2, 1/2\rangle$ state by an RF π pulse. This allows the ${}^6\text{Li}$ imaging light to be employed for detecting the number of ground state molecules. Nevertheless, the background from Feshbach molecules remains unmitigated. To avoid the over-counting of the ground state molecules, an independent measurement of the background is conducted. This involves applying only the pump laser using the same sequence as in the STIRAP process. In the absence of the coherent transfer, the Pump laser excites the Feshbach state to the excited state via single-photon process, with the remaining number representing the detection background. This method enables the subtraction of both residual atoms and Feshbach molecules that did not undergo the STIRAP process, indicating a background level in the thousands.

Another method is illustrated in Fig. 4.8 (b), which includes an intermediate holding time for the ground state molecules, allowing for the removal of residual atoms and molecules. The cleaning pulses described in Section 3.3, are applied during the holding period to expel all residual atoms or Feshbach molecules from the trap, leaving only the ground state molecules. Therefore, when the ground state molecules are transferred back to Feshbach molecules, both ${}^6\text{Li}$ and ${}^6\text{K}$ imaging light can be utilized to detect the number of Feshbach molecules, eliminating concerns regarding the overestimation of the number of ground states. The detection background is further verified using the same sequence (b) without activating the pump and Stokes lasers, resulting in a reduction of the detection background to the hundreds level.

In both experimental sequences, it is thus feasible to accurately count the number of ground state molecules, which is instrumental in enhancing our understanding of the properties of these ground states in later experiments.

4.3.4. Evolution Fitting

The STIRAP evolution can be simulated and fitted by numerically solving the master equation for a four-level system (Yang, 2021b), which includes two closely separated excited states ($|2\rangle$ and $|3\rangle$),

$$\dot{\rho} = -\frac{i}{\hbar}[H, \rho] + \Gamma(\rho) \quad .$$

As mentioned in Section 2.1, ρ is a four by four density matrix describing the population and

coherence of the system and $\Gamma(\rho)$ represents the decoherence due to spontaneous emission from the population in excited state. H is the interaction Hamiltonian

$$\mathbf{H}(t) = \frac{\hbar}{2} \begin{bmatrix} 2\delta & \Omega_p(t) & \Omega'_p(t) & 0 \\ \Omega_p(t) & 2\Delta & 0 & \Omega_s(t) \\ \Omega'_p(t) & 0 & 2\Delta_1 & \Omega'_s(t) \\ 0 & \Omega_s(t) & \Omega'_s(t) & 0 \end{bmatrix}.$$

The state vector for the four level system is $|\Psi(t)\rangle = [C_1(t); C_2(t); C_3(t); C_4(t)]$, where $C_i(t)$ is the probability amplitude for state $|i\rangle$. The $|2\rangle$ and $|3\rangle$ is only energetically separated by $\Delta - \Delta_1 = 2\pi \times 500$ kHz, where Δ_1 is the single-photon detuning when coupling to the second excited state. The envelopes of the $\Omega_p(t)$ and $\Omega_s(t)$ are extracted from the reading of two photodiodes. To achieve the fit results in Fig. 4.9, the $\delta = 0$, $\Delta = 2\pi \times 10$ MHz, and the undesired coupling strength of $\Omega'_{s/p}(t) \sim 0.1\Omega_{s/p}(t)$ are applied. A python package QuTIP ([Johansson et al., 2012, 2013](#)) is used to solve the master equation. The fit results agrees well with our measurements.

4.4. Efficiency Analysis

Starting from the association of weekly-bound Feshbach molecules, the ro-vibrational ground state ${}^6\text{Li}{}^{40}\text{K}$ molecules are produced via the STIRAP process. The efficiency of this pathway is, on the one hand, limited by the conversion efficiency into heteronuclear Feshbach molecules, which is typically below 50% ([Heo et al., 2012](#); [Köppinger et al., 2014](#); [Ospelkaus et al., 2006](#); [Takekoshi et al., 2014](#); [Wang et al., 2015](#); [Weber et al., 2008](#); [Wu et al., 2012](#)) in optical traps. The efficiency can be improved by increasing the density overlap of the atomic mixture in a bichromatic optical trap (80%) ([Duda et al., 2023](#)) or optical lattice ($\lesssim 100\%$) ([Covey et al., 2016](#)). On the other hand, the reported efficiencies for molecular STIRAP transfer vary between 50-93% ([Bause et al., 2021](#); [Guo et al., 2018a](#); [Li et al., 2023b](#)) and a summary table is shown in Table. B.1. In this section, we focus on the improvements of STIRAP efficiency and show the methods of how to achieve them.

4.4.1. Non-adiabatic Loss

In experiment, the adiabatic criteria given by Eq. 2.8 ([Kuklinski et al., 1989](#)) and Eq. 2.9 ([Vitanov et al., 2017](#)) need to be fulfilled during STIRAP transfer. In practice, $\Omega_{\text{peak}}T \geq 3\pi$ can guarantee a transfer efficiency $\geq 95\%$. The adiabatic criteria limit the selection of Rabi frequency and pulse duration. In our experiment, Rabi frequencies of several MHz and pulse duration of few microseconds consistently satisfy the criteria. However, even with the fulfilled criteria, non-adiabatic loss could still happen. The probability of non-adiabatic loss P_A , using a cosine-shaped waveform, is proposed by [Yatsenko et al. \(2002\)](#). The expression takes both the pulse duration τ and excited decay rate Γ into account

$$P_A(\Omega_0, \tau) = 1 - \exp\left(-\frac{\Gamma\pi^2}{\Omega_0^2\tau}\right) . \quad (4.7)$$

where Ω_0 is peak Rabi frequency of Pump and Stokes laser. This expression applies in situations where Ω_0 is comparable to the excited decay rate Γ . For our case $\Gamma = 2\pi \times 6.6 \text{ MHz}$, which requires a large Rabi frequency up to mega-Hertz level. So two TAs are implemented in the setups to amplifier the Pump and Stokes laser as shown in Fig. 3.2 and Fig. 3.3. The maximum power applied to the molecular cloud is now achieved as 50 mW for Pump laser and 12 mW for Stokes laser, corresponding to the Rabi frequency $\Omega_P = 2\pi \times 6.80 \text{ MHz}$ and $\Omega_S = 2\pi \times 11.67 \text{ MHz}$ can fulfill the requirement. However, even the P_A for STIRAP is suppressed by the increase of Rabi frequencies, the STIRAP process can be still of low efficiency. The detrimental effects for the STIRAP would be dominated due to the fast laser phase noise, which will be presented in next section.

4.4.2. Fast Laser Phase Noise Loss

Laser phase noise is typically quantified as the single-sideband (SSB) power spectral density relative to the carrier power $\mathcal{L}(f)$, expressed in dBc/Hz, at a specific frequency offset from the carrier. To estimate the detrimental effect of the phase noise, it is often useful to evaluate the root-mean-squared (RMS) integrated phase noise ϕ_{RMS} ([William, 2003](#))

$$\phi_{\text{RMS}} = \sqrt{2 \int_{-f_a}^{f_b} \mathcal{L}(f) df} , \quad (4.8)$$

where f_a, f_b is the frequency region of interest relative to the carrier frequency.

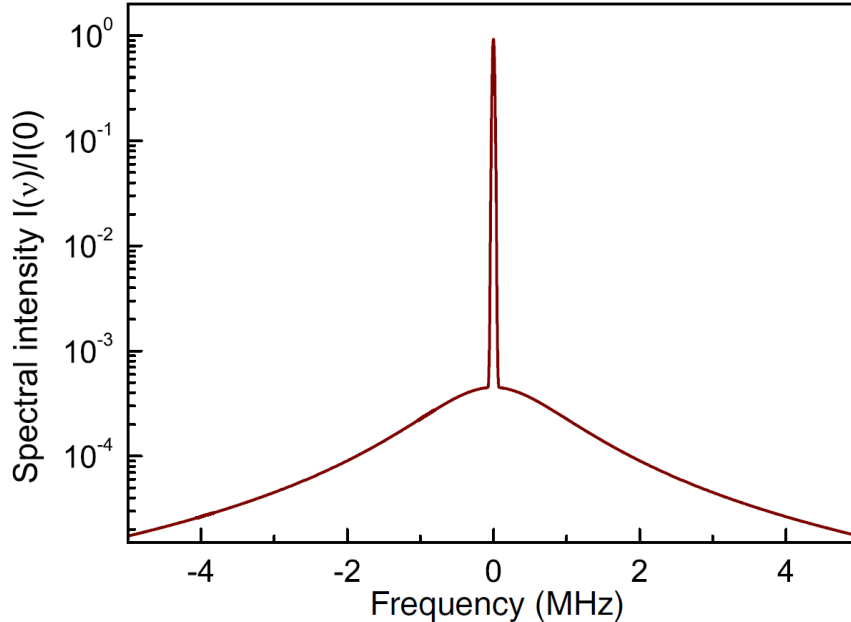


Figure 4.10.: The spectral density of a stabilized laser. The majority of the carrier power of laser is contained within the narrow peak, while the power in the noise pedestal is usually few percent of the total laser power. Figure is taken from [Yatsenko et al. \(2014\)](#).

Although STIRAP is less sensitive to laser amplitude noise, it is inherently vulnerable to fast laser phase noise because it depends on the adiabatic evolution of a dark state ([Vitanov et al., 2017](#)). A model proposed by [Yatsenko et al. \(2014\)](#) is adopted to evaluate the impact of fast laser phase noise on STIRAP. In their paper, the power spectral density $\mathcal{L}(f)$ of the measured laser is characterized as a δ -distribution superimposed on a broad and weak Lorentz distribution. As shown in Fig. 4.10, the majority of the carrier power of laser is contained within the narrow δ -distribution, while the partially suppressed noise is assumed to follow the Lorentz distribution with a bandwidth of G . Then the loss probability is expressed as

$$P_N(\Omega_0, \tau) = \frac{1}{4} \Omega_0^2 \left(\varepsilon_p^2 \frac{G_p \tau}{4 G_p^2 + 2 G_p \Gamma + \Omega_0^2} + \varepsilon_s^2 \frac{G_s \tau}{4 G_s^2 + 2 G_s \Gamma + \Omega_0^2} \right) , \quad (4.9)$$

where balanced peak Rabi frequency Ω_0 are assumed for Pump and Stokes, $G_{p/s}$ is the bandwidth of Pump and Stokes, and τ is the pulse duration. Here, $\varepsilon_{p/s}$ represents the power contained in the sidebands P_{SB} relative to the power contained in the carrier P_C , also related to the integrated phase noise ϕ_{RMS} ([Telle, 1996](#)):

$$\varepsilon_{p/s}^2 = \frac{P_{SB}}{P_{SB} + P_C} = 1 - e^{-\phi_{RMS}^2} . \quad (4.10)$$

The Eq. 4.9 is used when applying a cosine-shaped waveform, and the adiabatic criteria

$(\Omega_0 T \geq 3\pi)$ is fulfilled. The loss probability is proportional to the ratio of powers contained in the sidebands to the total laser power. As a result, increasing the peak Rabi frequency Ω_0 alone cannot completely eliminate the rapid fluctuations that contribute to phase noise.

For $\Omega_0 \rightarrow \infty$ condition, the P_N saturates to

$$P_N \rightarrow \frac{1}{4} (\varepsilon_p^2 G_p \tau + \varepsilon_s^2 G_s \tau) , \quad (4.11)$$

which depends on the noise properties of Raman laser and pulse duration. Therefore, with a high laser Rabi frequency, the non-adiabatic loss can be effectively suppressed, as described by Eq. 4.7. And P_N can be minimized by reducing the phase noise of laser.

4.4.3. Phase Noise Improvement

The phase noise of the spectroscopy lasers can be measured using two different methods inspired by Schmid et al. (2019). One method involves analyzing the in-loop error signal of the lock to access the noise performance of spectroscopy laser relative to a reference. This requires determining the slope of the PDH error signal to extract the laser frequency fluctuations from the voltage fluctuations of the error signal. Results obtained using the in-loop method are included in Fig. 4.11, with a detailed discussion provided in section 5.3.1 of a previous PhD thesis of our group (Yang, 2021b).

The second method involves measuring the beat signal between the direct output of the laser and the filtered light of the same laser transmitted through a high finesse cavity, which is also used for PDH stabilization of the laser. The setup is illustrated in Fig. 3.5. The cavity acts as a low-pass filter to ensure the low-noise of the transmitted light. And a frequency offset f_{off} is introduced to shift the transmitted light and generate the beat signal. To improve the SNR and suppress amplitude noise compared to a single photodetector, a balanced photodiode (PD) is used (Carleton and Maloney, 1968). The beat signal, which carries the phase noise of the spectroscopy beams, is then analyzed using a spectrum analyze (SA) in phase noise measurement mode. In this mode, the beat signal is automatically converted into a SSB power spectral density normalized to the carrier power $\mathcal{L}(f)$ at a 1 Hz resolution bandwidth. Based on the spectral density $\mathcal{L}(f)$, the integrated phase noise ϕ_{RMS} is also calculated.

The phase noise was initially measured using an older laser setup, resulting in transfer efficiencies that were too low to distinguish molecular state transfer from the background. The

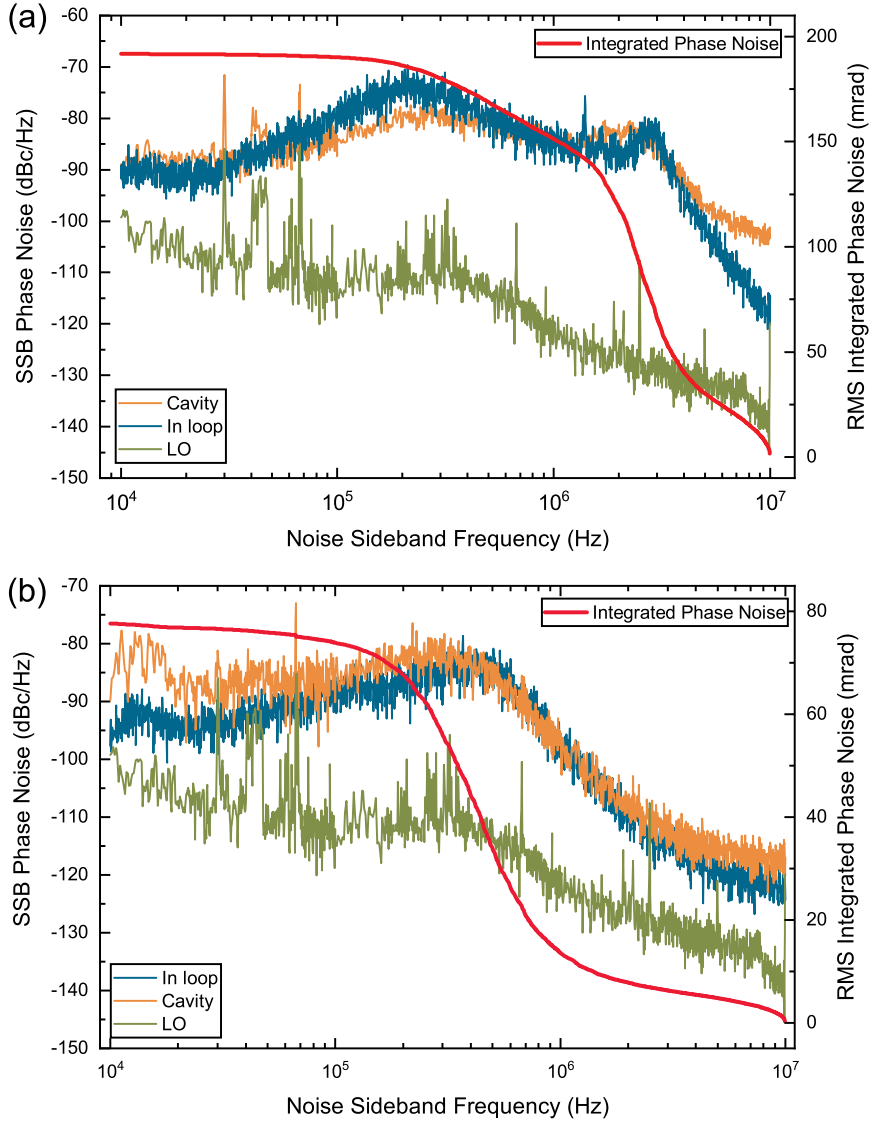


Figure 4.11.: Phase noise measurements for Stokes (a) and for Pump (b) are presented using optical beat measurement method (orange curve), in-loop error signal measurement method (blue curve), the phase noise of RF oscillator (green curve), and the integrated phase noise (red solid line). The measurements were done before the updates of the Raman laser setup.

phase noise measurements for the Pump and Stokes laser are depicted in Fig. 4.11. Fig. 4.11 (a) presents the spectral density $\mathcal{L}(f)$ and the integrated phase noise ϕ_{RMS} for Stokes laser. The blue curve represents the spectral density results obtained using the in-loop error signal measurement method, while the orange curve corresponds to results from the optical beat measurement method. Additionally, the green curve shows the measured phase noise of the RF local oscillator utilized for generating the offset frequency f_{off} . The red solid line indicates the integrated phase noise ϕ_{RMS} calculated from the optical beat measurement method. The corresponding phase noise measurements for the Pump laser are shown in Fig. 4.11 (b).

From the plots, we observe that the results of the in-loop measurement agree quite well with

those of the optical beat measurement for frequencies below 5 MHz. And at higher frequencies, the phase noise reaches the same level as the background noise of the SA. Consequently, there is no apparent difference between two methods, later measurements are conducted using the optical beat measurement method. Additionally, the green curves in the plots demonstrate that the RF local oscillator, as described in Section 3.2.3, exhibits a significantly lower phase noise level compared to both the Pump and Stokes lasers. Consequently, the contribution of the RF local oscillator to the measured laser phase noise can be considered negligible for later discussion. Additionally, spurious noise signals are detected in both the RF noise spectral density plot and the laser noise spectral density plot, which we attribute to the noise from the FlexDDS signal generator transferred through the feedback loop. The phase noise is integrated from 10 kHz to 10 MHz frequency range. The minimum frequency range is determined by the HWHM of the cavity resonance. For the Stokes laser, the $\phi_{\text{RMS}} = 192 \text{ mrad}$, while for the Pump laser it is 78 mrad. The bandwidth of frequency spectrum for Pump and Stokes ($G_{\text{p/s}}$) can be approximately by the lasers' servo bumps, $G_{\text{p}} \approx 2\pi \times 500 \text{ kHz}$ and $G_{\text{s}} \approx 2\pi \times 2.5 \text{ MHz}$. Despite the Pump laser exhibiting much lower phase noise than the Stokes laser, the phase noise for both lasers remains quite high, leading to detrimental effects on the loss probability as predicted by Eq. 4.9.

Improving the transfer efficiency involves reducing the phase noise of the Raman lasers while simultaneously maintaining high Rabi frequencies. Replacing an ECDL with a short external cavity with one that has a long external cavity can effectively narrow the linewidth and reduce phase noise (Riehle, 2003). The minimum linewidth Δv of an ECDL structure is given by

$$\Delta v = \Delta v_{\text{LD}} / (1 + l_{\text{d}} / (n L_{\text{LD}}))^2 \quad , \quad (4.12)$$

where Δv_{LD} , n , and L_{LD} are the spectral linewidth, refractive index, and length of the laser diode, respectively. While l_{d} denotes the external cavity length. Inspired by the work of Kolachevsky et al. (2011), who developed an ECDL in a Littrow configuration with $l_{\text{d}} = 20 \text{ cm}$ and demonstrated a noise power spectral density suppression of more than 10 dB compared to a short external cavity ECDL, we extended the external cavity length in our ECDL structure. The view of the long external cavity ECDL is shown in Fig. 4.12.

In the new ECDL setup, the distance from the front surface of the diode to the grating has

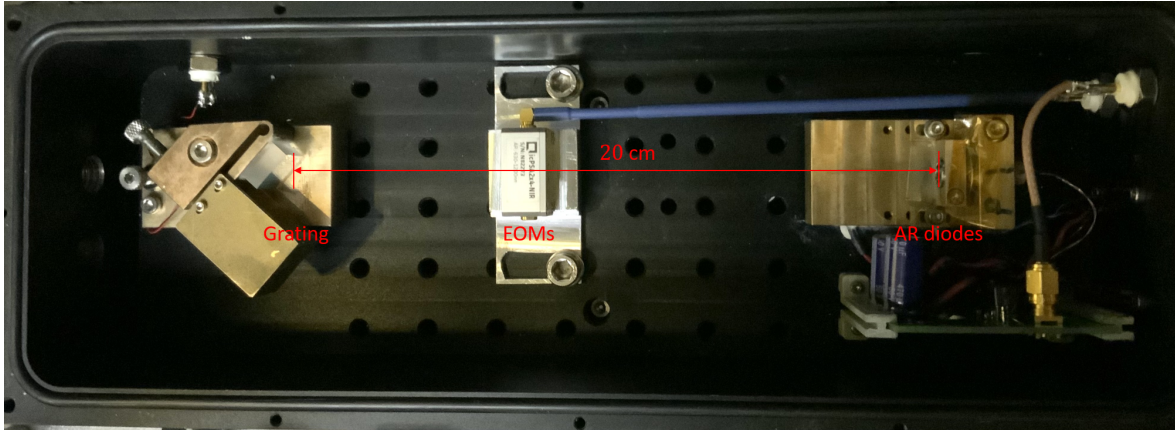


Figure 4.12.: The top view of the ECDL setup with long external cavity. The distance between the front surface of the laser diode and the optical grating is extended from 3 cm to 20 cm. AN EOM is implemented in the cavity path for the laser modulation.

been extended from 3 cm to 20 cm. The phase noise of the new setup was then measured using the optical beat measurement method, and the results are presented in Fig. 4.13 (a) and (b). From the figure, a significant reduction in phase noise can be observed. For the Stokes laser, the RMS integrated phase noise is calculated to be 48 mrad, which is 144 mrad lower than that measured with the shorter external cavity. Similarly, for the Pump laser, the RMS integrated phase noise is calculated to be 25 mrad, representing a 53 mrad reduction compared to the previous setup.

As shown in Fig. 3.2 (Fig. 3.3), two TAs are implemented in the setups to achieve higher Rabi frequencies for the Pump and Stokes lasers. One concern is whether the phase noise increases after amplification. To investigate this, we measured the phase noise of the output from the seeded TAs, and the results are presented in Fig. 4.13 (c) and (d). No significant difference has been found. A similar observation was reported by Hänsch group ([Kolachevsky et al., 2011](#)). The possible explanation is that during the amplification process, both the carrier frequency and the noise from the seed ECDL are amplified together, preserving the ratio between the carrier power and the sideband noise power. As a result, the phase noise level remains unchanged. Table. 4.1 provides a summary of the phase noise for different Raman laser setups.

Further suppression of the phase noise has been achieved by implementing an intra-cavity EOM (icPSA2x4-NIR, QUBIGGMBH) to stabilize the laser, replacing the current modulation method. With the EOM, the servo bandwidth can be increased from 250 kHz to 1 MHz, reducing the integrated phase noise of Pump laser to 17.5 mrad. However, in our experiments,

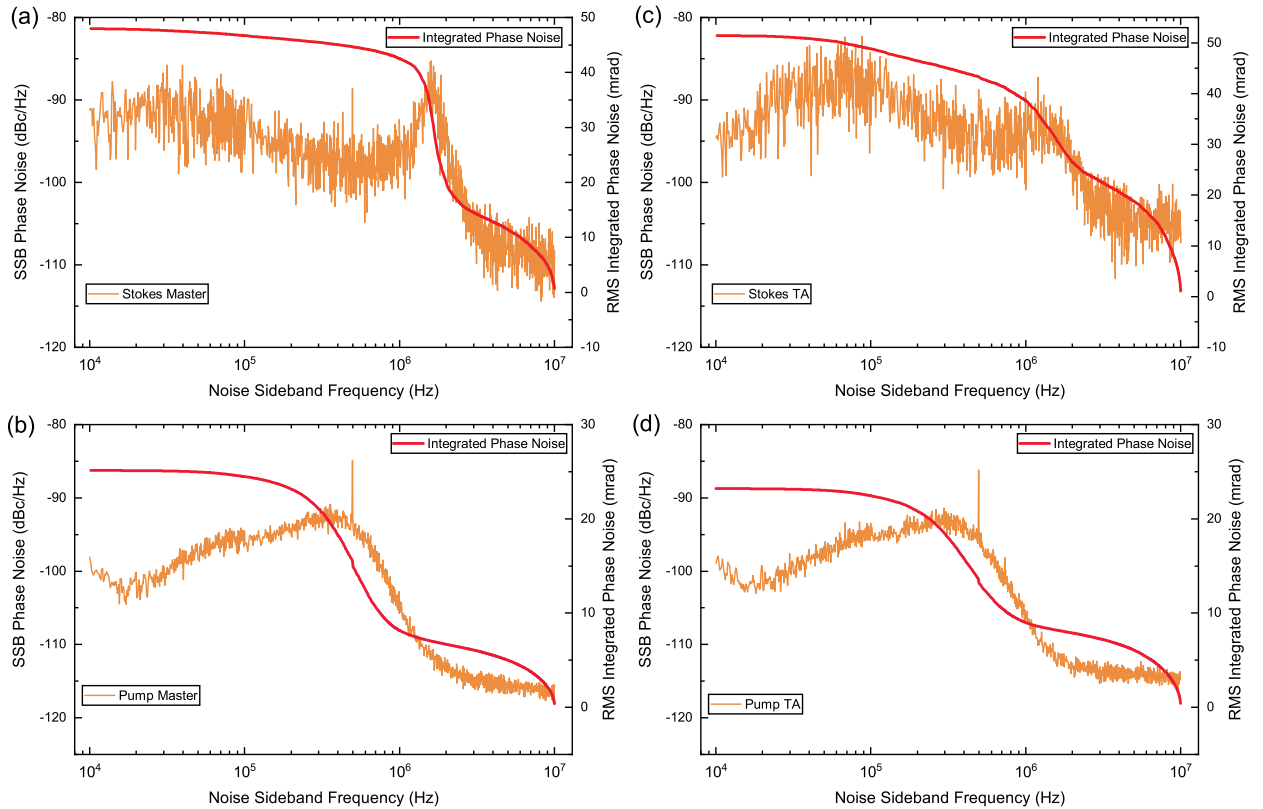


Figure 4.13.: Phase noise measurements of the Raman lasers for Stokes (a) and for Pump (b) are showed after extending the length of external cavity. Also, the phase noise are showed for the output of the seeded TAs in (c) (Stokes) and (d) (Pump). The orange curve presents the spectral density of measured laser and the red solid line is the integrated phase noise.

the relatively high phase noise of the Stokes laser posed a significant limitation, preventing further reductions in the total phase noise. Additionally, the use of the intra-cavity EOM introduces a higher chance of mode jumps in the Pump laser. To ensure a more stable locking scheme while maintaining an acceptable phase noise level, current modulation is ultimately chosen over the use of the EOM for the actual experiments.

Another most recent method to reduce laser phase noise, proposed by Chao et al. (2024); Li et al. (2022) relies on a feedforward noise cancellation system designed to suppress servo bumps generated during PDH locking at high frequencies. Using the feedforward noise cancellation technique, Maddox et al. (2024) declares a improved transfer efficiency from 94.2(6)% to 98.7(1)%. This same technique is expected to be implemented in future experimental setups to further reduce the phase noise in our experiments.

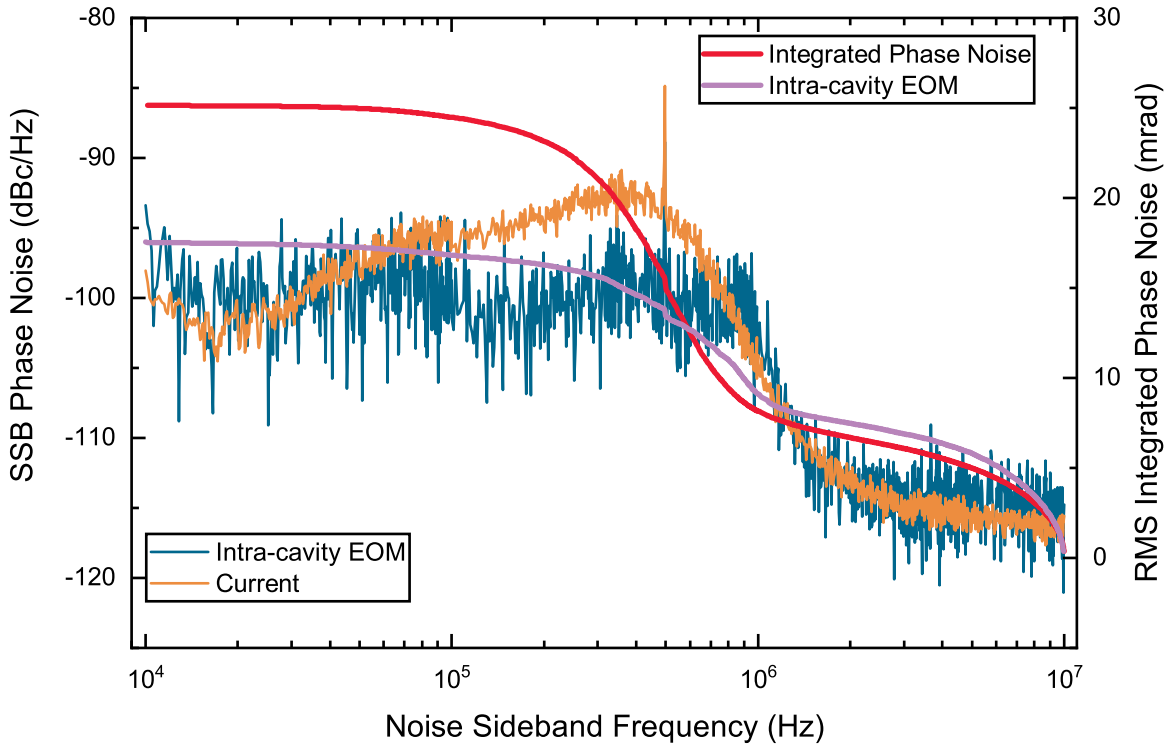


Figure 4.14.: Phase noise measurements for Pump laser are performed with current modulation and intra-cavity EOM modulation. The orange and blue curves present the spectral density of the measured laser. The red and purple solid lines are the integrated phase noise.

Laser	Stokes			Pump		
	Short ECDL	Long ECDL	+ TA	Short ECDL	Long ECDL	+ TA
ϕ_{RMS} (mrad)	192	48	51	78	25	23
ε^2	3.6%	0.2%	0.3%	0.6%	0.06%	0.05%

Table 4.1.: Phase noise measurements for different Raman laser setups.

4.4.4. Loss Probability

Using the measured phase noise of Pump and Stokes lasers, the population loss due to fast laser phase noise P_N can be estimated. Combined with the contribution of the loss P_A from the violation of adiabatic criteria, the total loss model P_{Loss} can be expressed as

$$P_{\text{Loss}} = P_A + P_N = 1 - \exp\left(-\frac{\Gamma\pi^2}{\Omega_0^2\tau}\right) + \frac{1}{4}\Omega_0^2 \left(\varepsilon_p^2 \frac{G_p\tau}{4G_p^2 + 2G_p\Gamma + \Omega_0^2} + \varepsilon_s^2 \frac{G_s\tau}{4G_s^2 + 2G_s\Gamma + \Omega_0^2} \right) , \quad (4.13)$$

where the bandwidth of Pump and Stokes $G_{p/s}$ is approximated by the lasers' servo-bumps, which can be inferred from the phase noise measurement Fig. 4.11 and Fig. 4.14. And the $\varepsilon_{p/s}^2$ is inferred from Table. 4.1. The excited state linewidth $\Gamma = 2\pi \times 6.6(1.3)$ MHz is measured

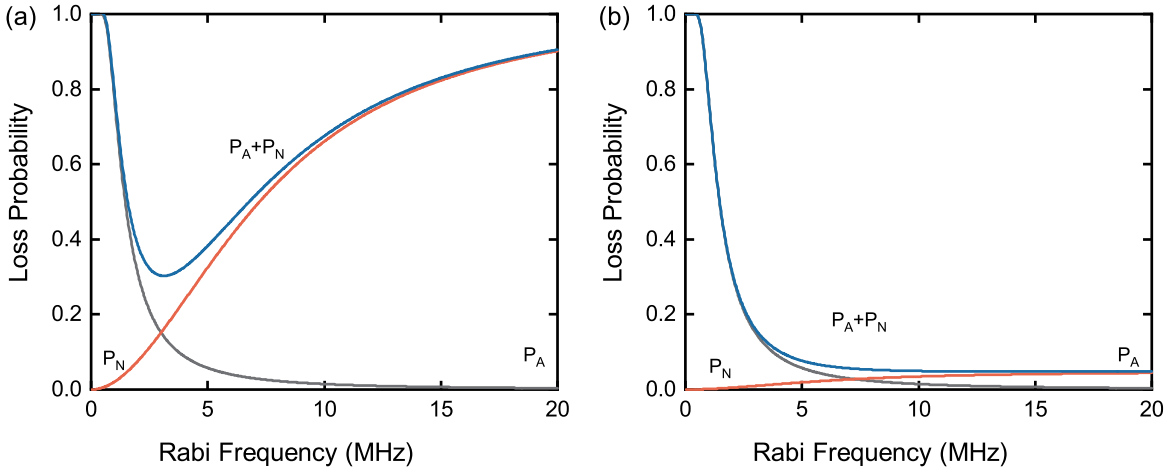


Figure 4.15.: Estimated loss probability for STIRAP process. The bandwidth is selected to be $G_p = 2\pi \times 0.5$ MHz and $G_s = 2\pi \times 2.5$ MHz. The pulse duration is fixed at $\tau = 7\ \mu\text{s}$. (a) The loss probability is calculated at high laser phase noise with short external cavity. (b) The loss probability is calculated at low laser phase noise with long external cavity.

in Fig. 4.1 (c). Considering the relative broader Γ among those bi-alkali species (Table. B.1), achieving high Rabi frequency (or high laser intensity) is necessary to suppress the non-adiabatic loss P_A . And the requirement for high Rabi frequencies gives rise to the more stringent requirement on low laser phase noise conditions. This challenge has been successfully addressed through the use of long external cavity lasers in our setup.

The estimated loss probability for STIRAP processes using the short external cavity (high phase noise) and the long external cavity (low phase noise) are calculated based on Eq. 4.13 and shown in Fig. 4.15. In Fig. 4.15 (a), the STIRAP losses for the short external cavity are plotted as a function of the peak Rabi frequency Ω_0 , with the pulse duration fixed at $\tau = 7\ \mu\text{s}$. Before the suppression of phase noise, the minimum loss rate exceeds 30%. Even when P_A is suppressed by increasing the Rabi frequency, P_N rises rapidly due to the high phase noise. In contrast, the improved results with the long external cavity, which reduces the phase noise of the Pump and Stokes lasers, are shown in Fig. 4.15 (b). With the same pulse duration, the loss rate is significantly reduced due to the lower P_N . Consequently, the total loss rate can be minimized by increasing the Rabi frequency, achieving a loss rate below 5%.

Fig. 4.16 provides 2D density plots of the loss probability as a function of pulse duration τ and peak Rabi frequency Ω_0 , under both high and low phase noise conditions. The red regions in the plots represent high loss probabilities, while the blue regions indicate low loss probabilities. These plots clearly show that high phase noise severely restricts the viable combinations of pulse duration and Rabi frequency. Specifically, for high phase noise condi-

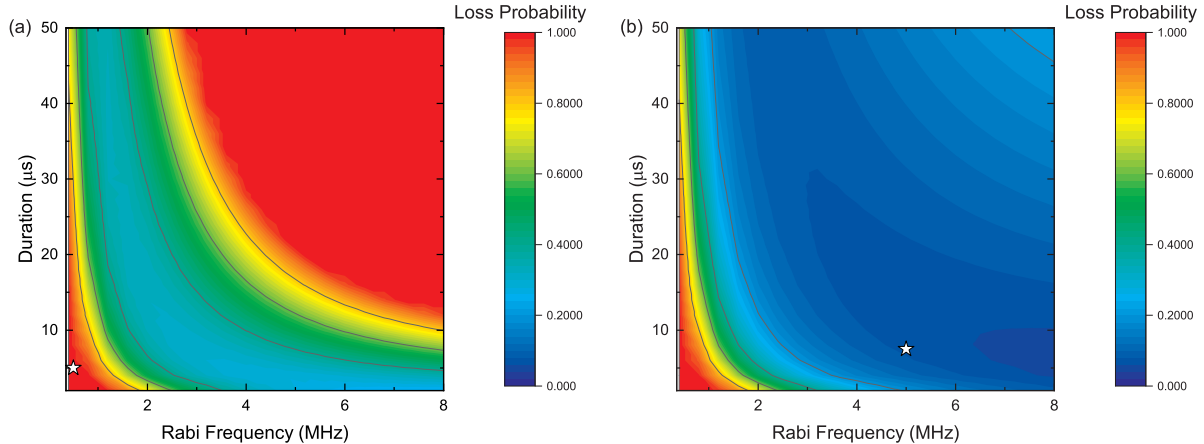


Figure 4.16.: 2D density loss probability various pulse duration and peak Rabi frequency. Plot for short external cavity (a) and for long external cavity (b). The white stars in (a) and (b) indicate the pulse parameters used in our experiments to perform the STIRAP transfer before and after updating the laser setups.

tion, combinations of high Rabi frequency with long pulse duration, or low Rabi frequency with short pulse duration, result in loss probabilities approaching 100%. Under low phase noise condition, however, the range of acceptable combinations for Rabi frequency and pulse duration is much broader. A relatively low loss probabilities can be achieved under high Rabi frequency plus long pulse duration.

In general, the loss probability is governed by two competing factors. At low Rabi frequency and short pulse duration, the high loss rate is primarily due to the violation of adiabatic criteria (P_N). Conversely, with high Rabi frequency and long pulse duration, the dominant factor is fast laser phase noise (P_A), which significantly increases the loss rate. These two effects act in opposition to each other. To achieve minimal loss probabilities, reducing the phase noise is crucial, as it suppresses the P_A , resulting in a lower overall loss rate. Additionally, careful optimization of Rabi frequency and pulse duration is required. Based on the density plots, optimal combinations include either high Rabi frequency with short pulse duration or low Rabi frequency with long pulse duration. In our experiments, we selected a combination of high Rabi frequency (around 5 MHz) and short pulse duration (7.5 μ s) to minimize the loss probability effectively.

The estimated loss probability explains the low transfer efficiency observed during the initial attempts, as discussed in section 5.2.1 of (Yang, 2021b). With the initially high phase noise and limit Rabi frequency (500 kHz), the loss rate was relatively high, resulting in poor transfer efficiency. The updated Raman laser setup, featuring a long external cavity ECDL structure

and the implementation of TAs in the new system, effectively suppressed phase noise and enabled higher Rabi frequencies. This improvement allowed us to perform the ground state transfer via STIRAP with high efficiency, as demonstrated in Fig. 4.9.

4.4.5. Detuning Conditions

The dependences of the transfer efficiency on two-photon detuning δ and single-photon detuning Δ , as a characterizing feature of STIRAP, are investigated. As discussed in Section 2.1, the application of the dark state relies on two-photon detuning condition $\delta = 0$. When $\delta \neq 0$, the deviation from this resonance cause the population to remain in the excited state, leading to decoherence of the system and a high loss rate. In contrast, the formation of dark state is not prevented by single-photon detuning Δ . However, the effective Rabi frequency $\Omega_{\text{eff}} = \frac{\Omega_0^2}{4\Delta}$ still depends on Δ , which must satisfy the adiabatic condition. Using the extended four-level system introduced in Section 2.1.4, the OBE (Eq. 2.10) is solved to simulate the STIRAP transfer process with different δ and Δ conditions. The simulation employs the same method and software package used for the Evolution fitting in Section 4.3.4. The results are shown in this section.

Fig. 4.17 shows the simulation results of STIRAP efficiency as a function of two-photon detuning δ and single-photon detuning Δ . The parameters are same as those used in Section 4.3.4, with a balanced Peak Rabi frequency of 5 MHz for both Pump and Stokes laser. As predicted, the population transfer to the ground state decreases rapidly when δ deviates from the resonance condition. The linewidth of the two-photon detuning is defined as the full width at half maximum (FWHM) Δ_{FWHM} of the two-photon line profile. From Fig. 4.17 (a), the two-photon detuning profile shows a linewidth of Δ_{FWHM} is 550 kHz and the two-way transfer efficiency $\eta^2 < 1\%$ when $|\delta| > 700$ kHz. For single-photon detuning in Fig. 4.17 (b), the simulation results indicates a high tolerance for deviations form the resonance. The $\eta^2 > 80\%$ as long as $|\delta| < 27.5$ MHz. Fig. 4.17 (c) presents a 2D density plot of the two-way efficiency η^2 as a function of both Δ and δ . From the simulation results, it can be concluded that the transfer efficiency exhibits different sensitivities to δ and Δ . In general, the efficiency is highly sensitive to the δ , while it is more tolerant to deviations in the Δ .

The simulation results for the two-photon detuning δ are compared with experiments as shown in Fig. 4.18 (a). The red and blue lines represent the simulation curves for pulse

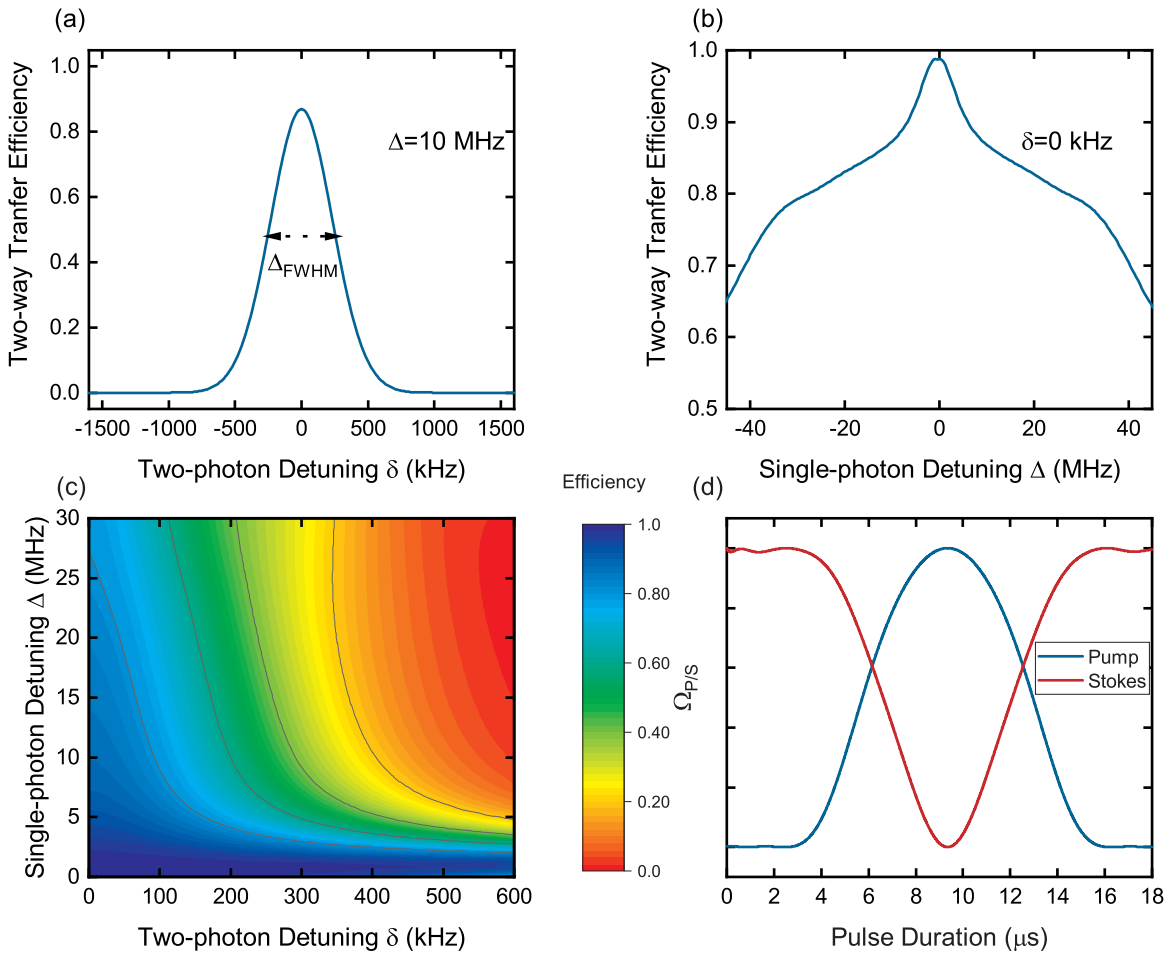


Figure 4.17.: (a) Numerical simulation of transfer efficiency as a function of two-photon detuning δ at $\Delta = 2\pi \times 10 \text{ MHz}$. (b) Numerical simulation of transfer efficiency as a function of single-photon detuning Δ at $\delta = 0 \text{ kHz}$. (c) 2D density plot for STIRAP efficiency various δ and Δ . (d) The STIRAP pulse envelope used in the simulation. The parameters are same as those used in Section 4.3.4. Notably, the $\zeta_{\text{s/p}} = \Omega'_{\text{s/p}}/\Omega_{\text{s/p}} = 0.1$ for both Pump and Stokes laser. $\zeta_{\text{s/p}}$ defined as the proportion of polarization impurity which would be discussed later.

duration of $16 \mu\text{s}$ and $64 \mu\text{s}$, as δ is varied. The corresponding experimental data points are shown in red and blue circles. From the figure, the linewidth Δ_{FWHM} is extracted. For a $16 \mu\text{s}$ pulse $\Delta_{\text{FWHM},16\mu\text{s}} = 580 \text{ kHz}$, while for $64 \mu\text{s}$ pulse $\Delta_{\text{FWHM},64\mu\text{s}} = 290 \text{ kHz}$. Fig. 4.18 (b) shows the simulation results for the linewidth Δ_{FWHM} as a function of varying laser Rabi frequency and pulse duration. The results indicate that applying a high Rabi frequency or short pulse duration narrow the linewidth Δ_{FWHM} , whereas a low Rabi frequency or short pulse duration broaden it. Furthermore, Fig. 4.18 (c) and (d) demonstrate that the Δ_{FWHM} is inversely proportional to the pulse duration τ and proportional to the Peak Rabi frequency Ω_0 . These relationships depend on the adiabaticity condition (Vitanov et al., 2017).

For the case of single-photon detuning Δ , the situation differs significantly. Based on the

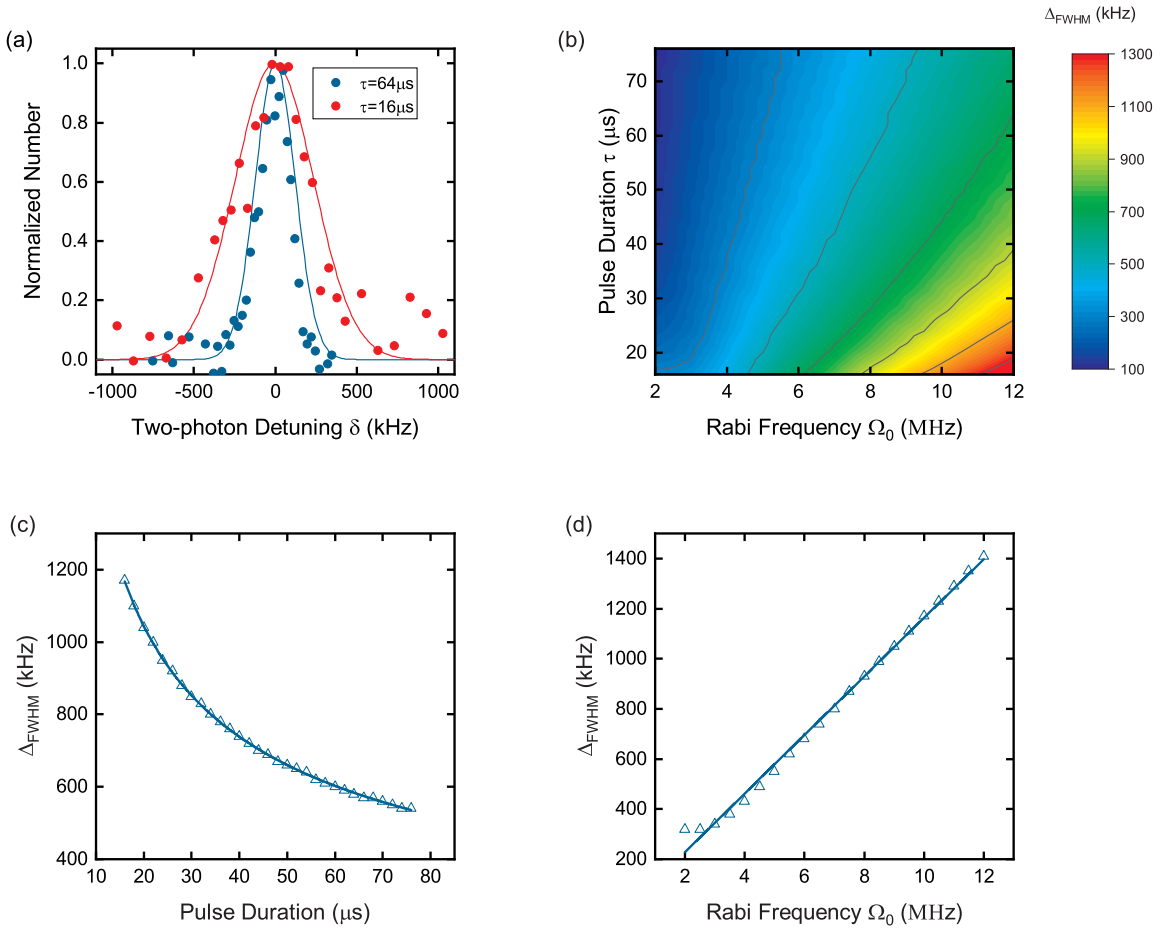


Figure 4.18.: (a) Two-photon detuning δ scan for STIRAP process under $16\mu s$ and $64\mu s$ pulse duration. Red and blue circles are the measured data after round trip STIRAP. Red and blue lines represent the simulation results. (b) The linewidth of two-photon detuning as a function of laser Rabi frequency and pulse duration. (c) Δ_{FWHM} is inversely proportional to the pulse duration τ . (d) Δ_{FWHM} is proportional to the Peak Rabi frequency Ω_0 . In (c) and (d) the triangle points represent simulation points and blue solid lines are the fit curves.

simulation results in Fig. 4.17 (b), the highest transfer efficiency is predicted to occur at $\Delta = 0$ MHz. In experiments, however, the first attempt with $\Delta = 0$ MHz yielded a relatively low transfer efficiency as illustrated in Fig. 4.19 (a). The one-way transfer efficiency was approximately 60%, which is much lower than the efficiency achieved at $\Delta = 2\pi \times 10$ MHz, as shown in Fig. 4.9. This discrepancy is attributed to differences in polarization impurities between the Pump and Stokes lasers (Section 5.5.2 of Yang (2021b)).

As discussed in Section 2.1.4 and Section 4.3.4, the undesired polarization components can drive molecules from the ground state to the wrong excited state. In the experiments, it is assumed that the undesired polarization component cannot be fully canceled and amounts to approximately 2% of the total laser power. This results in an undesired coupling strength of $\Omega'_{s/p}(t) \sim 0.1\Omega_{s/p}(t)$. Here, the proportion of polarization impurities is defined as $\zeta_{s/p} =$

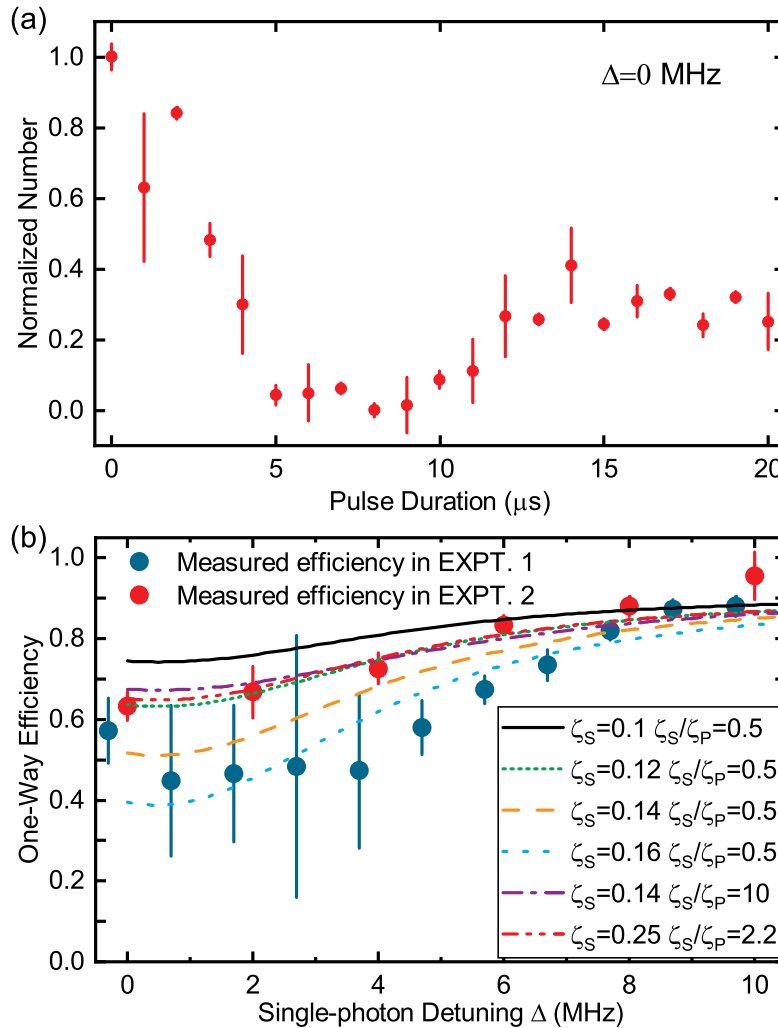


Figure 4.19.: (a) Evolution of molecular population in the $|FB\rangle$ state at $\Delta = 0$ MHz condition. The red circles are data points for the measured molecular number. (b) The STIRAP efficiency based on different Δ . The red and blue circles represent data points from two separate measurements. In measurement 1 the mirror placed before UHV chamber (see Fig. 3.4) is a gold mirror, while in measurement 2 the mirror is replaced with a dielectric mirror. The colored and styled lines represent numerical simulation results for various combinations of ζ_s and ζ_s/ζ_p . Error bars in both plot represent the standard deviation of a 3 times average.

$\Omega'_{s/p}/\Omega_{s/p}$. Initially, the condition $\zeta_s/\zeta_p = 1$ ($\zeta_s = \zeta_p = 0.1$) is applied, indicating balanced polarization impurities for the Pump and Stokes lasers. Then, the case of $\zeta_s/\zeta_p \neq 1$ is considered. The Hamiltonian H for the OBE Eq. 2.10 is now modified as

$$\mathbf{H}(t) = \frac{\hbar}{2} \begin{bmatrix} 0 & \Omega_p(t) & \zeta_p \Omega_p(t) & 0 \\ \Omega_p(t) & 2\Delta & 0 & \Omega_s(t) \\ \zeta_p \Omega_p(t) & 0 & 2\Delta_1 & \zeta_s \Omega_s(t) \\ 0 & \Omega_s(t) & \zeta_s \Omega_s(t) & 0 \end{bmatrix}. \quad (4.14)$$

By varying ζ_s and ζ_p , the STIRAP process can be simulated for different values of Δ . Fig. 4.19 (b) presents the measured STIRAP efficiencies for various Δ values alongside simulation results for different ζ_s and ζ_p conditions. The red and blue circles represent data from two separate measurements conducted on different days, where slight variations in polarization impurity may have affected the results. Both measurements show that the transfer efficiency improves at relatively larger value of Δ . The colored and styled lines represent simulation results for various combinations of ζ_s and ζ_s/ζ_p . Notably, the simulation curves can appear similar for different combinations of these parameters. For example, the simulation results for $\zeta_s = 0.12 \& \zeta_s/\zeta_p = 0.5$, $\zeta_s = 0.25 \& \zeta_s/\zeta_p = 2.2$, and $\zeta_s = 0.14 \& \zeta_s/\zeta_p = 10$ all align closely with the measurements of red circles.

To further distinguish the effects for different ζ_s and ζ_s/ζ_p , Fig. 4.20 (a) and (b) present the efficiency as a function of ζ_s and ζ_s/ζ_p at $\Delta = 0$ MHz and $\Delta = 2\pi \times 10$ MHz, respectively. The white dashed lines in the density plots indicate the efficiency at $\zeta_s/\zeta_p = 1$. Several conclusions can be drawn from these figures.

Firstly, the situation of $\zeta_s/\zeta_p = 1$ is considered. This corresponds to the case where the couplings to the undesired intermediate state are the same for Pump and Stokes. It was pointed out by Vitanov and Stenholm (1999) that for this case, theoretically, the STIRAP efficiency remains high. Secondly, the efficiency also remains high when $\zeta_s = 0$. This indicates the case without polarization impurity, the four-level system is reduced to a typical 3-level system. Outside of these two special cases, the efficiency decreases rapidly at $\Delta = 0$ MHz under two conditions: (1) when ζ_s/ζ_p deviates from 1 for a fixed ζ_s , and (2) when ζ_s increases for a fixed

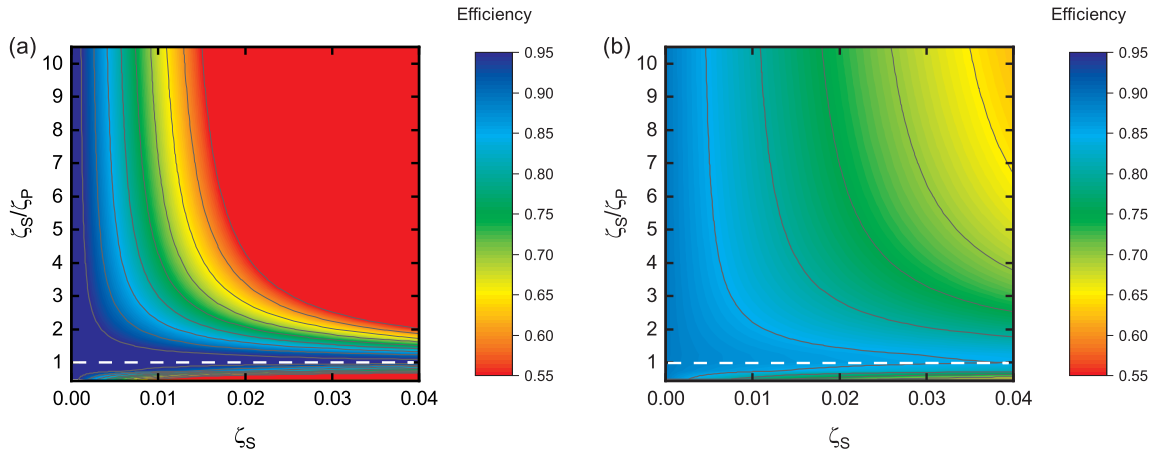


Figure 4.20.: The simulation results of STIRAP efficiency as a function of ζ_s and ζ_s/ζ_p for (a) $\Delta = 0 \text{ MHz}$ and (b) $\Delta = 2\pi \times 10 \text{ MHz}$. The white dashed lines represent the special case $\zeta_s/\zeta_p = 1$, where always give high efficiency in spite of the value ζ_s . And the black solid lines are contour lines for different efficiency.

ζ_s/ζ_p . This indicates that the efficiency is highly sensitive to both the magnitude and imbalance of polarization impurities. However, this sensitivity is reduced when $\Delta = 2\pi \times 10 \text{ MHz}$, as the suppression of light scattering scales as $1/\Delta^2$. Additionally, by observing the contour lines in the efficiency density plots, it is evident that many combinations of ζ_s and ζ_s/ζ_p result in the same efficiency in both $\Delta = 0 \text{ MHz}$ and $\Delta = 2\pi \times 10 \text{ MHz}$. This observation explains the simulation results in Fig. 4.19(b), where different parameter combinations produce similar outcomes.

Here, a possible combination of $\zeta_s = 0.12$ and $\zeta_s/\zeta_p = 0.5$ is selected to fit the data and adjust the simulation in Fig. 4.17. The corrected results are shown in Fig. 4.21. Focusing on the single-photon detuning, the efficiency is relatively low around $\Delta = 0 \text{ MHz}$ and can be enhanced up to approximately 90% one-way efficiency by gradually increasing the $\Delta \rightarrow 2\pi \times 12 \text{ MHz}$.

In summary, the simulation results suggest that the highest STIRAP transfer efficiency can be achieved with either pure polarization or balanced polarization impurities. However, due to limitations in our experimental setups, the actual conditions often involve either significant undesired polarization components or large imbalances in the polarization impurities, caused by the multiple possible combinations of ζ_s and ζ_s/ζ_p . Also, the situation could vary from different measurements due to the imperfect control of the setups. To mitigate these issues, a single-photon detuning $\Delta = 2\pi \times 10 \text{ MHz}$ is generally chosen to suppress light scattering and maintain high efficiency.

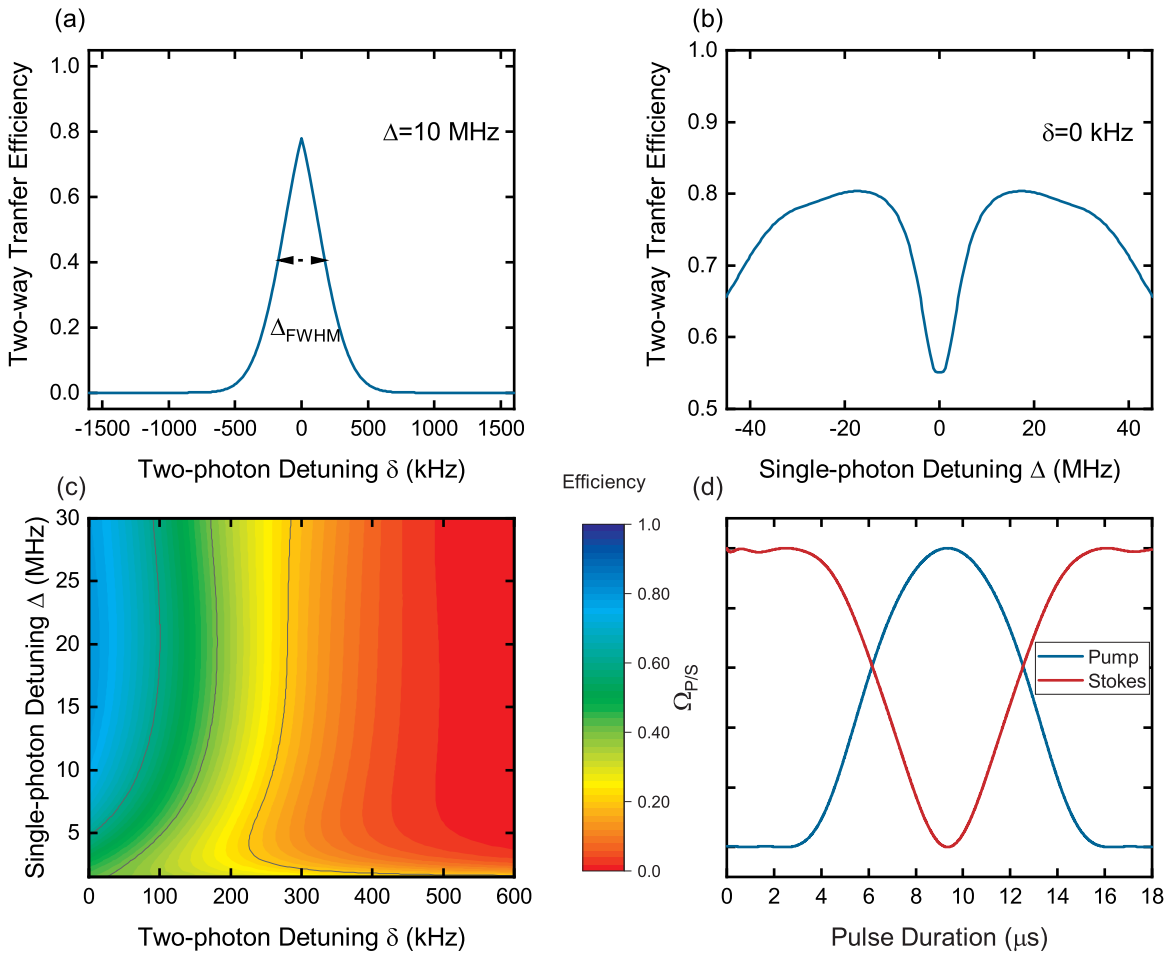


Figure 4.21.: (a) Numerical simulation of transfer efficiency various two-photon detuning δ at $\Delta = 2\pi \times 10 \text{ MHz}$. (b) Numerical simulation of transfer efficiency various single-photon detuning Δ at $\delta = 0 \text{ kHz}$. (c) 2D density plot for STIRAP efficiency various δ and Δ . (d) The STIRAP pulse envelope used in the simulation. Now the parameters $\zeta_s = 0.12$ and $\zeta_s/\zeta_p = 0.5$ are applied.

4.4.6. Magnetic Field Around Feshbach Resonance

The STIRAP efficiency can also be influenced by the magnetic field, which is associated with closed-channel fraction of Feshbach molecules. The dependence of STIRAP efficiency on the magnetic field has been reported in [Bause et al. \(2021\)](#); [Ni \(2009\)](#). By ramping the magnetic field away from the Feshbach resonance point, a larger closed-channel fraction can be achieved, leading to stronger coupling between the Feshbach state and the excited state. Also, the closed-channel fraction significantly depends on the width of the Feshbach resonance ([Aikawa et al., 2009](#); [Köhler et al., 2006](#)). For broad resonance conditions, molecules are strongly perturbed by the atomic channel, resulting in a smaller closed-channel fraction, even far from resonance. In contrast, under narrow resonance conditions, the molecules are dominated by close-channel and exhibit a larger fraction, except when they are very close to

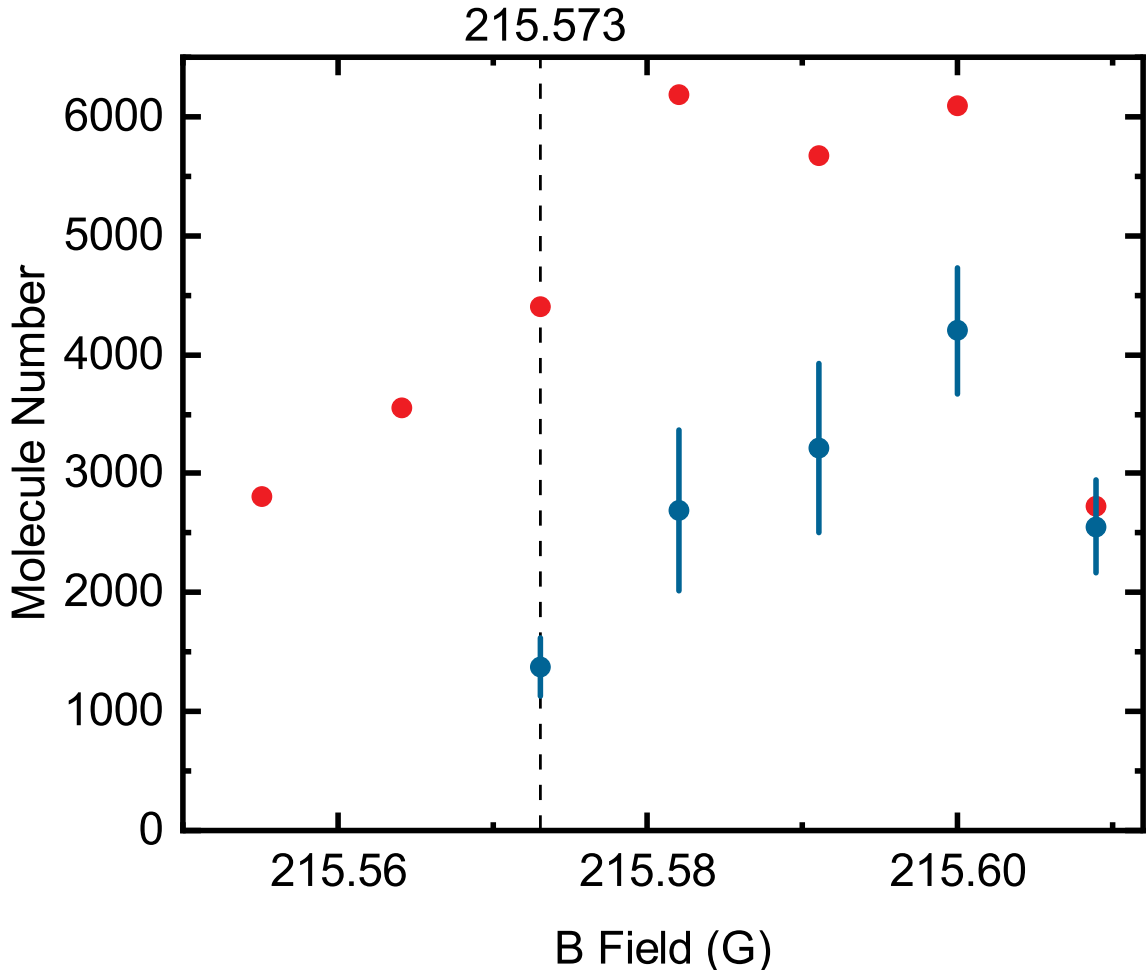


Figure 4.22.: The effect of the Pump excitation at different magnetic field. The red circles are data points for the number of Feshbach molecules when scanning the magnetic filed around Feshbach resonance field. The blue circles represents the number of Feshbach molecules with same sequence but switching on Pump pulse, which also used in STIRAP process. The dashed black line represents the magnetic filed used in STIRAP process.

the resonance.

In our case, the ${}^6\text{Li}{}^{40}\text{K}$ in Feshbach state at the 215.6 G resonance is close-channel dominated (Costa et al., 2010; Wille et al., 2008). In principle, the coupling strength for the Pump transition can be strong enough to achieve high STIRAP efficiency when the magnetic field is tuned away from the resonance point. However, the lifetime of the ${}^6\text{Li}{}^{40}\text{K}$ Feshbach molecules also strongly depends on the magnetic field, which has been discussed by Voigt (2009). The molecule lifetime decreases rapidly when the magnetic filed is moved away from the resonance, leading to a reduction in the number of Feshbach molecules. Consequently, a lower number ground state molecules can be achieved. Fig. 4.22 illustrates the effect of the magnetic field on the number of Feshbach molecules. The red circles represent the number of Feshbach

molecules after Feshbach association, while the blue circles indicate the number of Feshbach molecules after excitation with the Pump light. When the coupling strength is strong, the Feshbach molecules are excited to the $A^1\Sigma^+ |v' = 23, J' = 1\rangle$ state and subsequently decay out of the system. Thus, a higher remaining number of Feshbach molecules corresponds to a weaker coupling strength.

When the magnetic field is very close to the resonance point at 215.6 G, The number of Feshbach molecules is high, but the coupling strength is weak. This results in a lower STIRAP efficiency but a relatively higher number of ground state molecules number. Conversely, as the magnetic field is ramped further away from the resonance, the number of Feshbach molecules decreases due to shorter lifetimes, but the coupling strength increases. This leads to higher STIRAP efficiency but a relatively lower number of ground state molecules. Therefore, the magnetic field must be carefully optimized to strike a balance between STIRAP efficiency and the number of ground state molecules. In experiments, the endpoint of the magnetic field is set to 215.573 G, as indicated by the black dashed line in the plot.

5. Properties of Ground State ${}^6\text{Li}{}^{40}\text{K}$ Molecules

In this chapter, several properties of the ground state ${}^6\text{Li}{}^{40}\text{K}$ molecules are investigated. Firstly, the temperature of the molecular sample is determined. Then, the lifetime of the ground state ${}^6\text{Li}{}^{40}\text{K}$ is measured, and the two-body decay rate constant is extracted from the measurements, which is comparable with theoretical prediction. Additionally, the dipole moment of the ground state is revealed by measuring the Stark shift in an external electric field. Moreover, the preliminary results of MW spectroscopy for the first rotationally excited state $N = 1$ are discussed. Finally, the potential solution for short coherence time of the rotational transition is explored.

5.1. Temperature Measurements

The determination of temperature for the molecules is realized by observing the thermal expansion of the molecular cloud using absorption imaging in TOF (Lett et al., 1988). In our case, direct imaging of the ground state molecules is still under development at the time of writing this thesis. As a result, the temperature of the ground state sample cannot be directly measured by fitting the TOF expansion of the ground state molecules.

However, since the STIRAP process is adiabatic, no heating should occur during the transfer, meaning that the temperature of the molecular sample should remain unchanged. Hence, the temperature of the molecular sample in the Feshbach state $|\text{F.B.}\rangle$ is measured and used as an approximation for the temperature of the ground state sample. This approach has been adopted in previous studies of KRb, NaK, and NaCs (Ni, 2009; Park et al., 2015a; Stevenson et al., 2023).

Fig. 5.1 shows the measured TOF expansion of the Feshbach molecular cloud along the

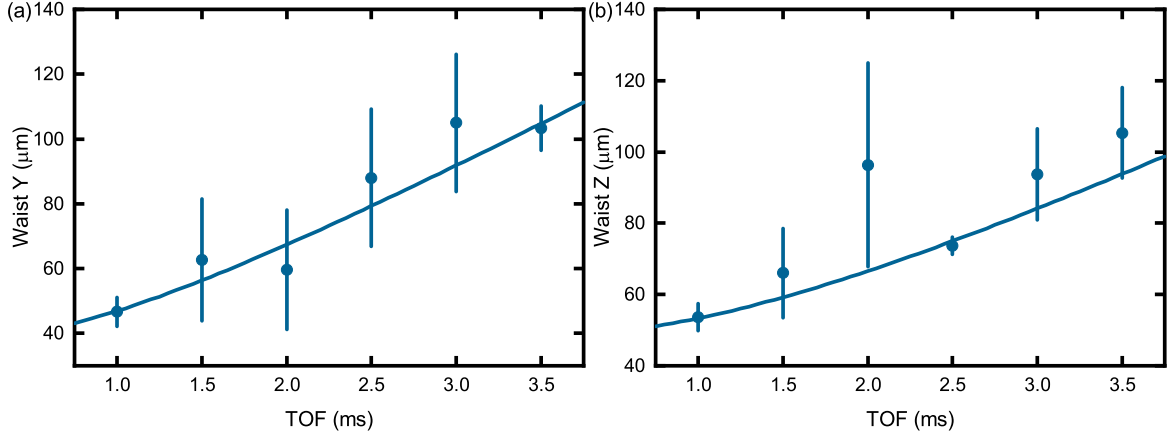


Figure 5.1.: The TOF measurement of Feshbach molecular cloud along (a) y-direction and (b) z-direction. The blue circles are the measured cloud waist during the TOF and blue lines are the fit curve with formula Eq. 5.1. The error bars represent the standard deviation obtained after three different experimental runs.

y- and z-directions. The blue lines represent the fit curves based on formula

$$\sigma_{y/z} = \sqrt{w_{y/z}^2 + 4 \frac{T_{y/z} k_B}{m} t^2} , \quad (5.1)$$

where $\sigma_{y/z}$ is the waist of cloud, $w_{y/z}$ is the initial waist, $T_{y/z}$ is the cloud temperature, and t is the TOF duration. From the fits, the extracted temperatures are $T_y = 1.08(8) \mu\text{K}$ and $T_z = 0.73(11) \mu\text{K}$. The average temperature is then calculated to be $\bar{T} = \frac{T_y + T_z}{2} = 0.91(7) \mu\text{K}$.

The temperature of the molecular cloud can also be inferred based on the temperature and number of ${}^6\text{Li}$ and ${}^{40}\text{K}$ atomic cloud. As we adiabatically ramp the magnetic field to associate the Feshbach molecules, the entropy of the system should remain conserved during the association process. The average entropy of Fermi gas ${}^6\text{Li}$ and ${}^{40}\text{K}$ in the harmonic trap is calculated to be (Pitaevskii and Stringari, 2016)

$$s_{\text{Li,K}} = \frac{S}{N_{\text{Li,K}}} = k_B \left(4 \frac{\text{Li}_4(-e^{\beta \mu_{\text{Li,K}}})}{\text{Li}_3(-e^{\beta \mu_{\text{Li,K}}})} - \beta \mu_{\text{Li,K}} \right) , \quad (5.2)$$

where $\beta = \frac{1}{k_B T}$. $\mu_{\text{Li,K}}$ is the chemical potential, which can be extracted by solving

$$N_{\text{Li,K}} = \int_0^\infty \frac{\epsilon^2}{2\hbar^3 \omega_{\text{Li,K}}^3} \frac{1}{e^{(\epsilon - \mu_{\text{Li,K}})\beta} + 1} d\epsilon , \quad (5.3)$$

where ω is the trapping frequency. $\text{Li}_s(z) = \sum_k z^k / k^s$ is the polylogarithm, which can be expressed as

$$-\text{Li}_{s+1}(-z) = \frac{1}{\Gamma(1+s)} \int_0^\infty \frac{\epsilon^s}{e^\epsilon/z + 1} d\epsilon \quad , \quad (5.4)$$

where $\Gamma(x)$ is the Gamma function. For Bose gas ${}^6\text{Li}{}^{40}\text{K}$, the average entropy is calculated to be ([Pitaevskii and Stringari, 2016](#))

$$s_{\text{LiK}} = s_{\text{Li}} + s_{\text{K}} = \frac{S}{N_{\text{LiK}}} = k_{\text{B}} \left(4 \frac{g_4(-e^{\beta\mu_{\text{LiK}}})}{g_3(-e^{\beta\mu_{\text{LiK}}})} - \beta\mu_{\text{LiK}} \right) \quad , \quad (5.5)$$

where

$$-g_{s+1}(-z) = \frac{1}{\Gamma(1+s)} \int_0^\infty \frac{\epsilon^s}{e^\epsilon/z - 1} d\epsilon \quad . \quad (5.6)$$

Also, the chemical potential of μ_{LiK} follows the equation

$$N_{\text{LiK}} = \int_0^\infty \frac{\epsilon^2}{2\hbar^3\omega_{\text{LiK}}^3} \frac{1}{e^{(\epsilon-\mu_{\text{LiK}})\beta} - 1} d\epsilon \quad . \quad (5.7)$$

By solving the system of Eq. 5.5 and Eq. 5.7, the temperature and chemical potential of ${}^6\text{Li}{}^{40}\text{K}$ can be extracted. Assuming the scenario where ${}^{40}\text{K}$ (300 nK, $N_{\text{K}} \approx 1 \times 10^5$, $\omega_{\text{K}} = 2\pi \times 313 \text{ Hz}$) and ${}^6\text{Li}$ (500 nK, $N_{\text{Li}} \approx 1 \times 10^5$, $\omega_{\text{Li}} = 2\pi \times 503 \text{ Hz}$) are fully associated into ${}^6\text{Li}{}^{40}\text{K}$ Feshbach molecules, the temperature of the molecular cloud is calculated to be $0.89 \mu\text{K}$. This value agrees well with our experimental measurement.

5.2. Lifetime Measurement

Rovibrational ground state ${}^6\text{Li}{}^{40}\text{K}$ molecules are expected to be chemically unstable with respect to the following two body atom-exchange collisions ([Żuchowski and Hutson, 2010](#)):



Based on the predicted two-body inelastic collision rate constant $K_0 = 7.9 \times 10^{-10} \text{ cm}^3\text{s}^{-1}$ and the measurement of cloud density $\bar{n} = 0.53(26) \times 10^{12} \text{ cm}^{-3}$ (the calculation is introduced later), the lifetime of the ground state molecules is expected to be 2.4 ms short. The decay time of the ground state molecules in the optical dipole trap is measured and shown in Fig. 5.2. The measurement sequence follows Fig. 4.8 (b), where a variable trap holding

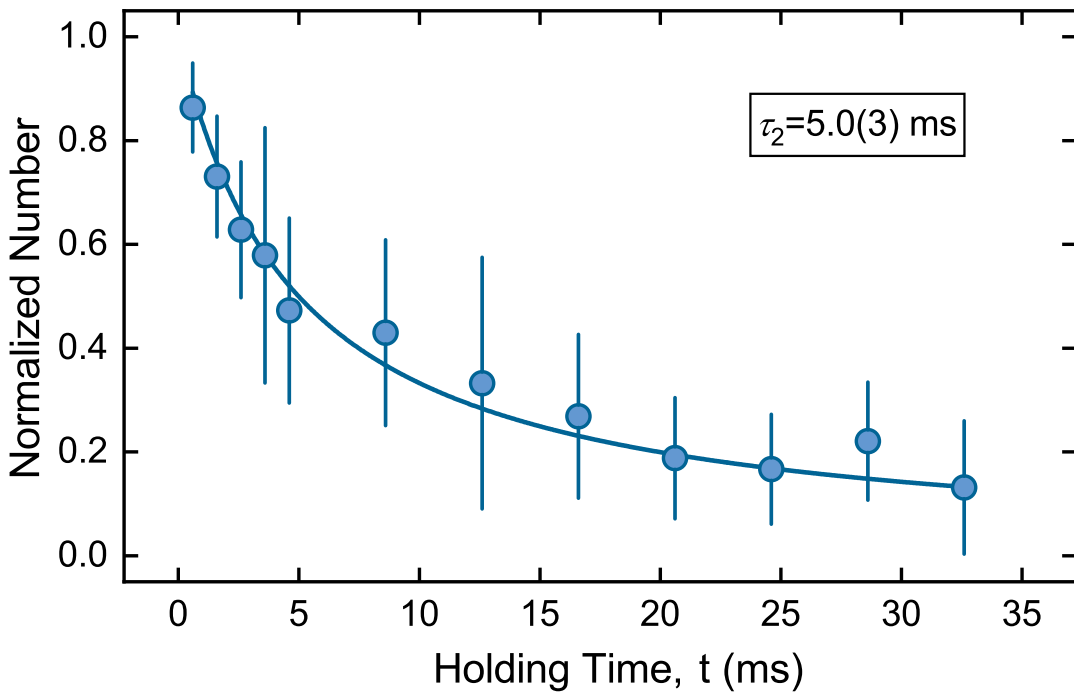


Figure 5.2.: Lifetime of ground state molecules. The blue points are measurements performed with only pure ground state ${}^6\text{Li}{}^{40}\text{K}$. The data are normalized to the max number of molecules from fitting of each measurement. The fitting is based on two-body loss model. The error bars represent the standard deviation obtained after four different experimental runs. Figure is taken from [He et al. \(2024\)](#).

period, x , is inserted before the reverse transfer back to the Feshbach molecules. Since atoms of both species remain in the trap due to incomplete Feshbach molecule formation, these atoms need to be removed to prevent atom-molecule collisional losses. This is achieved by applying resonant light pulses of $36\ \mu\text{s}$ and $500\ \mu\text{s}$ duration for Li and K on their respective D2 transitions. These light pulses are applied during the trap holding period and the relevant setups and procedures have been discussed in Section 3.3.

The data is fitted with a two-body decay model

$$N(t) = N_0 / (1 + \tau / \tau_2) \quad , \quad (5.9)$$

where N_0 is the initial number of molecules and τ_2 is the expected decay time. The decay time obtained from the fit is $\tau_2 = 5.0(3)\ \text{ms}$, which is relatively short compared to other bi-alkali species (see Table. B.1).

5.3. Two-body Loss Rate Constant

With the temperature and decay time of the molecules, the two-body loss rate constant can be calculated by

$$K_0 = \frac{1}{\tau_2 \bar{n}} , \quad (5.10)$$

where \bar{n} is the average density of molecules. When the molecules are trapped in a harmonic trap, the \bar{n} is given by $\bar{n} = n(0)/2^{3/2}$, where $n(0)$ represents the peak density of the thermal cloud. For the Bose gas in a harmonic trap, the $n(0)$ is calculated to be

$$n(0) = \frac{1}{\lambda_T^3} g_{3/2}(\tilde{z}) , \quad (5.11)$$

where $\lambda_T = \sqrt{2\pi\hbar^2/mk_B T}$ is thermal wavelength, $g_{3/2}(z)$ is the Bose function, and $\tilde{z} = N_0(\frac{\omega\hbar}{k_B T})^3$ is the fugacity. In our case, the initial molecules number $N_0 = 4815(2306)$ and the trapping frequency for the ODT is $\omega = 343$ Hz. Then the peak density is calculated to be $n(0) = 1.49(74) \times 10^{12} \text{ cm}^{-3}$, thus the loss rate constant is $K_0 = 3.8(1.9) \times 10^{-10} \text{ cm}^3 \text{s}^{-1}$.

The theoretical prediction of K_0 is provided by [Julienne et al. \(2011\)](#). In this paper, the universal rate constant serves as an upper boundary, is calculated using the formulation with quantum defect theory (QDT) ([Idziaszek and Julienne, 2010](#); [Idziaszek et al., 2010](#)). Here, the "universal" implies that the elastic, inelastic, and reactive rates depend solely on the quantum scattering governed by the long-range potential at distances $R \gtrsim \bar{a}$. The \bar{a} is characteristic van der Waals length and given by

$$\bar{a} = \left[\frac{2\pi}{\Gamma(1/4)^2} \right] \left(\frac{2\mu C_6}{\hbar^2} \right)^{1/4} , \quad (5.12)$$

where $\Gamma(x)$ refers to the Gamma function, $\mu = \frac{m_{\text{Li}} + m_{\text{K}}}{2}$ is the reduced mass of the molecule, and C_6 is the isotropic van der Waals coefficient. For the polar molecules, the contributions of C_6 are from three aspects: the rotational dipole part C_6^{rot} , the transitions to electronically excited states C_6^{el} , and an interference between the first two contributions C_6^{inf} ([Quéméner et al., 2011](#)). A simple approximation is given by

$$C_6 \approx C_6^{\text{rot}} + C_6^{\text{el}} = \frac{d^4}{6B_0} + \frac{3}{4} U \alpha^2 , \quad (5.13)$$

where $d = 3.6$ Debye ([Aymar and Dulieu, 2005](#)) is the dipole moment, $B_0 = h \times 8.742(3)$ GHz is the rotational constant, $U \approx 0.055(7)$ in atomic units is the mean excitation energy, and $\alpha = 320.7$ in atomic units ([Deiglmayr et al., 2008b](#)) is the dipole polarizability. Additionally, more precise values for C_6 based on *ab initio* calculations ([Żuchowski et al., 2013; Lepers et al., 2013](#)) are available, which can be incorporated into the calculations.

Then for the identical bosonic samples, the theoretical predicted value of K_0 is given by

$$K_0 = \frac{8\pi\hbar}{\mu} \bar{a} \quad . \quad (5.14)$$

By substituting Eq. 5.12 and Eq. 5.13 into Eq. 5.14, the universal rate constant is calculated to be $K_0 = 7.9 \times 10^{-10}$ cm³s⁻¹, which closely matches the value obtained from the experiment. In addition to our measurement results, most observed loss rates for other species are smaller than the universal limit (see Table B.1), which could be attributed to specific orientations of the dipoles during the collision ([Gregory et al., 2019](#)).

5.4. Stark Shift Spectroscopy

5.4.1. Permanent Dipole Moment from Stark Shift Measurement

The dipole moment of the ground state is measured via the dc Stark shift in the presence of a high external dc electric field. The measured dipole moment is an induced dipole, whose magnitude depends on the strength of the external electric field. The fundamental role of the electric field is to mix the rotational states of the molecules, thereby breaking the parity symmetry. For molecules in a given rotational state without an external field, the orientation of the molecular axis cannot be fixed, resulting in an average electric dipole moment of 0. However, when the external field is applied, it couples rotational states of opposite parity, polarizing the molecules along the direction of the field. The interaction Hamiltonian can be expressed as $H = H_{\text{rot}} + H_{\text{stark}}$ in $|N, m_N\rangle$ basis. The first term, $H_{\text{rot}} = B_0 N(N+1) - D_0 N^2(N+1)^2$, represents the rotational energy in the absence of an electric field. Here, B_0 and D_0 are the rotational and centrifugal distortion constants of the molecule. The second term describes the Stark effect and is given by ([Brown and Carrington, 2003b; Ni, 2009](#))

$$\langle N', m_{N'} | H_{\text{stark}} | N, m_N \rangle = B_0 \cdot N(N+1) \delta_{NN', m_N m_{N'}} \\ -d_0 \cdot E \sqrt{(2N+1)(2N'+1)} \times (-1)^{m_N} \begin{pmatrix} N & 1 & N' \\ -m_N & 0 & m_{N'} \end{pmatrix} \begin{pmatrix} N & 1 & N' \\ 0 & 0 & 0 \end{pmatrix} , \quad (5.15)$$

where d_0 is the permanent dipole moment, E is the external electric field, and the Wigner 3-j symbols enforce selection rules. The Stark effect couples rotational states with the same m_J , but with opposite parities, as required by the triangle rule for the Wigner's 3-j symbols. When considering the Stark effect on rotational ground state molecules with $|N = 0, m_N = 0\rangle$, the interaction includes all rotational states $|N, m_N = 0\rangle$ permitted by the 3-j symbols. The primary contribution to the Stark effect comes from the $N' = 1$ state, typically, rotational states up to $N' < 6$ are included for sufficient accuracy ([Lam, 2016](#); [Ni, 2009](#)). In our calculation, states up to $N' = 11$ are considered to ensure precision. It is worth noting that, for the ground state of ${}^6\text{Li}{}^{40}\text{K}$, there is no orbital angular momentum or electronic spin. As a result, the total angular momentum (excluding nuclear spin) originates solely from the rotational quantum number N , while the hyperfine structure is neglected here.

Then the Stark shift of the ground state is measured by combining one-photon and two-photon spectroscopy ([Sofia, 2022](#); [Yang, 2021b](#)). The one-photon shift is determined by the Stark shift of the excited state $|A^1\Sigma^+, v' = 23, J' = 1, m_{J'} = -1\rangle$ using one-photon spectroscopy. For two-photon spectroscopy, the shift in the Stokes laser frequency at two-photon resonance reflects contributions from both the excited state and the ground state. By subtracting the Stark shift of the pump laser resonance frequency from the Stokes laser frequency shift, the Stark shift of the ground state can be obtained, as shown in Fig. 5.3.

For small electric fields, where the Stark interaction is much weaker compared to the rotational energy, the induced dipole moment increases linearly with the electric field (inset of Fig. 5.3). In this linear regime case the Stark shift can be well approximated by $\Delta E = -d_0^2 E^2 / (6B_0)$. From a fit to the data we obtained $d_0 = 3.1(3)$ D, which is 10% smaller than the expected dipole moment ([Aymar and Dulieu, 2005](#); [Dagdigian and Wharton, 2003](#)). We attribute this deviation to a systematic error in our determination of the electric field strength from a simulation of the electrode system (Section 5.4.2). We measured up to an

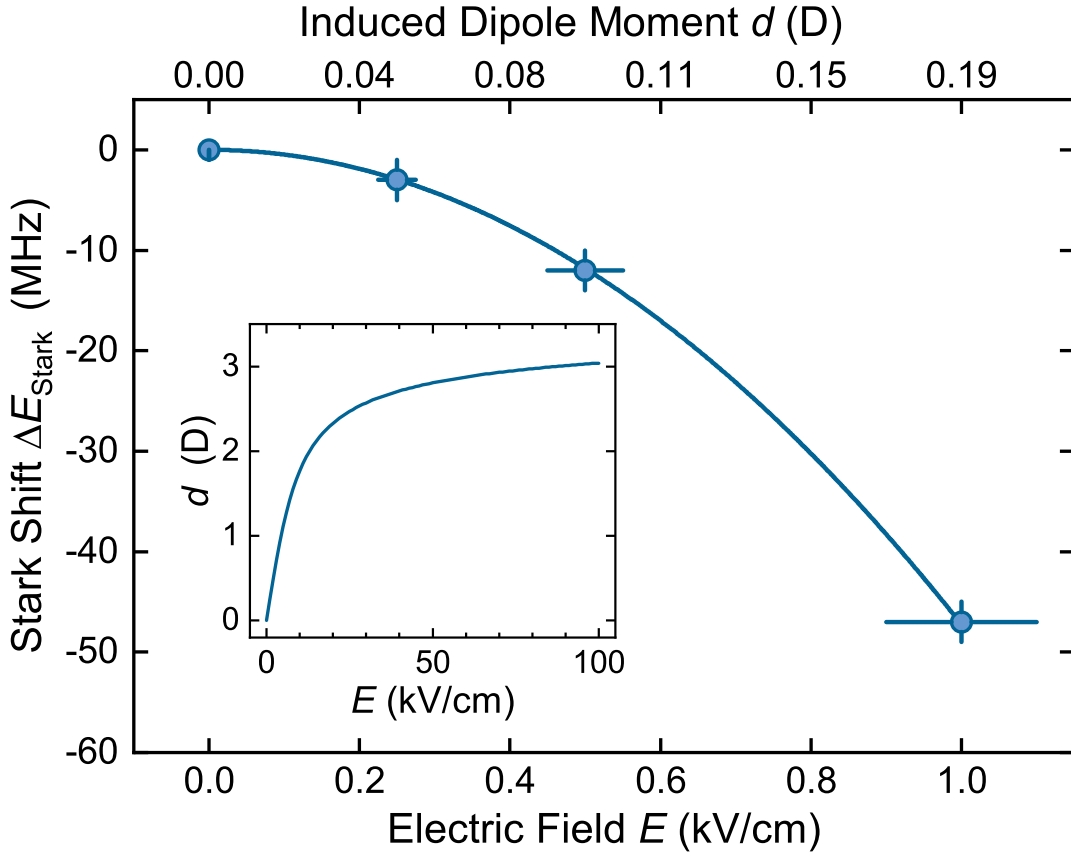


Figure 5.3.: Stark shift of the ro-vibrational ground state of ${}^6\text{Li}{}^{40}\text{K}$. The horizontal error bars represent a 10% systematic uncertainty in the electric field strength, which originates from the uncertainty of the position of the trap center relative to the electrode assembly. The inset shows the theoretically predicted value for the induced dipole moment d extending to higher electric fields. Figure is taken from [He et al. \(2024\)](#)

electric field of 1 kV/cm, and inferred an induced dipole moment of $d = 0.19(4)$ D from the fitted curve. With our high-voltage electrode setup, a dc-electric field up to 10 kV/cm can be generated at the trap center, corresponding to an induced dipole moment of ≈ 1.8 D. However, achieving the full dipole moment of $d_0 = 3.6$ D would require an electric field $E > 100$ kV/cm, which exceeds the capability of our current setup. Reaching such a high dipole moment would rely on microwave transitions (Section 5.5).

5.4.2. Simulation of Electric Field

The electric field discussed in the previous section is generated using a system of four independent electrodes inside the vacuum chamber. The details of the setup have been previously described in ([Lam, 2016](#)), and a basic schematic of the setup is shown in in Fig. 5.4.

In this work, the electric field along Feshbach magnetic field direction (z-direction) has been

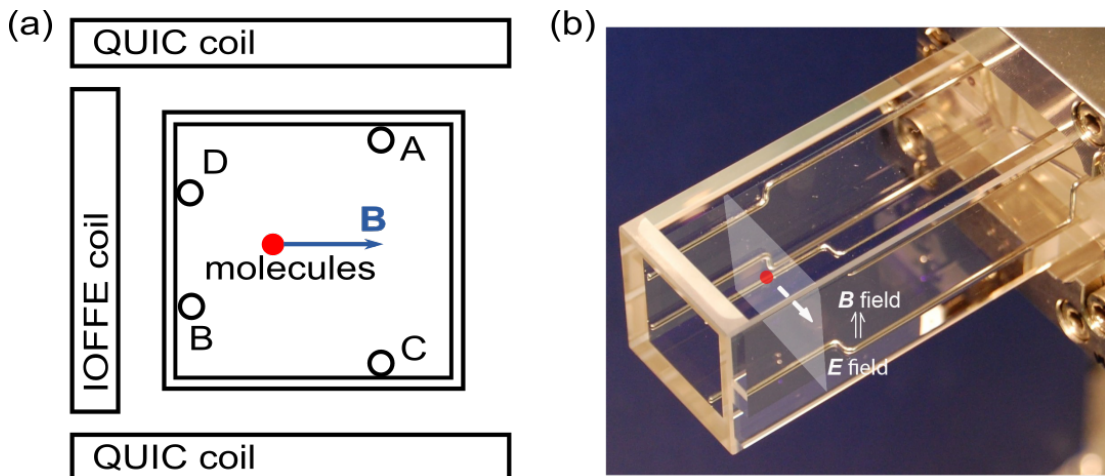


Figure 5.4.: (a) Scheme of the high-voltage electrode setup in UHV chamber. A, B, C, D represent four independent electrodes.(b) Photograph of the high-voltage electrode setup within UHV chamber. To compensate for the finite length of the electrodes near the edges of the vacuum cell, the rods were bent in a tapered fashion to reduce gradients of the electric field. By independently controlling the voltages on the four electrodes, the electric field at the position of the molecules (indicated by the red circle) can be rotated within the specified plane.

simulated using finite element analysis with the CST Studio Suite software. To generate a electric field $E = 5.0 \text{ kV/cm}$ at the intended trapping center, the voltages applied to the four electrodes (D, B, A, C) are set to $(-0.15 \text{ kV}, -2.8 \text{ kV}, -10.8 \text{ kV}, -20.0 \text{ kV})$, respectively. The simulation results of the electric field strength are presented in Fig. 5.5.

All four electrode potentials are carefully adjusted to achieve the desired electric field strength and direction while minimizing field gradients at the intended trap center. The resulting electric field gradients are shown in Fig. 5.6. At the trap center, the gradients are extracted to be $\frac{\partial E_z}{\partial z} = -0.23 \text{ kV/cm}^2$, $\frac{\partial E_z}{\partial y} = 0.72 \text{ kV/cm}^2$, $\frac{\partial E_y}{\partial z} = 0.71 \text{ kV/cm}^2$, and $\frac{\partial E_y}{\partial y} = 0.69 \text{ kV/cm}^2$. However, due to the experimental uncertainty of the trap center relative to the electrodes, as well as the influence of conducting elements within the vacuum and trapping assemblies, a deviation of approximately 10% in the applied electric field from our simulation is expected. This deviation is believed to be the primary source of the discrepancy between the measured permanent electric dipole moment and its expected value.

5.5. MW Transition

Apart from using the external electric filed, another method used to polarize the rovibrational ground state molecules involves applying MW signals to drive rotational transitions. MW signals also enable full control over hyperfine degrees of freedom, serving as a tool for precision

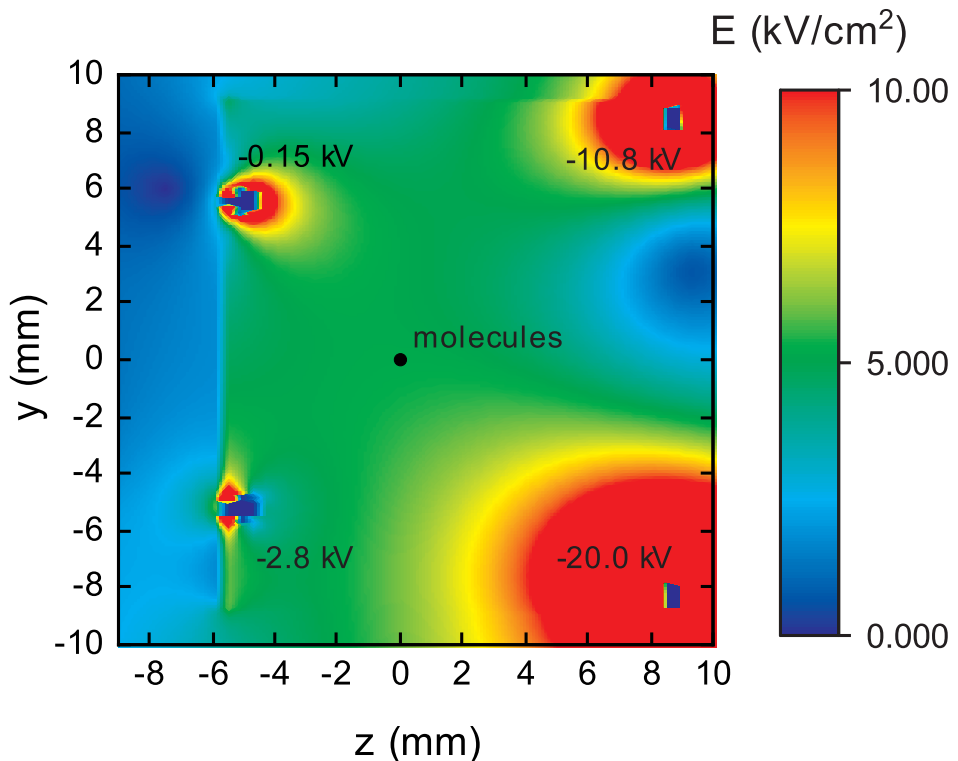


Figure 5.5.: Simulation of the electric field in the plane of the trapped molecules is shown. The electric field is generated by four electrodes, with the simulation performed using the finite element analysis method in CST. The black circle indicates the location of the molecular cloud.

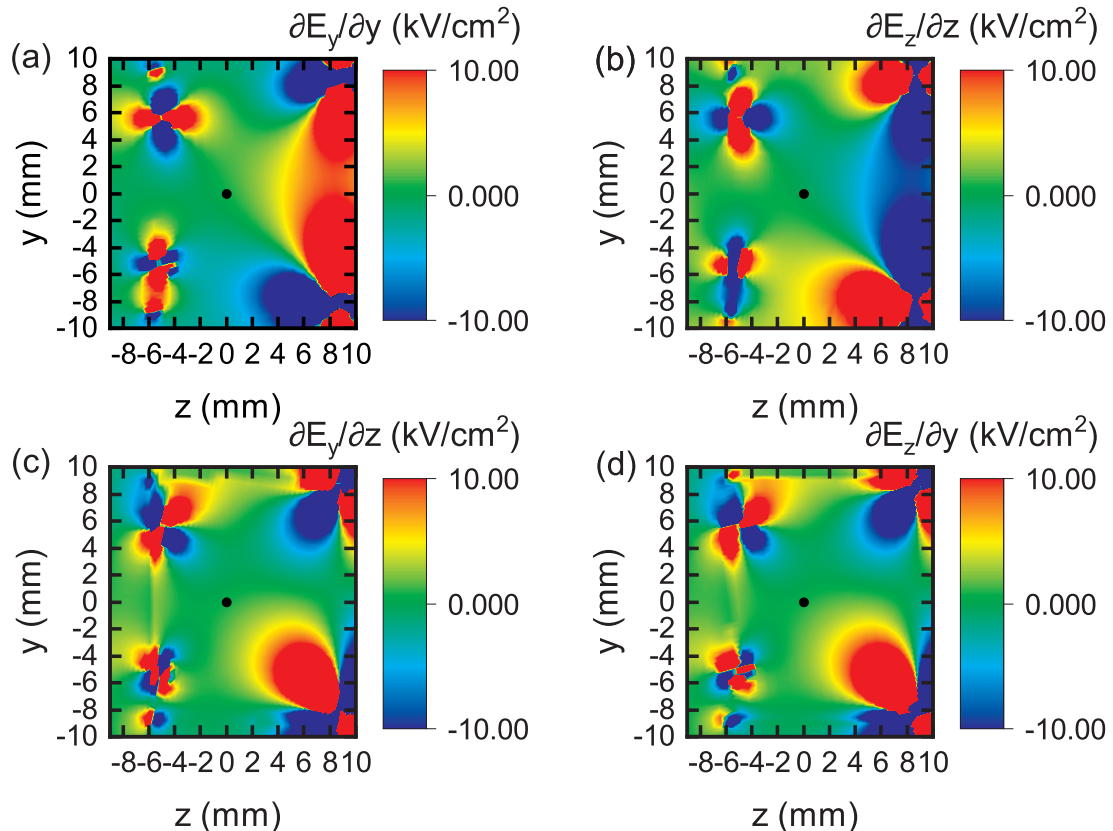


Figure 5.6.: Simulation of the electric field gradient is shown. The voltage of the four electrodes has been adjusted to minimize the electric field gradient at the position of the molecular cloud. The black circle indicates the location of the molecular cloud.

measurements (Andreev et al., 2018) and quantum computation (Picard et al., 2024). For bi-alkali molecules, MW control over rotational and hyperfine degrees of freedom has been demonstrated in systems such as $^{40}\text{K}^{87}\text{Rb}$ (Ospelkaus et al., 2010a), $^{87}\text{Rb}^{133}\text{Cs}$ (Gregory et al., 2016), $^{23}\text{Na}^{40}\text{K}$ (Will et al., 2016), $^{23}\text{Na}^{87}\text{Rb}$ (Guo et al., 2018b), $^{23}\text{Na}^{133}\text{Cs}$ (Stevenson et al., 2023). This section introduces the initial attempt to drive MW transitions with $^6\text{Li}^{40}\text{K}$ and explains the reasons for the short coherence time. In addition, an outlook on the application of MW shielding to suppress two-body inelastic collisions is provided in Section 5.5.5.

5.5.1. Molecular Hamiltonian

In Section 5.4.2, the rotational energy under an external electric field has been discussed without accounting for the presence of a magnetic field or nuclear spin. When an external magnetic field is applied, the nuclear spins experience a Zeeman effect, leading to $(2N + 1)(2I_{\text{Li}} + 1)(2I_{\text{K}} + 1)$ hyperfine levels, where $I_{\text{Li},\text{K}}$ represents the nuclear spin. Then the full Hamiltonian for $\text{X}^1\Sigma^+ |v'' = 0\rangle$ state can be written as (Aldegunde et al., 2008; Brown and Carrington, 2003b)

$$H = H_{\text{rot}} + H_{\text{strak}} + H_{\text{ZM}} + H_{\text{hf}} \quad , \quad (5.16)$$

where H_{rot} and H_{strak} are the rotational energy term and Stark effect term. H_{ZM} represents the Zeeman splitting can be expressed as

$$H_{\text{ZM}} = -g_r\mu_N \mathbf{N} \cdot \mathbf{B} - \sum_i^{\text{Li,K}} g_i(1 - \sigma_i)\mu_N \mathbf{I}_i \cdot \mathbf{B} \quad , \quad (5.17)$$

where g_r is the rotational g -factor, μ_N is the nuclear magneton, g_i is the nuclear g -factor, σ_i is the nuclear shielding tensors, and \mathbf{B} represents the magnetic field. The hyperfine interaction term H_{hf} is

$$H_{\text{hf}} = \sum_i^{\text{Li,K}} \mathbf{V}_i \mathbf{Q}_i + \sum_i^{\text{Li,K}} c_i \mathbf{N} \cdot \mathbf{I}_i + c_3 \mathbf{I}_{\text{Li}} \cdot \mathbf{T} \cdot \mathbf{I}_{\text{K}} + c_4 \mathbf{I}_{\text{Li}} \cdot \mathbf{I}_{\text{K}} \quad , \quad (5.18)$$

where the first term is the electric quadrupole interaction associated with quadrupole coupling constant $(eqQ)_i$ and dominates for $N'' = 1$. c_i is the spin-rotation coupling constant for two nuclei, and c_3 and c_4 are spin-spin coupling constant. Table. 5.1 shows the predicted value for the parameter relative to H_{ZM} and H_{hf} . Due to the hyperfine coupling interactions,

Constant	Value	Constant	Value
$(eqQ)_{\text{Li}}$	400 Hz	c_3	-28.7 Hz
$(eqQ)_{\text{K}}$	1.066 MHz	c_4	-72.8 Hz
c_{Li}	48.2 Hz	$g_{\text{Li}}(1 - \sigma_{\text{Li}})$	0.8219
c_{K}	-295.5 Hz	$g_{\text{K}}(1 - \sigma_{\text{K}})$	-0.3236
g_r	0.0386	B_0	$h \times 8.742(3)$ GHz

Table 5.1.: The Coupling constants in Equation 5.17 and Equation 5.18 for $v = 0$ ${}^6\text{Li}{}^{40}\text{K}$ molecules are presented. B_0 is extracted from this work, while other values are taken from [Aldegunde and Hutson \(2017\)](#); [Brooks et al. \(1964\)](#).

the eigenstates of the system are superposition of the bare states $|N, m_N, m_{I,\text{Li}}, m_{I,\text{K}}\rangle$. The fully-resolved hyperfine structures have been measured by our group during the writing of this thesis, and the results will be published in the future. Here, the initial attempt at MW spectroscopy provides a preliminary understanding of the MW setups and procedures for operating the MW signals. Additionally, the transition frequencies for a few unresolved hyperfine structures are located with an accuracy of sub-MHz. This preliminary work facilitates the identification of all hyperfine structures in the vicinity.

5.5.2. Prediction of N=1 Transition Frequency

The target transition is from the rotational ground state to the first rotationally excited state, $|v'' = 0, N'' = 0\rangle \rightarrow |v'' = 0, N'' = 1\rangle$. The calculation of the MW transition frequency is based on the two-photon spectroscopy of the rotational ground state $\text{X}^1\Sigma^+ |v'' = 0, N'' = 0\rangle$ (Section 4.1.2) and second rotationally excited state $\text{X}^1\Sigma^+ |v'' = 0, N'' = 2\rangle$ ([Yang et al., 2020](#)). As shown in Fig. 5.7, the separation between the two resonance signal, $N'' = 0$ and $N'' = 2$ is 52.452 GHz. The $N'' = 1$ resonance signal is not observable due to the electric dipole selection rule $\Delta N = \pm 1$ when the intermediate state is $\text{A}^1\Sigma^+ |v' = 23, N' = 1\rangle$. The rotational energy term $H_{\text{rot}} = B_0 N''(N'' + 1) - D_0 N''^2(N'' + 1)^2$ can be approximated to be $H_{\text{rot}} \approx B_0 N''(N'' + 1)$ as the centrifugal distortion constant term D_0 (kHz level) is much smaller than the rotational constant term B_0 (GHz level). Using the separation between $N'' = 0$ and $N'' = 2$, the rotational constant is calculated to be $B_0 = h \times 8.742(3)$ GHz, which agrees well with results reported in [Bednarska et al. \(1996\)](#). Consequently, the separation between $N'' = 0$ and $N'' = 1$ is predicted to be 17.484(6) GHz.

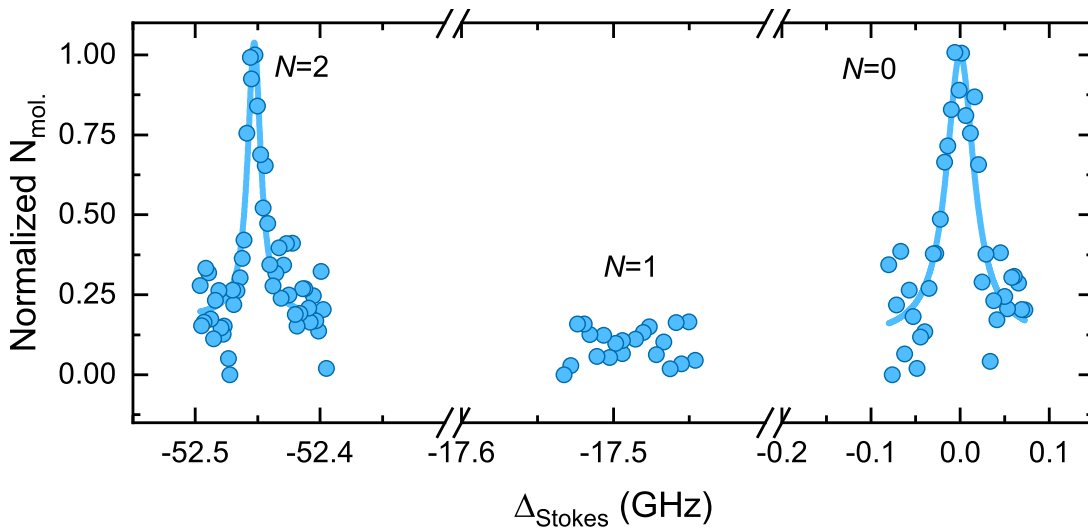


Figure 5.7.:]

The two-photon ground state spectroscopy including the second rotationally excited state.

The resonance at $N'' = 1$ is invalid due to the selection rule of $\Delta N = \pm 1$. Results and figures taken from [Yang et al. \(2020\)](#).

5.5.3. MW Spectroscopy

The MW setups are designed and detailed in Section 3.6 of a previous PhD thesis of our group ([Sofia, 2022](#)) and a bit more discussions are presented here. Fig. 5.8 (a) illustrates the scheme for MW generation. The MW signal is generated by mixing a ~ 100 MHZ RF signal from a FlexDDS signal generator (Wieserlabs) with a fixed 17.3785 GHz MW signal from low-noise synthesizer (Systron Donner 1720). The final output frequency can be tuned by adjusting the RF signal frequency. The MW source also provides 6.8 GHz signal used during the evaporative cooling process of ^{87}Rb at the beginning of the experimental sequence. A fast double throw switch (Pasternack PE71S6241) allows the switching between these two applications. The integrated phase noise ϕ_{RMS} of the MW signals at 17.5 GHz is measured to be less than 10 mrad within the 1 kHz-100 kHz frequency range, showing the low phase noise performance. A pre-amplifier (Mini Circuits, ZX60-183-S+) combined with a Variable Voltage Attenuator (VVA) (Pasternack, PE70A2900) is used to fully saturate a 3 W water water-cooled amplifier (Mini Circuits, ZVE-3W-183+). The amplified signal, with a power of approximately 30 dBm, is sent to the gain horn antenna (Pasternack, PE9853A-20) (Fig. 5.8 (b)). Along the signal path, a directional coupler (Pasternack, PE2207-30) is inserted to monitor the output signal, and a single junction circulator (Pasternack, PE8405) offers 20 dB isolation to prevent back reflection from the antenna. The antenna is placed outside the UHV

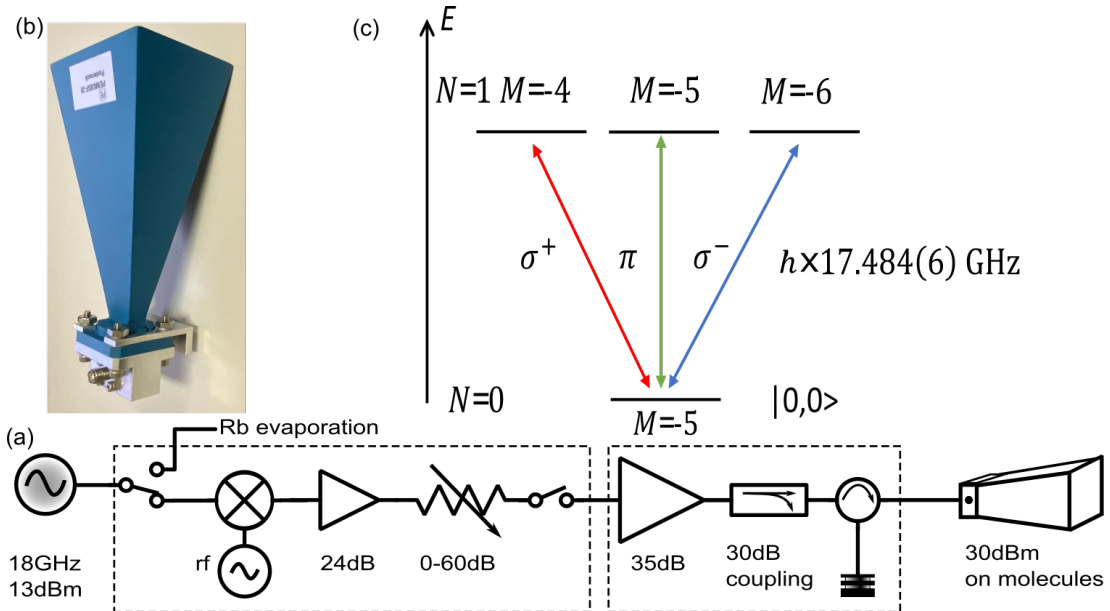


Figure 5.8.: (a) The schematic of the MW setup. The MW source generates the MW signal for both evaporative cooling and ground state rotational transition. (b) A horn antenna used to generate the MW signal. The polarization control of the is antenna limited, as testing revealed that the emitted polarization is always a mix. This antenna has been updated in subsequent experiments to improve performance. (c) The coupling between rotational ground state $N'' = 0$ and rotationally excited state $N'' = 1$. The total projection quantum number $M = m_N + m_{I,\text{Li}} + m_{I,\text{K}}$ is taken into account due to hyperfine coupling interactions. Figure (a) is taken from [Sofia \(2022\)](#).

chamber approximately 10 cm away from the molecules. Its orientation can be adjusted to be either perpendicular or parallel to the Feshbach magnetic field, enabling the drive of σ^\pm or π transitions.

With the known value of B_0 and predicted transition frequency of 17.484(6) GHz for the $N'' = 0 \rightarrow N'' = 1$ transition, the MW spectroscopy is performed to locate the transition frequencies for different hyperfine levels. A square pulse of MW signal is used to drive the two-level Rabi oscillation. The pulse duration is set to be 650 μs to ensure that the system reaches full decoherence. The results are shown in Fig. 5.9 with a 50 kHz frequency scanning step. The deep appears in the experimental data indicates that the ground state molecules are driven to the rotationally excited state and subsequently mixed with the ground state due to decoherence, resulting in a reduced number of ground state at these frequencies. Three MW transition frequencies are identified within the spectroscopy scanning range at 17.47930 GHz for a σ^+ transition, 17.47945 GHz for a σ^- transition, and 17.47975 GHz for a π transition.

By fixing the MW frequencies at the identified transitions, the pulse duration is scanned to independently extract the coherence time for each transition. The results are shown in Fig. 5.10. The coherence time extracted from the measurements is $\tau = 4(3) \mu\text{s}$ for the σ^+

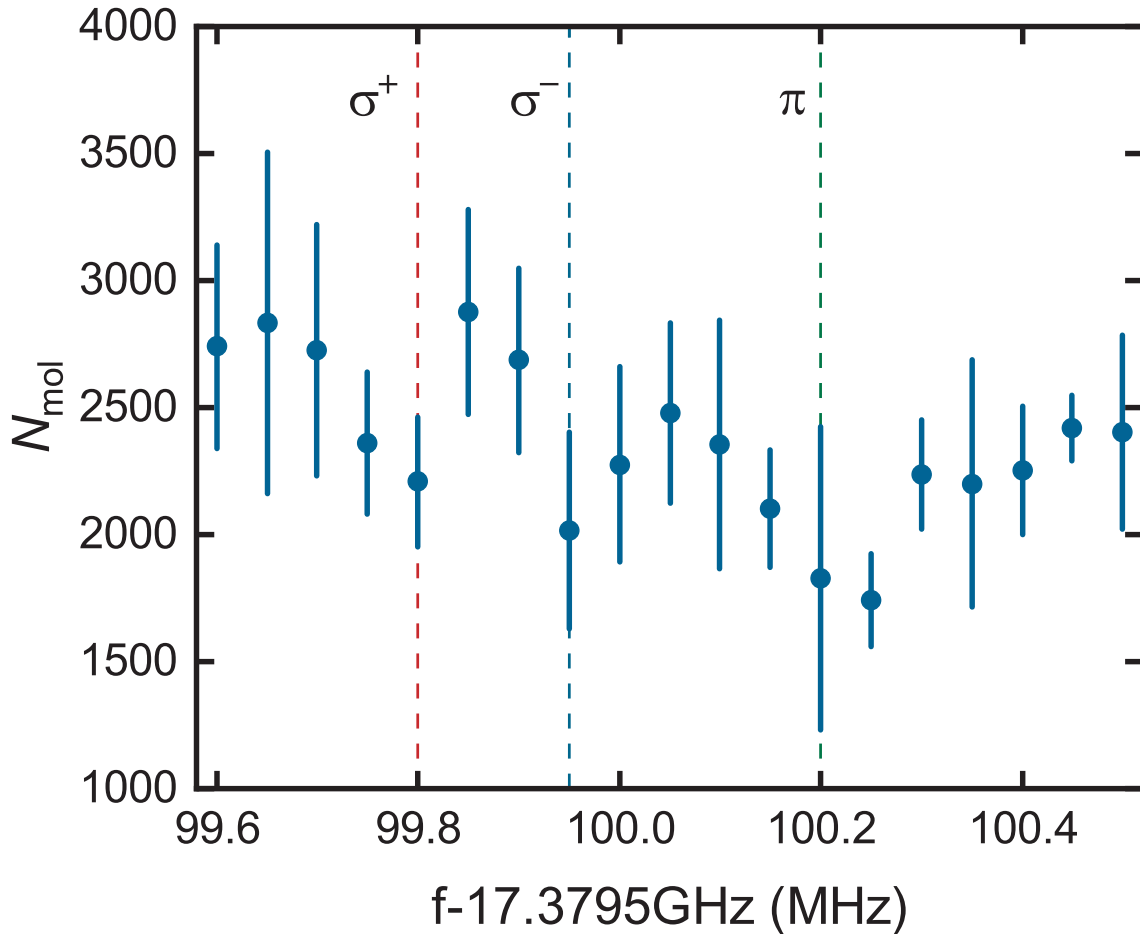


Figure 5.9.: MW spectroscopy for $N'' = 0$ to $N'' = 1$ transitions. Three transitions correspond to σ^+ , σ^- , and π transitions are observed. However, at this stage, the full understanding of the hyperfine structure has not been achieved yet. So the exact hyperfine components are not labeled. Also, the measurement is conducted in the ODT trap, where the ac Stark effect can mix the hyperfine structures. The primary goal of this measurement is to locate the transition frequencies with sub-MHz precision.

transition, $\tau = 11(4)\mu\text{s}$ for the σ^- transition, and $\tau = 5(1)\mu\text{s}$ for the π transition. The coherence time is too short to complete even one oscillation period, which is insufficient for inducing the desired DDI. A more detailed discussion on this issue is provided in the following section.

5.5.4. Discussion

There are two main reasons lead to this short coherence time. The first cause is related to the design of the MW setup. In the current setup, the polarization of the MW signal cannot be fully controlled. For a fixed transition frequency, polarization impurities can lead to accidental near-resonant dressing with other hyperfine levels, resulting in decoherence of the two-level system. This can be mitigated by implementing mechanical phase shifters and

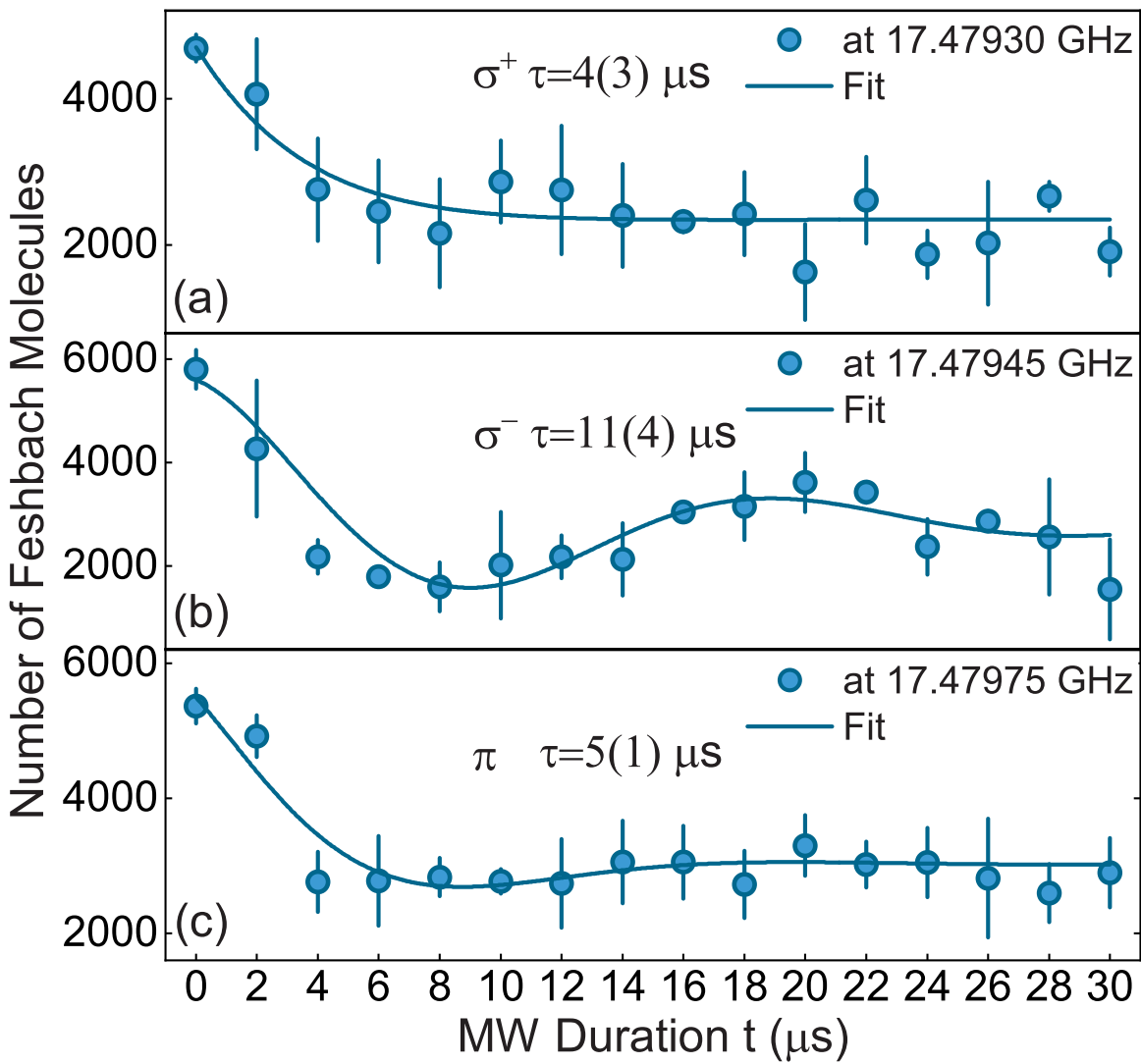


Figure 5.10.: Coherent population transfer for (a) σ^+ , (b) σ^- , and (c) π transitions. The MW signal is fixed at the resonant frequency and the coherence time is calculated for each transition.

specially designed antennas, such as helical antennas (Anderegg et al., 2021; Lin et al., 2023; Schindewolf et al., 2022).

Another significant factor is the difference in ac polarizability α between the rotational ground state and the rotationally excited state. This effect was first explored by Neyenhuis et al. (2012) for the ground state $^{40}\text{K}^{87}\text{Rb}$ molecules. The energy perturbation experienced by molecules with polarizability α in a light trap with intensity I is expressed as αI . For the rotational ground state $N'' = 0$ with spherical symmetry, the polarizability α does not depend on the relative orientation of the laser polarization and the quantization axis. The polarizability is given by

$$\alpha^0 = \frac{1}{3}(\alpha_{\parallel} + 2\alpha_{\perp}) \quad , \quad (5.19)$$

where α_{\parallel} and α_{\perp} represent the parallel and perpendicular polarizabilities respect to the internuclear axis, which are wavelength dependent. For the rotationally excited state $N'' = 1$, the spherical symmetric is broken, and the relative orientation is defined. The polarizability of the rotationally excited state at an angel θ to the internuclear axis is given by ([Gregory et al., 2017](#))

$$\alpha(\theta) = \alpha_{\parallel} \cos^2 \theta + \alpha_{\perp} \sin^2 \theta \quad . \quad (5.20)$$

As a result, molecules in the rotational ground state and excited states experience different polarizability in a light trap, resulting in a differential energy shift of $(\alpha(\theta) - \alpha^0)I$. This energy shift between $N'' = 0$ and $N'' = 1$, which creates frequency shift for the MW transition. The frequency shift depends on the orientation angle θ and the trap intensity I . Moreover, as shown in Fig. 4.6, the intensity of the ODT beam varies spatially due to its Gaussian distribution. Since the size of the molecular cloud is comparable to the waist of the ODT beams, the detuning of the transition frequency varies across the molecules cloud, contributing to decoherence in the two-level system. By considering both polarization mismatch and spatially varying energy shifts ΔE over the molecular cloud, the coherence time of the systems can be expressed as ([Neyenhuis et al., 2012](#))

$$\tau = 1/\sqrt{(1/T_2)^2 + \left(\frac{\partial E_{N''=1}/\partial I - \partial E_{N''=0}/\partial I}{\partial E_{N''=0}/\partial I}\Delta E/\hbar\right)^2} \quad , \quad (5.21)$$

where T_2 is the coherence time excluding the effect of the polarizability. $\partial E_{N''=1}/\partial I$ and $\partial E_{N''=0}/\partial I$ are the "local polarizability" at a given intensity for rotational ground and excited state. A special case occurs when $\alpha(\theta) = \alpha^0$, which can be achieved by tuning either the wavelength of light or the orientation angle θ , meaning that the differential energy shift is zero and independent on trap intensity I . Then the coherence time can be extended due to $\Delta E = 0$. This is called "magic" condition and will be implemented in our future setups to improve coherence time. Another possible strategy is to drive the MW transition during TOF instead of within the ODT. In this case, the energy perturbation is eliminated because the trap intensity $I = 0$.

In summary, the first attempt for driving MW transition from the ground state to rotationally excited state provides a foundational understanding of the setups and procedures to achieve the MW spectroscopy. Several unresolved hyperfine levels are observed, and their corresponding coherence times are measured. However, the low resolution of the spectroscopy requires the technology improvements in the generation of the MW signals to reduce polarization impurities. Additionally, the short coherence time emphasizes the necessity of implementing alternative trapping strategies, such as the applying "magic" condition or driving transition in TOF, to extend the coherence time.

5.5.5. Outlook

Once the full control over the rotational states and long coherence time are achieved, an immediate prospect is to apply MW shielding to suppress the two-body inelastic collision, which can substantially extend the lifetime of the ground state molecules (Anderegg et al., 2021; Bigagli et al., 2023a; Deng et al., 2023; Karman and Hutson, 2018, 2019; Karman et al., 2022; Lin et al., 2023). The basic principle of MW shielding involves coupling molecules to a dressed state. In the internal-state Hilbert space, the Hamiltonian of the molecular rotational states coupled with σ^+ MW signal is given by (Deng et al., 2023)

$$H_{\text{MW}} = \frac{\hbar\Omega}{2} e^{-i\omega_0 t} |1, 1\rangle \langle 0, 0| , \quad (5.22)$$

where Ω represents the Rabi frequency of the MW signal and ω_0 represents the MW frequency. When only considering the rotational energy term, the total energy of the internal-state is

$$H_{\text{in}} = H_{\text{MW}} + H_{\text{rot}} . \quad (5.23)$$

one eigenstate of H_{in} is $|+\rangle \equiv u|0, 0\rangle + v|1, 1\rangle$, where $u = \sqrt{(1 - \Delta/\Omega_{\text{eff}})/2}$ and $v = \sqrt{(1 + \Delta/\Omega_{\text{eff}})/2}$ with Δ being the detuning of the MW frequency and $\Omega_{\text{eff}} = \sqrt{\Delta^2 + \Omega^2}$. Two molecules in the state $|+\rangle$ interact through DDI with a repulsive potential. The potential of the two dressed state molecules, $|+, +\rangle$, can be given by an approximate expression (Deng et al., 2023)

$$V_{\text{dd}} = \frac{C_3}{r^3} P_2(\cos \theta) + \frac{C_6}{r^6} A(\theta) , \quad (5.24)$$

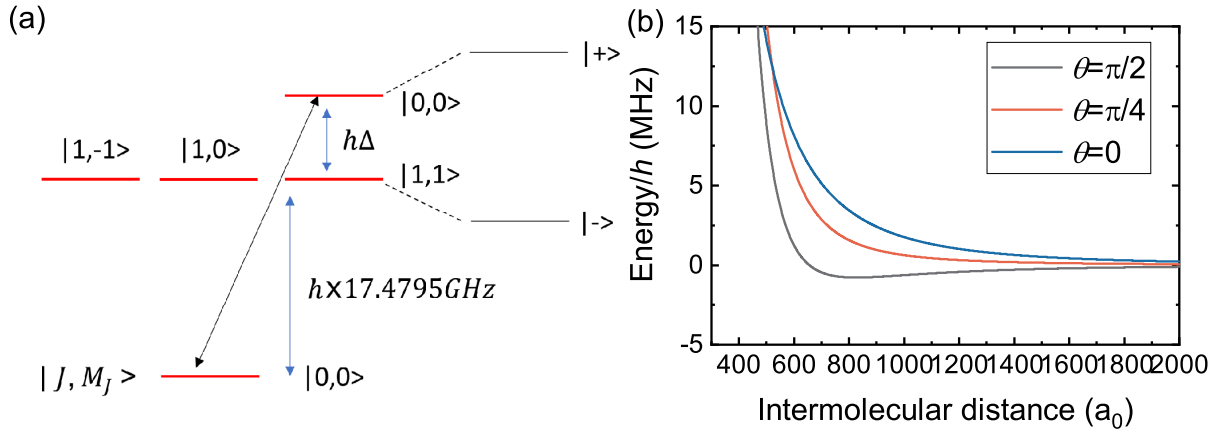


Figure 5.11.: (a) Schematic representation of the MW dressed ${}^6\text{Li}{}^{40}\text{K}$ level structure. (b) Interaction potentials between two MW shielded ${}^6\text{Li}{}^{40}\text{K}$ ground state molecules. The black, red, and blue lines represent $\theta = \pi/2$, $\theta = \pi/4$, and $\theta = 0$, respectively. For this plot, the MW detuning Δ is fixed at $2\pi \times 5\text{ MHz}$, and the Rabi frequency Ω is set to $2\pi \times 10\text{ MHz}$.

where $P_l(\cos \theta)$ is the Legendre polynomial, $A(\theta) = 7 - 5P_2(\cos \theta) - 2P_4(\cos \theta)$, and

$$C_3 = d^2/[24\pi\epsilon_0(1 + \delta_r^2)] \quad C_6 = d^4/[1120\pi^2\epsilon_0^2\Omega(1 + \delta_r^2)^{3/2}] \quad , \quad (5.25)$$

with $\delta_r = \Delta/\Omega$. θ is the angle between the rotation axis of the induced dipole and the intermolecular axis. The approximation of C_6 is valid when $\Omega > d_0^2/(4\pi\epsilon_0 r^3)$. A level schematic of the dressed state shielded with MW is shown in Fig. 5.11 (a). For ${}^6\text{Li}{}^{40}\text{K}$ ground state molecules, the potentials for different angle θ are presented in Fig. 5.11 (b). And the θ can be interpreted as the angle between the molecular collision axis and the propagation direction of the MW signal, with $\theta = 0$ indicating parallel alignment and $\theta = \pi/2$ indicating orthogonal alignment. By generating a repulsive potential, the MW shielding prevents molecules from approaching each other too closely, thereby suppressing collisional losses and extending the molecular lifetime.

6. Exploration of a 3D Lattice

In this chapter, the construction and alignment of a free-space optical lattice are described. Then, the implementation of the lattice is verified through the observation of atoms and the phase transition between the superfluid and Mott-insulator. Moreover, loading of ^{87}Rb and ^{40}K is investigated by the method of band mapping. Additionally, Kapitza-Dirac scattering is used to calibrate the trap depth of the lattice. Finally, Feshbach association of $^6\text{Li}^{40}\text{K}$ in the lattice is discussed.

6.1. 3D Lattice Implementation

The optical setup for implementing the free-space 3D lattice has been shown in Section 3.4. One key challenge in constructing the lattice is to properly overlap the retroreflected beams with their forward counterparts. Due to limitations of the lattice and imaging beam configurations, for each pair of forward and retroreflected beams, only one of them can be aligned using the in-situ imaging by our camera. To address this issue, additional fibers are incorporated into the setup to assist with alignment, as illustrated in Fig. 6.1. The alignment process for the lattice setup along the z-direction is described as follows. The forward beam (red arrow) is aligned on the atomic cloud of ^{87}Rb with the help of the CCD camera and coupled into alignment fiber 1. Then an alignment beam (brown arrow) is sent out through alignment fiber 2, aligned on the atomic cloud, and coupled into alignment fiber 1. This step ensures that the alignment beam precisely overlaps with the forward lattice beam. Finally, the retro-mirror is adjusted so that the retroreflected beam (blue arrow) is coupled into alignment fiber 2. This step ensures proper overlap between the forward and retroreflected beams. This alignment strategy applies to the lattice beams for the other 2 axes as well.

As discussed in Section 3.1 and shown in Fig. 4.8, after evaporative cooling, atoms are loaded into the ODT for Feshbach association and STIRAP transfer. To load the atoms into

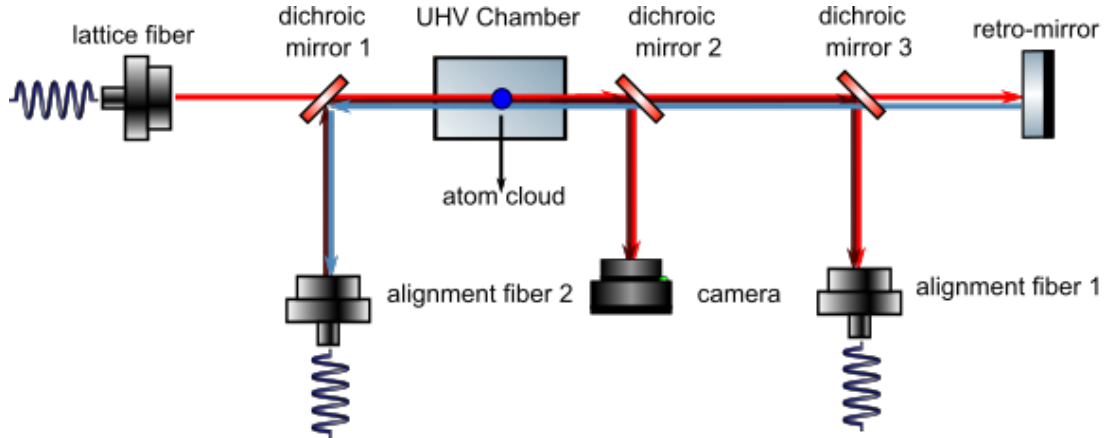


Figure 6.1.: Illustration of aligning lattice beam using alignment fibers. The design aims to ensure precise overlap of the forward and retroreflected beams, addressing the limitation that the camera can only provide a reference for one direction of the beams. The lattice along z-direction is shown as an example.

the optical lattice, we adiabatically ramp up the power of the lattice beams while ramping down the current in the QUIC coils. The waveform profile for ramping up the lattice beam power follows the same waveform used for the ODT beams. To prevent the population transfer from the ground band to higher energy bands, the lattice should be switched on slowly enough. Here, the adiabaticity criterion for non interacting gas is given by ([Ben Dahan et al., 1996](#))

$$|\langle n, q | d/dt | 0, q \rangle| \ll |E_n^q - E_0^q|/\hbar \quad , \quad (6.1)$$

which applies to the transfer process from the lowest into the n -th energy band. Here, $|n, q\rangle$ is the bloch wave with momentum q in the n -th band. When considering the population transfer from the 0th band to the 1st band, the energy difference is $E_1^0 - E_0^0 \approx 4E_r$ for a shallow lattice potential. This corresponds to the initial stage where the lattice has just been switched on. And the Equation 6.1 can be rewritten as ([Ben Dahan et al., 1996](#))

$$\frac{d}{dt} V_0/E_r \ll 32\sqrt{2}E_r/\hbar \quad , \quad (6.2)$$

at $q = 0$. For a deep lattice potential, the energy gap $E_1^0 - E_0^0$ increases as discussed in Section 2.3.2 and the adiabaticity can be achieved easily. Therefore, the ramping pulse during the initial stage of switching on the lattice must be carefully designed based on Eq. 6.2.

After ramping down the QUIC trap, the atomic cloud can be held in a pure optical lattice potential given enough trapping power. To confirm the presence of the optical lattice, rather

than atoms being simply trapped by the ODT effect with the forward beams, we follow the approach described in [Greiner \(2003\)](#); [Greiner et al. \(2002\)](#), which demonstrated the superfluid to Mott-insulator phase transition in a 3D optical lattice with a pure ^{87}Rb BEC. Additionally, the phase transition in a 2D lattice has been theoretically investigated by [Gangardt et al. \(2006\)](#). In our experiments, we focus on a 2D optical lattice with standing waves along x- and y-directions. The results are shown in Fig. 6.2 (a) and (b). The images are taken along side axial (z-direction) and the lattice power is set to 32 mW for the y-direction and 23 mW for the x-direction.

The observation of the superfluid phase requires a low trap depth, which delocalizes the atoms over the lattice. Increasing the trap depth localizes the atoms at individual lattice sites, forming the Mott-insulator phase. The phase transition from superfluid to Mott-insulator in a 2D lattice is shown in Fig. 6.2 (c) and (d). As the interference pattern in momentum space disappears when the lattice x power is increased from 40 mW to 60 mW. The corresponding pulse sequences are illustrated in Fig. 6.2 (e). To extend the holding time of atoms in the low trap depth, the QUIC trap remains switched on to provide additional confinement against gravity. The lattice beams are adiabatically ramped up at time t_0 . At time t_1 , both QUIC trap and lattice are rapidly switched off by the AOMs within 100 ns. After 10 ms TOF, images of the atomic cloud are taken.

By observing the phase transition from superfluid to Mott-insulator, the formation of the lattice along each direction is confirmed. Another important aspect is determining the population distribution of atoms in different bands of the lattice, which can be measured by analyzing the momentum distribution after switching off the lattice. This procedure follows [Neyenhuis \(2012\)](#), and the results for loading ^{87}Rb and ^{40}K atoms are shown in Fig. 6.3 (a) and (b), with the corresponding pulse sequence illustrated in (c). In Fig. 6.3 (a), the ^{87}Rb atoms are first cooled down to BEC and then adiabatically loaded into the 3D optical lattice. The power of the lattice beams is set to 600 mW for each direction. Then the momentum distribution is measured in free-space after 10 ms TOF, with most of the population mapped onto the first Brillouin zone. Note that the QUIC trap is switched off earlier than the lattice, ensuring that the phase coherence of the Rb BEC is destroyed by gravity, regardless of whether the lattice trap depth is deep or shallow. This dephasing process ensures that the Rb atoms are homogeneously distributed in the 0th band. Subsequently, the lattice is adiabatically

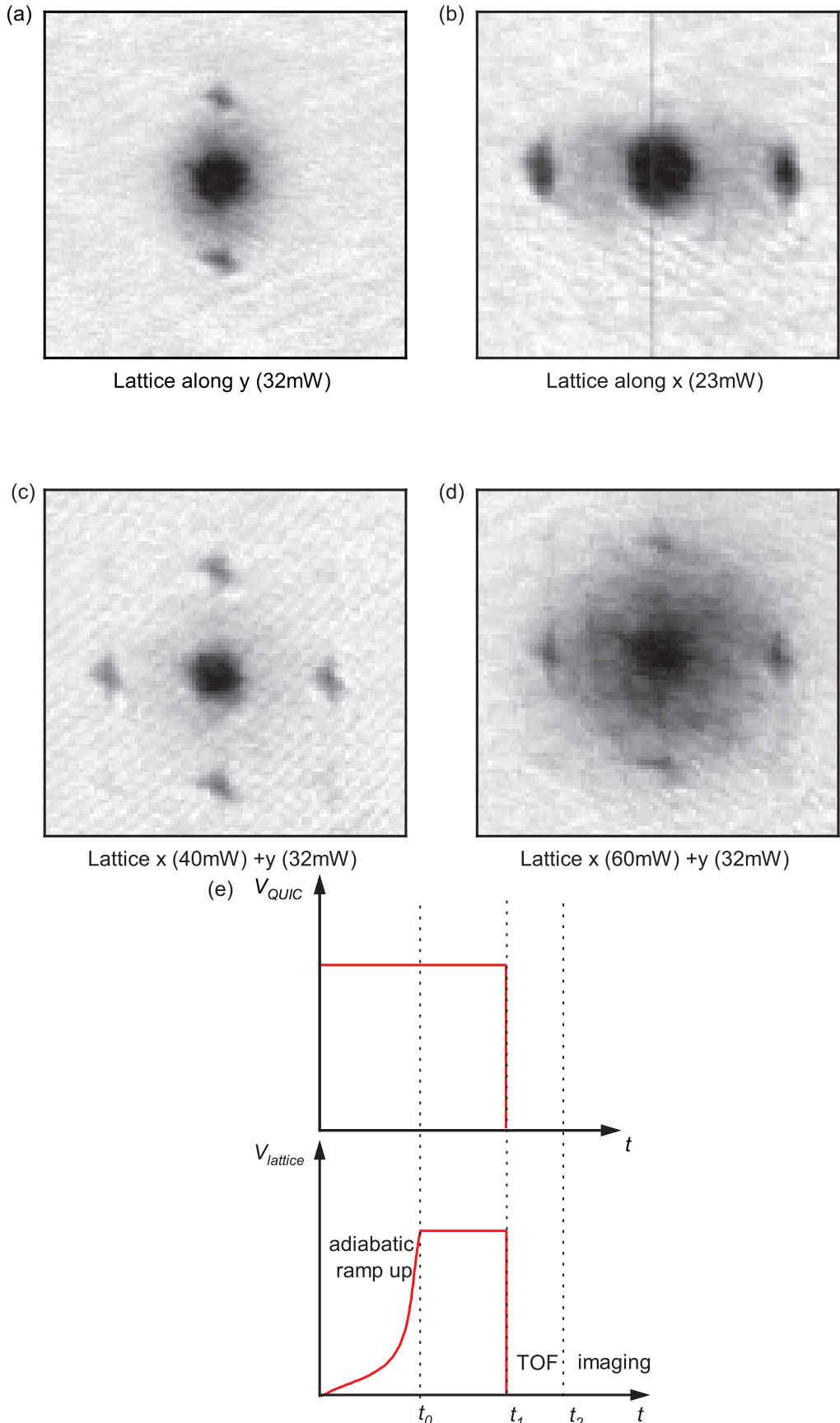


Figure 6.2.: Superfluidity of ^{87}Rb atoms in 1D optical lattice along (a) y- and (b) x-direction. (c) and (d) shows a phase transition from superfluid to Mott-insulator in a 2D lattice of increasing depth, achieved by increasing the power of the lattice beam. (e) The pulse sequence used to form the superfluid in the lattice trap. Due to the low power of the lattice beam, the QUIC trap is kept switched on to provide additional confinement for the atomic cloud. All the images are taken along z-direction after a 10 ms TOF

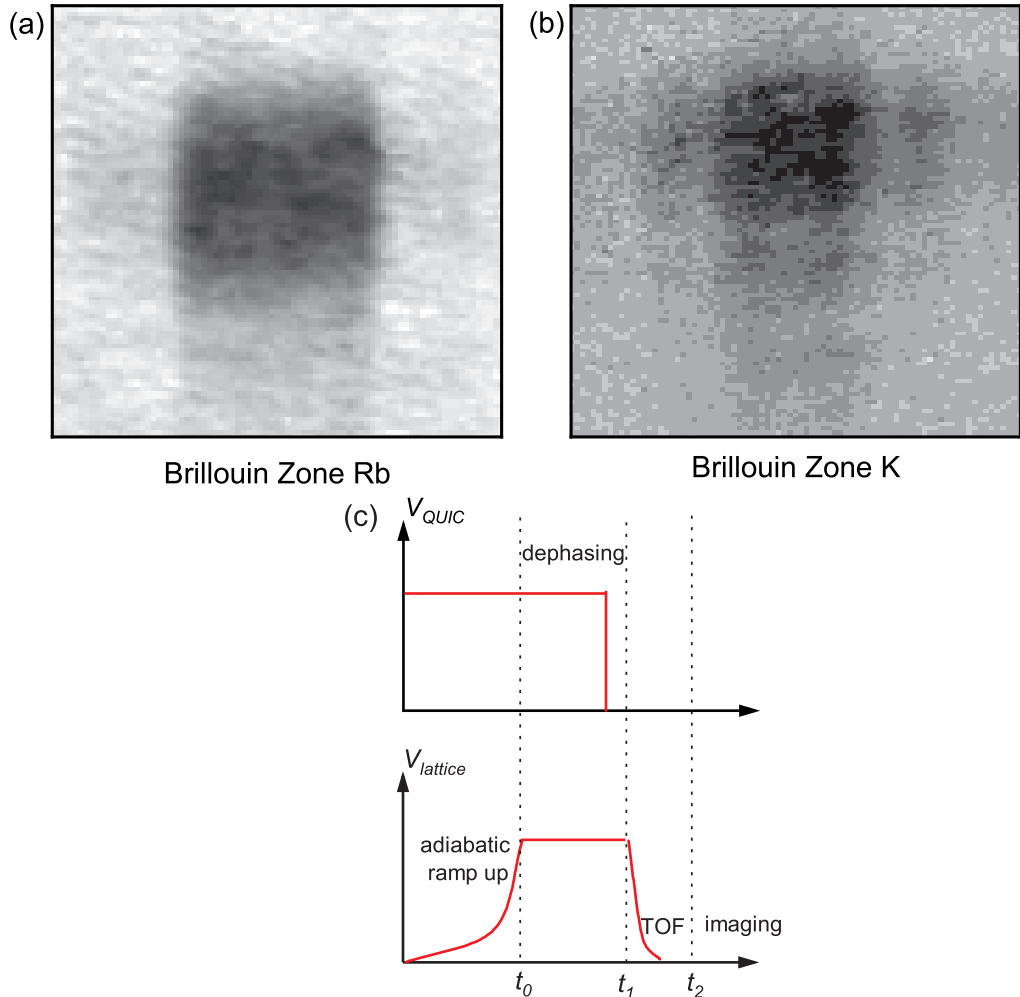


Figure 6.3.: The first Brillouin zone in a 3D optical lattice is observed. (a) The ^{87}Rb BEC is loaded into lattice and the coherence is destroyed by switching off the QUIC trap. The band mapping reveals that most of the population is homogeneously distributed within the first Brillouin zone, indicating that the ^{87}Rb BEC is loaded into the 0th band. (b) The degenerate ^{40}K atoms are loaded into the lattice. Band mapping shows that approximately 20% ^{40}K atoms occupy higher bands. (c) The pulse sequence for band mapping process. Images are taken along z-direction after a 10 ms TOF.

switched off to map the bands onto momentum space. Most Rb atoms are observed in the first Brillouin zone. In Fig. 6.3 (b) the degenerate fermionic ^{40}K atoms ($0.32T_F$, $N_K \approx 1 \cdot 10^5$) are loaded into the lattice. Following the the same procedure, the momentum distribution is measured. Approximately 20% of the ^{40}K atoms are mapped onto higher bands by observing the population distribution in Brillouin zone. The mapping to higher order bands occurs because the energy of ^{40}K is higher than the recoil energy (explained later).

For future experiments, achieving single occupancy of molecules in each lattice site is critical to prevent two-body collision. To ensure this, the ^{40}K and ^{6}Li atoms are preferred to be loaded exclusively into the 0th band of the lattice. Besides the satisfaction of adiabaticity criterion, the initial conditions of the atoms must also be taken into account. The process for loading

atoms into the 0th band has been discussed in [Neyenhuis \(2012\)](#). Before the lattice is ramped up, the band structure can be simply regarded as atoms with energy $\frac{p^2}{2m}$ traveling and being reflected at the edges of the Brillouin zone within one lattice period. Once the lattice is switched on, atoms with $p > \hbar k$ are transported into higher bands of the lattice. This creates an energy limitation for loading atoms into a single band, defined as $E = \frac{\hbar^2 k^2}{2m} = E_r$, where E_r is the recoil energy. To confine atoms to the 0th band, the gas temperature T , and the Fermi temperature T_F , must be smaller than $\frac{E_r}{k_B}$. If T or T_F exceeds this threshold, atoms will populate higher bands. Since $\frac{E_r}{k_B}$ is inversely proportional to the mass m of the particle, heavier particles require a lower temperature to remain in the 0th band. Considering this, loading atoms into the lattice is a better strategy than loading Feshbach molecules directly, as molecules tend to require lower temperature. For our specific case, the recoil energies are $E_r^K = 211 \text{ nk}$ and $E_r^{\text{Li}} = 1.41 \mu\text{k}$. These recoil energies indicate that achieving the necessary conditions for single band loading is feasible by improving the efficiency of evaporative cooling.

6.2. Kapitza-Dirac Scattering

As the lattice setup is verified through the observation of superfluidity and band mapping of the 1st Brillouin zone, the next step is to determine the achievable lattice trap depth. One method to calibrate the lattice trap depth is through Kapitza-Dirac (KD) scattering ([Denschlag et al., 2002](#)). In our case, the scattering occurs outside the Raman-Nath regime, meaning that the pulse duration is not significantly shorter than the harmonic oscillation period within one lattice potential well ([Gadway et al., 2009; Ovchinnikov et al., 1999](#)). As a result, the population evolution among different momentum orders cannot be approximated using Bessel functions. Instead, the population distribution can be calculated using the following steps, as described in [Andersen \(2008\)](#).

Considering the ^{87}Rb BEC can be regarded as a plane wave $\phi_q = e^{iqx/\hbar}$ with quasimomentum q . As discussed in Section [2.3.2](#), the lattice can be described by the band theory with Bloch wave function $\psi_{n,q} = c_{l,n,q} e^{i(2kl+q/\hbar)x} = c_{l,n,q} |\phi_{2klh+q}\rangle$, where n is referred as band index and l denotes the momentum order. At time $t = 0$, the ^{87}Rb BEC is loaded into the lattice, which means the plane wave is projected to the Bloch state basis. Then the wave function can be expressed as

$$|\Psi(t=0)\rangle = \langle\psi_{n,q}|\phi_q\rangle |\psi_{n,q}\rangle \quad , \quad (6.3)$$

where

$$\langle\psi_{n,q}|\phi_q\rangle = c_{l,n,q}^* \langle\phi_{2k\hbar+q}|\phi_q\rangle = c_{0,n,q}^* \quad . \quad (6.4)$$

Then, the time-dependent wave function is given by

$$|\Psi(t)\rangle = c_{0,n,q}^* |\psi_{n,q}\rangle e^{-i\frac{E_{n,q}t}{\hbar}} \quad , \quad (6.5)$$

where $E_{n,q} = \epsilon_{n,q} E_r$ is solved by Equation 2.35. Next, we consider the time evolution of BEC in the lattice for duration Δt . The lattice is kept on Δt and then suddenly switched off, the wave function $|\Psi(\Delta t)\rangle$ is projected to the plane wave basis with form

$$|\Psi(\Delta t)\rangle = c_{0,n,q}^* c_{l,n,q} |\phi_{2k\hbar+q}\rangle e^{-i\frac{\epsilon_{n,q} E_r \Delta t}{\hbar}} = b_{l,n,q} |\phi_{2k\hbar+q}\rangle \quad , \quad (6.6)$$

where the coefficients $b_{l,n,q}$ is given

$$b_{l,n,q} = c_{0,n,q}^* c_{l,n,q} e^{-i\frac{\epsilon_{n,q} E_r \Delta t}{\hbar}} \quad . \quad (6.7)$$

The $|b_{l,n,q}|^2$ represents the population of atoms in l momentum orders, n -th band and q quasimomentum at a fixed trap depth s , where $s \equiv \frac{U_0}{E_r}$. For coherent BEC $q = 0$, the coefficient can be simplified to $|b_{l,n,0}|^2$.

Here, we discuss the procedure for measuring KD scattering. The KD scattering pulse sequence is illustrated in Fig. 6.4. The measurement starts with the preparation of a coherent ^{87}Rb BEC. At t_0 , the lattice is rapidly switched on to load the ^{87}Rb BEC into the lattice. The non-adiabatic loading results in the ^{87}Rb populating multiple lattice bands. The lattice is then held for a duration Δt , after which it is rapidly switched off. Atoms from different bands are mapped to distinct momentum orders l . The images are taken in momentum space after 10 ms TOF. It is important to note that atoms in different momentum orders l can originate from multiple bands. Therefore, the population in each momentum order l should be calculated to be $\sum_{n=0}^{\infty} |b_{l,n,0}|^2$, where the summation accounts for contributions from all bands.

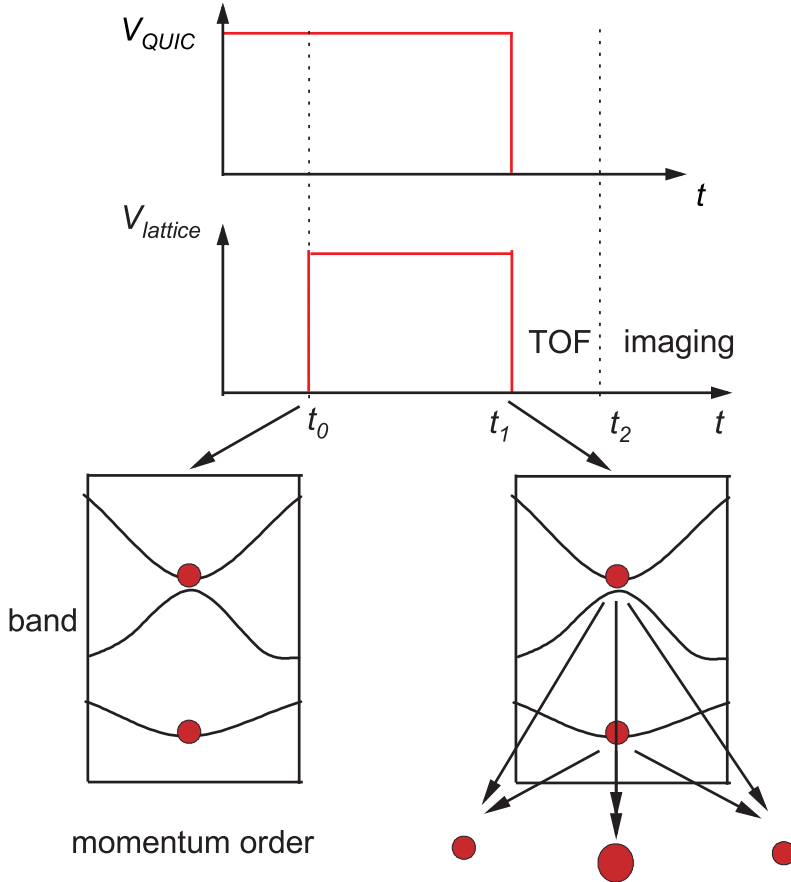


Figure 6.4.: The loading pulse sequence for KD scattering. The lattice is non-adiabatically switched on to populate the ^{87}Rb BEC across all bands. The lattice is then held on Δt before being non-adiabatically switched off. The BEC is mapped onto different momentum orders, and the scattering pattern is recorded after 10 ms TOF.

The 1D scattering patterns for the lattice along x-, y-, and z-directions are shown in Fig. 6.5 (a), (b), and (c) respectively. The lattice beam power for each direction is 70 mW, 73 mW, and 100 mW. By varying the lattice holding time Δt , the population of atoms mapped to different momentum orders l changes, following the coefficient $\sum_{n=0}^{\infty} |b_{l,n,0}(\Delta t)|^2$. By numerically solving $\sum_{n=0}^{\infty} |b_{l,n,0}(\Delta t)|^2$, the lattice trap depth s can be determined by fitting the population evolution in different momentum orders. The summation over bands n is limited to six bands. This choice is based on Fig. 2.5, which shows that for $s = 40$, the expected lattice depth in this measurement, only 4 bands are significantly populated within the lattice trap. And the fit results are shown in Fig. 6.6. The black, red, and blue circles are the measured atomic population in $l = 0$, $l = \pm 1$, and $l = \pm 2$ momentum orders as shown in Fig. 6.5. The solid lines represent the corresponding fit curves for lattice along three directions.

By measuring and fitting the KD scattering process, the relationship between the laser power P and trap depth s has been established, as the trap depth is proportional to the beam

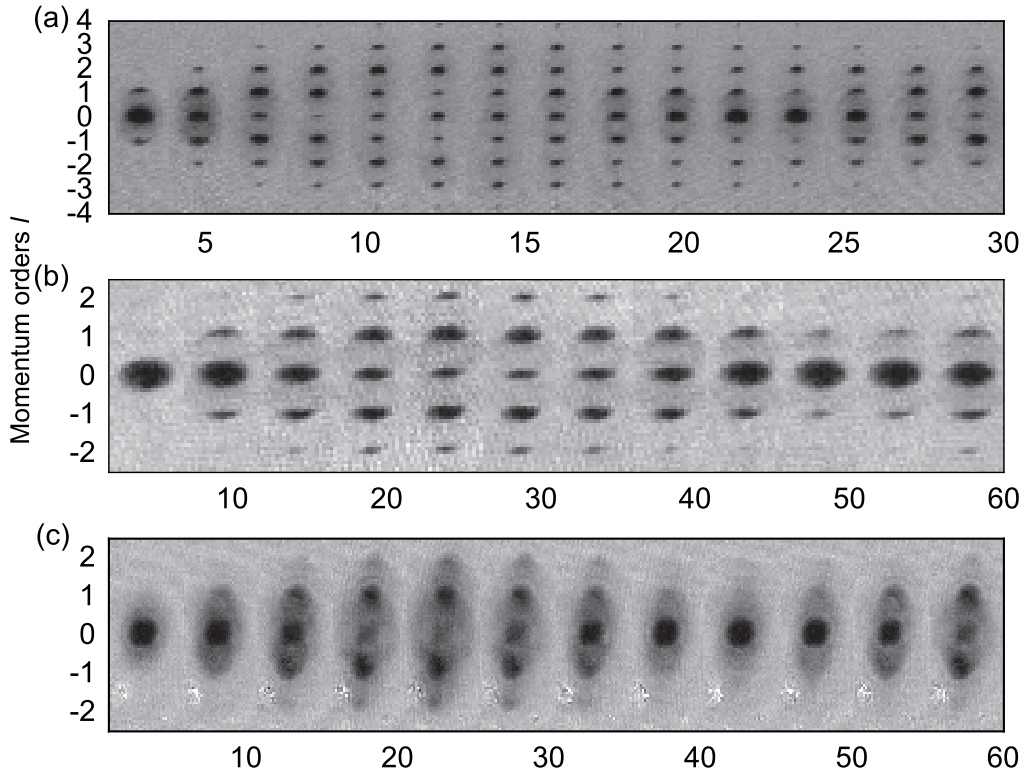


Figure 6.5.: 1D KD scattering pattern for lattice along (a) x-, (b) y-, and (c) z-direction. The scattering patterns are recorded for different lattice holding time Δt . Then population distribution in different momentum orders is used to calibrate the lattice trap depth.

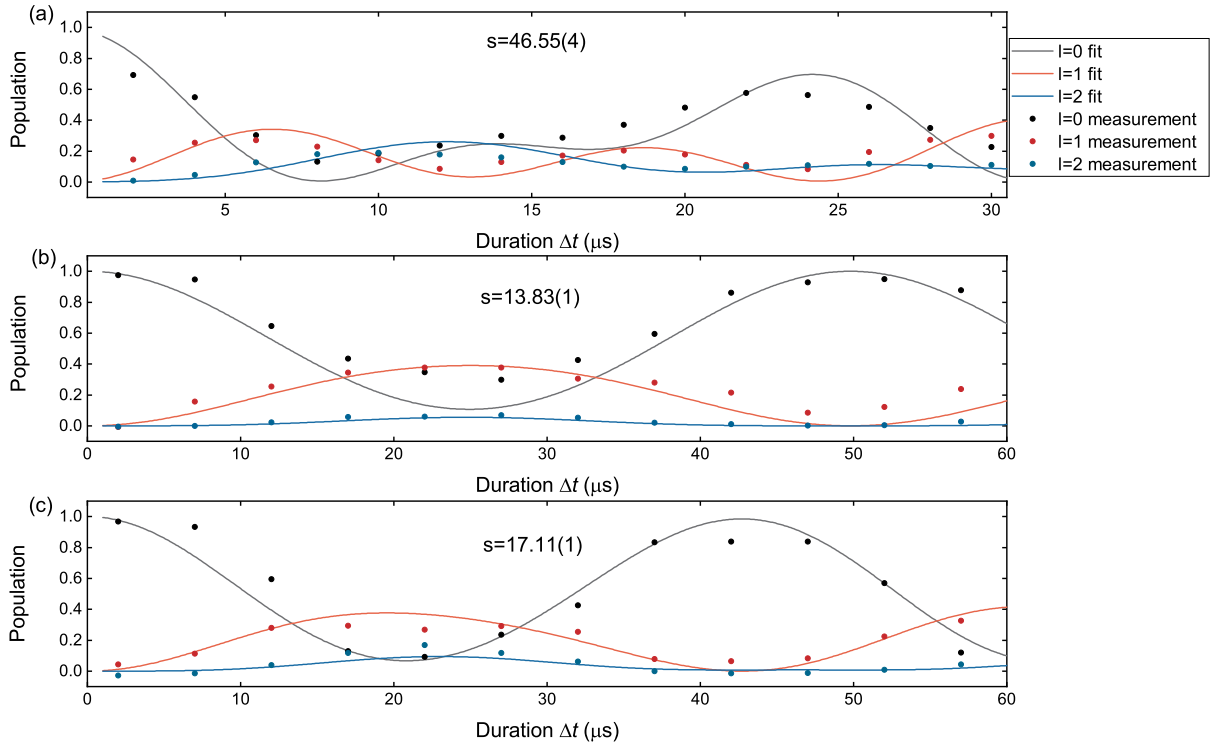


Figure 6.6.: The population distribution in different momentum orders as a function of holding time Δt . The circles in (a), (b), and (c) represent the normalized population measured from Fig. 6.5 (a), (b), and (c), respectively. The lines correspond to the fit results for different trap depth s . The black, red, and blue markers represent the $l = 0$, $l = 1$, and $l = 2$ momentum orders. Based on the fit results, the trap depths for those measurements are estimated to be $s = 46.55(4)$, $s = 13.83(1)$, and $s = 17.11(1)$.

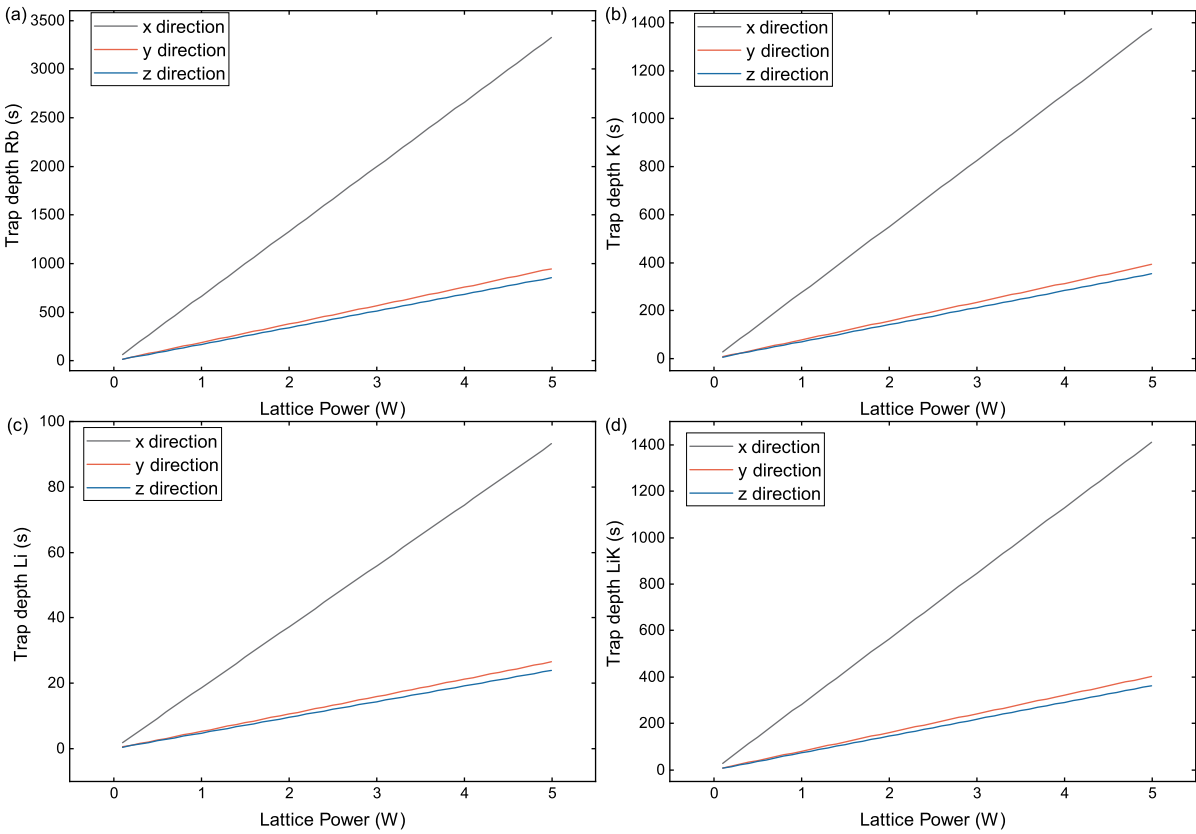


Figure 6.7.: The lattice trap depth s versus laser power P along three directions. The relation is extracted from the KD scattering measurements for (a) ^{87}Rb and then extended to (b) ^{40}K , (c) ^6Li , and (d) ground state $^6\text{Li}^{40}\text{K}$.

power, and is shown in Fig. 6.7. Notably, the trap depth along the x-direction is significantly larger than that along the other two directions for the same power. This discrepancy is attributed to less attenuation of the lattice beam along the x-direction compared to the y- and z-directions. To achieve balanced trap depths across all directions, it is preferable to redistribute the laser power among the three directions. With current power distribution, the lattice along the z-direction is discussed as an example. The corresponding trap depths for different species at the maximum lattice power of 5 W are $s_z = 855.72(50)$ for ^{87}Rb , $s_z = 354.15(21)$ for ^{40}K , $s_z = 23.98(1)$ for ^6Li , and $s_z = 363.19(21)$ for ground state $^6\text{Li}^{40}\text{K}$. And the corresponding band structures for ^6Li , ^{40}K , and ground state $^6\text{Li}^{40}\text{K}$ at 5 W laser power are shown in Fig. 6.8.

In addition to characterizing the trap depth, the KD scattering pattern can also be used to fine align the lattice beams. By fixing the lattice beam power P and holding time Δt , the population distribution in different momentum orders can be monitored daily. Any misalignment of the lattice beam would lead to a reduction in the trap depth, thereby altering the

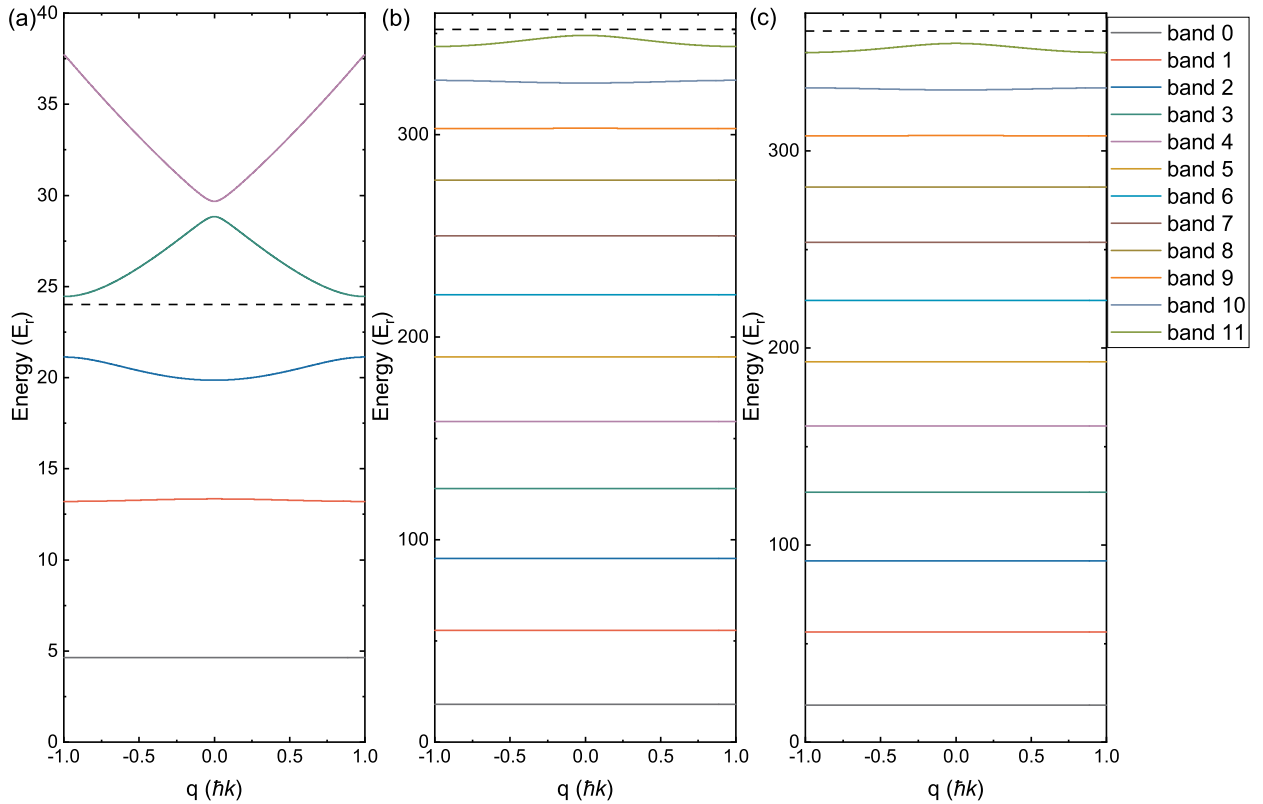


Figure 6.8.: Band structures under the maximum lattice power for (a) ${}^6\text{Li}$, (b) ${}^{40}\text{K}$, and (c) ground state ${}^6\text{Li}{}^{40}\text{K}$. The trap depths correspond to trap depths of $s = 23.98(1)$, $s = 354.15(21)$, and $s = 363.19(21)$, respectively. The dashed black lines indicate the trap depths s for each species. All bands below the trap depth are displayed in the plots.

population distribution in the momentum orders. Thus, the KD scattering pattern provides a useful reference for the daily maintenance and alignment of the lattice beams.

6.3. Creation of Molecules in the Lattice

As discussed in Section 3.4, instead of direct loading ${}^6\text{Li}{}^{40}\text{K}$ molecules into the optical lattice, loading ${}^6\text{Li}$ and ${}^{40}\text{K}$ atoms first is a more effective approach to achieving single occupancy at each lattice site. Following this, the Feshbach association of ${}^6\text{Li}$ and ${}^{40}\text{K}$ atoms in the lattice is tested. In the experiments, the magnetic field for the Feshbach association is scanned under 1D, 2D, and 3D optical lattice configurations. Additionally, in the 3D optical lattice, the beam power is varied between 300 mW and 600 mW. The preliminary results are presented in Fig. 6.9. By increasing the lattice dimensionality or power, the Feshbach resonance width becomes broader. This broadening indicates that, prior to ramping the magnetic field down to the resonance point at 215.6 G, atoms are already associated into the Feshbach state. This effect, known as confinement-induced resonance, has been extensively discussed in the

literature (Bergeman et al., 2003; Haller et al., 2010; Lamporesi et al., 2010; Moritz et al., 2005; Olshanii, 1998). However, for the ground state transfer process, both the number of Feshbach molecules and the coupling strength between the Feshbach state and the excited state are critical. Following the measurements described in Section 4.4.6, the Pump laser is used to excite the Feshbach molecules, and the results are shown in Fig. 6.10. The red squares represents the number of Feshbach molecules in the optical lattice, while the blue circles indicates the number of Feshbach molecules after Pump excitation. The results show that even though the Feshbach molecules are formed via confinement-induced resonance before reaching the magnetic field resonance point, the coupling strength between the Feshbach state and excited state is too weak to achieve high transfer efficiency to the ground state. Therefore, the ending point of the magnetic field ramp remains the same as that used in the ODT. Additionally, STIRAP was tested in the 3D optical lattice. However, at the time of writing this thesis, no clear signal of ground state molecules had been observed. Updates to the lattice setup are currently in progress by other group members. In summary, the creation of a 3D optical lattice has been successfully demonstrated in the lab, with several strategies adapted during the setup and alignment process. The trap depth of the lattice has been fully characterized, providing a method for fine-tuning of the alignment of the lattice beams. Feshbach ${}^6\text{Li}{}^{40}\text{K}$ molecules have been successfully associated in the lattice, paving the way for future exploration of ground state molecule transfer process.

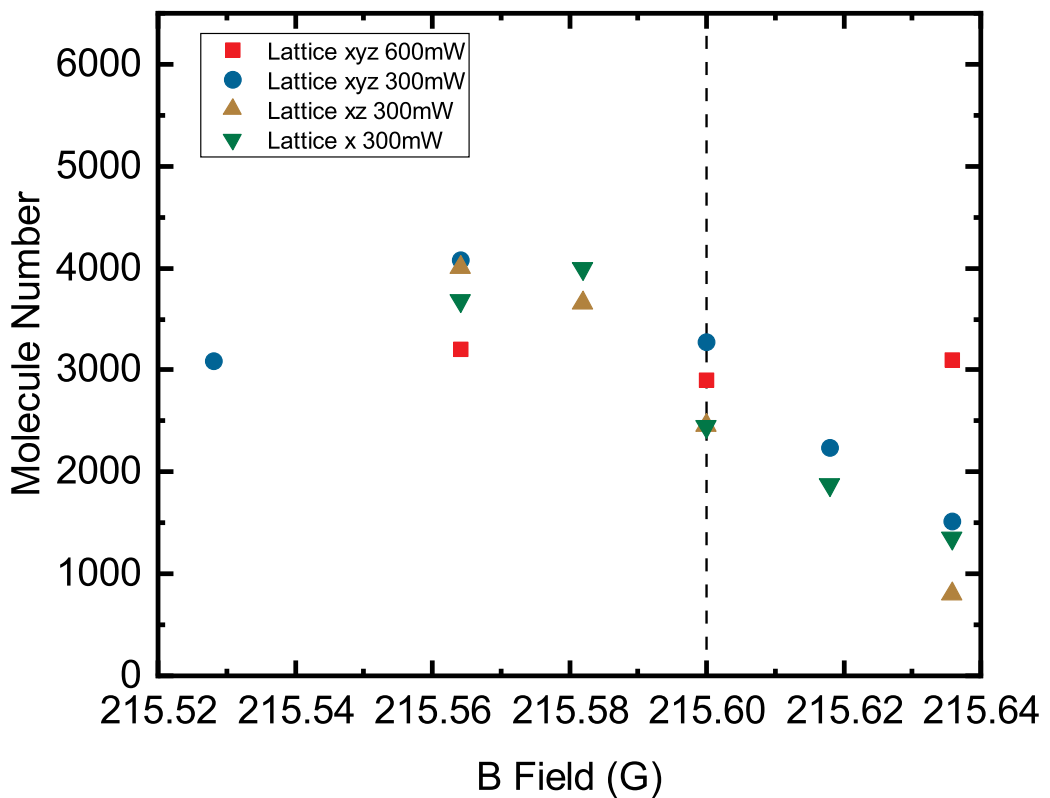


Figure 6.9.: The Feshbach association in 1D, 2D, and 3D optical lattice. The number of Feshbach molecules in the lattice is measured as the magnetic field is scanned around the resonance field (215.6 G). By increasing the lattice dimensionality or lattice power, confinement-induced molecules appear before the magnetic field reaches the resonance point.

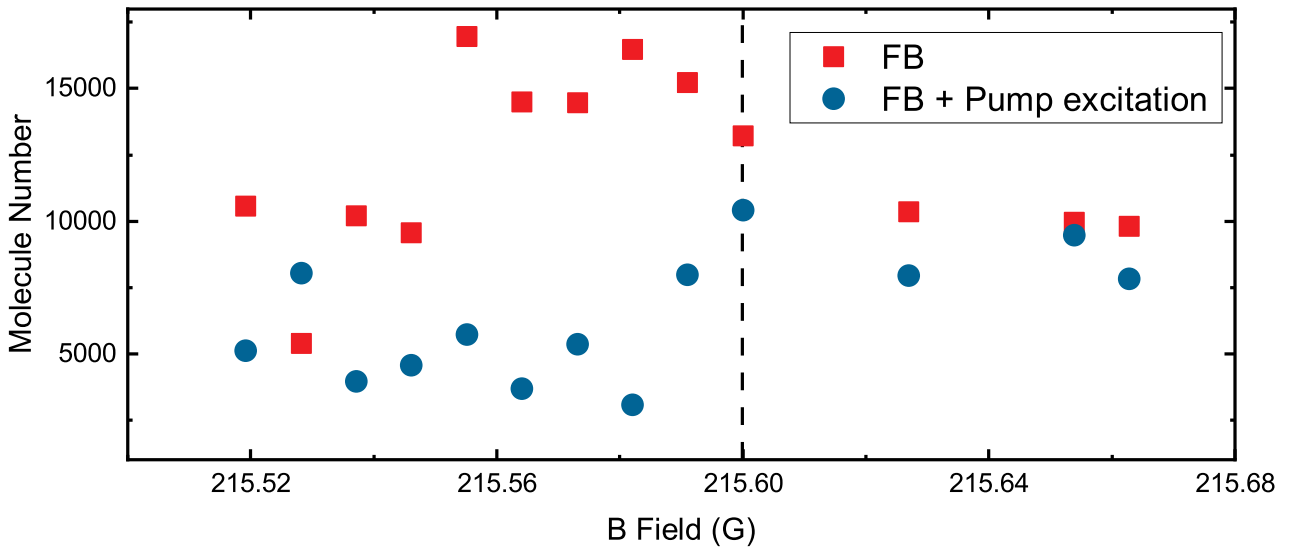


Figure 6.10.: The Feshbach association in lattice with Pump excitation. The red squares represent the number of Feshbach molecules in the optical lattice at different magnetic field endpoints. The blue circles correspond to the same conditions but with additional Pump light excitation. The dashed line indicates the resonant magnetic field.

7. Conclusions and Outlook

In this thesis, I have demonstrated the creation of ultracold rovibrational ground state ${}^6\text{Li}{}^{40}\text{K}$ molecules, investigated the key parameters influencing the transfer efficiency from the Feshbach state to the ground state, characterized the properties of these molecules in their ground state, and upgraded the experimental setups, including the construction of an optically plugged trap and a 3D optical lattice. The main result of this work is the achievement of a high one-way STIRAP transfer efficiency of up to 96(4)% ([He et al., 2024](#)), which at the time was a significant improvement and set a record among bialkali molecule experiments. Additionally, a detailed analysis of the factors contributing to this success is provided.

The thesis builds upon the demonstration of the singlet pathway implemented in previous work ([Yang et al., 2020](#)). To perform the STRIAP transfer process, the transition frequencies and transition strengths were determined from the dark resonance spectroscopy, with the ac Stark shift calculated to be less than 90 kHz under the conditions applied in STIRAP measurements. An off-resonance Raman oscillation with a single-photon detuning of $\Delta = 2\pi \times 580$ MHz was tested to further refine the transition frequencies within 50 kHz and calibrate the laser Rabi frequency. Ground state molecules were first achieved through the Raman oscillation process, achieving a transfer efficiency of 92(2)%. The dephasing time for this process was measured to be $42(1)$ μs , primarily attributed to the inhomogeneous intensity distribution of the Raman laser. With the understanding of the transition frequencies and Rabi frequency, STIRAP was subsequently performed, achieving a one-way transfer efficiency of up to 96(4)%, representing one of the highest efficiencies reported among bi-alkali species.

To achieve this high transfer efficiency, several factors were analyzed, and the experimental setups were upgraded accordingly. As theoretically investigated by [Yatsenko et al. \(2014\)](#), fast laser phase noise has a detrimental effect on STIRAP efficiency, particularly for intermediate states with large linewidth. A setup based on the beat measurement method ([Schmid et al., 2019](#)) was constructed to measure fast phase noise. Phase noise suppression was achieved

by replacing laser diodes with high-quality alternatives and extending the external cavity length of the ECDL structure from 3 cm to 20 cm. Additional techniques, such as intra-cavity EOM modulation and a feedforward noise cancellation system, were explored to further reduce phase noise (Maddox et al., 2024). Moreover, high Rabi frequencies were introduced to mitigate non-adiabatic loss, achieved by integrating TAs into the laser system. The STIRAP efficiency under single-photon and two-photon detuning was also investigated. Ideally, the σ^- polarized Raman lasers were utilized to ensure pure singlet-to-singlet transitions. However, due to polarization imperfections in our setup, a 10 MHz single-photon detuning was introduced to suppress off-resonance excitation to undesired hyperfine states. Incorporating these considerations, a four-level system with decoherence was developed to model the STIRAP process.

With the successful creation of ground state ${}^6\text{Li}{}^{40}\text{K}$ molecules, the properties were investigated. The temperature of the ground state sample was estimated to be $0.91(7)\,\mu\text{K}$, inferred from TOF measurements of the Feshbach state, as the transfer process was considered adiabatic. Additionally, the temperature was predicted to be $0.89\,\mu\text{K}$ based on entropy conservation during the Feshbach association process, which agrees well with the measurement results. Molecule-molecule collisions were studied by removing residual atoms with imaging light. The lifetime of the ground state was measured to be $5.0(3)\,\text{ms}$ and the decay rate constant was calculated to be $3.8(1.9) \times 10^{-10}\,\text{cm}^3\text{s}^{-1}$, in close agreement with theoretical predictions (Julienne et al., 2011). The permanent dipole moment of the ground state ${}^6\text{Li}{}^{40}\text{K}$ was determined using Stark shift spectroscopy in an external electric field. The maximum dipole moment extracted from the measurement was $3.1(3)\,\text{D}$, approximately 10% smaller than the expected value (Dagdigian and Wharton, 2003). This was attributed to systematic errors in determining the electric field strength during simulations. Additionally, MW spectroscopy was used to locate the rotational transition frequencies. The $N'' = 0$ to $N'' = 1$ transition frequency was predicted to be $17.484(6)\,\text{GHz}$, and MW scanning revealed transitions around $17.4795\,\text{GHz}$. However, at this stage, hyperfine structures of the ground state were unresolved, and MW polarization was uncontrolled. Furthermore, coherence time for the transitions was on the order of a few microseconds but was expected to improve under magic conditions. This initial exploration of MW spectroscopy provided foundational knowledge for future studies.

In addition, to accelerate the experimental sequence and explore many-body physics, an

optically plugged trap and a free-space 3D optical lattice were developed as part of this work. The plugged trap was tested using ^{87}Rb evaporative cooling, and the plug effect was observed. However, due to the undesired interference, the plugged trap has not been implemented in the our experimental procedures. A 3D optical lattice was successfully implemented and verified through the observation of superfluidity and band mapping. The lattice depth was further calibrated using KD scattering. Before completing this thesis, both ^6Li and ^{40}K atoms were loaded into the lattice, and the Feshbach association was achieved within the lattice. Meanwhile, a confinement-induced molecule association was observed in the lattice. The creation of ground state $^6\text{Li}^{40}\text{K}$ molecules is anticipated to be realized in the 3D optical lattice, providing a promising platform for future studies.

7.1. Outlook

During the period of writing this thesis, the hyperfine structure of the first rotational excited state has been fully resolved, and the magic wavelength for the rotational transition was both predicted and experimentally located. Additionally, a specially designed MW antenna was developed, offering full polarization control. Combined with the understanding of MW spectroscopy obtained in this work, complete control over the internal states of $^6\text{Li}^{40}\text{K}$ molecules, including vibrational, rotational and hyperfine degrees of freedom, has been achieved and the coherence time for these MW transitions has been significantly extended. As discussed in Section 5.5.5, one immediate prospect is to apply MW shielding to suppress the two-body inelastic collision. Moreover, the collisional losses can be further minimized by carefully controlling the polarization of the MW signals. With fully-suppressed losses, evaporative cooling of the molecular sample can be performed, making it possible to achieve a molecular BEC ([Bigagli et al., 2024](#)).

Another promising direction for future research is the creation of ground state molecules in a 3D optical lattice operating at the magic wavelength. The deep optical lattice can significantly extend the lifetime of the ground state molecules by suppressing two-body inelastic collisions, while the coherence time of rotational transitions can be extended under the magic condition ([Lin et al., 2022](#)). This setup would provide a robust platform for exploring many-body physics, enabling studies of phenomena such as lattice-spin models and dipolar interactions in a highly controlled environment.

Bibliography

MOLPRO, version 2015.1, a package of ab initio programs, H.-J. Werner, P. J. Knowles, G. Knizia, F. R. Manby, M. Schütz, and others, see. www.molpro.net/.

See Supplemental Material at [URL will be inserted by publisher] for details on the fitting formula for the dark resonance spectroscopy, the numerical result of STIRAP transfer for the four-level system, the fitting of the Stark shift, and the experimental high-voltage electrode setup.

E. R. I. Abraham, W. I. McAlexander, C. A. Sackett, and Randall G. Hulet. Spectroscopic determination of the s-wave scattering length of lithium. *Phys. Rev. Lett.*, 74(8):1315–1318, February 1995a. doi:[10.1103/PhysRevLett.74.1315](https://doi.org/10.1103/PhysRevLett.74.1315).

E. R. I. Abraham, N. W. M. Ritchie, W. I. McAlexander, and R. G. Hulet. Photoassociative spectroscopy of long-range states of ultracold ${}^6\text{Li}_2$ and ${}^7\text{Li}_2$. *J. Chem. Phys.*, 103(18): 7773–7778, November 1995b. doi:[10.1063/1.470296](https://doi.org/10.1063/1.470296).

E. R. I. Abraham, W. I. McAlexander, J. M. Gerton, R. G. Hulet, R. Côté, and A. Dalgarno. Singlet s-wave scattering lengths of ${}^6\text{Li}$ and ${}^7\text{Li}$. *Phys. Rev. A*, 53(6):R3713–R3715, June 1996a. doi:[10.1103/PhysRevA.53.R3713](https://doi.org/10.1103/PhysRevA.53.R3713).

E. R. I. Abraham, W. I. McAlexander, J. M. Gerton, R. G. Hulet, R. Côté, and A. Dalgarno. Singlet s-wave scattering lengths of ${}^6\text{Li}$ and ${}^7\text{Li}$. *Phys. Rev. A*, 53(6):R3713–R3715, June 1996b. doi:[10.1103/PhysRevA.53.R3713](https://doi.org/10.1103/PhysRevA.53.R3713).

E. R. I. Abraham, W. I. McAlexander, J. M. Gerton, R. G. Hulet, R. Côté, and A. Dalgarno. Triplet s-wave resonance in ${}^6\text{Li}$ collisions and scattering lengths of ${}^6\text{Li}$ and ${}^7\text{Li}$. *Phys. Rev. A*, 55(5):R3299–R3302, May 1997. doi:[10.1103/PhysRevA.55.R3299](https://doi.org/10.1103/PhysRevA.55.R3299).

ACME collaboration, J Baron, Wesley C Campbell, David DeMille, JM Doyle, Gerald Gabrielse, YV Gurevich, PW Hess, Nicholas R Hutzler, E Kirilov, et al. Order of magnitude smaller limit on the electric dipole moment of the electron. *Science*, 343(6168):269–272, 2014. doi:[10.1126/science.1248213](https://doi.org/10.1126/science.1248213).

Kestutis Aidas, Celestino Angeli, Keld L. Bak, Vebjorn Bakken, Radovan Bast, Linus Boman, Ove Christiansen, Renzo Cimiraglia, Sonia Coriani, Pal Dahle, Erik K. Dalskov, Ulf Ekstrom, Thomas Enevoldsen, Janus J. Eriksen, Patrick Ettenhuber, Berta Fernandez, Lara Ferrighi, Heike Fliegl, Luca Frediani, Kasper Hald, Asger Halkier, Christof Hattig, Hanne Heiberg, Trygve Helgaker, Alf Christian Hennum, Hinne Hettema, Eirik Hjertenaes, Stinne Host, Ida-Marie Hoyvik, Maria Francesca Iozzi, Branislav Jansik, Hans Jorgen Aa. Jensen, Dan Jonsson, Poul Jorgensen, Joanna Kauczor, Sheela Kirpekar, Thomas Kjaergaard, Wim Klopper, Stefan Knecht, Rika Kobayashi, Henrik Koch, Jacob Kongsted, Andreas Krapp, Kasper Kristensen, Andrea Ligabue, Ola B. Lutnaes, Juan I. Melo, Kurt V. Mikkelsen, Rolf H. Myhre, Christian Neiss, Christian B. Nielsen, Patrick Norman, Jeppe Olsen, Jørgen Magnus H. Olsen, Anders Osted, Martin J. Packer, Filip Pawłowski, Thomas B. Pedersen, Patricio F. Provasi, Simen Reine, Zilvinas Rinkevičius, Torgeir A. Ruden, Kenneth Ruud, Vladimir V. Rybkin, Paweł Salek, Claire C. M. Samson, Alfredo Sanchez de Meras, Trond Saue, Stephan P. A. Sauer, Bernd Schimmelpfennig, Kristian Sneskov,

- Arnfinn H. Steindal, Kristian O. Sylvester-Hvid, Peter R. Taylor, Andrew M. Teale, Erik I. Tellgren, David P. Tew, Andreas J. Thorvaldsen, Lea Thogersen, Olav Vahtras, Mark A. Watson, David J. D. Wilson, Marcin Ziolkowski, and Hans Agren. The dalton quantum chemistry program system. *WIREs Computational Molecular Science*, 4(3):269–284, 2014. doi:<https://doi.org/10.1002/wcms.1172>.
- K Aikawa, D Akamatsu, J Kobayashi, M Ueda, T Kishimoto, and S Inouye. Toward the production of quantum degenerate bosonic polar molecules, 41k87rb. *New Journal of Physics*, 11(5):055035, may 2009. doi:[10.1088/1367-2630/11/5/055035](https://doi.org/10.1088/1367-2630/11/5/055035).
- K. Aikawa, A. Frisch, M. Mark, S. Baier, A. Rietzler, R. Grimm, and F. Ferlaino. Bose-einstein condensation of erbium. *Phys. Rev. Lett.*, 108:210401, May 2012. doi:[10.1103/PhysRevLett.108.210401](https://doi.org/10.1103/PhysRevLett.108.210401).
- Nitzan Akerman, Nir Navon, Shlomi Kotler, Yinnon Glickman, and Roee Ozeri. Universal gate-set for trapped-ion qubits using a narrow linewidth diode laser. *New Journal of Physics*, 17(11):113060, nov 2015. doi:[10.1088/1367-2630/17/11/113060](https://doi.org/10.1088/1367-2630/17/11/113060).
- Victor V. Albert, Jacob P. Covey, and John Preskill. Robust encoding of a qubit in a molecule. *Phys. Rev. X*, 10:031050, Sep 2020. doi:[10.1103/PhysRevX.10.031050](https://doi.org/10.1103/PhysRevX.10.031050).
- C. B. Alcock, V. P. Itkin, and M. K. Horrigan. Vapour pressure equations for the metallic elements: 2982500 K. *Can. Metall. Q.*, 23(3):309, 1984.
- J. Aldegunde, Ben A. Rivington, Piotr S. Żuchowski, and Jeremy M. Hutson. Hyperfine energy levels of alkali-metal dimers: Ground-state polar molecules in electric and magnetic fields. *Phys. Rev. A*, 78:033434, Sep 2008. doi:[10.1103/PhysRevA.78.033434](https://doi.org/10.1103/PhysRevA.78.033434).
- Jesus Aldegunde and Jeremy M. Hutson. Hyperfine structure of alkali-metal diatomic molecules. *Phys. Rev. A*, 96:042506, Oct 2017. doi:[10.1103/PhysRevA.96.042506](https://doi.org/10.1103/PhysRevA.96.042506).
- D.W. Allan. Statistics of atomic frequency standards. *Proceedings of the IEEE*, 54(2):221–230, 1966. doi:[10.1109/PROC.1966.4634](https://doi.org/10.1109/PROC.1966.4634).
- A. R. Allouche. Website of A.R. Allouche. <https://sites.google.com/site/alloucheard/diatomic>.
- Abdul-Rahman Allouche. Web: <http://sites.google.com/site/alloucheard/diatomic>. 2011.
- L. Anderegg, L. W. Cheuk, Y. C. Bao, S. Burchesky, W. Ketterle, K. K. Ni, and J. M. Doyle. An optical tweezer array of ultracold molecules. *Science*, 365(6458):1156, 09 2019. doi:[DOI: 10.1126/science.aax126](https://doi.org/10.1126/science.aax126).
- Loïc Anderegg, Benjamin L. Augenbraun, Eunmi Chae, Boerge Hemmerling, Nicholas R. Hutzler, Aakash Ravi, Alejandra Collopy, Jun Ye, Wolfgang Ketterle, and John M. Doyle. Radio frequency magneto-optical trapping of caf with high density. *Phys. Rev. Lett.*, 119: 103201, Sep 2017. doi:[10.1103/PhysRevLett.119.103201](https://doi.org/10.1103/PhysRevLett.119.103201).
- Loïc Anderegg, Benjamin L Augenbraun, Yicheng Bao, Sean Burchesky, Lawrence W Cheuk, Wolfgang Ketterle, and John M Doyle. Laser cooling of optically trapped molecules. *Nature Physics*, 14(9):890–893, 2018. doi:[10.1038/s41567-018-0191-z](https://doi.org/10.1038/s41567-018-0191-z).
- Loïc Anderegg, Sean Burchesky, Yicheng Bao, Scarlett S Yu, Tijs Karman, Eunmi Chae, Kang-Kuen Ni, Wolfgang Ketterle, and John M Doyle. Observation of microwave shielding of ultracold molecules. *Science*, 373(6556):779, 08 2021. doi:[10.1126/science.abg9502](https://doi.org/10.1126/science.abg9502).

- Henrik Kjær Andersen. Bose-einstein condensates in optical lattices. *University of Aarhus, Ph.D Thesis*, 16:17, 2008.
- M. H. Anderson, J. R. Ensher, M. R. Matthews, C. E. Wieman, and E. A. Cornell. Observation of Bose-Einstein condensation in a dilute atomic vapor. *Science*, 269(5221):198–201, 1995. doi:[10.1126/science.269.5221.198](https://doi.org/10.1126/science.269.5221.198).
- P. W. Anderson. *Ten Years of Superconductivity: 19801990*, chapter The Resonating Valence Bond State in La₂CuO₄and Superconductivity, pages 278–280. Springer Netherlands, Dordrecht, 1993. ISBN 978-94-011-1622-0. doi:[10.1007/978-94-011-1622-0_35](https://doi.org/10.1007/978-94-011-1622-0_35).
- V. Andreev, D. G. Ang, D. DeMille, J. M. Doyle, G. Gabrielse, J. Haefner, N. R. Hutzler, Z. Lasner, C. Meisenhelder, B. R. OLeary, C. D. Panda, A. D. West, E. P. West, and X. Wu. Improved limit on the electric dipole moment of the electron. *Nature*, 562:355–360, 2018. doi:[10.1038/s41586-018-0599-8](https://doi.org/10.1038/s41586-018-0599-8).
- DRT Appadoo, RJ LeRoy, PF Bernath, S Gerstenkorn, P Luc, J Verges, J Sinzelle, J Chevillard, and Y Daignaux. Comprehensive analysis of the a-x spectrum of i-2: An application of near-dissociation theory. *J. Chem. Phys.*, 104(3):903–913, JAN 15 1996. doi:[10.1063/1.470814](https://doi.org/10.1063/1.470814).
- F. Arecchi and R. Bonifacio. Theory of optical maser amplifiers. *IEEE Journal of Quantum Electronics*, 1(4):169–178, 1965. doi:[10.1109/JQE.1965.1072212](https://doi.org/10.1109/JQE.1965.1072212).
- E. Arimondo, M. Inguscio, and P. Violino. Experimental determinations of the hyperfine structure in the alkali atoms. *Rev. Mod. Phys.*, 49(1):31–75, January 1977. doi:[10.1103/RevModPhys.49.31](https://doi.org/10.1103/RevModPhys.49.31).
- A. Aspect, E. Arimondo, R. Kaiser, N. Vansteenkiste, and C. Cohen-Tannoudji. Laser cooling below the one-photon recoil energy by velocity-selective coherent population trapping. *Phys. Rev. Lett.*, 61:826–829, Aug 1988. doi:[10.1103/PhysRevLett.61.826](https://doi.org/10.1103/PhysRevLett.61.826).
- Benjamin L. Augenbraun, Londeregg, Christian Hallas, Zack D. Lasner, Nathaniel B. Vilas, and John M. Doyle. Chapter two - direct laser cooling of polyatomic molecules. In Louis F. DiMauro, Hne Perrin, and Susanne F. Yelin, editors, *Advances in Atomic, Molecular, and Optical Physics*, volume 72 of *Advances In Atomic, Molecular, and Optical Physics*, pages 89–182. Academic Press, 2023. doi:<https://doi.org/10.1016/bs.aamop.2023.04.005>.
- Bastian Aurand, Stephan Kuschel, Christian Rödel, Martin Heyer, Frank Wunderlich, Oliver Jäckel, Malte C. Kaluza, Gerhard G. Paulus, and Thomas Kühl. Creating circularly polarized light with a phase-shifting mirror. *Opt. Express*, 19(18):17151–17157, Aug 2011. doi:[10.1364/OE.19.017151](https://doi.org/10.1364/OE.19.017151).
- S. H. Autler and C. H. Townes. Stark effect in rapidly varying fields. *Phys. Rev.*, 100:703–722, Oct 1955. doi:[10.1103/PhysRev.100.703](https://doi.org/10.1103/PhysRev.100.703).
- Victor Avalos, Xiaoyu Nie, Anbang Yang, Canming He, Sunil Kumar, and Kai Dieckmann. Field-programmable-gate-array-based digital frequency stabilization of low-phase-noise diode lasers. *Review of Scientific Instruments*, 94(6):063001, 06 2023. doi:[10.1063/5.0152305](https://doi.org/10.1063/5.0152305).
- M Aymar and O Dulieu. Calculation of accurate permanent dipole moments of the lowest $\sigma+1, 3$ states of heteronuclear alkali dimers using extended basis sets. *J. Chem. Phys.*, 122(20):204302, 05 2005. doi:[10.1063/1.1903944](https://doi.org/10.1063/1.1903944).

- Vanderlei Bagnato, David E. Pritchard, and Daniel Kleppner. Bose-einstein condensation in an external potential. *Phys. Rev. A*, 35:4354–4358, May 1987. doi:[10.1103/PhysRevA.35.4354](https://doi.org/10.1103/PhysRevA.35.4354).
- Waseem S. Bakr, Jonathon I. Gillen, Amy Peng, Simon Folling, and Markus Greiner. A quantum gas microscope for detecting single atoms in a hubbard-regime optical lattice. *Nature*, 462(7269):74–77, November 2009. doi:[10.1038/nature08482](https://doi.org/10.1038/nature08482).
- N. Balakrishnan. Perspective: Ultracold molecules and the dawn of cold controlled chemistry. *J. Chem. Phys.*, 145(15):150901, OCT 21 2016. doi:[10.1063/1.4964096](https://doi.org/10.1063/1.4964096).
- B. Barakat, R. Bacis, F. Carrot, S. Churassy, P. Crozet, F. Martin, and J. Verges. Extensive analysis of the $X^1\Sigma_g^+$ ground state of ${}^7\text{Li}_2$ by laser-induced fluorescence Fourier transform spectrometry. *Chem. Phys.*, 102(1&2):215–227, February 1986. doi:[10.1016/0301-0104\(86\)85133-3](https://doi.org/10.1016/0301-0104(86)85133-3).
- M. Baranov, L. Dobrek, K. Goral, L. Santos, and M. Lewenstein. Ultracold dipolar gases - a challenge for experiments and theory. *Physica Scripta*, T102(1):74, 2002. doi:[10.1238/physica.topical.102a00074](https://doi.org/10.1238/physica.topical.102a00074).
- M. A. Baranov, M. Dalmonte, G. Pupillo, and P. Zoller. Condensed matter theory of dipolar quantum gases. *Chemical Reviews*, 112(9):5012–5061, aug 2012. doi:[10.1021/cr2003568](https://doi.org/10.1021/cr2003568).
- J. Bardeen, L. N. Cooper, and J. R. Schrieffer. Theory of superconductivity. *Phys. Rev.*, 108: 1175–1204, Dec 1957. doi:[10.1103/PhysRev.108.1175](https://doi.org/10.1103/PhysRev.108.1175).
- Ryan Barnett, Dmitry Petrov, Mikhail Lukin, and Eugene Demler. Quantum magnetism with multicomponent dipolar molecules in an optical lattice. *Phys. Rev. Lett.*, 96:190401, May 2006. doi:[10.1103/PhysRevLett.96.190401](https://doi.org/10.1103/PhysRevLett.96.190401).
- M. D. Barrett, J. A. Sauer, and M. S. Chapman. All-optical formation of an atomic Bose-Einstein condensate. *Phys. Rev. Lett.*, 87:010404, Jun 2001. doi:[10.1103/PhysRevLett.87.010404](https://doi.org/10.1103/PhysRevLett.87.010404).
- Thomas E. Barrett, Samuel W. Dapone-Schwartz, Mark D. Ray, and Gregory P. Lafyatis. Slowing atoms with σ^- polarized light. *Phys. Rev. Lett.*, 67:3483–3486, Dec 1991. doi:[10.1103/PhysRevLett.67.3483](https://doi.org/10.1103/PhysRevLett.67.3483).
- M. Bartenstein, A. Altmeyer, S. Riedl, S. Jochim, C. Chin, J. Hecker Denschlag, and R. Grimm. Crossover from a molecular Bose-Einstein condensate to a degenerate fermi gas. *Phys. Rev. Lett.*, 92:120401, Mar 2004. doi:[10.1103/PhysRevLett.92.120401](https://doi.org/10.1103/PhysRevLett.92.120401).
- M G Bason, M Tanasittikosol, A Sargsyan, A K Mohapatra, D Sarkisyan, R M Potvliege, and C S Adams. Enhanced electric field sensitivity of rf-dressed rydberg dark states. *New Journal of Physics*, 12(6):065015, jun 2010. doi:[10.1088/1367-2630/12/6/065015](https://doi.org/10.1088/1367-2630/12/6/065015).
- Louis Baum, Nathaniel B. Vilas, Christian Hallas, Benjamin L. Augenbraun, Shivam Raval, Debayan Mitra, and John M. Doyle. Establishing a nearly closed cycling transition in a polyatomic molecule. *Phys. Rev. A*, 103(4), 04 2021. doi:[10.1103/PhysRevA.103.043111](https://doi.org/10.1103/PhysRevA.103.043111).
- Roman Bause, Ming Li, Andreas Schindewolf, Xing-Yan Chen, Marcel Duda, Svetlana Kotchigova, Immanuel Bloch, and Xin-Yu Luo. Tune-out and magic wavelengths for ground-state ${}^{23}\text{Na}{}^{40}\text{K}$ molecules. *Phys. Rev. Lett.*, 125:023201, Jul 2020. doi:[10.1103/PhysRevLett.125.023201](https://doi.org/10.1103/PhysRevLett.125.023201).

- Roman Bause, Akira Kamijo, Xing-Yan Chen, Marcel Duda, Andreas Schindewolf, Immanuel Bloch, and Xin-Yu Luo. Efficient conversion of closed-channel-dominated feshbach molecules of $^{23}\text{Na}^{40}\text{K}$ to their absolute ground state. *Phys. Rev. A*, 104:043321, Oct 2021. doi:[10.1103/PhysRevA.104.043321](https://doi.org/10.1103/PhysRevA.104.043321).
- V. Bednarska, P. Kowalczyk, and W Jastrzebski. Improved rotational constants for kli molecule. *Journal of Molecular Spectroscopy*, 1996. doi:[10.1006/jmsp.1996.0268](https://doi.org/10.1006/jmsp.1996.0268).
- V. Bednarska, I. Jackowska, W. Jastrzebski, and P. Kowalczyk. The Molecular Constants and Potential Energy Curve of the Ground State $X^1\Sigma^+$ in KLi. *J. Mol. Spectrosc.*, 189(2): 244 – 248, 1998. doi:<http://dx.doi.org/10.1006/jmsp.1998.7543>.
- Maxime Ben Dahan, Ekkehard Peik, Jakob Reichel, Yvan Castin, and Christophe Salomon. Bloch oscillations of atoms in an optical potential. *Phys. Rev. Lett.*, 76:4508–4511, Jun 1996. doi:[10.1103/PhysRevLett.76.4508](https://doi.org/10.1103/PhysRevLett.76.4508).
- Giel Berden, Rudy Peeters, and Gerard Meijer. Cavity ring-down spectroscopy: Experimental schemes and applications. *International reviews in physical chemistry*, 19(4):565–607, 2000. doi:[10.1080/014423500750040627](https://doi.org/10.1080/014423500750040627).
- S. V. Berdyugina and S. K. Solanki. The molecular zeeman effect and diagnostics of solar and stellar magnetic fields - i. theoretical spectral patterns in the zeeman regime. *Astron. Astrophys.*, 385(2):701–715, April 2002. doi:[10.1051/0004-6361:20020130](https://doi.org/10.1051/0004-6361:20020130).
- T. Bergeman, Gidon Erez, and Harold J. Metcalf. Magnetostatic trapping fields for neutral atoms. *Phys. Rev. A*, 35(4):1535–1546, February 1987. doi:[10.1103/PhysRevA.35.1535](https://doi.org/10.1103/PhysRevA.35.1535).
- T. Bergeman, M. G. Moore, and M. Olshanii. Atom-atom scattering under cylindrical harmonic confinement: Numerical and analytic studies of the confinement induced resonance. *Phys. Rev. Lett.*, 91:163201, Oct 2003. doi:[10.1103/PhysRevLett.91.163201](https://doi.org/10.1103/PhysRevLett.91.163201).
- K. Bergmann, H. Theuer, and B. W. Shore. Coherent population transfer among quantum states of atoms and molecules. *Rev. Mod. Phys.*, 70:1003–1025, Jul 1998. doi:[10.1103/RevModPhys.70.1003](https://doi.org/10.1103/RevModPhys.70.1003).
- Klaas Bergmann, Hanns-Christoph Nrl, Cristian Panda, Gerald Gabrielse, Eduard Miloglyadov, Martin Quack, Georg Seyfang, Gunther Wichmann, Silke Ospelkaus, Axel Kuhn, Stefano Longhi, Alexander Szameit, Philipp Pirro, Burkard Hillebrands, Xue-Feng Zhu, Jie Zhu, Michael Drewsen, Winfried K Hensinger, Sebastian Weidt, Thomas Halfmann, Hai-Lin Wang, Gheorghe Sorin Paraoanu, Nikolay V Vitanov, Jordi Mompart, Thomas Busch, Timothy J Barnum, David D Grimes, Robert W Field, Mark G Raizen, Edvardas Narevicius, Marcis Auzinsh, Dmitry Budker, Adriana Pfy, and Christoph H Keitel. Roadmap on stirap applications. *Journal of Physics B: Atomic, Molecular and Optical Physics*, 52(20): 202001, sep 2019. doi:[10.1088/1361-6455/ab3995](https://doi.org/10.1088/1361-6455/ab3995).
- Hans A. Bethe and Edwin E. Salpeter. *Quantum Mechanics of One- and Two-Electron Atoms*. Dover Publications, 2008. doi:[10.1007/978-1-4613-4104-8](https://doi.org/10.1007/978-1-4613-4104-8).
- Hendrick L. Bethlem, Giel Berden, and Gerard Meijer. Decelerating neutral dipolar molecules. *Phys. Rev. Lett.*, 83:1558–1561, Aug 1999. doi:[10.1103/PhysRevLett.83.1558](https://doi.org/10.1103/PhysRevLett.83.1558).
- Hendrick L. Bethlem, Giel Berden, Floris M. H. Crompvoets, Rienk T. Jongma, Andr A. van Roij, and Gerard Meijer. Electrostatic trapping of ammonia molecules. *Nature*, 406(6795): 491–494, 2000. doi:[10.1038/35020030](https://doi.org/10.1038/35020030).

- Niccolò Bigagli, Claire Warner, Weijun Yuan, Siwei Zhang, Ian Stevenson, Tijs Karman, and Sebastian Will. Collisionally stable gas of bosonic dipolar ground-state molecules. *Nature Physics*, 19(11):1579–1584, September 2023a. doi:[10.1038/s41567-023-02200-6](https://doi.org/10.1038/s41567-023-02200-6).
- Niccolò Bigagli, Weijun Yuan, Siwei Zhang, Boris Bulatovic, Tijs Karman, Ian Stevenson, and Sebastian Will. Observation of bose-einstein condensation of dipolar molecules. *arXiv preprint arXiv:2312.10965*, 2023b. doi:doi.org/10.48550/arXiv.2312.10965.
- Niccolagli, Weijun Yuan, Siwei Zhang, Boris Bulatovic, Tijs Karman, Ian Stevenson, and Sebastian Will. Observation of bose-einstein condensation of dipolar molecules. *Nature*, 631(8020):289–293, 2024. doi:[10.1038/s41586-024-07492-z](https://doi.org/10.1038/s41586-024-07492-z).
- G. C. Bjorklund, M. D. Levenson, W. Lenth, and C. Ortiz. Frequency modulation (FM) spectroscopy. *Appl. Phys. B*, 32(3):145–152, 1983. doi:[10.1007/BF00688820](https://doi.org/10.1007/BF00688820).
- Eric D. Black. An introduction to pound-drever-hall laser frequency stabilization. *Am. J. Phys.*, 69:79, 2001. doi:[10.1119/1.1286663](https://doi.org/10.1119/1.1286663).
- Alexandre Blais, Arne L. Grimsmo, S. M. Girvin, and Andreas Wallraff. Circuit quantum electrodynamics. *Rev. Mod. Phys.*, 93:025005, May 2021. doi:[10.1103/RevModPhys.93.025005](https://doi.org/10.1103/RevModPhys.93.025005).
- Günther Blasbichler. Ein Lambdameter mit 10^{-7} Meßunsicherheit. Diploma thesis, 2000.
- Immanuel Bloch, Jean Dalibard, and Wilhelm Zwerger. Many-body physics with ultracold gases. *Rev. Mod. Phys.*, 80(3):885–964, July 2008. doi:[10.1103/RevModPhys.80.885](https://doi.org/10.1103/RevModPhys.80.885).
- Immanuel Bloch, Jean Dalibard, and Sylvain Nascimbene. Quantum simulations with ultracold quantum gases. *Nature Physics*, 8(4):267–276, 2012. doi:[10.1038/nphys2259](https://doi.org/10.1038/nphys2259).
- H. M. J. M. Boesten, A. J. Moerdijk, and B. J. Verhaar. Dipolar decay in two recent bose-einstein condensation experiments. *Phys. Rev. A*, 54:R29–R32, Jul 1996. doi:[10.1103/PhysRevA.54.R29](https://doi.org/10.1103/PhysRevA.54.R29).
- I. Boettcher, L. Bayha, D. Kedar, P. A. Murthy, M. Neidig, M. G. Ries, A. N. Wenz, G. Zürn, S. Jochim, and T. Enss. Equation of state of ultracold fermions in the 2D bec-bcs crossover region. *Phys. Rev. Lett.*, 116:045303, Jan 2016. doi:[10.1103/PhysRevLett.116.045303](https://doi.org/10.1103/PhysRevLett.116.045303).
- D. Bohm. Note on a theorem of bloch concerning possible causes of superconductivity. *Phys. Rev.*, 75:502–504, Feb 1949. doi:[10.1103/PhysRev.75.502](https://doi.org/10.1103/PhysRev.75.502).
- John L. Bohn, Ana Maria Rey, and Jun Ye. Cold molecules: Progress in quantum engineering of chemistry and quantum matter. *Science*, 357(6355, SI):1002–1010, SEP 8 2017. doi:[10.1126/science.aam6299](https://doi.org/10.1126/science.aam6299).
- D. Boiron, A. Michaud, P. Lemonde, Y. Castin, C. Salomon, S. Weyers, K. Szymaniec, L. Cognet, and A. Clairon. Laser cooling of cesium atoms in gray optical molasses down to 1.1 ??k . *Phys. Rev. A*, 53(6):R3734–R3737, June 1996. doi:[10.1103/PhysRevA.53.R3734](https://doi.org/10.1103/PhysRevA.53.R3734).
- K.-J. Boller, A. Imamoğlu, and S. E. Harris. Observation of electromagnetically induced transparency. *Phys. Rev. Lett.*, 66:2593–2596, May 1991. doi:[10.1103/PhysRevLett.66.2593](https://doi.org/10.1103/PhysRevLett.66.2593).
- Mateusz Borkowski. Optical lattice clocks with weakly bound molecules. *Phys. Rev. Lett.*, 120(8):083202, FEB 22 2018. doi:[10.1103/PhysRevLett.120.083202](https://doi.org/10.1103/PhysRevLett.120.083202).

- Mateusz Borkowski, Alexei A. Buchachenko, Roman Ciurylo, Paul S. Julienne, Hirotaka Yamada, Yuu Kikuchi, Yosuke Takasu, and Yoshiro Takahashi. Weakly bound molecules as sensors of new gravity like forces. *Sci. Rep.*, 9:14807, OCT 15 2019. doi:[10.1038/s41598-019-51346-y](https://doi.org/10.1038/s41598-019-51346-y).
- M. Born and R. Oppenheimer. Zur quantentheorie der molekeln. *Annalen der Physik*, 389(20):457–484, 1927. doi:<https://doi.org/10.1002/andp.19273892002>.
- Fabian Böttcher, Jan-Niklas Schmidt, Matthias Wenzel, Jens Hertkorn, Mingyang Guo, Tim Langen, and Tilman Pfau. Transient supersolid properties in an array of dipolar quantum droplets. *Phys. Rev. X*, 9:011051, Mar 2019. doi:[10.1103/PhysRevX.9.011051](https://doi.org/10.1103/PhysRevX.9.011051).
- Nadia Bouloufa, Anne Crubellier, and Olivier Dulieu. Photoassociative molecular spectroscopy for atomic radiative lifetimes. *Phys. Scr.*, 2009(T134):014014, 2009. doi:[10.1088/0031-8949/2009/T134/014014](https://doi.org/10.1088/0031-8949/2009/T134/014014).
- T. Bourdel, J. Cubizolles, L. Khaykovich, K. M. F. Magalhães, S. J. J. M. F. Kokkelmans, G. V. Shlyapnikov, and C. Salomon. Measurement of the interaction energy near a feshbach resonance in a ${}^6\text{Li}$ fermi gas. *Phys. Rev. Lett.*, 91:020402, Jul 2003. doi:[10.1103/PhysRevLett.91.020402](https://doi.org/10.1103/PhysRevLett.91.020402).
- T. Bourdel, L. Khaykovich, J. Cubizolles, J. Zhang, F. Chevy, M. Teichmann, L. Tarruell, S. J. J. M. F. Kokkelmans, and C. Salomon. Experimental study of the bec-bcs crossover region in lithium 6. *Phys. Rev. Lett.*, 93(5):050401–, July 2004. doi:[10.1103/PhysRevLett.93.050401](https://doi.org/10.1103/PhysRevLett.93.050401).
- Johannes F. S. Brachmann, Thomas Kinder, and Kai Dieckmann. Calibrating an interferometric laser frequency stabilization to megahertz precision. *Appl. Opt.*, 51(22):5517–5521, Aug 2012. doi:[10.1364/AO.51.005517](https://doi.org/10.1364/AO.51.005517).
- Johannes Felix Simon Brachmann. *Towards ${}^6\text{Li}$ - ${}^{40}\text{K}$ ground state molecules*. PhD thesis, Ludwig-Maximilians-Universität, München, 2012a.
- Johannes Felix Simon Brachmann. *Towards ${}^6\text{Li}$ - ${}^{40}\text{K}$ ground state molecules*. PhD thesis, MPQ-LMU, Munich, 2012b.
- C. C. Bradley, C. A. Sackett, J. J. Tollett, and R. G. Hulet. Evidence of bose-einstein condensation in an atomic gas with attractive interactions. *Phys. Rev. Lett.*, 75:1687–1690, Aug 1995. doi:[10.1103/PhysRevLett.75.1687](https://doi.org/10.1103/PhysRevLett.75.1687).
- Joachain Bransden, B.H. *Physics of atoms and molecules*. Prentice Hall, 2003.
- R. A. Brooks, C. H. Anderson, and N. F. Ramsey. Rotational magnetic moments of the alkali molecules. *Phys. Rev.*, 136:A62–A68, Oct 1964. doi:[10.1103/PhysRev.136.A62](https://doi.org/10.1103/PhysRev.136.A62).
- J. M. Brown and A. Carrington. *Rotational Spectroscopy of Diatomic Molecules*, chapter 10.7.1., page 813. Cambridge University Press, 2003a.
- M. John Brown and Alan Carrington. *Rotational Spectroscopy of Diatomic Molecules*. Cambridge University Press, 2003b.
- Pablo J. Bruna and Friedrich Grein. The $\text{X}^2\Pi$ and $\text{A}^2\Sigma^+$ states of FH^+ , ClH^+ and BrH^+ : theoretical study of their g-factors and fine/hyperfine structures. *Molecular Physics*, 104(3):429–446, 2006. doi:[10.1080/00268970500404380](https://doi.org/10.1080/00268970500404380).

- Nikolous Walter Buchheim. *Dual-species apparatus for creating a dipolar quantum gas of $^{23}\text{Na}^{40}\text{K}$ molecules*. PhD thesis, Ludwig-Maximilians-Universität-München, 2015.
- H. P. Büchler, E. Demler, M. Lukin, A. Micheli, N. Prokof'ev, G. Pupillo, and P. Zoller. Strongly Correlated 2D Quantum Phases with Cold Polar Molecules: Controlling the Shape of the Interaction Potential. *Phys. Rev. Lett.*, 98:060404, Feb 2007. doi:[10.1103/PhysRevLett.98.060404](https://doi.org/10.1103/PhysRevLett.98.060404).
- A. Burchianti, G. Valtolina, J. A. Seman, E. Pace, M. De Pas, M. Inguscio, M. Zaccanti, and G. Roati. Efficient all-optical production of large ^6Li quantum gases using D_1 gray-molasses cooling. *Phys. Rev. A*, 90:043408, Oct 2014. doi:[10.1103/PhysRevA.90.043408](https://doi.org/10.1103/PhysRevA.90.043408).
- Philip George Burke. *R-Matrix Theory of Atomic Collisions*. Springer, 2011. doi:[10.1007/978-3-642-15931-2](https://doi.org/10.1007/978-3-642-15931-2).
- Béatrice Bussery, Yamina Achkar, and Monique Aubert-Frécon. Long-range molecular states dissociating to the three or four lowest asymptotes for the ten heteronuclear diatomic alkali molecules. *Chem. Phys.*, 116(3):319–338, 1987. doi:[http://dx.doi.org/10.1016/0301-0104\(87\)80202-1](http://dx.doi.org/10.1016/0301-0104(87)80202-1).
- D. A. Butts and D. S. Rokhsar. Trapped fermi gases. *Phys. Rev. A*, 55(6):4346–4350, June 1997. doi:[10.1103/PhysRevA.55.4346](https://doi.org/10.1103/PhysRevA.55.4346).
- W. B. Cairncross and J. Ye. Atoms and molecules in the search for time-reversal symmetry violation. *Nat. Rev. Phys.*, 1(8):510–521, August 2019.
- William B. Cairncross, Daniel N. Gresh, Matt Grau, Kevin C. Cossel, Tanya S. Roussy, Yiqi Ni, Yan Zhou, Jun Ye, and Eric A. Cornell. Precision measurement of the electron's electric dipole moment using trapped molecular ions. *Phys. Rev. Lett.*, 119:153001, Oct 2017. doi:[10.1103/PhysRevLett.119.153001](https://doi.org/10.1103/PhysRevLett.119.153001).
- William B. Cairncross, Jessie T. Zhang, Lewis R. B. Picard, Yichao Yu, Kenneth Wang, and Kang-Kuen Ni. Assembly of a rovibrational ground state molecule in an optical tweezer. *Phys. Rev. Lett.*, 126:123402, Mar 2021. doi:[10.1103/PhysRevLett.126.123402](https://doi.org/10.1103/PhysRevLett.126.123402).
- H. R. Carleton and W. T. Maloney. A balanced optical heterodyne detector. *Appl. Opt.*, 7 (6):1241–1243, Jun 1968. doi:[10.1364/AO.7.001241](https://doi.org/10.1364/AO.7.001241).
- J. Carlson, Stefano Gandolfi, Kevin E. Schmidt, and Shiwei Zhang. Auxiliary-field quantum Monte Carlo method for strongly paired fermions. *Phys. Rev. A*, 84:061602, Dec 2011. doi:[10.1103/PhysRevA.84.061602](https://doi.org/10.1103/PhysRevA.84.061602).
- Lincoln D Carr, David DeMille, Roman V Krems, and Jun Ye. Cold and ultracold molecules: science, technology and applications. *New J. Phys.*, 11(5):055049, 2009.
- A Carrington, CA Leach, AJ Marr, AM Shaw, MR Viant, JM Hutson, and MM Law. Microwave spectroscopy and interaction potential of the long-range He^+ -ion. *J. Chem. Phys.*, 102(6) : 2379 – 2403, FEB81995. doi : [10.1063/1.468670](https://doi.org/10.1063/1.468670).
- Y. Castin and R. Dum. Bose-einstein condensates in time dependent traps. *Phys. Rev. Lett.*, 77:5315–5319, Dec 1996. doi:[10.1103/PhysRevLett.77.5315](https://doi.org/10.1103/PhysRevLett.77.5315).
- Y. Castin, H. Wallis, and J. Dalibard. Limit of Doppler cooling. *Journal of the Optical Society of America B*, 6:2046–2057, 1989. doi:[10.1364/JOSAB.6.002046](https://doi.org/10.1364/JOSAB.6.002046).

- F. S. Cataliotti, E. A. Cornell, C. Fort, M. Inguscio, F. Marin, M. Prevedelli, L. Ricci, and G. M. Tino. Magneto-optical trapping of fermionic potassium atoms. *Phys. Rev. A*, 57:1136–1138, Feb 1998. doi:[10.1103/PhysRevA.57.1136](https://doi.org/10.1103/PhysRevA.57.1136).
- T Chanelière, L He, R. Kaiser, and D. Wilkowski. Three dimensional cooling and trapping with a narrow line. *Eur. Phys. J. D*, 46:507–515, 2008. doi:[10.1140/epjd/e2007-00329-8](https://doi.org/10.1140/epjd/e2007-00329-8).
- Yu-Xin Chao, Zhen-Xing Hua, Xin-Hui Liang, Zong-Pei Yue, Li You, and Meng Khoon Tey. Pound–drever–hall feedforward: laser phase noise suppression beyond feedback. *Optica*, 11(7):945–950, Jul 2024. doi:[10.1364/OPTICA.516838](https://doi.org/10.1364/OPTICA.516838).
- Saptarishi Chaudhuri. *Bose-Einstein Condensation of Rubidium Atoms in an Infra-Red Optical Dipole Trap*. PhD thesis, Tata Institute of Fundamental Research, 2008.
- P. Cheiney, C. R. Cabrera, J. Sanz, B. Naylor, L. Tanzi, and L. Tarruell. Bright soliton to quantum droplet transition in a mixture of bose-einstein condensates. *Phys. Rev. Lett.*, 120: 135301, Mar 2018. doi:[10.1103/PhysRevLett.120.135301](https://doi.org/10.1103/PhysRevLett.120.135301).
- Xing-Yan Chen, Marcel Duda, Andreas Schindewolf, Roman Bause, Immanuel Bloch, and Xin-Yu Luo. Suppression of unitary three-body loss in a degenerate bose-fermi mixture. *Physical Review Letters*, 128(15):153401, 2022. doi:doi.org/10.1103/PhysRevLett.128.153401.
- Xing-Yan Chen, Andreas Schindewolf, Sebastian Eppelt, Roman Bause, Marcel Duda, Shrestha Biswas, Tijs Karman, Timon Hilker, Immanuel Bloch, and Xin-Yu Luo. Field-linked resonances of polar molecules. *Nature*, 614(7946):59, 02 2023. doi:[10.1038/s41586-022-05651-8](https://doi.org/10.1038/s41586-022-05651-8).
- Xing-Yan Chen, Shrestha Biswas, Sebastian Eppelt, Andreas Schindewolf, Fulin Deng, Tao Shi, Su Yi, Timon A Hilker, Immanuel Bloch, and Xin-Yu Luo. Ultracold field-linked tetratomic molecules. *Nature*, 626(7998):283–287, 2024. doi:doi.org/10.1038/s41586-023-06986-6.
- L. W. Cheuk, M. A. Nichols, K.R. Lawrence, M. Okan, H. Zhang, E. Khatami, N. Trivedi, T. Paiva, M. Rigol, and M. W. Zwierlein. Observation of spatial charge and spin correlations in the 2D fermi-hubbard model. arXiv:1606.04089, 2016a.
- Lawrence W. Cheuk, Matthew A. Nichols, Katherine R. Lawrence, Melih Okan, Hao Zhang, and Martin W. Zwierlein. Observation of 2D fermionic mott insulators of ^{40}K with single-site resolution. *Phys. Rev. Lett.*, 116:235301, Jun 2016b. doi:[10.1103/PhysRevLett.116.235301](https://doi.org/10.1103/PhysRevLett.116.235301).
- Lawrence W. Cheuk, Loïc Anderegg, Yicheng Bao, Sean Burchesky, Scarlett S. Yu, Wolfgang Ketterle, Kang-Kuen Ni, and John M. Doyle. Observation of collisions between two ultracold ground-state caf molecules. *Phys. Rev. Lett.*, 125:043401, Jul 2020. doi:[10.1103/PhysRevLett.125.043401](https://doi.org/10.1103/PhysRevLett.125.043401).
- Ananth P. Chikkatur. *Colliding and Moving Bose-Einstein Condensates: Studies of superfluidity and optical tweezers for condensate transport*. PhD thesis, MASSACHUSETTS INSTITUTE OF TECHNOLOGY, 2002.
- C. Chin, M. Bartenstein, A. Altmeyer, S. Riedl, S. Jochim, J. Hecker Denschlag, and R. Grimm. Observation of the pairing gap in a strongly interacting fermi gas. *Science*, 305(5687):1128–1130, 2004. doi:[10.1126/science.1100818](https://doi.org/10.1126/science.1100818).
- Cheng Chin. A simple model of feshbach molecules, February 2008.
- Cheng Chin and Rudolf Grimm. Thermal equilibrium and efficient evaporation of an ultracold atom-molecule mixture. *Phys. Rev. A*, 69(3):033612–, March 2004. doi:[10.1103/PhysRevA.69.033612](https://doi.org/10.1103/PhysRevA.69.033612).

- Cheng Chin, Andrew J Kerman, Vladan Vuletić, and Steven Chu. Sensitive detection of cold cesium molecules formed on feshbach resonances. *Physical review letters*, 90(3):033201, 2003.
- Cheng Chin, Rudolf Grimm, Paul Julienne, and Eite Tiesinga. Feshbach resonances in ultracold gases. *Rev. Mod. Phys.*, 82:1225–1286, Apr 2010. doi:[10.1103/RevModPhys.82.1225](https://doi.org/10.1103/RevModPhys.82.1225).
- M. L. Chiofalo, S. J. J. M. F. Kokkelmans, J. N. Milstein, and M. J. Holland. Signatures of resonance superfluidity in a quantum fermi gas. *Phys. Rev. Lett.*, 88:090402, Feb 2002. doi:[10.1103/PhysRevLett.88.090402](https://doi.org/10.1103/PhysRevLett.88.090402).
- Amodsen Chotia, Brian Neyenhuis, Steven A. Moses, Bo Yan, Jacob P. Covey, Michael Foss-Feig, Ana Maria Rey, Deborah S. Jin, and Jun Ye. Long-lived dipolar molecules and feshbach molecules in a 3d optical lattice. *Phys. Rev. Lett.*, 108:080405, Feb 2012. doi:[10.1103/PhysRevLett.108.080405](https://doi.org/10.1103/PhysRevLett.108.080405).
- Lysander Christakis, Jason S. Rosenberg, Ravin Raj, Sungjae Chi, Alan Morningstar, David A. Huse, Zoe Z. Yan, and Waseem S. Bakr. Probing site-resolved correlations in a spin system of ultracold molecules. *Nature*, 614(7946):64–69, 2023. doi:[10.1038/s41586-022-05558-4](https://doi.org/10.1038/s41586-022-05558-4).
- Arthur Christianen, Martin W. Zwierlein, Gerrit C. Groenenboom, and Tijs Karman. Photoinduced two-body loss of ultracold molecules. *Phys. Rev. Lett.*, 123:123402, 2019. doi:[10.1103/PhysRevLett.123.123402](https://doi.org/10.1103/PhysRevLett.123.123402).
- Steven Chu, L. Hollberg, J. E. Bjorkholm, Alex Cable, and A. Ashkin. Three-dimensional viscous confinement and cooling of atoms by resonance radiation pressure. *Phys. Rev. Lett.*, 55(1):48–51, July 1985. doi:[10.1103/PhysRevLett.55.48](https://doi.org/10.1103/PhysRevLett.55.48).
- Steven Chu, J. E. Bjorkholm, A. Ashkin, and A. Cable. Experimental observation of optically trapped atoms. *Phys. Rev. Lett.*, 57(3):314–317, July 1986. doi:[10.1103/PhysRevLett.57.314](https://doi.org/10.1103/PhysRevLett.57.314).
- Logan W Clark, Anita Gaj, Lei Feng, and Cheng Chin. Collective emission of matter-wave jets from driven bose-einstein condensates. *Nature*, 551(7680):356–359, 2017. doi:[10.1038/nature24272](https://doi.org/10.1038/nature24272).
- CODATA2018.
- C. Cohen-Tannoudji and D. Guéry-Odelin. *Advances in Atomic Physics*. World Scientific, 2011.
- Claude Cohen-Tannoudji, Jacques Dupont-Roc, and Gilbert Grynberg. *Atom - Photon Interactions: Basic Process and Applications*. Wiley-VCH Verlag GmbH, 2008. ISBN 9783527617197. doi:[10.1002/9783527617197.fmatter](https://doi.org/10.1002/9783527617197.fmatter).
- Alejandra L. Collopy, Shiqian Ding, Yewei Wu, Ian A. Finneran, Loïc Anderegg, Benjamin L. Augenbraun, John M. Doyle, and Jun Ye. 3d magneto-optical trap of yttrium monoxide. *Phys. Rev. Lett.*, 121:213201, Nov 2018. doi:[10.1103/PhysRevLett.121.213201](https://doi.org/10.1103/PhysRevLett.121.213201).
- D Comparat. Improved leroy-bernstein near-dissociation expansion formula, and prospect for photoassociation spectroscopy. *J. Chem. Phys.*, 120(3):1318–1329, JAN 15 2004. doi:[10.1063/1.1626539](https://doi.org/10.1063/1.1626539).
- S. L. Cornish, N. R. Claussen, J. L. Roberts, E. A. Cornell, and C. E. Wieman. Stable ^{85}Rb Bose-Einstein condensates with widely tunable interactions. *Phys. Rev. Lett.*, 85:1795–1798, Aug 2000. doi:[10.1103/PhysRevLett.85.1795](https://doi.org/10.1103/PhysRevLett.85.1795).
- L. Costa, J. Brachmann, A.-C. Voigt, C. Hahn, M. Taglieber, T. W. Hänsch, and K. Dieckmann. *s*-wave Interaction in a Two-Species Fermi-Fermi Mixture at a Narrow Feshbach Resonance. *Phys. Rev. Lett.*, 105:123201, Sep 2010. doi:[10.1103/PhysRevLett.105.123201](https://doi.org/10.1103/PhysRevLett.105.123201).

- Louis Costa. *An interacting Fermi-Fermi mixture at the crossover of a narrow Feshbach resonance*. PhD thesis, Ludwig-Maximilians-Universität München, 2011.
- Joseph Noël Robin Côté. *Ultra-Cold Collisions of Identical Atoms*. PhD thesis, MASSACHUSETTS INSTITUTE OF TECHNOLOGY, 1995.
- R. Côté and A. Dalgarno. Photoassociation intensities and radiative trap loss in lithium. *Phys. Rev. A*, 58:498–508, Jul 1998. doi:[10.1103/PhysRevA.58.498](https://doi.org/10.1103/PhysRevA.58.498).
- R. Côté, A. Dalgarno, and M. J. Jamieson. Elastic scattering of two ^7Li atoms. *Phys. Rev. A*, 50:399–404, Jul 1994. doi:[10.1103/PhysRevA.50.399](https://doi.org/10.1103/PhysRevA.50.399).
- Ph. Courteille, R. S. Freeland, D. J. Heinzen, F. A. van Abeelen, and B. J. Verhaar. Observation of a feshbach resonance in cold atom scattering. *Phys. Rev. Lett.*, 81:69–72, Jul 1998. doi:[10.1103/PhysRevLett.81.69](https://doi.org/10.1103/PhysRevLett.81.69).
- A. Couvert, T. Kawalec, G. Reinaudi, and D. Guéry-Odelin. Optimal transport of ultracold atoms in the non-adiabatic regime. *EPL (Europhysics Letters)*, 83(1):13001, 2008. doi:[10.1209/0295-5075/83/13001](https://doi.org/10.1209/0295-5075/83/13001).
- Jacob P Covey, Steven A Moses, Martin Gärttner, Arghavan Safavi-Naini, Matthew T Mieckowski, Zhengkun Fu, Johannes Schachenmayer, Paul S Julienne, Ana Maria Rey, Deborah S Jin, et al. Doublon dynamics and polar molecule production in an optical lattice. *Nature communications*, 7(1):11279, 2016. doi:doi.org/10.1038/ncomms11279.
- Jacob P Covey, Luigi De Marco, Óscar L Acevedo, Ana Maria Rey, and Jun Ye. An approach to spin-resolved molecular gas microscopy. *New Journal of Physics*, 20(4):043031, 2018. doi:[10.1088/1367-2630/aaba65](https://doi.org/10.1088/1367-2630/aaba65).
- J. Cubizolles, T. Bourdel, S. J. J. M. F. Kokkelmans, G. V. Shlyapnikov, and C. Salomon. Production of long-lived ultracold li_2 molecules from a fermi gas. *Phys. Rev. Lett.*, 91:240401, Dec 2003. doi:[10.1103/PhysRevLett.91.240401](https://doi.org/10.1103/PhysRevLett.91.240401).
- Paul J. Dagdigian and Lennard Wharton. Molecular Beam Electric Deflection and Resonance Spectroscopy of the Heteronuclear Alkali Dimers: $^{39}\text{K}7\text{Li}$, $\text{Rb}7\text{Li}$, $^{39}\text{K}23\text{Na}$, $\text{Rb}23\text{Na}$, and $^{133}\text{Cs}23\text{Na}$. *J. Chem. Phys.*, 57(4):1487–1496, 09 2003. doi:[10.1063/1.1678429](https://doi.org/10.1063/1.1678429).
- J. Dalibard and C. Cohen-Tannoudji. Laser cooling below the Doppler limit by polarization gradients: simple theoretical models. *Journal of the Optical Society of America B*, 6:2023–2045, 1989. doi:[10.1364/JOSAB.6.002023](https://doi.org/10.1364/JOSAB.6.002023).
- Johann G. Danzl, Elmar Haller, Mattias Gustavsson, Manfred J. Mark, Russell Hart, Nadia Bouloufa, Olivier Dulieu, Helmut Ritsch, and Hanns-Christoph Nägerl. Quantum Gas of Deeply Bound Ground State Molecules. *Science*, 321(5892):1062–1066, 2008. doi:[10.1126/science.1159909](https://doi.org/10.1126/science.1159909).
- Riadh Dardouri, Héla Habli, Brahim Oujia, and Florent Xavier Gadéa. Theoretical study of the electronic structure of kli molecule: Adiabatic and diabatic potential energy curves and dipole moments. *Chemical Physics*, 399:65–79, 2012. doi:<https://doi.org/10.1016/j.chemphys.2011.07.010>. New trends in atomic and molecular clusters.
- Nikesh S. Dattani. Analytic potentials and vibrational energies for Li_2 states dissociating to Li ($2S$) + Li ($3P$). part 1: The $^{2S+1}\Pi_{u/g}$ states. arXiv:1509.07041, September 2015.

- Nikesh S. Dattani and Robert J. LeRoy. A DPF data analysis yields accurate analytic potentials for $\text{Li}_2(\text{A}^1\Sigma_u^+)$ and $\text{Li}_2(1^3\Sigma_g^+)$ that incorporate 3-state mixing near the $\text{Li}_2(1^3\Sigma_g^+)$ state asymptote. *J. Mol. Spectrosc.*, 268:199 – 210, 2011. doi:[10.1016/j.jms.2011.03.030](https://doi.org/10.1016/j.jms.2011.03.030).
- K. B. Davis, M. O. Mewes, M. R. Andrews, N. J. van Druten, D. S. Durfee, D. M. Kurn, and W. Ketterle. Bose-einstein condensation in a gas of sodium atoms. *Phys. Rev. Lett.*, 75: 3969–3973, Nov 1995. doi:[10.1103/PhysRevLett.75.3969](https://doi.org/10.1103/PhysRevLett.75.3969).
- Luigi De Marco, Giacomo Valtolina, Kyle Matsuda, William G Tobias, Jacob P Covey, and Jun Ye. A degenerate fermi gas of polar molecules. *Science*, 363(6429):853–856, 2019a.
- Luigi De Marco, Giacomo Valtolina, Kyle Matsuda, William G. Tobias, Jacob P. Covey, and Jun Ye. A degenerate Fermi gas of polar molecules. *Science*, 363(6429):853, FEB 22 2019b. doi:[10.1126/science.aau7230](https://doi.org/10.1126/science.aau7230).
- M. H. G. de Miranda, A. Chotia, B. Neyenhuis, D. Wang, G. Quner, S. Ospelkaus, J. L. Bohn, J. Ye, and D. S. Jin. Controlling the quantum stereodynamics of ultracold bimolecular reactions. *Nature Physics*, 7(6):502–507, 2011. doi:[10.1038/nphys1939](https://doi.org/10.1038/nphys1939).
- Markus Debatin, Tetsu Takekoshi, Raffael Rameshan, Lukas Reichsollner, Francesca Ferlaino, Rudolf Grimm, Romain Vexiau, Nadia Bouloufa, Olivier Dulieu, and Hanns-Christoph Nagerl. Molecular spectroscopy for ground-state transfer of ultracold rbcs molecules. *Phys. Chem. Chem. Phys.*, 13:18926–18935, 2011. doi:[10.1039/C1CP21769K](https://doi.org/10.1039/C1CP21769K).
- J. Deiglmayr, A. Grochola, M. Repp, K. Mörtlbauer, C. Glück, J. Lange, O. Dulieu, R. Wester, and M. Weidemüller. Formation of ultracold polar molecules in the rovibrational ground state. *Phys. Rev. Lett.*, 101:133004, Sep 2008a. doi:[10.1103/PhysRevLett.101.133004](https://doi.org/10.1103/PhysRevLett.101.133004).
- Johannes Deiglmayr, Mireille Aymar, Roland Wester, Matthias Weidemüller, and Olivier Dulieu. Calculations of static dipole polarizabilities of alkali dimers: Prospects for alignment of ultracold molecules. *J. Chem. Phys.*, 129(6):064309, 2008b. doi:[10.1063/1.2960624](https://doi.org/10.1063/1.2960624).
- B. DeMarco and D. S. Jin. Onset of fermi degeneracy in a trapped atomic gas. *Science*, 285 (5434):1703–1706, 1999. doi:[10.1126/science.285.5434.1703](https://doi.org/10.1126/science.285.5434.1703).
- B. DeMarco, H. Rohner, and D. S. Jin. An enriched 40k source for fermionic atom studies. *Review of Scientific Instruments*, 70(4):1967–1969, 1999. doi:[10.1063/1.1149695](https://doi.org/10.1063/1.1149695).
- D. DeMille. Quantum computation with trapped polar molecules. *Phys. Rev. Lett.*, 88:067901, Jan 2002. doi:[10.1103/PhysRevLett.88.067901](https://doi.org/10.1103/PhysRevLett.88.067901).
- D. DeMille, S. B. Cahn, D. Murphree, D. A. Rahmlow, and M. G. Kozlov. Using molecules to measure nuclear spin-dependent parity violation. *Phys. Rev. Lett.*, 100:023003, Jan 2008. doi:[10.1103/PhysRevLett.100.023003](https://doi.org/10.1103/PhysRevLett.100.023003).
- Fulin Deng, Xing-Yan Chen, Xin-Yu Luo, Wenxian Zhang, Su Yi, and Tao Shi. Effective potential and superfluidity of microwave-shielded polar molecules. *Phys. Rev. Lett.*, 130: 183001, May 2023. doi:[10.1103/PhysRevLett.130.183001](https://doi.org/10.1103/PhysRevLett.130.183001).
- J Hecker Denschlag, J E Simsarian, H Hner, C McKenzie, A Browaeys, D Cho, K Helmerson, S L Rolston, and W D Phillips. A bose-einstein condensate in an optical lattice. *Journal of Physics B: Atomic, Molecular and Optical Physics*, 35(14):3095, jul 2002. doi:[10.1088/0953-4075/35/14/307](https://doi.org/10.1088/0953-4075/35/14/307).

- Marshall T DePue, S Lukman Winoto, D.J Han, and David S Weiss. Transient compression of a {MOT} and high intensity fluorescent imaging of optically thick clouds of atoms. *Opt. Commun.*, 180(1-3):73 – 79, 2000a. doi:[10.1016/S0030-4018\(00\)00701-X](https://doi.org/10.1016/S0030-4018(00)00701-X).
- Marshall T DePue, S Lukman Winoto, D.J Han, and David S Weiss. Transient compression of a {MOT} and high intensity fluorescent imaging of optically thick clouds of atoms. *Opt. Commun.*, 180(1-3):73 – 79, 2000b. doi:[10.1016/S0030-4018\(00\)00701-X](https://doi.org/10.1016/S0030-4018(00)00701-X).
- B. J. DeSalvo, M. Yan, P. G. Mickelson, Y. N. Martinez de Escobar, and T. C. Killian. Degenerate fermi gas of ^{87}Sr . *Phys. Rev. Lett.*, 105:030402, Jul 2010. doi:[10.1103/PhysRevLett.105.030402](https://doi.org/10.1103/PhysRevLett.105.030402).
- Scott A. Diddams, David J. Jones, Jun Ye, Steven T. Cundiff, John L. Hall, Jinendra K. Ranka, Robert S. Windeler, Ronald Holzwarth, Thomas Udem, and T. W. Hänsch. Direct link between microwave and optical frequencies with a 300 thz femtosecond laser comb. *Phys. Rev. Lett.*, 84:5102–5105, May 2000. doi:[10.1103/PhysRevLett.84.5102](https://doi.org/10.1103/PhysRevLett.84.5102).
- K. Dieckmann, C. A. Stan, S. Gupta, Z. Hadzibabic, C. H. Schunck, and W. Ketterle. Decay of an ultracold fermionic lithium gas near a feshbach resonance. *Phys. Rev. Lett.*, 89:203201, Oct 2002. doi:[10.1103/PhysRevLett.89.203201](https://doi.org/10.1103/PhysRevLett.89.203201).
- Kai Dieckmann. *Bose-Einstein Condensation with High Atom Number in a Deep Magnetic Trap*. PhD thesis, Universiteit van Amsterdam, 2001.
- Shiqian Ding, Yewei Wu, Ian A. Finneran, Justin J. Burau, and Jun Ye. Sub-doppler cooling and compressed trapping of yo molecules at μK temperatures. *Phys. Rev. X*, 10:021049, Jun 2020. doi:[10.1103/PhysRevX.10.021049](https://doi.org/10.1103/PhysRevX.10.021049).
- Elizabeth A Donley, Neil R Claussen, Sarah T Thompson, and Carl E Wieman. Atom–molecule coherence in a Bose–Einstein condensate. *Nature*, 417(6888):529–533, 2002. doi:[10.1038/417529a](https://doi.org/10.1038/417529a).
- R.W.P. Drever, J.L. Hall, F.V. Kowalski, J. Hough, G.M. Ford, A.J. Munley, and H. Ward. Laser phase and frequency stabilization using an optical resonator. *Appl. Phys. B*, 31(2):97–105–, 1983. doi:[10.1007/BF00702605](https://doi.org/10.1007/BF00702605).
- P. M. Duarte, R. A. Hart, J. M. Hitchcock, T. A. Corcovilos, T.-L. Yang, A. Reed, and R. G. Hulet. All-optical production of a lithium quantum gas using narrow-line laser cooling. *Phys. Rev. A*, 84(6):061406–, December 2011. doi:[10.1103/PhysRevA.84.061406](https://doi.org/10.1103/PhysRevA.84.061406).
- R. Dubessy, K. Merloti, L. Longchambon, P.-E. Pottie, T. Liennard, A. Perrin, V. Lorent, and H. Perrin. Rubidium-87 bose-einstein condensate in an optically plugged quadrupole trap. *Phys. Rev. A*, 85:013643, Jan 2012. doi:[10.1103/PhysRevA.85.013643](https://doi.org/10.1103/PhysRevA.85.013643).
- Marcel Duda, Xing-Yan Chen, Andreas Schindewolf, Roman Bause, Jonas von Milczewski, Richard Schmidt, Immanuel Bloch, and Xin-Yu Luo. Transition from a polaronic condensate to a degenerate fermi gas of heteronuclear molecules. *Nature Physics*, 19:720–725, 02 2023. doi:[10.1038/s41567-023-01948-1](https://doi.org/10.1038/s41567-023-01948-1).
- R.A. Duine and H.T.C. Stoof. Atom-molecule coherence in Bose gases. *Phys. Rep.*, 396(3):115 – 195, 2004. doi:[10.1016/j.physrep.2004.03.003](https://doi.org/10.1016/j.physrep.2004.03.003).
- O Dulieu and C Gabbanini. The formation and interactions of cold and ultracold molecules: new challenges for interdisciplinary physics. *Reports on Progress in Physics*, 72(8):086401, jul 2009. doi:[10.1088/0034-4885/72/8/086401](https://doi.org/10.1088/0034-4885/72/8/086401).

J. L. Dunham. The energy levels of a rotating vibrator. *Phys. Rev.*, 41:721–731, Sep 1932. doi:[10.1103/PhysRev.41.721](https://doi.org/10.1103/PhysRev.41.721).

Stephan Dürr, Thomas Volz, Andreas Marte, and Gerhard Rempe. Observation of molecules produced from a Bose-Einstein condensate. *Phys. Rev. Lett.*, 92:020406, Jan 2004a. doi:[10.1103/PhysRevLett.92.020406](https://doi.org/10.1103/PhysRevLett.92.020406).

Stephan Dürr, Thomas Volz, Andreas Marte, and Gerhard Rempe. Observation of molecules produced from a bose-einstein condensate. *Phys. Rev. Lett.*, 92:020406, Jan 2004b. doi:[10.1103/PhysRevLett.92.020406](https://doi.org/10.1103/PhysRevLett.92.020406).

P.Paul Dyke. *Quasi Two-Dimensional 6Li Fermi ga*. PhD thesis, Swinburne University of Technology, 2010.

Sepehr Ebadi, Tout T Wang, Harry Levine, Alexander Keesling, Giulia Semeghini, Ahmed Omran, Dolev Bluvstein, Rhine Samajdar, Hannes Pichler, Wen Wei Ho, et al. Quantum phases of matter on a 256-atom programmable quantum simulator. *Nature*, 595(7866):227–232, 2021. doi:[10.1038/s41586-021-03582-4](https://doi.org/10.1038/s41586-021-03582-4).

Christoph Eigenwillig. Optimierte herstellung einer ultrakalten bose-fermi-mischung in der magnetfalle. Diploma Thesis, 2007.

F Engelke, H Hage, and U Sprick. The b1p-x1s+ system of k39li6 and k39li7_{highresolutionlaserexcitationandfluorescencespectroscopyusingselectivelydetectedlaser-inducedfluorescence(sdlif)inmolecular-beamandinjectionheatpipe(ihp)}. *Chem. Phys.*, 88(3) : 443 – 453, 1984. doi : [10.1016/0301-0104\(84\)87010-X](https://doi.org/10.1016/0301-0104(84)87010-X).

K. Enomoto, K. Kasa, M. Kitagawa, and Y. Takahashi. Optical feshbach resonance using the intercombination transition. *Phys. Rev. Lett.*, 101:203201, Nov 2008. doi:[10.1103/PhysRevLett.101.203201](https://doi.org/10.1103/PhysRevLett.101.203201).

Tilman Esslinger. Fermi-hubbard physics with atoms in an optical lattice. *Annu. Rev. Condens. Matter Phys.*, 1(1):129–152, July 2010. doi:[10.1146/annurev-conmatphys-070909-104059](https://doi.org/10.1146/annurev-conmatphys-070909-104059).

Tilman Esslinger, Immanuel Bloch, and Theodor W. Hänsch. Bose-einstein condensation in a quadrupole-ioffe-configuration trap. *Phys. Rev. A*, 58:R2664–R2667, Oct 1998. doi:[10.1103/PhysRevA.58.R2664](https://doi.org/10.1103/PhysRevA.58.R2664).

Stephan Falke, Eberhard Tiemann, Christian Lisdat, Harald Schnatz, and Gesine Grosche. Transition frequencies of the d lines of ³⁹K, ⁴⁰K, and ⁴¹K measured with a femtosecond laser frequency comb. *Phys. Rev. A*, 74:032503, Sep 2006. doi:[10.1103/PhysRevA.74.032503](https://doi.org/10.1103/PhysRevA.74.032503).

D. Rio Fernandes, F. Sievers, N. Kretzschmar, S. Wu, C. Salomon, and F. Chevy. Sub-Doppler laser cooling of fermionic 40 k atoms in three-dimensional gray optical molasses. *EPL (Europhysics Letters)*, 100(6):63001, 2012. doi:[10.1209/0295-5075/100/63001](https://doi.org/10.1209/0295-5075/100/63001).

Igor Ferrier-Barbut, Holger Kadau, Matthias Schmitt, Matthias Wenzel, and Tilman Pfau. Observation of quantum droplets in a strongly dipolar bose gas. *Phys. Rev. Lett.*, 116:215301, May 2016. doi:[10.1103/PhysRevLett.116.215301](https://doi.org/10.1103/PhysRevLett.116.215301).

A. Fioretti, D. Comparat, A. Crubellier, O. Dulieu, F. Masnou-Seeuws, and P. Pillet. Formation of cold cs₂ molecules through photoassociation. *Phys. Rev. Lett.*, 80:4402–4405, May 1998. doi:[10.1103/PhysRevLett.80.4402](https://doi.org/10.1103/PhysRevLett.80.4402).

- Matthew P. A. Fisher, Peter B. Weichman, G. Grinstein, and Daniel S. Fisher. Boson localization and the superfluid-insulator transition. *Phys. Rev. B*, 40:546–570, Jul 1989. doi:[10.1103/PhysRevB.40.546](https://doi.org/10.1103/PhysRevB.40.546).
- N.J. Fitch and M.R. Tarbutt. Chapter three - laser-cooled molecules. volume 70 of *Advances In Atomic, Molecular, and Optical Physics*, pages 157–262. Academic Press, 2021. doi:<https://doi.org/10.1016/bs.aamop.2021.04.003>.
- Michael Fleischhauer, Atac Imamoglu, and Jonathan P. Marangos. Electromagnetically induced transparency: Optics in coherent media. *Rev. Mod. Phys.*, 77:633–673, Jul 2005. doi:[10.1103/RevModPhys.77.633](https://doi.org/10.1103/RevModPhys.77.633).
- Christopher J. Foot. *Atomic Physics*. Oxford University Press, 2005.
- C. Fort, A. Bambini, L. Cacciapuoti, F.S. Cataliotti, M. Prevedelli, G.M. Tino, and M. Inguscio. Cooling mechanisms in potassium magneto-optical traps. *The European Physical Journal D - Atomic, Molecular, Optical and Plasma Physics*, 3(2):113–118, 1998. doi:[10.1007/s100530050154](https://doi.org/10.1007/s100530050154).
- James Franck and EG Dymond. Elementary processes of photochemical reactions. *Transactions of the Faraday Society*, 21(February):536–542, 1926.
- B. Fröhlich, T. Lahaye, B. Kaltenhäuser, H. Kübler, S. Müller, T. Koch, M. Fattori, and T. Pfau. Two-frequency acousto-optic modulator driver to improve the beam pointing stability during intensity ramps. *Rev. Sci. Instrum.*, 78(4):043101, 2007. doi:[10.1063/1.2720725](https://doi.org/10.1063/1.2720725).
- Han Fu, Lei Feng, Brandon M. Anderson, Logan W. Clark, Jiazhong Hu, Jeffery W. Andrade, Cheng Chin, and K. Levin. Density waves and jet emission asymmetry in bose fireworks. *Phys. Rev. Lett.*, 121:243001, Dec 2018. doi:[10.1103/PhysRevLett.121.243001](https://doi.org/10.1103/PhysRevLett.121.243001).
- Takeshi Fukuhara, Yosuke Takasu, Mitsutaka Kumakura, and Yoshiro Takahashi. Degenerate fermi gases of ytterbium. *Phys. Rev. Lett.*, 98:030401, Jan 2007. doi:[10.1103/PhysRevLett.98.030401](https://doi.org/10.1103/PhysRevLett.98.030401).
- F Fuso, D Ciampini, E Arimondo, and C Gabbanini. Ion processes in the photoionization of laser cooled alkali atoms. *Opt. Commun.*, 173(1?6):223 – 232, 2000. doi:[10.1016/S0030-4018\(99\)00609-4](https://doi.org/10.1016/S0030-4018(99)00609-4).
- Marko Gacesa and Robin Côté. Photoassociation of ultracold molecules near a feshbach resonance as a probe of the electron-proton mass ratio variation. *J. Mol. Spectrosc.*, 300:124–130, June 2014. doi:[10.1016/j.jms.2014.03.005](https://doi.org/10.1016/j.jms.2014.03.005).
- Bryce Gadway, Daniel Pertot, René Reimann, Martin G. Cohen, and Dominik Schneble. Analysis of kapitza-dirac diffraction patterns beyond the raman-nath regime. *Opt. Express*, 17(21):19173–19180, Oct 2009. doi:[10.1364/OE.17.019173](https://doi.org/10.1364/OE.17.019173).
- Thomas F. Gallagher. *Rydberg Atoms*, pages 231–240. Springer International Publishing, Cham, 2023. ISBN 978-3-030-73893-8. doi:[10.1007/978-3-030-73893-8_15](https://doi.org/10.1007/978-3-030-73893-8_15).
- D. M. Gangardt, P. Pedri, L. Santos, and G. V. Shlyapnikov. Mott-insulator phase of coupled one-dimensional atomic gases in a two-dimensional optical lattice. *Phys. Rev. Lett.*, 96:040403, Jan 2006. doi:[10.1103/PhysRevLett.96.040403](https://doi.org/10.1103/PhysRevLett.96.040403).
- Davide Gatti, Riccardo Gotti, Tommaso Sala, Nicola Coluccelli, Michele Belmonte, Marco Prevedelli, Paolo Laporta, and Marco Marangoni. Wide-bandwidth pound-drever-hall locking through a single-sideband modulator. *Opt. Lett.*, 40(22):5176–5179, Nov 2015. doi:[10.1364/OL.40.005176](https://doi.org/10.1364/OL.40.005176).

- U. Gaubatz, P. Rudecki, S. Schiemann, and K. Bergmann. Population transfer between molecular vibrational levels by stimulated raman scattering with partially overlapping laser fields. a new concept and experimental results. *J. Chem. Phys.*, 92(9):5363–5376, 1990. doi:[10.1063/1.458514](https://doi.org/10.1063/1.458514).
- M. E. Gehm, K. M. O’Hara, T. A. Savard, and J. E. Thomas. Dynamics of noise-induced heating in atom traps. *Phys. Rev. A*, 58(5):3914–3921, November 1998. doi:[10.1103/PhysRevA.58.3914](https://doi.org/10.1103/PhysRevA.58.3914).
- Michael Eric Gehm. *PREPARATION OF AN OPTICALLY-TRAPPED DEGENERATE FERMI GAS OF 6Li: FINDING THE ROUTE TO DEGENERACY*. PhD thesis, Duke University, 2003.
- Philipp Gersema, Kai K. Voges, Mara Meyer zum Alten Borgloh, Leon Koch, Torsten Hartmann, Alessandro Zenesini, Silke Ospelkaus, Junyu Lin, Junyu He, and Dajun Wang. Probing photoinduced two-body loss of ultracold nonreactive bosonic $^{23}\text{Na}^{87}\text{Rb}$ and $^{23}\text{Na}^{39}\text{K}$ molecules. *Phys. Rev. Lett.*, 127:163401, Oct 2021. doi:[10.1103/PhysRevLett.127.163401](https://doi.org/10.1103/PhysRevLett.127.163401).
- S. Giorgini, L. P. Pitaevskii, and S. Stringari. Condensate fraction and critical temperature of a trapped interacting bose gas. *Phys. Rev. A*, 54:R4633–R4636, Dec 1996a. doi:[10.1103/PhysRevA.54.R4633](https://doi.org/10.1103/PhysRevA.54.R4633).
- S. Giorgini, L. P. Pitaevskii, and S. Stringari. Condensate fraction and critical temperature of a trapped interacting bose gas. *Phys. Rev. A*, 54:R4633–R4636, Dec 1996b. doi:[10.1103/PhysRevA.54.R4633](https://doi.org/10.1103/PhysRevA.54.R4633).
- Stefano Giorgini, Lev P. Pitaevskii, and Sandro Stringari. Theory of ultracold atomic fermi gases. *Rev. Mod. Phys.*, 80:1215–1274, Oct 2008. doi:[10.1103/RevModPhys.80.1215](https://doi.org/10.1103/RevModPhys.80.1215).
- Vandna Gokhroo, G Rajalakshmi, R Kollengode Easwaran, and C S Unnikrishnan. Sub-Doppler deep-cooled bosonic and fermionic isotopes of potassium in a compact 2D⁺-3D mot set-up. *J. Phys. B: At., Mol. Opt. Phys.*, 44(11):115307, 2011. doi:[10.1088/0953-4075/44/11/115307](https://doi.org/10.1088/0953-4075/44/11/115307).
- Krzysztof Góral, Kazimierz Rzażewski, and Tilman Pfau. Bose-einstein condensation with magnetic dipole-dipole forces. *Phys. Rev. A*, 61:051601, Mar 2000. doi:[10.1103/PhysRevA.61.051601](https://doi.org/10.1103/PhysRevA.61.051601).
- A. V. Gorshkov, P. Rabl, G. Pupillo, A. Micheli, P. Zoller, M. D. Lukin, and H. P. Büchler. Suppression of inelastic collisions between polar molecules with a repulsive shield. *Phys. Rev. Lett.*, 101:073201, Aug 2008. doi:[10.1103/PhysRevLett.101.073201](https://doi.org/10.1103/PhysRevLett.101.073201).
- O Goscinski and O Tapia. Predissociation by rotation and long-range interactions. *Mol. Phys.*, 24(3):641, 1972. doi:[10.1080/00268977200101751](https://doi.org/10.1080/00268977200101751).
- Philip D. Gregory, Jesus Aldegunde, Jeremy M. Hutson, and Simon L. Cornish. Controlling the rotational and hyperfine state of ultracold $^{87}\text{Rb}^{133}\text{Cs}$ molecules. *Phys. Rev. A*, 94:041403, Oct 2016. doi:[10.1103/PhysRevA.94.041403](https://doi.org/10.1103/PhysRevA.94.041403).
- Philip D. Gregory, Jacob A. Blackmore, Jesus Aldegunde, Jeremy M. Hutson, and Simon L. Cornish. ac stark effect in ultracold polar $^{87}\text{Rb}^{133}\text{Cs}$ molecules. *Phys. Rev. A*, 96:021402, Aug 2017. doi:[10.1103/PhysRevA.96.021402](https://doi.org/10.1103/PhysRevA.96.021402).
- Philip D Gregory, Matthew D Frye, Jacob A Blackmore, Elizabeth M Bridge, Rahul Sawant, Jeremy M Hutson, and Simon L Cornish. Sticky collisions of ultracold rbcs molecules. *Nature communications*, 10(1):3104, 2019. doi:[10.1038/s41467-019-11033-y](https://doi.org/10.1038/s41467-019-11033-y).

- Philip D. Gregory, Jacob A. Blackmore, Sarah L. Bromley, and Simon L. Cornish. Loss of ultracold $^{87}\text{Rb}^{133}\text{Cs}$ molecules via optical excitation of long-lived two-body collision complexes. *Phys. Rev. Lett.*, 124:163402, Apr 2020. doi:[10.1103/PhysRevLett.124.163402](https://doi.org/10.1103/PhysRevLett.124.163402).
- Philip D Gregory, Jacob A Blackmore, Sarah L Bromley, Jeremy M Hutson, and Simon L Cornish. Robust storage qubits in ultracold polar molecules. *Nature Physics*, 17(10):1149–1153, 2021. doi:<https://doi.org/10.1038/s41567-021-01328-7>.
- Philip D Gregory, Luke M Fernley, Albert Li Tao, Sarah L Bromley, Jonathan Stepp, Zewen Zhang, Svetlana Kotochigova, Kaden RA Hazzard, and Simon L Cornish. Second-scale rotational coherence and dipolar interactions in a gas of ultracold polar molecules. *Nature Physics*, pages 1–7, 2024. doi:doi.org/10.1038/s41567-023-02328-5.
- Daniel Greif, Thomas Uehlinger, Gregor Jotzu, Leticia Tarruell, and Tilman Esslinger. Short-range quantum magnetism of ultracold fermions in an optical lattice. *Science*, 340(6138):1307–1310, 2013. doi:[10.1126/science.1236362](https://doi.org/10.1126/science.1236362).
- Daniel Greif, Gregor Jotzu, Michael Messer, Rémi Desbuquois, and Tilman Esslinger. Formation and dynamics of antiferromagnetic correlations in tunable optical lattices. *Phys. Rev. Lett.*, 115:260401, Dec 2015. doi:[10.1103/PhysRevLett.115.260401](https://doi.org/10.1103/PhysRevLett.115.260401).
- Daniel Greif, Maxwell F. Parsons, Anton Mazurenko, Christie S. Chiu, Sebastian Blatt, Florian Huber, Geoffrey Ji, and Markus Greiner. Site-resolved imaging of a fermionic mott insulator. *Science*, 351(6276):953–957, 2016. doi:[10.1126/science.aad9041](https://doi.org/10.1126/science.aad9041).
- Markus Greiner. *Ultracold quantum gases in three-dimensional optical lattice potentials*. PhD thesis, lmu, 2003.
- Markus Greiner, Immanuel Bloch, Theodor W. Hänsch, and Tilman Esslinger. Magnetic transport of trapped cold atoms over a large distance. *Phys. Rev. A*, 63:031401, Feb 2001. doi:[10.1103/PhysRevA.63.031401](https://doi.org/10.1103/PhysRevA.63.031401).
- Markus Greiner, Olaf Mandel, Tilman Esslinger, Theodor W Hänsch, and Immanuel Bloch. Quantum phase transition from a superfluid to a mott insulator in a gas of ultracold atoms. *Nature*, 415(6867):39–44, 2002. doi:[10.1038/415039a](https://doi.org/10.1038/415039a).
- Markus Greiner, Cindy A. Regal, and Deborah S. Jin. Emergence of a molecular Bose-Einstein condensate from a fermi gas. *Nature*, 426(6966):537–540, December 2003. doi:[10.1038/nature02199](https://doi.org/10.1038/nature02199).
- G. F. Gribakin and V. V. Flambaum. Calculation of the scattering length in atomic collisions using the semiclassical approximation. *Phys. Rev. A*, 48:546–553, Jul 1993. doi:[10.1103/PhysRevA.48.546](https://doi.org/10.1103/PhysRevA.48.546).
- Andrew T. Grier, Igor Ferrier-Barbut, Benno S. Rem, Marion Delehaye, Lev Khaykovich, Frédéric Chevy, and Christophe Salomon. λ -enhanced sub-Doppler cooling of lithium atoms in d_1 gray molasses. *Phys. Rev. A*, 87(6):063411–, June 2013. doi:[10.1103/PhysRevA.87.063411](https://doi.org/10.1103/PhysRevA.87.063411).
- Axel Griesmaier, Jörg Werner, Sven Hensler, Jürgen Stuhler, and Tilman Pfau. Bose-einstein condensation of chromium. *Phys. Rev. Lett.*, 94:160401, Apr 2005. doi:[10.1103/PhysRevLett.94.160401](https://doi.org/10.1103/PhysRevLett.94.160401).
- Rudolf Grimm, Matthias Weidmüller, and Yurii B. Ovchinnikov. Optical dipole traps for neutral atoms. *Adv. At., Mol., Opt. Phys.*, Volume 42:95–170, 2000a. doi:[10.1016/S1049-250X\(08\)60186-X](https://doi.org/10.1016/S1049-250X(08)60186-X).

- Rudolf Grimm, Matthias Weidmüller, and Yurii B. Ovchinnikov. Optical dipole traps for neutral atoms. volume 42 of *Advances In Atomic, Molecular, and Optical Physics*, pages 95–170. Academic Press, 2000b. doi:[https://doi.org/10.1016/S1049-250X\(08\)60186-X](https://doi.org/10.1016/S1049-250X(08)60186-X).
- A. Grochola, J. Szczepkowski, W. Jastrzebski, and P. Kowalczyk. The $A^1\Sigma^+$ electronic state of KLi molecule. *Chemical Physics Letters*, 535:17–20, 2012. doi:<https://doi.org/10.1016/j.cplett.2012.03.011>.
- Ch. Gross, H. C. J. Gan, and K. Dieckmann. All-optical production and transport of a large ${}^6\text{Li}$ quantum gas in a crossed optical dipole trap. *Phys. Rev. A*, 93:053424, May 2016. doi:[10.1103/PhysRevA.93.053424](https://doi.org/10.1103/PhysRevA.93.053424).
- G. Grynberg and J.-Y. Courtois. Proposal for a magneto-optical lattice for trapping atoms in nearly-dark states. *EPL (Europhysics Letters)*, 27(1):41, 1994. doi:[10.1209/0295-5075/27/1/008](https://doi.org/10.1209/0295-5075/27/1/008).
- Will Gunton, Mariusz Semczuk, Nikesh S. Dattani, and Kirk W. Madison. High-resolution photoassociation spectroscopy of the ${}^6\text{Li}_2 A \ (1^1\Sigma_u^+)$ state. *Phys. Rev. A*, 88:062510, Dec 2013a. doi:[10.1103/PhysRevA.88.062510](https://doi.org/10.1103/PhysRevA.88.062510).
- Will Gunton, Mariusz Semczuk, and Kirk W. Madison. Realization of bec-bcs-crossover physics in a compact oven-loaded magneto-optic-trap apparatus. *Phys. Rev. A*, 88:023624, Aug 2013b. doi:[10.1103/PhysRevA.88.023624](https://doi.org/10.1103/PhysRevA.88.023624).
- Mingyang Guo. *An Ultracold Dipolar Gas of Ground-state ${}^{23}\text{Na}{}^{87}\text{Rb}$ Molecules*. PhD thesis, Chinese University of Hong Kong, 2017.
- Mingyang Guo, Bing Zhu, Bo Lu, Xin Ye, Fudong Wang, Romain Vexiau, Nadia Bouloufa-Maafa, Goulven Quéméner, Olivier Dulieu, and Dajun Wang. Creation of an ultracold gas of ground-state dipolar ${}^{23}\text{Na}{}^{87}\text{Rb}$ molecules. *Phys. Rev. Lett.*, 116:205303, May 2016. doi:[10.1103/PhysRevLett.116.205303](https://doi.org/10.1103/PhysRevLett.116.205303).
- Mingyang Guo, Romain Vexiau, Bing Zhu, Bo Lu, Nadia Bouloufa-Maafa, Olivier Dulieu, and Dajun Wang. High-resolution molecular spectroscopy for producing ultracold absolute-ground-state ${}^{23}\text{Na}{}^{87}\text{Rb}$ molecules. *Phys. Rev. A*, 96:052505, Nov 2017. doi:[10.1103/PhysRevA.96.052505](https://doi.org/10.1103/PhysRevA.96.052505).
- Mingyang Guo, Xin Ye, Junyu He, Maykel L. González-Martínez, Romain Vexiau, Goulven Quéméner, and Dajun Wang. Dipolar collisions of ultracold ground-state bosonic molecules. *Phys. Rev. X*, 8:041044, Dec 2018a. doi:[10.1103/PhysRevX.8.041044](https://doi.org/10.1103/PhysRevX.8.041044).
- Mingyang Guo, Xin Ye, Junyu He, Goulven Quéméner, and Dajun Wang. High-resolution internal state control of ultracold ${}^{23}\text{Na}{}^{87}\text{Rb}$ molecules. *Phys. Rev. A*, 97:020501, Feb 2018b. doi:[10.1103/PhysRevA.97.020501](https://doi.org/10.1103/PhysRevA.97.020501).
- S Gupta, Z Hadzibabic, MW Zwierlein, CA Stan, K Dieckmann, CH Schunck, EGM Van Kempen, BJ Verhaar, and W Ketterle. Radio-frequency spectroscopy of ultracold fermions. *Science*, 300(5626):1723–1726, 2003. doi:[10.1126/science.1085335](https://doi.org/10.1126/science.1085335).
- T. L. Gustavson, A. P. Chikkatur, A. E. Leanhardt, A. G?rlitz, S. Gupta, D. E. Pritchard, and W. Ketterle. Transport of Bose-Einstein condensates with optical tweezers. *Phys. Rev. Lett.*, 88(2):020401–, December 2001. doi:[10.1103/PhysRevLett.88.020401](https://doi.org/10.1103/PhysRevLett.88.020401).
- Lucia Hackermüller, Ulrich Schneider, Maria Moreno-Cardoner, Takuya Kitagawa, Thorsten Best, Sebastian Will, Eugene Demler, Ehud Altman, Immanuel Bloch, and Belén Paredes.

- Anomalous expansion of attractively interacting fermionic atoms in an optical lattice. *Science*, 327(5973):1621–1624, 2010.
- Z. Hadzibabic, S. Gupta, C. A. Stan, C. H. Schunck, M. W. Zwierlein, K. Dieckmann, and W. Ketterle. Fiftyfold improvement in the number of quantum degenerate fermionic atoms. *Phys. Rev. Lett.*, 91:160401, Oct 2003. doi:[10.1103/PhysRevLett.91.160401](https://doi.org/10.1103/PhysRevLett.91.160401).
- John Hall, Jun Ye, and M.S. Taubman. *Laser Stabilization, Handbook of Optics*, chapter IV. McGraw-Hill Professional, New York, 1999.
- Christian Hallas, Nathaniel B. Vilas, Loic Anderegg, Paige Robichaud, Andrew Winnicki, Chaoqun Zhang, Lan Cheng, and John M. Doyle. Optical trapping of a polyatomic molecule in an l-type parity doublet state. *Phys. Rev. Lett.*, 130(15), 04 2023. doi:[10.1103/PhysRevLett.130.153202](https://doi.org/10.1103/PhysRevLett.130.153202).
- Elmar Haller, Manfred J. Mark, Russell Hart, Johann G. Danzl, Lukas Reichsöllner, Vladimir Melezik, Peter Schmelcher, and Hanns-Christoph Nägerl. Confinement-induced resonances in low-dimensional quantum systems. *Phys. Rev. Lett.*, 104:153203, Apr 2010. doi:[10.1103/PhysRevLett.104.153203](https://doi.org/10.1103/PhysRevLett.104.153203).
- Paul Hamilton, Geena Kim, Trinity Joshi, Biswaroop Mukherjee, Daniel Tiarks, and Holger Müller. Sisyphus cooling of lithium. *Phys. Rev. A*, 89:023409, Feb 2014. doi:[10.1103/PhysRevA.89.023409](https://doi.org/10.1103/PhysRevA.89.023409).
- P.R. Hammond. Laser dye dcm, its spectral properties, synthesis and comparison with other dyes in the red. *Optics Communications*, 29(3):331–333, 1979. doi:[https://doi.org/10.1016/0030-4018\(79\)90111-1](https://doi.org/10.1016/0030-4018(79)90111-1).
- T.W. Hänsch and A.L. Schawlow. Cooling of gases by laser radiation. *Opt. Commun.*, 13(1): 68–69, January 1975. doi:[10.1016/0030-4018\(75\)90159-5](https://doi.org/10.1016/0030-4018(75)90159-5).
- John C. Hansen. *Schroedinger.m: A Mathematica Package for Solving the Time-Independent Schrödinger Equation*. Southwest State University, Marshall, MN 56258, 1996.
- Russell A. Hart, Pedro M. Duarte, Tsung-Lin Yang, Xinxing Liu, Thereza Paiva, Ehsan Khatami, Richard T. Scalettar, Nandini Trivedi, David A. Huse, and Randall G. Hulet. Observation of antiferromagnetic correlations in the hubbard model with ultracold atoms. *Nature*, 519(7542):211–214, March 2015. doi:[10.1038/nature14223](https://doi.org/10.1038/nature14223).
- C. He, X. Nie, V. Avalos, S. Botsi, S. Kumar, A. Yang, and K. Dieckmann. Efficient creation of ultracold ground state ${}^6\text{Li}{}^{40}\text{K}$ polar molecules. *Phys. Rev. Lett.*, 132:243401, Jun 2024. doi:[10.1103/PhysRevLett.132.243401](https://doi.org/10.1103/PhysRevLett.132.243401).
- Junyu He, Xin Ye, Junyu Lin, Mingyang Guo, Goulven Quéméner, and Dajun Wang. Observation of resonant dipolar collisions in ultracold ${}^{23}\text{Na}{}^{87}\text{Rb}$ rotational mixtures. *Phys. Rev. Research*, 3:013016, Jan 2021. doi:[10.1103/PhysRevResearch.3.013016](https://doi.org/10.1103/PhysRevResearch.3.013016).
- X. D. He, K. P. Wang, J. Zhuang, P. Xu, X. Gao, R. J. Guo, C. Sheng, M. Liu, J. Wang, J. M. Li, G. V. Shlyapnikov, and M. S. Zhan. Coherently forming a single molecule in an optical trap. *Science*, 370(6514):331, October 2020.
- Florian Alexander Henkel. *Photoionisation detection of single ${}^{87}\text{Rb}$ -atoms using channel electron multipliers*. PhD thesis, Ludwig MaximiliansUniversität, 2011.

- Myoung-Sun Heo, Jae-yoon Choi, and Yong-il Shin. Fast production of large ^{23}Na bose-einstein condensates in an optically plugged magnetic quadrupole trap. *Phys. Rev. A*, 83:013622, Jan 2011. doi:[10.1103/PhysRevA.83.013622](https://doi.org/10.1103/PhysRevA.83.013622).
- Myoung-Sun Heo, Tout T. Wang, Caleb A. Christensen, Timur M. Rvachov, Dylan A. Cotta, Jae-Hoon Choi, Ye-Ryoung Lee, and Wolfgang Ketterle. Formation of ultracold fermionic NaLi feshbach molecules. *Phys. Rev. A*, 86:021602(R), Aug 2012. doi:[10.1103/PhysRevA.86.021602](https://doi.org/10.1103/PhysRevA.86.021602).
- Jens Herbig, Tobias Kraemer, Michael Mark, Tino Weber, Cheng Chin, Hanns-Christoph Nägerl, and Rudolf Grimm. Preparation of a pure molecular quantum gas. *Science*, 301(5639):1510–1513, 2003. doi:[10.1126/science.1088876](https://doi.org/10.1126/science.1088876).
- J Hertkorn, J-N Schmidt, M Guo, F Böttcher, KSH Ng, SD Graham, P Uerlings, T Langen, M Zwierlein, and T Pfau. Pattern formation in quantum ferrofluids: from supersolids to superglasses. *arXiv preprint arXiv:2103.13930*, 2021.
- Gerhard Herzberg. *Molecular Spectra and Molecular Structure*, volume I. Spectra of Diatomic Molecules. D. Van Nostrand Company Inc., 1950.
- Tin-Lun Ho. Universal thermodynamics of degenerate quantum gases in the unitarity limit. *Phys. Rev. Lett.*, 92:090402, Mar 2004. doi:[10.1103/PhysRevLett.92.090402](https://doi.org/10.1103/PhysRevLett.92.090402).
- M. Houbiers, H. T. C. Stoof, W. I. McAlexander, and R. G. Hulet. Elastic and inelastic collisions of ^6Li atoms in magnetic and optical traps. *Phys. Rev. A*, 57(3):R1497–R1500, March 1998. doi:[10.1103/PhysRevA.57.R1497](https://doi.org/10.1103/PhysRevA.57.R1497).
- M-G Hu, Yu Liu, David D Grimes, Y-W Lin, Andrei H Gheorghe, Romain Vexiau, Nadia Bouloufa-Maafa, Olivier Dulieu, Till Rosenband, and K-K Ni. Direct observation of bimolecular reactions of ultracold krb molecules. *Science*, 366(6469):1111–1115, 2019. doi:[10.1126/science.aay9531](https://doi.org/10.1126/science.aay9531).
- Kerson Huang. *Statistical Mechanics*. Wiley, 1987a.
- Kerson Huang. *Statistical Mechanics*. Wiley, 1987b.
- J. H. Huckans, J. R. Williams, E. L. Hazlett, R. W. Stites, and K. M. O’Hara. Three-body recombination in a three-state fermi gas with widely tunable interactions. *Phys. Rev. Lett.*, 102:165302, Apr 2009. doi:[10.1103/PhysRevLett.102.165302](https://doi.org/10.1103/PhysRevLett.102.165302).
- Eric R. Hudson, Nathan B. Gilfoy, S. Kotochigova, Jeremy M. Sage, and D. DeMille. Inelastic collisions of ultracold heteronuclear molecules in an optical trap. *Phys. Rev. Lett.*, 100:203201, May 2008. doi:[10.1103/PhysRevLett.100.203201](https://doi.org/10.1103/PhysRevLett.100.203201).
- M. Hughes, M. D. Frye, R. Sawant, G. Bhole, J. A. Jones, S. L. Cornish, M. R. Tarbutt, J. M. Hutson, D. Jaksch, and J. Mur-Petit. Robust entangling gate for polar molecules using magnetic and microwave fields. *Phys. Rev. A*, 101(6):062308, June 2020.
- Randall G. Hulet, Pedro M. Duarte, Russell A. Hart, and Tsung-Lin Yang. Antiferromagnetism with ultracold atoms. *arXiv:1512.05311*, 2015a. To be published in the Proceedings of the 22nd International Conference on Laser Spectroscopy (Singapore, 2015).
- Randall G. Hulet, Pedro M. Duarte, Russell A. Hart, and Tsung-Lin Yang. Antiferromagnetism with ultracold atoms. *arXiv:1512.05311*, 2015b. To be published in the Proceedings of the 22nd International Conference on Laser Spectroscopy (Singapore, 2015).

- Keith Hulme. Private communication. Starna Scientific Ltd, 2014.
- F Hund. *Hundbuch der Physik*, volume 24. 1933.
- Zbigniew Idziaszek and Paul S. Julienne. Universal rate constants for reactive collisions of ultracold molecules. *Phys. Rev. Lett.*, 104:113202, Mar 2010. doi:[10.1103/PhysRevLett.104.113202](https://doi.org/10.1103/PhysRevLett.104.113202).
- Zbigniew Idziaszek, Goulven Quéméner, John L. Bohn, and Paul S. Julienne. Simple quantum model of ultracold polar molecule collisions. *Phys. Rev. A*, 82:020703, Aug 2010. doi:[10.1103/PhysRevA.82.020703](https://doi.org/10.1103/PhysRevA.82.020703).
- P. S. Żuchowski, M. Kosicki, M. Kodrycka, and P. Soldán. van der waals coefficients for systems with ultracold polar alkali-metal molecules. *Phys. Rev. A*, 87:022706, Feb 2013. doi:[10.1103/PhysRevA.87.022706](https://doi.org/10.1103/PhysRevA.87.022706).
- Piotr S. Żuchowski and Jeremy M. Hutson. Reactions of ultracold alkali-metal dimers. *Phys. Rev. A*, 81:060703(R), Jun 2010. doi:[10.1103/PhysRevA.81.060703](https://doi.org/10.1103/PhysRevA.81.060703).
- S Inouye, MR Andrews, J Stenger, H-J Miesner, Dan M Stamper-Kurn, and W Ketterle. Observation of feshbach resonances in a bose-einstein condensate. *Nature*, 392(6672):151–154, 1998. doi:[10.1038/32354](https://doi.org/10.1038/32354).
- S. Inouye, J. Goldwin, M. L. Olsen, C. Ticknor, J. L. Bohn, and D. S. Jin. Observation of heteronuclear feshbach resonances in a mixture of bosons and fermions. *Phys. Rev. Lett.*, 93: 183201, Oct 2004. doi:[10.1103/PhysRevLett.93.183201](https://doi.org/10.1103/PhysRevLett.93.183201).
- E.P. Ippen and R.H. Stolen. Stimulated brillouin scattering in optical fibers. *Applied Physics Letters*, 21(11):539–541, 1972. doi:[10.1063/1.1654249](https://doi.org/10.1063/1.1654249).
- R. C. Isler, S. Marcus, and R. Novick. Hyperfine structure of the 3^2p and 4^2p states of lithium and lifetime of the 3^2p state. *Phys. Rev.*, 187:76–84, Nov 1969a. doi:[10.1103/PhysRev.187.76](https://doi.org/10.1103/PhysRev.187.76).
- R. C. Isler, S. Marcus, and R. Novick. Fine structure of the 3^2p and 4^2p states of lithium. *Phys. Rev.*, 187:66–75, Nov 1969b. doi:[10.1103/PhysRev.187.66](https://doi.org/10.1103/PhysRev.187.66).
- A. O. Jamison. Private communication, 2023.
- Alan Jamison. private communications.
- P. Jasik and J.E. Sienkiewicz. Calculation of adiabatic potentials of Li₂. *Chem. Phys.*, 323 (2?3):563 – 573, 2006a. doi:[10.1016/j.chemphys.2005.10.025](https://doi.org/10.1016/j.chemphys.2005.10.025).
- P. Jasik and J.E. Sienkiewicz. Calculation of adiabatic potentials of Li₂. *Chem. Phys.*, 323 (2?3):563 – 573, 2006b. doi:[10.1016/j.chemphys.2005.10.025](https://doi.org/10.1016/j.chemphys.2005.10.025).
- Patryk Jasik and Jósef Sienkiewicz. Transition dipole moments of the Lithium dimer. *At. Data Nucl. Data Tables*, 99(2):115–155, March 2013. doi:[10.1016/j.adt.2011.06.003](https://doi.org/10.1016/j.adt.2011.06.003).
- Jasik, P., Wilczyński, J., and Sienkiewicz, J. E. Calculation of adiabatic potentials of li2+. *Eur. Phys. J. Special Topics*, 144:85–91, 2007a. doi:[10.1140/epjst/e2007-00111-2](https://doi.org/10.1140/epjst/e2007-00111-2).
- Jasik, P., Wilczyński, J., and Sienkiewicz, J. E. Calculation of adiabatic potentials of li2+. *Eur. Phys. J. Special Topics*, 144:85–91, 2007b. doi:[10.1140/epjst/e2007-00111-2](https://doi.org/10.1140/epjst/e2007-00111-2).
- W Jastrzebski, P Kowalczyk, and A Pashov. The perturbation of the $B^1\Pi+$ and $C^1\Sigma+$ states in KLi. *J. Mol. Spectrosc.*, 209(1):50 – 56, 2001. doi:[10.1006/jmsp.2001.8389](https://doi.org/10.1006/jmsp.2001.8389).

- B. Ji, C. C. Tsai, and W. C. Stwalley. Proposed modification of the criterion for the region of validity of the inverse-power expansion in diatomic long-range potentials. *Chem. Phys. Lett.*, 236(3):242–246, April 1995. doi:[10.1016/0009-2614\(95\)00216-Q](https://doi.org/10.1016/0009-2614(95)00216-Q).
- S. Jochim, M. Bartenstein, A. Altmeyer, G. Hendl, C. Chin, J. Hecker Denschlag, and R. Grimm. Pure gas of optically trapped molecules created from fermionic atoms. *Phys. Rev. Lett.*, 91: 240402, Dec 2003a. doi:[10.1103/PhysRevLett.91.240402](https://doi.org/10.1103/PhysRevLett.91.240402).
- S. Jochim, M. Bartenstein, A. Altmeyer, G. Hendl, S. Riedl, C. Chin, J. Hecker Denschlag, and R. Grimm. Bose-Einstein condensation of molecules. *Science*, 302(5653):2101–2103, 2003b. doi:[10.1126/science.1093280](https://doi.org/10.1126/science.1093280).
- J.R. Johansson, P.D. Nation, and Franco Nori. Qutip: An open-source python framework for the dynamics of open quantum systems. *Computer Physics Communications*, 183(8):1760–1772, 2012. doi:<https://doi.org/10.1016/j.cpc.2012.02.021>.
- J.R. Johansson, P.D. Nation, and Franco Nori. Qutip 2: A python framework for the dynamics of open quantum systems. *Computer Physics Communications*, 184(4):1234–1240, 2013. doi:<https://doi.org/10.1016/j.cpc.2012.11.019>.
- Walter R. Johnson. *Atomic Structure Theory*. Springer, 2007.
- David J Jones, Scott A Diddams, Jinendra K Ranka, Andrew Stentz, Robert S Windeler, John L Hall, and Steven T Cundiff. Carrier-envelope phase control of femtosecond mode-locked lasers and direct optical frequency synthesis. *Science*, 288(5466):635–639, 2000. doi:[10.1126/science.288.5466.635](https://doi.org/10.1126/science.288.5466.635).
- Kevin M. Jones, Eite Tiesinga, Paul D. Lett, and Paul S. Julienne. Ultracold photoassociation spectroscopy: Long-range molecules and atomic scattering. *Rev. Mod. Phys.*, 78(2):483–535, May 2006. doi:[10.1103/RevModPhys.78.483](https://doi.org/10.1103/RevModPhys.78.483).
- Robert Jordens, Niels Strohmaier, Kenneth Gunter, Henning Moritz, and Tilman Esslinger. A mott insulator of fermionic atoms in an optical lattice. *Nature*, 455(7210):204–207, September 2008. doi:[10.1038/nature07244](https://doi.org/10.1038/nature07244).
- Paul S. Julienne and Jeremy M. Hutson. Contrasting the wide feshbach resonances in ${}^6\text{Li}$ and ${}^7\text{Li}$. *Phys. Rev. A*, 89:052715, May 2014. doi:[10.1103/PhysRevA.89.052715](https://doi.org/10.1103/PhysRevA.89.052715).
- Paul S. Julienne, Thomas M. Hanna, and Zbigniew Idziaszek. Universal ultracold collision rates for polar molecules of two alkali-metal atoms. *Phys. Chem. Chem. Phys.*, 13:19114–19124, 2011. doi:[10.1039/C1CP21270B](https://doi.org/10.1039/C1CP21270B).
- P.S. Julienne, A.M. Smith, and K. Burnett. Theory of collisions between laser cooled atoms. In David Bates and Benjamin Bederson, editors, *Advances In Atomic, Molecular, and Optical Physics*, volume Volume 30, pages 141–198. Academic Press, 1992. doi:[10.1016/S1049-250X\(08\)60175-5](https://doi.org/10.1016/S1049-250X(08)60175-5).
- M. Junker, D. Dries, C. Welford, J. Hitchcock, Y. P. Chen, and R. G. Hulet. Photoassociation of a Bose-Einstein condensate near a feshbach resonance. *Phys. Rev. Lett.*, 101:060406, Aug 2008. doi:[10.1103/PhysRevLett.101.060406](https://doi.org/10.1103/PhysRevLett.101.060406).
- Yu. Kagan, E. L. Surkov, and G. V. Shlyapnikov. Evolution of a bose-condensed gas under variations of the confining potential. *Phys. Rev. A*, 54:R1753–R1756, Sep 1996. doi:[10.1103/PhysRevA.54.R1753](https://doi.org/10.1103/PhysRevA.54.R1753).

- Tijs Karman and Jeremy M. Hutson. Microwave shielding of ultracold polar molecules. *Phys. Rev. Lett.*, 121:163401, Oct 2018. doi:[10.1103/PhysRevLett.121.163401](https://doi.org/10.1103/PhysRevLett.121.163401).
- Tijs Karman and Jeremy M. Hutson. Microwave shielding of ultracold polar molecules with imperfectly circular polarization. *Phys. Rev. A*, 100:052704, Nov 2019. doi:[10.1103/PhysRevA.100.052704](https://doi.org/10.1103/PhysRevA.100.052704).
- Tijs Karman, Zoe Z. Yan, and Martin Zwierlein. Resonant and first-order dipolar interactions between ultracold $^1\Sigma$ molecules in static and microwave electric fields. *Phys. Rev. A*, 105: 013321, Jan 2022. doi:[10.1103/PhysRevA.105.013321](https://doi.org/10.1103/PhysRevA.105.013321).
- Mark Kasevich and Steven Chu. Atomic interferometry using stimulated raman transitions. *Phys. Rev. Lett.*, 67:181–184, Jul 1991. doi:[10.1103/PhysRevLett.67.181](https://doi.org/10.1103/PhysRevLett.67.181).
- Mark Kasevich and Steven Chu. Laser cooling below a photon recoil with three-level atoms. *Phys. Rev. Lett.*, 69:1741–1744, Sep 1992. doi:[10.1103/PhysRevLett.69.1741](https://doi.org/10.1103/PhysRevLett.69.1741).
- T. Kessler, C. Hagemann, C. Grebing, T. Legero, U. Sterr, F. Riehle, M. J. Martin, L. Chen, and J. Ye. A sub-40-mhz-linewidth laser based on a silicon single-crystal optical cavity. *Nature Photonics*, 6(10):687–692, OCT 2012. doi:[10.1038/NPHOTON.2012.217](https://doi.org/10.1038/NPHOTON.2012.217).
- W. Ketterle and M. W. Zwierlein. Making, probing and understanding ultracold fermi gases, January 2008a.
- W. Ketterle and M. W. Zwierlein. Making, probing and understanding ultracold fermi gases, January 2008b.
- W Ketterle, D.S. Durfee, and D.M. Stamper-Kurn. Making, probing and understanding Bose-Einstein condensates, 1999.
- Wolfgang Ketterle and N.J. Van Druten. Evaporative cooling of trapped atoms. volume 37 of *Advances In Atomic, Molecular, and Optical Physics*, pages 181–236. Academic Press, 1996. doi:[https://doi.org/10.1016/S1049-250X\(08\)60101-9](https://doi.org/10.1016/S1049-250X(08)60101-9).
- Wolfgang Ketterle, Kendall B. Davis, Michael A. Joffe, Alex Martin, and David E. Pritchard. High densities of cold atoms in a dark spontaneous-force optical trap. *Phys. Rev. Lett.*, 70 (15):2253–2256, April 1993. doi:[10.1103/PhysRevLett.70.2253](https://doi.org/10.1103/PhysRevLett.70.2253).
- Keysight. Phase noise 101: Basics, applications and measurements. Online.
- L. Khaykovich, F. Schreck, G. Ferrari, T. Bourdel, J. Cubizolles, L. D. Carr, Y. Castin, and C. Salomon. Formation of a matter-wave bright soliton. *Science*, 296(5571):1290–1293, 2002. doi:[10.1126/science.1071021](https://doi.org/10.1126/science.1071021).
- Mineo Kimura and Yukikazu Itikawa. *Advances in Atomic, Molecular, and Optical Physics: Electron Collisions with Molecules in Gases: Applications to Plasma Diagnostics and Modeling*. Elsevier, 2000.
- Joseph Kinast, Andrey Turlapov, John E. Thomas, Qijin Chen, Jelena Stajic, and Kathryn Levin. Heat capacity of a strongly interacting fermi gas. *Science*, 307(5713):1296–1299, 2005. doi:[10.1126/science.1109220](https://doi.org/10.1126/science.1109220).
- Charles Kittel and Paul McEuen. *Introduction to solid state physics*. John Wiley & Sons, 2018.
- O. Klein. For the calculation of potential curves for diatomic molecules with spectral help. *Z. Phys.*, 76(3-4):226–235, MAR 1932. doi:[10.1007/BF01341814](https://doi.org/10.1007/BF01341814).

- Peter J. Knowles and H.-J. Werner. An Efficient Method for the Evaluation of Coupling Coefficients in Configuration Interaction Calculations. *Chem. Phys. Letters*, 145:514–522, 1988a. doi:[10.1016/0009-2614\(88\)87412-8](https://doi.org/10.1016/0009-2614(88)87412-8).
- Peter J. Knowles and H.-J. Werner. An Efficient Method for the Evaluation of Coupling Coefficients in Configuration Interaction Calculations. *Chem. Phys. Letters*, 145:514–522, 1988b. doi:[10.1016/0009-2614\(88\)87412-8](https://doi.org/10.1016/0009-2614(88)87412-8).
- Peter J. Knowles and H.-J. Werner. Internally Contracted Multiconfiguration Reference Configuration Interaction Calculations for Excited States. *Theor. Chim. Acta.*, 84(1-2):95–103, OCT 1992a. doi:[10.1007/BF01117405](https://doi.org/10.1007/BF01117405).
- Peter J. Knowles and H.-J. Werner. Internally Contracted Multiconfiguration Reference Configuration Interaction Calculations for Excited States. *Theor. Chim. Acta.*, 84(1-2):95–103, OCT 1992b. doi:[10.1007/BF01117405](https://doi.org/10.1007/BF01117405).
- Christiane P. Koch, José P. Palao, Ronnie Kosloff, and Françoise Masnou-Seeuws. Stabilization of ultracold molecules using optimal control theory. *Phys. Rev. A*, 70:013402, Jul 2004. doi:[10.1103/PhysRevA.70.013402](https://doi.org/10.1103/PhysRevA.70.013402).
- Thorsten Köhler, Krzysztof Góral, and Paul S. Julienne. Production of cold molecules via magnetically tunable feshbach resonances. *Rev. Mod. Phys.*, 78:1311–1361, Dec 2006. doi:[10.1103/RevModPhys.78.1311](https://doi.org/10.1103/RevModPhys.78.1311).
- N. Kolachevsky, J. Alnis, C. G. Parthey, A. Matveev, R. Landig, and T. W. Hänsch. Low phase noise diode laser oscillator for 1s–2s spectroscopy in atomic hydrogen. *Opt. Lett.*, 36(21):4299–4301, Nov 2011. doi:[10.1364/OL.36.004299](https://doi.org/10.1364/OL.36.004299).
- Daniel D. Konowalow and Mark L. Olson. The electronic structure and spectra of the $X^1\Sigma_g^+$ and $A^1\Sigma_u^+$ states of Li_2 . *J. Chem. Phys.*, 71(1):450–457, 1979. doi:[10.1063/1.438090](https://doi.org/10.1063/1.438090).
- Daniel D. Konowalow, Rebecca M. Regan, and Marcy E. Rosenkrantz. The “most likely” potential energy curve for the lowest $^3\Sigma^+$ state of Li_2 . *J. Chem. Phys.*, 81(10):4534–4536, 1984. doi:[10.1063/1.447424](https://doi.org/10.1063/1.447424).
- Michael P. Köppinger, Daniel J. McCarron, Daniel L. Jenkin, Peter K. Molony, Hung-Wen Cho, Simon L. Cornish, C. Ruth Le Sueur, Caroline L. Blackley, and Jeremy M. Hutson. Production of optically trapped $^{87}RbCs$ feshbach molecules. *Phys. Rev. A*, 89:033604, Mar 2014. doi:[10.1103/PhysRevA.89.033604](https://doi.org/10.1103/PhysRevA.89.033604).
- Svetlana Kotochigova and David DeMille. Electric-field-dependent dynamic polarizability and state-insensitive conditions for optical trapping of diatomic polar molecules. *Phys. Rev. A*, 82:063421, Dec 2010. doi:[10.1103/PhysRevA.82.063421](https://doi.org/10.1103/PhysRevA.82.063421).
- Svetlana Kotochigova, Eite Tiesinga, and Paul S Julienne. Multi-channel modelling of the formation of vibrationally cold polar krb molecules. *New Journal of Physics*, 11(5):055043, may 2009. doi:[10.1088/1367-2630/11/5/055043](https://doi.org/10.1088/1367-2630/11/5/055043).
- T. Kraemer, M. Mark, P. Waldburger, J. G. Danzl, C. Chin, B. Engeser, A. D. Lange, K. Pilch, A. Jaakkola, H.-C. Nrl, and R. Grimm. Evidence for efimov quantum states in an ultracold gas of caesium atoms. *Nature*, 440(7082):315–318, 2006. doi:[10.1038/nature04626](https://doi.org/10.1038/nature04626).
- A. Kramida, Yu.Ralchenko, J. Reader, and NIST ASD Team. Nist atomic spectra database (version 5.3), [online]. National Institute of Standards and Technology, Gaithersburg, MD., June 2016. Available: <http://physics.nist.gov/asd>.

- Andreas Kruckenhauser, Lukas M. Sieberer, Luigi De Marco, Jun-Ru Li, Kyle Matsuda, William G. Tobias, Giacomo Valtolina, Jun Ye, Ana Maria Rey, Mikhail A. Baranov, and Peter Zoller. Quantum many-body physics with ultracold polar molecules: Nanosstructured potential barriers and interactions. *Phys. Rev. A*, 102:023320, Aug 2020. doi:[10.1103/PhysRevA.102.023320](https://doi.org/10.1103/PhysRevA.102.023320).
- S. P. Krzyzewski, T. G. Akin, J. Dizikes, Michael A. Morrison, and E. R. I. Abraham. Observation of deeply bound $^{85}\text{Rb}_2$ vibrational levels using feshbach optimized photoassociation. *Phys. Rev. A*, 92:062714, Dec 2015. doi:[10.1103/PhysRevA.92.062714](https://doi.org/10.1103/PhysRevA.92.062714).
- Mark J. H. Ku, Ariel T. Sommer, Lawrence W. Cheuk, and Martin W. Zwierlein. Revealing the superfluid lambda transition in the universal thermodynamics of a unitary fermi gas. *Science*, 335(6068):563–567, February 2012. doi:[10.1126/science.1214987](https://doi.org/10.1126/science.1214987).
- A. Kuhn, G. W. Coulston, G. Z. He, S. Schiemann, K. Bergmann, and W. S. Warren. Population transfer by stimulated raman scattering with delayed pulses using spectrally broad light. *J. Chem. Phys.*, 96(6):4215–4223, 1992. doi:[10.1063/1.462840](https://doi.org/10.1063/1.462840).
- J. R. Kuklinski, U. Gaubatz, F. T. Hioe, and K. Bergmann. Adiabatic population transfer in a three-level system driven by delayed laser pulses. *Phys. Rev. A*, 40:6741–6744, Dec 1989. doi:[10.1103/PhysRevA.40.6741](https://doi.org/10.1103/PhysRevA.40.6741).
- S. J. M. Kuppens, K. L. Corwin, K. W. Miller, T. E. Chupp, and C. E. Wieman. Loading an optical dipole trap. *Phys. Rev. A*, 62(1):013406–, June 2000. doi:[10.1103/PhysRevA.62.013406](https://doi.org/10.1103/PhysRevA.62.013406).
- Henning Labuhn, Daniel Barredo, Sylvain Ravets, Sylvain De Léséleuc, Tommaso Macrì, Thierry Lahaye, and Antoine Browaeys. Tunable two-dimensional arrays of single rydberg atoms for realizing quantum ising models. *Nature*, 534(7609):667–670, 2016. doi:[10.1038/nature18274](https://doi.org/10.1038/nature18274).
- T Lahaye, C Menotti, L Santos, M Lewenstein, and T Pfau. The physics of dipolar bosonic quantum gases. *Reports on Progress in Physics*, 72(12):126401, nov 2009. doi:[10.1088/0034-4885/72/12/126401](https://doi.org/10.1088/0034-4885/72/12/126401).
- Thierry Lahaye, Tobias Koch, Bernd Fröhlich, Marco Fattori, Jonas Metz, Axel Griesmaier, Stefano Giovanazzi, and Tilman Pfau. Strong dipolar effects in a quantum ferrofluid. *Nature*, 448(7154):672–675, 2007.
- Jayanti Lahiri and Steven T. Manson. Radiative recombination and excited-state photoionization of lithium. *Phys. Rev. A*, 48:3674–3679, Nov 1993. doi:[10.1103/PhysRevA.48.3674](https://doi.org/10.1103/PhysRevA.48.3674).
- Aden Z. Lam, Niccolò Bigagli, Claire Warner, Weijun Yuan, Siwei Zhang, Eberhard Tiemann, Ian Stevenson, and Sebastian Will. High phase-space density gas of nacs feshbach molecules. *Phys. Rev. Res.*, 4:L022019, Apr 2022. doi:[10.1103/PhysRevResearch.4.L022019](https://doi.org/10.1103/PhysRevResearch.4.L022019).
- Mark Lam. *Molecular Spectroscopy of Ultracold $^6\text{Li}^{40}\text{K}$ Molecules*. PhD thesis, National University of Singapore, 2016.
- G. Lamporesi, J. Catani, G. Barontini, Y. Nishida, M. Inguscio, and F. Minardi. Scattering in mixed dimensions with ultracold gases. *Phys. Rev. Lett.*, 104:153202, Apr 2010. doi:[10.1103/PhysRevLett.104.153202](https://doi.org/10.1103/PhysRevLett.104.153202).
- L. D. Landau and E. M. Lifshitz. *Quantum mechanics - and non-relativistic theory*. Pergamon Press, 1977.

- M. Landini, S. Roy, L. Carcagní, D. Trypogeorgos, M. Fattori, M. Inguscio, and G. Modugno. Sub-Doppler laser cooling of potassium atoms. *Phys. Rev. A*, 84(4):043432–, October 2011. doi:[10.1103/PhysRevA.84.043432](https://doi.org/10.1103/PhysRevA.84.043432).
- Lucas Lassablière and Goulven Quéméner. Controlling the scattering length of ultracold dipolar molecules. *Phys. Rev. Lett.*, 121:163402, Oct 2018. doi:[10.1103/PhysRevLett.121.163402](https://doi.org/10.1103/PhysRevLett.121.163402).
- Robert J. Le Roy. Rkr1: A computer program implementing the first-order rkr method for determining diatomic molecule potential energy functions. *J. Quant. Spectrosc. Radiat. Transf.*, 186(SI):158–166, JAN 2017. doi:[10.1016/j.jqsrt.2016.03.030](https://doi.org/10.1016/j.jqsrt.2016.03.030).
- Robert J Le Roy and Margaret G Barwell. Ground state d 2 dissociation energy from the near-dissociation behaviour of rotational level spacings. *Canadian Journal of Physics*, 53(19):1983–1990, 1975.
- Patrick A. Lee, Naoto Nagaosa, and Xiao-Gang Wen. Doping a mott insulator: Physics of high-temperature superconductivity. *Rev. Mod. Phys.*, 78:17–85, Jan 2006. doi:[10.1103/RevModPhys.78.17](https://doi.org/10.1103/RevModPhys.78.17).
- J. Léonard, A. P. Mosk, M. Walhout, P. van der Straten, M. Leduc, and C. Cohen-Tannoudji. Analysis of photoassociation spectra for giant helium dimers. *Phys. Rev. A*, 69:032702, Mar 2004. doi:[10.1103/PhysRevA.69.032702](https://doi.org/10.1103/PhysRevA.69.032702).
- Julian Léonard, Moonjoo Lee, Andrea Morales, Thomas M Karg, Tilman Esslinger, and Tobias Donner. Optical transport and manipulation of an ultracold atomic cloud using focus-tunable lenses. *New J. Phys.*, 16(9):093028, 2014. doi:[10.1088/1367-2630/16/9/093028](https://doi.org/10.1088/1367-2630/16/9/093028).
- M. Lepers, R. Vexiau, M. Aymar, N. Bouloufa-Maafa, and O. Dulieu. Long-range interactions between polar alkali-metal diatoms in external electric fields. *Phys. Rev. A*, 88:032709, Sep 2013. doi:[10.1103/PhysRevA.88.032709](https://doi.org/10.1103/PhysRevA.88.032709).
- R. J. LeRoy. Theory of deviations from the limiting near-dissociation behavior of diatomic-molecules. *J. Chem. Phys.*, 73(12):6003–6012, 1980. doi:[10.1063/1.440134](https://doi.org/10.1063/1.440134).
- RJ LeRoy. DEPENDENCE OF DIATOMIC ROTATIONAL CONSTANT BV ON LONG-RANGE INTERNUCLEAR POTENTIAL. *Can. J. Phys.*, 50(10):953, 1972. doi:[10.1139/p72-134](https://doi.org/10.1139/p72-134).
- Robert J. LeRoy and Richard B. Bernstein. Dissociation energy and long-range potential of diatomic molecules from vibrational spacings of higher levels. *J. Chem. Phys.*, 52(8):3869–3879, 1970. doi:[10.1063/1.1673585](https://doi.org/10.1063/1.1673585).
- Robert J. LeRoy, Nikesh S. Dattani, John A. Coxon, Amanda J. Ross, Patrick Crozet, and Colan Linton. Accurate analytic potentials for $\text{Li}_2(\text{X}^1\Sigma_g^+)$ and $\text{Li}_2(\text{A}^1\Sigma_u^+)$ from 2 to 90 Å, and the radiative lifetime of Li (2p). *J. Chem. Phys.*, 131(20):204309, 2009. doi:[10.1063/1.3264688](https://doi.org/10.1063/1.3264688).
- Robert J. LeRoy, Carl C. Haugen, Jason Tao, and Hui Li. Long-range damping functions improve the short-range behaviour of mlr potential energy functions. *Mol. Phys.*, 109(3):435–446, 2011. doi:[10.1080/00268976.2010.527304](https://doi.org/10.1080/00268976.2010.527304).
- P. D. Lett, W. D. Phillips, S. L. Rolston, C. E. Tanner, R. N. Watts, and C. I. Westbrook. Optical molasses. *J. Opt. Soc. Am. B*, 6(11):2084–2107, November 1989. doi:[10.1364/JOSAB.6.002084](https://doi.org/10.1364/JOSAB.6.002084).

- P. D. Lett, K. Helmerson, W. D. Phillips, L. P. Ratliff, S. L. Rolston, and M. E. Wagshul. Spectroscopy of na₂ by photoassociation of laser-cooled na. *Phys. Rev. Lett.*, 71:2200–2203, Oct 1993. doi:[10.1103/PhysRevLett.71.2200](https://doi.org/10.1103/PhysRevLett.71.2200).
- Paul D. Lett, Richard N. Watts, Christoph I. Westbrook, William D. Phillips, Phillip L. Gould, and Harold J. Metcalf. Observation of atoms laser cooled below the Doppler limit. *Phys. Rev. Lett.*, 61(2):169–172, July 1988. doi:[10.1103/PhysRevLett.61.169](https://doi.org/10.1103/PhysRevLett.61.169).
- K H Leung, E Tiberi, B Iritani, I Majewska, R Moszynski, and T Zelevinsky. Ultracold 88sr2 molecules in the absolute ground state. *New Journal of Physics*, 23(11):115002, oct 2021. doi:[10.1088/1367-2630/ac2dac](https://doi.org/10.1088/1367-2630/ac2dac).
- Harry Levine, Alexander Keesling, Ahmed Omran, Hannes Bernien, Sylvain Schwartz, Alexander S. Zibrov, Manuel Endres, Markus Greiner, Vladan Vuletić, and Mikhail D. Lukin. High-fidelity control and entanglement of rydberg-atom qubits. *Phys. Rev. Lett.*, 121:123603, Sep 2018. doi:[10.1103/PhysRevLett.121.123603](https://doi.org/10.1103/PhysRevLett.121.123603).
- H. J. Lewandowski, D. M. Harber, D. L. Whitaker, and E. A. Cornell. Simplified system for creating a Bose–Einstein condensate. *J. Low Temp. Phys.*, 132(5):309–367, 2003. doi:[10.1023/A:1024800600621](https://doi.org/10.1023/A:1024800600621).
- C. Y. Li, W. L. Liu, J. Z. Wu, X. F. Wang, Y. Q. Li, J. Ma, L. T. Xiao, and S. T. Jia. Highly sensitive photoassociation spectroscopy of ultracold (nacs)-na-23-c-133 molecular long-range states below the 3s(1/2)+6p(1/2) limit. *J. Quant. Spectrosc. Radiat. Transf.*, 225:214–218, March 2019. doi:[10.1016/j.jqsrt.2018.12.028](https://doi.org/10.1016/j.jqsrt.2018.12.028).
- Jun-Ru Li, Jeongwon Lee, Wujie Huang, Sean Burchesky, Boris Shteynas, Furkan Çağrı Top, Alan O Jamison, and Wolfgang Ketterle. A stripe phase with supersolid properties in spin-orbit-coupled bose-einstein condensates. *Nature*, 543(7643):91–94, 2017. doi:[10.1038/nature21431](https://doi.org/10.1038/nature21431).
- Jun-Ru Li, William G Tobias, Kyle Matsuda, Calder Miller, Giacomo Valtolina, Luigi De Marco, Reuben RW Wang, Lucas Lassablière, Goulven Quéméner, John L Bohn, et al. Tuning of dipolar interactions and evaporative cooling in a three-dimensional molecular quantum gas. *Nature Physics*, 17(10):1144–1148, 2021. doi:doi.org/10.1038/s41567-021-01329-6.
- Jun-Ru Li, Kyle Matsuda, Calder Miller, Annette N Carroll, William G Tobias, Jacob S Higgins, and Jun Ye. Tunable itinerant spin dynamics with polar molecules. *Nature*, 614(7946):70–74, 2023a. doi:[10.1038/s41586-022-05479-2](https://doi.org/10.1038/s41586-022-05479-2).
- Lintao Li, William Huie, Neville Chen, Brian DeMarco, and Jacob P. Covey. Active cancellation of servo-induced noise on stabilized lasers via feedforward. *Phys. Rev. Appl.*, 18:064005, Dec 2022. doi:[10.1103/PhysRevApplied.18.064005](https://doi.org/10.1103/PhysRevApplied.18.064005).
- Zi-Liang Li, Zheng-Yu Gu, Peng-Jun Wang, and Jing Zhang. Efficient production of ultracold polar molecules 23na40k in their absolute ground state via intermediate state of the coupled complex b 1π— ν= 4; c 3σ+— ν= 25;. *Science China Physics, Mechanics & Astronomy*, 66(9):293011, 2023b. doi:<https://doi.org/10.1007/s11433-023-2148-8>.
- IS Lim, H Stoll, and P Schwerdtfeger. Relativistic small-core energy-consistent pseudopotentials for the alkaline-earth elements from Ca to Ra. *J. Chem. Phys.*, 124(3):2148945, JAN 21 2006. doi:[10.1063/1.2148945](https://doi.org/10.1063/1.2148945).
- Junyu Lin, Junyu He, Xin Ye, and Dajun Wang. Anisotropic polarizability of ultracold ground-state ²³Na⁸⁷Rb molecules. *Phys. Rev. A*, 103:023332, Feb 2021. doi:[10.1103/PhysRevA.103.023332](https://doi.org/10.1103/PhysRevA.103.023332).

Junyu Lin, Junyu He, Mucan Jin, Guanghua Chen, and Dajun Wang. Seconds-scale coherence on nuclear spin transitions of ultracold polar molecules in 3d optical lattices. *Phys. Rev. Lett.*, 128:223201, Jun 2022. doi:[10.1103/PhysRevLett.128.223201](https://doi.org/10.1103/PhysRevLett.128.223201).

Junyu Lin, Guanghua Chen, Mucan Jin, Zhaopeng Shi, Fulin Deng, Wenxian Zhang, Goulven Quéméner, Tao Shi, Su Yi, and Dajun Wang. Microwave shielding of bosonic narb molecules. *Phys. Rev. X*, 13:031032, Sep 2023. doi:[10.1103/PhysRevX.13.031032](https://doi.org/10.1103/PhysRevX.13.031032).

Y.-J. Lin, A. R. Perry, R. L. Compton, I. B. Spielman, and J. V. Porto. Rapid production of ^{87}rb Bose-Einstein condensates in a combined magnetic and optical potential. *Phys. Rev. A*, 79(6):063631–, June 2009. doi:[10.1103/PhysRevA.79.063631](https://doi.org/10.1103/PhysRevA.79.063631).

Zhong Lin, Kazuko Shimizu, Mingsheng Zhan, Fujio Shimizu, and Hiroshi Takuma. Laser cooling and trapping of li. *Japanese Journal of Applied Physics*, 30:1324–1326, 1991. doi:[10.1143/JJAP.30.L1324](https://doi.org/10.1143/JJAP.30.L1324).

C. Linton, T. L. Murphy, F. Martin, R. Bacis, and J. Verges. Fourier transform spectroscopy of the $1^3\Sigma_g^+ - a^3\Sigma_u^+$ transition of ${}^6\text{Li}_2$ molecule. *J. Chem. Phys.*, 91(10):6036–6041, 1989. doi:[10.1063/1.457421](https://doi.org/10.1063/1.457421).

C. Linton, R. Bacis, P. Crozet, F. Martin, A.J. Ross, and J. Verges. Fourier transform spectroscopy of the $1^3\Delta_g - b^3\Pi_u$ transition in ${}^6\text{Li}_2$. *J. Mol. Spectrosc.*, 151(1):159–177, January 1992. doi:[10.1016/0022-2852\(92\)90012-D](https://doi.org/10.1016/0022-2852(92)90012-D).

C. Linton, F. Martin, I. Russier, A.J. Ross, P. Crozet, S. Churassy, and R. Bacis. Observation and analysis of the $A^1\Sigma_u^+$ state of ${}^6\text{Li}_2$ from $\nu = 0$ to the dissociation limit. *J. Mol. Spectrosc.*, 175(2):340–353, 1996. doi:[10.1006/jmsp.1996.0039](https://doi.org/10.1006/jmsp.1996.0039).

Lan Liu, De-Chao Zhang, Huan Yang, Ya-Xiong Liu, Jue Nan, Jun Rui, Bo Zhao, and Jian-Wei Pan. Observation of interference between resonant and detuned stirap in the adiabatic creation of ${}^{23}\text{Na}{}^{40}\text{K}$ molecules. *Phys. Rev. Lett.*, 122:253201, Jun 2019. doi:[10.1103/PhysRevLett.122.253201](https://doi.org/10.1103/PhysRevLett.122.253201).

Mingwu Lu, Nathaniel Q. Burdick, Seo Ho Youn, and Benjamin L. Lev. Strongly dipolar bose-einstein condensate of dysprosium. *Phys. Rev. Lett.*, 107:190401, Oct 2011. doi:[10.1103/PhysRevLett.107.190401](https://doi.org/10.1103/PhysRevLett.107.190401).

A. D. Ludlow, X. Huang, M. Notcutt, T. Zanon-Willette, S. M. Foreman, M. M. Boyd, S. Blatt, and J. Ye. Compact, thermal-noise-limited optical cavity for diode laser stabilization at 1×10^{-15} . *Opt. Lett.*, 32(6):641–643, Mar 2007. doi:[10.1364/OL.32.000641](https://doi.org/10.1364/OL.32.000641).

O. J. Luiten, M. W. Reynolds, and J. T. M. Walraven. Kinetic theory of the evaporative cooling of a trapped gas. *Phys. Rev. A*, 53:381–389, Jan 1996. doi:[10.1103/PhysRevA.53.381](https://doi.org/10.1103/PhysRevA.53.381).

L Luo, B Clancy, J Joseph, J Kinast, A Turlapov, and J E Thomas. Evaporative cooling of unitary fermi gas mixtures in optical traps. *New J. Phys.*, 8(9):213, 2006. doi:[10.1088/1367-2630/8/9/213](https://doi.org/10.1088/1367-2630/8/9/213).

Benjamin P. Maddox, Jonathan M. Mortlock, Tom R. Hepworth, Adarsh P. Raghuram, Philip D. Gregory, Alexander Guttridge, and Simon L. Cornish. Enhanced quantum state transfer via feedforward cancellation of optical phase noise, 2024.

E Majorana. Atomi orientati in campo magnetico variabile. *Nuovo Cim*, 9:43–50, 1932.

Louis Marchildon. *Quantum Mechanics*. Springer Berlin Heidelberg, 2002. doi:[10.1007/978-3-662-04750-7](https://doi.org/10.1007/978-3-662-04750-7).

- M. Marinescu and A. Dalgarno. Dispersion forces and long-range electronic transition dipole moments of alkali-metal dimer excited states. *Phys. Rev. A*, 52:311–328, Jul 1995. doi:[10.1103/PhysRevA.52.311](https://doi.org/10.1103/PhysRevA.52.311).
- M. Marinescu, H. R. Sadeghpour, and A. Dalgarno. Dispersion coefficients for alkali-metal dimers. *Phys. Rev. A*, 49:982–988, Feb 1994. doi:[10.1103/PhysRevA.49.982](https://doi.org/10.1103/PhysRevA.49.982).
- C. Clay Marston and Gabriel G. Balint-Kurti. The Fourier grid hamiltonian method for bound state eigenvalues and eigenfunctions. *J. Chem. Phys.*, 91(6):3571–3576, 1989. doi:[10.1063/1.456888](https://doi.org/10.1063/1.456888).
- F. Martin, P. Crozet, A. J. Ross, M. Aubert-Frecon, P. Kowalczyk, W. Jastrzebski, and A. Pashov. On the $X^1\Sigma^+$ state of KLi. *J. Chem. Phys.*, 115(9):4118–4124, 2001. doi:[10.1063/1.1388555](https://doi.org/10.1063/1.1388555).
- G. A. Martin and W. L. Wiese. Atomic oscillator-strength distributions in spectral series of the lithium isoelectronic sequence. *Phys. Rev. A*, 13:699–714, Feb 1976. doi:[10.1103/PhysRevA.13.699](https://doi.org/10.1103/PhysRevA.13.699).
- Kirill Martiyanov, Vasiliy Makhalov, and Andrey Turlapov. Observation of a two-dimensional fermi gas of atoms. *Phys. Rev. Lett.*, 105(3):030404–, July 2010a. doi:[10.1103/PhysRevLett.105.030404](https://doi.org/10.1103/PhysRevLett.105.030404).
- Kirill Martiyanov, Vasiliy Makhalov, and Andrey Turlapov. Observation of a two-dimensional fermi gas of atoms. *Phys. Rev. Lett.*, 105(3):030404–, July 2010b. doi:[10.1103/PhysRevLett.105.030404](https://doi.org/10.1103/PhysRevLett.105.030404).
- Françoise Masnou-Seeuws and Pierre Pillet. Formation of ultracold molecules ($t \leq 200\mu\text{K}$ via photoassociation in a gas of laser-cooled atoms. In Benjamin Bederson and Herbert Walther, editors, *Advances In Atomic, Molecular, and Optical Physics*, volume 47 of *Advances In Atomic, Molecular, and Optical Physics*, pages 53 – 127. Academic Press, 2001. doi:[10.1016/S1049-250X\(01\)80055-0](https://doi.org/10.1016/S1049-250X(01)80055-0).
- Kyle Matsuda, Luigi De Marco, Jun-Ru Li, William G Tobias, Giacomo Valtolina, Goulven Quéméner, and Jun Ye. Resonant collisional shielding of reactive molecules using electric fields. *Science*, 370(6522):1324–1327, 2020. doi:[10.1126/science.abe7370](https://doi.org/10.1126/science.abe7370).
- Michael Mayle, Brandon P. Ruzic, and John L. Bohn. Statistical aspects of ultracold resonant scattering. *Phys. Rev. A*, 85:062712, Jun 2012. doi:[10.1103/PhysRevA.85.062712](https://doi.org/10.1103/PhysRevA.85.062712).
- Michael Mayle, Goulven Quéméner, Brandon P. Ruzic, and John L. Bohn. Scattering of ultracold molecules in the highly resonant regime. *Phys. Rev. A*, 87:012709, Jan 2013. doi:[10.1103/PhysRevA.87.012709](https://doi.org/10.1103/PhysRevA.87.012709).
- Anton Mazurenko, Christie S. Chiu, Geoffrey Ji, Maxwell F. Parsons, Mon Kan-Nagy, Richard Schmidt, Fabian Grusdt, Eugene Demler, Daniel Greif, and Markus Greiner. A cold-atom fermi-hubbard antiferromagnet. *Nature*, 545(7655):462–466, 2017. doi:[10.1038/nature22362](https://doi.org/10.1038/nature22362).
- W. I. McAlexander, E. R. I. Abraham, N. W. M. Ritchie, C. J. Williams, H. T. C. Stoof, and R. G. Hulet. Precise atomic radiative lifetime via photoassociative spectroscopy of ultracold lithium. *Phys. Rev. A*, 51(2):R871–R874, February 1995. doi:[10.1103/PhysRevA.51.R871](https://doi.org/10.1103/PhysRevA.51.R871).
- W. I. McAlexander, E. R. I. Abraham, and R. G. Hulet. Radiative lifetime of the $2p$ state of lithium. *Phys. Rev. A*, 54(1):R5–R8, July 1996. doi:[10.1103/PhysRevA.54.R5](https://doi.org/10.1103/PhysRevA.54.R5).

- D J McCarron, S A King, and S L Cornish. Modulation transfer spectroscopy in atomic rubidium. *Meas. Sci. Technol.*, 19(10):105601, 2008. doi:[10.1088/0957-0233/19/10/105601](https://doi.org/10.1088/0957-0233/19/10/105601).
- D. C. McKay, D. Jervis, D. J. Fine, J. W. Simpson-Porco, G. J. A. Edge, and J. H. Thywissen. Low-temperature high-density magneto-optical trapping of potassium using the open $4s \rightarrow 5p$ transition at 405 nm. *Phys. Rev. A*, 84(6):063420–, December 2011. doi:[10.1103/PhysRevA.84.063420](https://doi.org/10.1103/PhysRevA.84.063420).
- J. Harold Metcalf and Peter van der Straten. *Laser Cooling and Trapping*. Springer, 1999.
- A. Micheli, G. K. Brennen, and P. Zoller. A toolbox for lattice-spin models with polar molecules. *Nat. Phys.*, 2(5):341, 2006. doi:[10.1038/nphys287](https://doi.org/10.1038/nphys287).
- A. Micheli, G. Pupillo, H. P. Büchler, and P. Zoller. Cold polar molecules in two-dimensional traps: Tailoring interactions with external fields for novel quantum phases. *Phys. Rev. A*, 76: 043604, Oct 2007. doi:[10.1103/PhysRevA.76.043604](https://doi.org/10.1103/PhysRevA.76.043604).
- Thomas Middelmann, Stephan Falke, Christian Lisdat, and Uwe Sterr. Long-range transport of ultracold atoms in a far-detuned one-dimensional optical lattice. *New J. Phys.*, 14(7):073020, 2012. doi:[10.1088/1367-2630/14/7/073020](https://doi.org/10.1088/1367-2630/14/7/073020).
- Frederick H. Mies, Carl J. Williams, Paul S. Julienne, and Morris Krauss. Estimating bounds on collisional relaxation rates of spin-polarized $(87)\text{rb}$ atoms at ultracold temperatures. *Journal of research of the National Institute of Standards and Technology*, 101:521–535, Jul-Aug 1996.
- Alan L. Migdall, John V. Prodan, William D. Phillips, Thomas H. Bergeman, and Harold J. Metcalf. First observation of magnetically trapped neutral atoms. *Phys. Rev. Lett.*, 54: 2596–2599, Jun 1985. doi:[10.1103/PhysRevLett.54.2596](https://doi.org/10.1103/PhysRevLett.54.2596).
- D. E. Miller, J. K. Chin, C. A. Stan, Y. Liu, W. Setiawan, C. Sanner, and W. Ketterle. Critical velocity for superfluid flow across the bec-bcs crossover. *Phys. Rev. Lett.*, 99:070402, Aug 2007. doi:[10.1103/PhysRevLett.99.070402](https://doi.org/10.1103/PhysRevLett.99.070402).
- J. D. Miller, R. A. Cline, and D. J. Heinzen. Photoassociation spectrum of ultracold rb atoms. *Phys. Rev. Lett.*, 71:2204–2207, Oct 1993a. doi:[10.1103/PhysRevLett.71.2204](https://doi.org/10.1103/PhysRevLett.71.2204).
- J. D. Miller, R. A. Cline, and D. J. Heinzen. Far-off-resonance optical trapping of atoms. *Phys. Rev. A*, 47:R4567–R4570, Jun 1993b. doi:[10.1103/PhysRevA.47.R4567](https://doi.org/10.1103/PhysRevA.47.R4567).
- G. Modugno, C. Benkő, P. Hannaford, G. Roati, and M. Inguscio. Sub-Doppler laser cooling of fermionic ^{40}k atoms. *Phys. Rev. A*, 60(5):R3373–R3376, November 1999. doi:[10.1103/PhysRevA.60.R3373](https://doi.org/10.1103/PhysRevA.60.R3373).
- A. J. Moerdijk and B. J. Verhaar. Collisional two- and three-body decay rates of dilute quantum gases at ultralow temperatures. *Phys. Rev. A*, 53:R19–R22, Jan 1996. doi:[10.1103/PhysRevA.53.R19](https://doi.org/10.1103/PhysRevA.53.R19).
- A. J. Moerdijk, B. J. Verhaar, and A. Axelsson. Resonances in ultracold collisions of ^6Li , ^7Li , and ^{23}Na . *Phys. Rev. A*, 51:4852–4861, Jun 1995. doi:[10.1103/PhysRevA.51.4852](https://doi.org/10.1103/PhysRevA.51.4852).
- Peter J. Mohr, Barry N. Taylor, and David B. Newell. Codata recommended values of the fundamental physical constants: 2010. *Journal of Physical and Chemical Reference Data*, 41 (4):043109, 2012. doi:<http://dx.doi.org/10.1063/1.4724320>.

- Peter K. Molony, Philip D. Gregory, Zhonghua Ji, Bo Lu, Michael P. Köppinger, C. Ruth Le Sueur, Caroline L. Blackley, Jeremy M. Hutson, and Simon L. Cornish. Creation of ultracold $^{87}\text{Rb}^{133}\text{Cs}$ molecules in the rovibrational ground state. *Phys. Rev. Lett.*, 113:255301, Dec 2014. doi:[10.1103/PhysRevLett.113.255301](https://doi.org/10.1103/PhysRevLett.113.255301).
- J. H. Moore, C. C. Davis, and M. A. Coplan. *Building Scientific Apparatus*. Cambridge University Press, 4th edition, 2009.
- Henning Moritz, Thilo Stöferle, Kenneth Günter, Michael Köhl, and Tilman Esslinger. Confinement induced molecules in a 1d fermi gas. *Phys. Rev. Lett.*, 94:210401, Jun 2005. doi:[10.1103/PhysRevLett.94.210401](https://doi.org/10.1103/PhysRevLett.94.210401).
- Steven A Moses. *A quantum gas of polar molecules in an optical lattice*. PhD thesis, University of Colorado at Boulder, 2016.
- Steven A Moses, Jacob P Covey, Matthew T Miecnikowski, Bo Yan, Bryce Gadway, Jun Ye, and Deborah S Jin. Creation of a low-entropy quantum gas of polar molecules in an optical lattice. *Science*, 350(6261):659–662, 2015. doi:[10.1126/science.aac6400](https://doi.org/10.1126/science.aac6400).
- A. Mosk, S. Jochim, H. Moritz, Th. Elsässer, M. Weidemüller, and R. Grimm. Resonator-enhanced optical dipole trap for fermionic lithium atoms. *Opt. Lett.*, 26(23):1837–1839, Dec 2001. doi:[10.1364/OL.26.001837](https://doi.org/10.1364/OL.26.001837).
- Torben Müller. *Microscopic Probing and Manipulation of Ultracold Fermions*. PhD thesis, ETH Zurich, 2011.
- Thomas Müller-Wirts. Patent US 6,178,002, DE19743493C2, 2001.
- Monika Musial and Stanislaw A. Kucharski. First principle calculations of the potential energy curves for electronic states of the lithium dimer. *J. Chem. Theory Comput.*, 10(3):1200–1211, March 2014. doi:[10.1021/ct401076e](https://doi.org/10.1021/ct401076e).
- W Nagourney. *Quantum Electronics for Atomic Physics and Telecommunication*. Oxford University, 2014a.
- W Nagourney. *Quantum Electronics for Atomic Physics and Telecommunication*. Oxford University, 2014b.
- D. S. Naik and C. Raman. Optically plugged quadrupole trap for bose-einstein condensates. *Phys. Rev. A*, 71:033617, Mar 2005. doi:[10.1103/PhysRevA.71.033617](https://doi.org/10.1103/PhysRevA.71.033617).
- Reginaldo Napolitano, John Weiner, Carl J. Williams, and Paul S. Julienne. Line shapes of high resolution photoassociation spectra of optically cooled atoms. *Phys. Rev. Lett.*, 73:1352–1355, Sep 1994. doi:[10.1103/PhysRevLett.73.1352](https://doi.org/10.1103/PhysRevLett.73.1352).
- S. Nascimbène, N. Navon, K. J. Jiang, F. Chevy, and C. Salomon. Exploring the thermodynamics of a universal fermi gas. *Nature*, 463(7284):1057–1060, February 2010. doi:[10.1038/nature08814](https://doi.org/10.1038/nature08814).
- B. Neyenhuis, B. Yan, S. A. Moses, J. P. Covey, A. Chotia, A. Petrov, S. Kotochigova, J. Ye, and D. S. Jin. Anisotropic polarizability of ultracold polar $^{40}\text{K}^{87}\text{Rb}$ molecules. *Phys. Rev. Lett.*, 109:230403, Dec 2012. doi:[10.1103/PhysRevLett.109.230403](https://doi.org/10.1103/PhysRevLett.109.230403).
- Brian Neyenhuis. *Ultracold polar krb molecules in optical lattices*. PhD thesis, University of Colorado at Boulder, 2012.

- K.-K. Ni, S. Ospelkaus, M. H. G. de Miranda, A. Pe'er, B. Neyenhuis, J. J. Zirbel, S. Kotochigova, P. S. Julienne, D. S. Jin, and J. Ye. A high phase-space-density gas of polar molecules. *Science*, 322(5899):231–235, 2008. doi:[10.1126/science.1163861](https://doi.org/10.1126/science.1163861).
- K-K Ni, S Ospelkaus, D Wang, G Quéméner, Brian Neyenhuis, MHG De Miranda, JL Bohn, Jun Ye, and DS Jin. Dipolar collisions of polar molecules in the quantum regime. *Nature*, 464(7293):1324–1328, 2010. doi:[10.1038/nature08953](https://doi.org/10.1038/nature08953).
- Kang-Kuen Ni. *A Quantum Gas of Polar Molecules*. PhD thesis, University of Colorado, 2009.
- Kang-Kuen Ni, Till Rosenband, and David D. Grimes. Dipolar exchange quantum logic gate with polar molecules. *Chem. Sci.*, 9:6830–6838, 2018. doi:[10.1039/C8SC02355G](https://doi.org/10.1039/C8SC02355G).
- Mark Notcutt, Long-Sheng Ma, Jun Ye, and John L. Hall. Simple and compact 1-Hz laser system via an improved mounting configuration of a reference cavity. *Opt. Lett.*, 30(14):1815–1817, Jul 2005. doi:[10.1364/OL.30.001815](https://doi.org/10.1364/OL.30.001815).
- P. Nozières and S. Schmitt-Rink. Bose condensation in an attractive fermion gas: From weak to strong coupling superconductivity. *J. Low Temp. Phys.*, 59(3):195–211, 1985a. doi:[10.1007/BF00683774](https://doi.org/10.1007/BF00683774).
- P. Nozières and S. Schmitt-Rink. Bose condensation in an attractive fermion gas: From weak to strong coupling superconductivity. *J. Low Temp. Phys.*, 59(3):195–211, 1985b. doi:[10.1007/BF00683774](https://doi.org/10.1007/BF00683774).
- K. M. O’Hara, S. R. Granade, M. E. Gehm, T. A. Savard, S. Bali, C. Freed, and J. E. Thomas. Ultrastable CO₂ laser trapping of lithium fermions. *Phys. Rev. Lett.*, 82(21):4204–4207, May 1999. doi:[10.1103/PhysRevLett.82.4204](https://doi.org/10.1103/PhysRevLett.82.4204).
- K. M. O’Hara, M. E. Gehm, S. R. Granade, and J. E. Thomas. Scaling laws for evaporative cooling in time-dependent optical traps. *Phys. Rev. A*, 64:051403, Oct 2001. doi:[10.1103/PhysRevA.64.051403](https://doi.org/10.1103/PhysRevA.64.051403).
- K. M. OHara, S. R. Granade, M. E. Gehm, and J. E. Thomas. Loading dynamics of CO₂ laser traps. *Phys. Rev. A*, 63(4):043403–, March 2001. doi:[10.1103/PhysRevA.63.043403](https://doi.org/10.1103/PhysRevA.63.043403).
- K. M. O’Hara, S. L. Hemmer, M. E. Gehm, S. R. Granade, and J. E. Thomas. Observation of a strongly interacting degenerate fermi gas of atoms. *Science*, 298(5601):2179–2182, 2002. doi:[10.1126/science.1079107](https://doi.org/10.1126/science.1079107).
- M. Olshanii. Atomic scattering in the presence of an external confinement and a gas of impenetrable bosons. *Phys. Rev. Lett.*, 81:938–941, Aug 1998. doi:[10.1103/PhysRevLett.81.938](https://doi.org/10.1103/PhysRevLett.81.938).
- Ahmed Omran, Martin Boll, Timon A. Hilker, Katharina Kleinlein, Guillaume Salomon, Immanuel Bloch, and Christian Gross. Microscopic observation of pauli blocking in degenerate fermionic lattice gases. *Phys. Rev. Lett.*, 115:263001, Dec 2015. doi:[10.1103/PhysRevLett.115.263001](https://doi.org/10.1103/PhysRevLett.115.263001).
- C. Ospelkaus, S. Ospelkaus, L. Humbert, P. Ernst, K. Sengstock, and K. Bongs. Ultracold heteronuclear molecules in a 3d optical lattice. *Phys. Rev. Lett.*, 97:120402, Sep 2006. doi:[10.1103/PhysRevLett.97.120402](https://doi.org/10.1103/PhysRevLett.97.120402).
- S. Ospelkaus, K.-K. Ni, G. Quéméner, B. Neyenhuis, D. Wang, M. H. G. de Miranda, J. L. Bohn, J. Ye, and D. S. Jin. Controlling the hyperfine state of rovibronic ground-state polar molecules. *Phys. Rev. Lett.*, 104:030402, Jan 2010a. doi:[10.1103/PhysRevLett.104.030402](https://doi.org/10.1103/PhysRevLett.104.030402).

- S Ospelkaus, K-K Ni, D Wang, MHG De Miranda, B Neyenhuis, 1 G Quéméner, PS Julienne, JL Bohn, DS Jin, and J Ye. Quantum-state controlled chemical reactions of ultracold potassium-rubidium molecules. *Science*, 327(5967):853–857, 2010b. doi:[10.1126/science.1184121](https://doi.org/10.1126/science.1184121).
- Yu. B. Ovchinnikov, J. H. Müller, M. R. Doery, E. J. D. Vredenbregt, K. Helmerson, S. L. Rolston, and W. D. Phillips. Diffraction of a released bose-einstein condensate by a pulsed standing light wave. *Phys. Rev. Lett.*, 83:284–287, Jul 1999. doi:[10.1103/PhysRevLett.83.284](https://doi.org/10.1103/PhysRevLett.83.284).
- Sambit B. Pal, Mark M. Lam, and K. Dieckmann. Stability of a frequency-comb-based transfer-lock using a passive fabry-perot resonator. *Opt. Lett.*, 41(23):5527–5530, DEC 1 2016. doi:[10.1364/OL.41.005527](https://doi.org/10.1364/OL.41.005527).
- Sambit Bikas Pal. *Molecular spectroscopy of ultracold ^6Li - ^{40}K molecules: Towards STIRAP transfer to absolute ground state*. PhD thesis, National University of Singapore, 2016.
- C. D. Panda, B. R. O’Leary, A. D. West, J. Baron, P. W. Hess, C. Hoffman, E. Kirilov, C. B. Overstreet, E. P. West, D. DeMille, J. M. Doyle, and G. Gabrielse. Stimulated raman adiabatic passage preparation of a coherent superposition of the $H^3\Delta_1$ states for an improved electron electric-dipole-moment measurement. *Phys. Rev. A*, 93:052110, May 2016. doi:[10.1103/PhysRevA.93.052110](https://doi.org/10.1103/PhysRevA.93.052110).
- Jee Woo Park. *An Ultracold Gas of Dipolar Fermionic $^{23}\text{Na}^{40}\text{K}$ Molecules*. PhD thesis, MASSACHUSETTS INSTITUTE OF TECHNOLOGY, 2016.
- Jee Woo Park, Sebastian A. Will, and Martin W. Zwierlein. Ultracold dipolar gas of fermionic $^{23}\text{Na}^{40}\text{K}$ molecules in their absolute ground state. *Phys. Rev. Lett.*, 114:205302, May 2015a. doi:[10.1103/PhysRevLett.114.205302](https://doi.org/10.1103/PhysRevLett.114.205302).
- Jee Woo Park, Sebastian A Will, and Martin W Zwierlein. Two-photon pathway to ultracold ground state molecules of $^{23}\text{Na}^{40}\text{K}$. *New Journal of Physics*, 17(7):075016, jul 2015b. doi:[10.1088/1367-2630/17/7/075016](https://doi.org/10.1088/1367-2630/17/7/075016).
- Jee Woo Park, Zoe Z Yan, Huanqian Loh, Sebastian A Will, and Martin W Zwierlein. Second-scale nuclear spin coherence time of ultracold $^{23}\text{Na}^{40}\text{K}$ molecules. *Science*, 357(6349):372–375, 2017. doi:[10.1126/science.aal5066](https://doi.org/10.1126/science.aal5066).
- M. F. Parsons, A. Mazurenko, C. S. Chiu, D. Ji, D. Greif, and M. Greiner. Site-resolved observations of antiferromagnetic correlations in the hubbard model. arXiv:1605.02704, 2016.
- G. B. Partridge, K. E. Strecker, R. I. Kamar, M. W. Jack, and R. G. Hulet. Molecular probe of pairing in the bec-bcs crossover. *Phys. Rev. Lett.*, 95(2):020404–, July 2005. doi:[10.1103/PhysRevLett.95.020404](https://doi.org/10.1103/PhysRevLett.95.020404).
- A. Pashov, W. Jastrzębski, and P. Kowalczyk. The $B^1\Pi+$ and $C^1\Sigma+$ states of KLi . *Chem. Phys. Lett.*, 292(4-6):615–620, 1998. doi:[10.1016/S0009-2614\(98\)00702-7](https://doi.org/10.1016/S0009-2614(98)00702-7).
- E. Peik, J. Abel, Th. Becker, J. von Zanthier, and H. Walther. Sideband cooling of ions in radio-frequency traps. *Phys. Rev. A*, 60:439–449, Jul 1999. doi:[10.1103/PhysRevA.60.439](https://doi.org/10.1103/PhysRevA.60.439).
- C. L. Pekeris. The rotation-vibration coupling in diatomic molecules. *Phys. Rev.*, 45:98–103, Jan 1934. doi:[10.1103/PhysRev.45.98](https://doi.org/10.1103/PhysRev.45.98).
- Philippe Pellegrini, Marko Gacesa, and Robin Côté. Giant formation rates of ultracold molecules via feshbach-optimized photoassociation. *Phys. Rev. Lett.*, 101:053201, Aug 2008. doi:[10.1103/PhysRevLett.101.053201](https://doi.org/10.1103/PhysRevLett.101.053201).

- C. J. Pethick and H. Smith. *Bose-Einstein condensation in dilute gases*. Cambridge University Press, 2008.
- Wolfgang Petrich, Michael H. Anderson, Jason R. Ensher, and Eric A. Cornell. Behavior of atoms in a compressed magneto-optical trap. *J. Opt. Soc. Am. B*, 11(8):1332–1335, Aug 1994. doi:[10.1364/JOSAB.11.001332](https://doi.org/10.1364/JOSAB.11.001332).
- D. S. Petrov. Three-body problem in fermi gases with short-range interparticle interaction. *Phys. Rev. A*, 67:010703, Jan 2003. doi:[10.1103/PhysRevA.67.010703](https://doi.org/10.1103/PhysRevA.67.010703).
- D. S. Petrov. Quantum mechanical stabilization of a collapsing bose-bose mixture. *Phys. Rev. Lett.*, 115:155302, Oct 2015. doi:[10.1103/PhysRevLett.115.155302](https://doi.org/10.1103/PhysRevLett.115.155302).
- D. S. Petrov, C. Salomon, and G. V. Shlyapnikov. Weakly bound dimers of fermionic atoms. *Phys. Rev. Lett.*, 93:090404, Aug 2004. doi:[10.1103/PhysRevLett.93.090404](https://doi.org/10.1103/PhysRevLett.93.090404).
- D. S. Petrov, C. Salomon, and G. V. Shlyapnikov. Scattering properties of weakly bound dimers of fermionic atoms. *Phys. Rev. A*, 71:012708, Jan 2005. doi:[10.1103/PhysRevA.71.012708](https://doi.org/10.1103/PhysRevA.71.012708).
- D. Petter, G. Natale, R. M. W. van Bijnen, A. Patscheider, M. J. Mark, L. Chomaz, and F. Ferlaino. Probing the roton excitation spectrum of a stable dipolar bose gas. *Phys. Rev. Lett.*, 122:183401, May 2019. doi:[10.1103/PhysRevLett.122.183401](https://doi.org/10.1103/PhysRevLett.122.183401).
- William D. Phillips and Harold Metcalf. Laser deceleration of an atomic beam. *Phys. Rev. Lett.*, 48(9):596–599, March 1982. doi:[10.1103/PhysRevLett.48.596](https://doi.org/10.1103/PhysRevLett.48.596).
- Lewis R. B. Picard, Annie J. Park, Gabriel E. Patenotte, Samuel Gebretsadkan, David Wellnitz, Ana Maria Rey, and Kang-Kuen Ni. Entanglement and iswap gate between molecular qubits. *Nature*, 2024. doi:[10.1038/s41586-024-08177-3](https://doi.org/10.1038/s41586-024-08177-3).
- Marin Pichler, Jianbing Qi, William C. Stwalley, Robert Beuc, and Goran Pichler. Observation of blue satellite bands and photoassociation at ultracold temperatures. *Phys. Rev. A*, 73: 021403, Feb 2006. doi:[10.1103/PhysRevA.73.021403](https://doi.org/10.1103/PhysRevA.73.021403).
- K. Pilch, A. D. Lange, A. Prantner, G. Kerner, F. Ferlaino, H.-C. Nägerl, and R. Grimm. Observation of interspecies feshbach resonances in an ultracold rb-cs mixture. *Phys. Rev. A*, 79:042718, Apr 2009. doi:[10.1103/PhysRevA.79.042718](https://doi.org/10.1103/PhysRevA.79.042718).
- P Pillet, A Crubellier, A Bleton, O Dulieu, P Nosbaum, I Mourachko, and F Masnou-Seeuws. Photoassociation in a gas of cold alkali atoms: I. perturbative quantum approach. *J. Phys. B: At., Mol. Opt. Phys.*, 30(12):2801, 1997. doi:[10.1088/0953-4075/30/12/010](https://doi.org/10.1088/0953-4075/30/12/010).
- Victor Andre Avalos Pinillos. *This PhD thesis is expected to be completed under the supervision of Prof. Kai Dieckmann by Victor at a later date*. PhD thesis, National University of Singapore, Expected 2025.
- Lev Pitaevskii and Sandro Stringari. *Bose-Einstein condensation and superfluidity*, volume 164. Oxford University Press, 2016.
- S. E. Pollack, D. Dries, M. Junker, Y. P. Chen, T. A. Corcovilos, and R. G. Hulet. Extreme tunability of interactions in a ^7Li Bose-Einstein Condensate. *Phys. Rev. Lett.*, 102:090402, Mar 2009a. doi:[10.1103/PhysRevLett.102.090402](https://doi.org/10.1103/PhysRevLett.102.090402).
- Scott E. Pollack, Daniel Dries, and Randall G. Hulet. Universality in three- and four-body bound states of ultracold atoms. *Science*, 326(5960):1683–1685, 2009b. doi:[10.1126/science.1182840](https://doi.org/10.1126/science.1182840).

- Goulven Quémener and Paul S. Julienne. Ultracold molecules under control! *Chem. Rev.*, 112(9, SI):4949–5011, SEP 2012. doi:[10.1021/cr300092g](https://doi.org/10.1021/cr300092g).
- Goulven Quéméner, John L. Bohn, Alexander Petrov, and Svetlana Kotochigova. Universalities in ultracold reactions of alkali-metal polar molecules. *Phys. Rev. A*, 84:062703, Dec 2011. doi:[10.1103/PhysRevA.84.062703](https://doi.org/10.1103/PhysRevA.84.062703).
- E. L. Raab, M. Prentiss, Alex Cable, Steven Chu, and D. E. Pritchard. Trapping of neutral sodium atoms with radiation pressure. *Phys. Rev. Lett.*, 59(23):2631–2634, December 1987. doi:[10.1103/PhysRevLett.59.2631](https://doi.org/10.1103/PhysRevLett.59.2631).
- Leon J. Radziemski, Jr. Engleman, Rolf, and James W. Brault. Fourier-transform-spectroscopy measurements in the spectra of neutral lithium, ${}^6\text{Li}$ i and ${}^7\text{Li}$ (li i). *Phys. Rev. A*, 52(6):4462–4470, December 1995. doi:[10.1103/PhysRevA.52.4462](https://doi.org/10.1103/PhysRevA.52.4462).
- Lyn B. Ratcliff, James L. Fish, and Daniel D. Konowalow. Electronic transition dipole moment functions for transitions among the twenty-six lowest-lying states of Li_2 . *J. Mol. Spectrosc.*, 122(2):293–312, 1987. doi:[10.1016/0022-2852\(87\)90006-3](https://doi.org/10.1016/0022-2852(87)90006-3).
- ALG Rees. The calculation of potential energy curves from band-spectroscopic data. *Proc. Phys. Soc.*, 59(336):998–1008, 1947. doi:[10.1088/0959-5309/59/6/310](https://doi.org/10.1088/0959-5309/59/6/310).
- C. A. Regal and D. S. Jin. Measurement of positive and negative scattering lengths in a fermi gas of atoms. *Phys. Rev. Lett.*, 90:230404, Jun 2003. doi:[10.1103/PhysRevLett.90.230404](https://doi.org/10.1103/PhysRevLett.90.230404).
- C. A. Regal, M. Greiner, and D. S. Jin. Observation of resonance condensation of fermionic atom pairs. *Phys. Rev. Lett.*, 92:040403, Jan 2004. doi:[10.1103/PhysRevLett.92.040403](https://doi.org/10.1103/PhysRevLett.92.040403).
- Cindy A. Regal, Christopher Ticknor, John L. Bohn, and Deborah S. Jin. Creation of ultracold molecules from a fermi gas of atoms. *Nature*, 424(6944):47–50, July 2003. doi:[10.1038/nature01738](https://doi.org/10.1038/nature01738).
- Lukas Reichsöllner, Andreas Schindewolf, Tetsu Takekoshi, Rudolf Grimm, and Hanns-Christoph Nägerl. Quantum engineering of a low-entropy gas of heteronuclear bosonic molecules in an optical lattice. *Phys. Rev. Lett.*, 118:073201, Feb 2017. doi:[10.1103/PhysRevLett.118.073201](https://doi.org/10.1103/PhysRevLett.118.073201).
- L. Ricci, M. Weidemüller, T. Esslinger, A. Hemmerich, C. Zimmermann, V. Vuletic, W. König, and T.W. Hänsch. A compact grating-stabilized diode laser system for atomic physics. *Opt. Commun.*, 117(5-6):541–549, June 1995. doi:[10.1016/0030-4018\(95\)00146-Y](https://doi.org/10.1016/0030-4018(95)00146-Y).
- A. Ridinger, S. Chaudhuri, T. Salez, U. Eismann, D.R. Fernandes, K. Magalh?es, D. Wilkowski, C. Salomon, and F. Chevy. Large atom number dual-species magneto-optical trap for fermionic ${}^6\text{Li}$ and ${}^{40}\text{K}$ atoms. *Eur. Phys. J. D*, 65(1-2):223–242, 2011a. doi:[10.1140/epjd/e2011-20069-4](https://doi.org/10.1140/epjd/e2011-20069-4).
- A. Ridinger, S. Chaudhuri, T. Salez, D. R. Fernandes, N. Bouloufa, O. Dulieu, C. Salomon, and F. Chevy. Photoassociative creation of ultracold heteronuclear ${}^6\text{Li}$ ${}^{40}\text{K}$ molecules. *EPL*, 96(3):33001, 2011b.
- Armin Ridinger. *Towards quantum degenerate Fermi mixtures: Photoassociation of weakly bound ${}^6\text{Li}{}^{40}\text{K}$ molecules*. PhD thesis, ENS Paris, Munich, 2011.
- Fritz Riehle. *Frequency Standards: Basics and Applications*, chapter 9, page 295. Wiley, 2003.

- M. G. Ries, A. N. Wenz, G. Zürn, L. Bayha, I. Boettcher, D. Kedar, P. A. Murthy, M. Neidig, T. Lompe, and S. Jochim. Observation of pair condensation in the quasi-2D bec-bcs crossover. *Phys. Rev. Lett.*, 114:230401, Jun 2015. doi:[10.1103/PhysRevLett.114.230401](https://doi.org/10.1103/PhysRevLett.114.230401).
- N. W. M. Ritchie, E. R. I. Abraham, and R. G. Hulet. Trap loss collisions of ^7Li : The role of trap depth. *Laser Phys.*, Vol. 4:1066, 1994.
- N. W. M. Ritchie, E. R. I. Abraham, Y. Y. Xiao, C. C. Bradley, R. G. Hulet, and P. S. Julienne. Trap-loss collisions of ultracold lithium atoms. *Phys. Rev. A*, 51(2):R890–R893, February 1995. doi:[10.1103/PhysRevA.51.R890](https://doi.org/10.1103/PhysRevA.51.R890).
- J. L. Roberts, N. R. Claussen, S. L. Cornish, E. A. Donley, E. A. Cornell, and C. E. Wieman. Controlled collapse of a bose-einstein condensate. *Phys. Rev. Lett.*, 86:4211–4214, May 2001. doi:[10.1103/PhysRevLett.86.4211](https://doi.org/10.1103/PhysRevLett.86.4211).
- Shai Ronen, Daniele C. E. Bortolotti, and John L. Bohn. Radial and angular rotons in trapped dipolar gases. *Phys. Rev. Lett.*, 98:030406, Jan 2007. doi:[10.1103/PhysRevLett.98.030406](https://doi.org/10.1103/PhysRevLett.98.030406).
- S. Rousseau, A.R. Allouche, M. Aubert-Frécon, S. Magnier, P. Kowalczyk, and W. Jastrzebski. Theoretical study of the electronic structure of $\{\text{KLi}\}$ and comparison with experiments. *Chem. Phys.*, 247(2):193 – 199, 1999. doi:[http://dx.doi.org/10.1016/S0301-0104\(99\)00206-2](http://dx.doi.org/10.1016/S0301-0104(99)00206-2).
- Tanya S. Roussy, Daniel A. Palken, William B. Cairncross, Benjamin M. Brubaker, Daniel N. Gresh, Matt Grau, Kevin C. Cossel, Kia Boon Ng, Yuval Shagam, Yan Zhou, Victor V. Flambaum, Konrad W. Lehnert, Jun Ye, and Eric A. Cornell. Experimental constraint on axionlike particles over seven orders of magnitude in mass. *Phys. Rev. Lett.*, 126:171301, Apr 2021. doi:[10.1103/PhysRevLett.126.171301](https://doi.org/10.1103/PhysRevLett.126.171301).
- Tanya S. Roussy, Luke Caldwell, Trevor Wright, William B. Cairncross, Yuval Shagam, Kia Boon Ng, Noah Schlossberger, Sun Yool Park, Anzhou Wang, Jun Ye, and Eric A. Cornell. An improved bound on the electrons electric dipole moment. *Science*, 381(6653): 46–50, 2023. doi:[10.1126/science.adg4084](https://doi.org/10.1126/science.adg4084).
- Daniel K Ruttle, Alexander Guttridge, Stefan Spence, Robert C Bird, C Ruth Le Sueur, Jeremy M Hutson, and Simon L Cornish. Formation of ultracold molecules by merging optical tweezers. *Physical Review Letters*, 130(22):223401, 2023.
- Daniel K Ruttle, Alexander Guttridge, Tom R Hepworth, and Simon L Cornish. Enhanced quantum control of individual ultracold molecules using optical tweezer arrays. *arXiv preprint*, 2024.
- Timur M. Rvachov, Hyungmok Son, Ariel T. Sommer, Sepehr Ebadi, Juliana J. Park, Martin W. Zwierlein, Wolfgang Ketterle, and Alan O. Jamison. Long-lived ultracold molecules with electric and magnetic dipole moments. *Phys. Rev. Lett.*, 119:143001, Oct 2017. doi:[10.1103/PhysRevLett.119.143001](https://doi.org/10.1103/PhysRevLett.119.143001).
- Timur M Rvachov, Hyungmok Son, Juliana J Park, Sepehr Ebadi, Martin W Zwierlein, Wolfgang Ketterle, and Alan O Jamison. Two-photon spectroscopy of the nali triplet ground state. *Physical Chemistry Chemical Physics*, 20(7):4739–4745, 2018a. doi:[10.1039/C7CP08481A](https://doi.org/10.1039/C7CP08481A).
- Timur M. Rvachov, Hyungmok Son, Juliana J. Park, Pascal M. Notz, Tout T. Wang, Martin W. Zwierlein, Wolfgang Ketterle, and Alan O. Jamison. Photoassociation of ultracold nali. *Phys. Chem. Chem. Phys.*, 20(7):4746–4751, FEB 21 2018b. doi:[10.1039/c7cp08480c](https://doi.org/10.1039/c7cp08480c).
- Ragnar Rydberg. Some potential curves of mercury hydrides. *Z. Phys.*, 80(7-8):514–524, JUL 1933. doi:[10.1007/BF02057312](https://doi.org/10.1007/BF02057312).

- A. Safavi-Naini, M. L. Wall, and A. M. Rey. Role of interspecies interactions in the preparation of a low-entropy gas of polar molecules in a lattice. *Phys. Rev. A*, 92:063416, Dec 2015. doi:[10.1103/PhysRevA.92.063416](https://doi.org/10.1103/PhysRevA.92.063416).
- M. Saffman, T. G. Walker, and K. Mølmer. Quantum information with rydberg atoms. *Rev. Mod. Phys.*, 82:2313–2363, Aug 2010. doi:[10.1103/RevModPhys.82.2313](https://doi.org/10.1103/RevModPhys.82.2313).
- M. S. Safronova, U. I. Safronova, and Charles W. Clark. Magic wavelengths for optical cooling and trapping of lithium. *Phys. Rev. A*, 86(4):042505–, October 2012. doi:[10.1103/PhysRevA.86.042505](https://doi.org/10.1103/PhysRevA.86.042505).
- M. S. Safronova, D. Budker, D. DeMille, D. F. J. Kimball, A. Derevianko, and C. W. Clark. Search for new physics with atoms and molecules. *Rev. Mod. Phys.*, 90(2):025008, June 2018.
- B.E.A Saleh and M.C. Teich. *Fundamental of Photonics*. Wiley-Interscience, 2009.
- G. Salomon, L. Fouché, P. Wang, A. Aspect, P. Bouyer, and T. Bourdel. Gray-molasses cooling of 39 k to a high phase-space density. *EPL (Europhysics Letters)*, 104(6):63002, 2013. doi:[10.1209/0295-5075/104/63002](https://doi.org/10.1209/0295-5075/104/63002).
- G. Salomon, L. Fouché, S. Lepoutre, A. Aspect, and T. Bourdel. All-optical cooling of ^{39}K to Bose-Einstein condensation. *Phys. Rev. A*, 90:033405, Sep 2014. doi:[10.1103/PhysRevA.90.033405](https://doi.org/10.1103/PhysRevA.90.033405).
- Craig J. Sansonetti, C. E. Simien, J. D. Gillaspy, Joseph N. Tan, Samuel M. Brewer, Roger C. Brown, Saijun Wu, and J. V. Porto. Absolute transition frequencies and quantum interference in a frequency comb based measurement of the $^{6,7}\text{Li}$ d lines. *Phys. Rev. Lett.*, 107(2):023001–, July 2011. doi:[10.1103/PhysRevLett.107.023001](https://doi.org/10.1103/PhysRevLett.107.023001).
- A Schadee. Zeeman effect in electronic-transitions of diatomic-molecules. *J. Quant. Spectrosc. Radiat. Transf.*, 19(5):517–531, 1978. doi:[10.1016/0022-4073\(78\)90020-1](https://doi.org/10.1016/0022-4073(78)90020-1).
- Nils Scharnhorst, Jannes B. Wübbena, Stephan Hannig, Cornelius Jakobsen, Johannes Kramer, Ian D. Leroux, and Piet O. Schmidt. High-bandwidth transfer of phase stability through a fiber frequency comb. *Opt. Express*, 23(15):19771–19776, Jul 2015. doi:[10.1364/OE.23.019771](https://doi.org/10.1364/OE.23.019771).
- Peter Schauß, Johannes Zeiher, Takeshi Fukuhara, Sebastian Hild, Marc Cheneau, Tommaso Macrì, Thomas Pohl, Immanuel Bloch, and Christian Groß. Crystallization in ising quantum magnets. *Science*, 347(6229):1455–1458, 2015. doi:[10.1126/science.1258351](https://doi.org/10.1126/science.1258351).
- Andreas Schindewolf, Roman Bause, Xing-Yan Chen, Marcel Duda, Tijs Karman, Immanuel Bloch, and Xin-Yu Luo. Evaporation of microwave-shielded polar molecules to quantum degeneracy. *Nature*, 607(7920):677, 07 2022. doi:[10.1038/s41586-022-04900-0](https://doi.org/10.1038/s41586-022-04900-0).
- Fabian Schmid, Johannes Weitenberg, Theodor W. Hänsch, Thomas Udem, and Akira Ozawa. Simple phase noise measurement scheme for cavity-stabilized laser systems. *Opt. Lett.*, 44(11):2709–2712, Jun 2019. doi:[10.1364/OL.44.002709](https://doi.org/10.1364/OL.44.002709).
- Stefan Schmid, Gregor Thalhammer, Klaus Winkler, Florian Lang, and Johannes Hecker Denschlag. Long distance transport of ultracold atoms using a 1D optical lattice. *New J. Phys.*, 8(8):159, 2006. doi:[10.1088/1367-2630/8/8/159](https://doi.org/10.1088/1367-2630/8/8/159).
- J.-N. Schmidt, J. Hertkorn, M. Guo, F. Böttcher, M. Schmidt, K. S. H. Ng, S. D. Graham, T. Langen, M. Zwierlein, and T. Pfau. Roton excitations in an oblate dipolar quantum gas. *Phys. Rev. Lett.*, 126:193002, May 2021. doi:[10.1103/PhysRevLett.126.193002](https://doi.org/10.1103/PhysRevLett.126.193002).

- P. O. Schmidt, S. Hensler, J. Werner, A. Griesmaier, A. Görlitz, T. Pfau, and A. Simoni. Determination of the *s*-wave scattering length of chromium. *Phys. Rev. Lett.*, 91:193201, Nov 2003. doi:[10.1103/PhysRevLett.91.193201](https://doi.org/10.1103/PhysRevLett.91.193201).
- Matthias Schmitt, Matthias Wenzel, Fabian Böttcher, Igor Ferrier-Barbut, and Tilman Pfau. Self-bound droplets of a dilute magnetic quantum liquid. *Nature*, 539(7628):259–262, 2016. doi:[10.1126/science.1258351](https://doi.org/10.1126/science.1258351).
- U. Schneider, L. Hackermüller, S. Will, Th. Best, I. Bloch, T. A. Costi, R. W. Helmes, D. Rasch, and A. Rosch. Metallic and insulating phases of repulsively interacting fermions in a 3D optical lattice. *Science*, 322(5907):1520–1525, 2008. doi:[10.1126/science.1165449](https://doi.org/10.1126/science.1165449).
- Alexander Schuckert. Wavemeter based on a moving michelson interferometer. Technical report, Centre for Quantum Technologies, National University of Singapore, 2014.
- U. Schünemann, H. Engler, M. Zielonkowski, M. Weidemüller, and R. Grimm. Magneto-optic trapping of lithium using semiconductor lasers. *Opt. Commun.*, 158(1?6):263–272, December 1998. doi:[10.1016/S0030-4018\(98\)00517-3](https://doi.org/10.1016/S0030-4018(98)00517-3).
- Franz Schwabl. *Statistical Mechanics*. Springer, 2006.
- Florian Schröder, Takeshi Fukuhara, Seiji Sugawa, Yosuke Takasu, and Yoshiro Takahashi. Tools for quantum simulation with ultracold atoms in optical lattices. *Nature Reviews Physics*, 2(8):411–425, 2020. doi:[10.1038/s42254-020-0195-3](https://doi.org/10.1038/s42254-020-0195-3).
- J. Sebastian, Ch. Gross, Ke Li, H. C. J. Gan, Wenhui Li, and K. Dieckmann. Two-stage magneto-optical trapping and narrow-line cooling of ${}^6\text{Li}$ atoms to high phase-space density. *Phys. Rev. A*, 90:033417, Sep 2014. doi:[10.1103/PhysRevA.90.033417](https://doi.org/10.1103/PhysRevA.90.033417).
- Frauke Seeßelberg, Nikolaus Buchheim, Zhen-Kai Lu, Tobias Schneider, Xin-Yu Luo, Eberhard Tiemann, Immanuel Bloch, and Christoph Gohle. Modeling the adiabatic creation of ultracold polar ${}^{23}\text{Na}{}^{40}\text{K}$ molecules. *Phys. Rev. A*, 97:013405, Jan 2018a. doi:[10.1103/PhysRevA.97.013405](https://doi.org/10.1103/PhysRevA.97.013405).
- Frauke Seeßelberg, Nikolaus Buchheim, Zhen-Kai Lu, Tobias Schneider, Xin-Yu Luo, Eberhard Tiemann, Immanuel Bloch, and Christoph Gohle. Modeling the adiabatic creation of ultracold polar ${}^{23}\text{Na}{}^{40}\text{K}$ molecules. *Phys. Rev. A*, 97:013405, Jan 2018b. doi:[10.1103/PhysRevA.97.013405](https://doi.org/10.1103/PhysRevA.97.013405).
- Mariusz Semczuk, Xuan Li, Will Gunton, Magnus Haw, Nikesh S. Dattani, Julien Witz, Arthur K. Mills, David J. Jones, and Kirk W. Madison. High-resolution photoassociation spectroscopy of the ${}^6\text{Li}_2 {}^{13}\Sigma_g^+$ state. *Phys. Rev. A*, 87(5):052505–, May 2013. doi:[10.1103/PhysRevA.87.052505](https://doi.org/10.1103/PhysRevA.87.052505).
- G. Semeghini, G. Ferioli, L. Masi, C. Mazzinghi, L. Wolswijk, F. Minardi, M. Modugno, G. Modugno, M. Inguscio, and M. Fattori. Self-bound quantum droplets of atomic mixtures in free space. *Phys. Rev. Lett.*, 120:235301, Jun 2018. doi:[10.1103/PhysRevLett.120.235301](https://doi.org/10.1103/PhysRevLett.120.235301).
- Rajdeep Sensarma, David Pekker, Ehud Altman, Eugene Demler, Niels Strohmaier, Daniel Greif, Robert Jördens, Leticia Tarruell, Henning Moritz, and Tilman Esslinger. Lifetime of double occupancies in the fermi-hubbard model. *Phys. Rev. B*, 82:224302, Dec 2010. doi:[10.1103/PhysRevB.82.224302](https://doi.org/10.1103/PhysRevB.82.224302).
- D. W. Sesko, T. G. Walker, and C. E. Wieman. Behavior of neutral atoms in a spontaneous force trap. *J. Opt. Soc. Am. B*, 8(5):946–958, May 1991. doi:[10.1364/JOSAB.8.000946](https://doi.org/10.1364/JOSAB.8.000946).

- Jon H. Shirley. Modulation transfer processes in optical heterodyne saturation spectroscopy. *Opt. Lett.*, 7(11):537–539, November 1982. doi:[10.1364/OL.7.000537](https://doi.org/10.1364/OL.7.000537).
- Bruce Shore. The theory of coherent atomic excitation, 1991.
- B.W Shore. Pre-history of the concepts underlying stimulated raman adiabatic passage. *Acta Physica Slovaca*, 63(6):361–481, 2013.
- E. S. Shuman, J. F. Barry, and D. DeMille. Laser cooling of a diatomic molecule. *Nature*, 467(7317):820–823, 2010. doi:[10.1038/nature09443](https://doi.org/10.1038/nature09443).
- Franz Sievers, Norman Kretzschmar, Diogo Rio Fernandes, Daniel Suchet, Michael Rabinovic, Saijun Wu, Colin V. Parker, Lev Khaykovich, Christophe Salomon, and Frédéric Chevy. Simultaneous sub-Doppler laser cooling of fermionic ^6Li and ^{40}K on the D_1 line: Theory and experiment. *Phys. Rev. A*, 91:023426, Feb 2015. doi:[10.1103/PhysRevA.91.023426](https://doi.org/10.1103/PhysRevA.91.023426).
- C. Silber, S. Günther, C. Marzok, B. Deh, Ph. W. Courteille, and C. Zimmermann. Quantum-degenerate mixture of fermionic lithium and bosonic rubidium gases. *Phys. Rev. Lett.*, 95:170408, Oct 2005. doi:[10.1103/PhysRevLett.95.170408](https://doi.org/10.1103/PhysRevLett.95.170408).
- Jonathan Simon, Waseem S. Bakr, Ruichao Ma, M. Eric Tai, Philipp M. Preiss, and Markus Greiner. Quantum simulation of antiferromagnetic spin chains in an optical lattice. *Nature*, 472(7343):307–312, 2011. doi:[10.1038/nature09994](https://doi.org/10.1038/nature09994).
- Horst Sjuts. *CEM Model KBL5RS/90*. Dr. Sjuts Optotechnik GmbH, June 2014a.
- Horst Sjuts. Private communication. Dr. Sjuts Optotechnik GmbH, 2014b.
- Horst Sjuts. Private communication. Dr. Sjuts Optotechnik GmbH, 2014c.
- J. J. Snyder, R. K. Raj, D. Bloch, and M. Ducloy. High-sensitivity nonlinear spectroscopy using a frequency-offset pump. *Opt. Lett.*, 5(4):163–165, Apr 1980. doi:[10.1364/OL.5.000163](https://doi.org/10.1364/OL.5.000163).
- Botsi Sofia. *Exploring the Dipolar Ground State of Ultracold ^6Li - ^{40}K Molecules via Singlet State*. PhD thesis, National University of Singapore, 2022.
- Maximilian Sohmen, Claudia Politi, Lauritz Klaus, Lauriane Chomaz, Manfred J. Mark, Matthew A. Norcia, and Francesca Ferlaino. Birth, life, and death of a dipolar supersolid. *Phys. Rev. Lett.*, 126:233401, Jun 2021. doi:[10.1103/PhysRevLett.126.233401](https://doi.org/10.1103/PhysRevLett.126.233401).
- Hyungmok Son, Juliana J Park, Wolfgang Ketterle, and Alan O Jamison. Collisional cooling of ultracold molecules. *Nature*, 580(7802):197–200, 2020.
- Jens L Sørensen, Ditte Møller, Theis Iversen, Jakob B Thomsen, Frank Jensen, Peter Staanum, Dirk Voigt, and Michael Drewsen. Efficient coherent internal state transfer in trapped ions using stimulated raman adiabatic passage. *New Journal of Physics*, 8(11):261–261, nov 2006. doi:[10.1088/1367-2630/8/11/261](https://doi.org/10.1088/1367-2630/8/11/261).
- A. M. Steane, M. Chowdhury, and C. J. Foot. Radiation force in the magneto-optical trap. *J. Opt. Soc. Am. B*, 9(12):2142–2158, Dec 1992. doi:[10.1364/JOSAB.9.002142](https://doi.org/10.1364/JOSAB.9.002142).
- Jochen Steinmann. *Multiphoton Ionization of Laser Cooled Lithium*. PhD thesis, Ruperto-Carola University of Heidelberg, 2007.
- J. Stenger, S. Inouye, M. R. Andrews, H.-J. Miesner, D. M. Stamper-Kurn, and W. Ketterle. Strongly enhanced inelastic collisions in a Bose-Einstein condensate near feshbach resonances. *Phys. Rev. Lett.*, 82:2422–2425, Mar 1999. doi:[10.1103/PhysRevLett.82.2422](https://doi.org/10.1103/PhysRevLett.82.2422).

- Jörn Stenger, Harald Schnatz, Christian Tamm, and Harald R. Telle. Ultraprecise measurement of optical frequency ratios. *Phys. Rev. Lett.*, 88:073601, Feb 2002. doi:[10.1103/PhysRevLett.88.073601](https://doi.org/10.1103/PhysRevLett.88.073601).
- Ian Stevenson, Aden Z. Lam, Niccolò Bigagli, Claire Warner, Weijun Yuan, Siwei Zhang, and Sebastian Will. Ultracold gas of dipolar nacs ground state molecules. *Phys. Rev. Lett.*, 130: 113002, Mar 2023. doi:[10.1103/PhysRevLett.130.113002](https://doi.org/10.1103/PhysRevLett.130.113002).
- Thilo Stöferle, Henning Moritz, Christian Schori, Michael Köhl, and Tilman Esslinger. Transition from a strongly interacting 1d superfluid to a mott insulator. *Phys. Rev. Lett.*, 92: 130403, Mar 2004. doi:[10.1103/PhysRevLett.92.130403](https://doi.org/10.1103/PhysRevLett.92.130403).
- H. T. C. Stoof, J. M. V. A. Koelman, and B. J. Verhaar. Spin-exchange and dipole relaxation rates in atomic hydrogen: Rigorous and simplified calculations. *Phys. Rev. B*, 38:4688–4697, Sep 1988. doi:[10.1103/PhysRevB.38.4688](https://doi.org/10.1103/PhysRevB.38.4688).
- J. G. Story and T. F. Gallagher. Temporal effects in multiphoton ionization of lithium. *Phys. Rev. A*, 47:5037–5040, Jun 1993. doi:[10.1103/PhysRevA.47.5037](https://doi.org/10.1103/PhysRevA.47.5037).
- Kevin E. Strecker, Guthrie B. Partridge, and Randall G. Hulet. Conversion of an atomic fermi gas to a long-lived molecular Bose gas. *Phys. Rev. Lett.*, 91:080406, Aug 2003. doi:[10.1103/PhysRevLett.91.080406](https://doi.org/10.1103/PhysRevLett.91.080406).
- J. Stuhler, A. Griesmaier, T. Koch, M. Fattori, T. Pfau, S. Giovanazzi, P. Pedri, and L. Santos. Observation of dipole-dipole interaction in a degenerate quantum gas. *Phys. Rev. Lett.*, 95: 150406, Oct 2005. doi:[10.1103/PhysRevLett.95.150406](https://doi.org/10.1103/PhysRevLett.95.150406).
- Jürgen Stuhler, Axel Griesmaier, Jörg Werner, Tobias Koch, Marco Fattori, and Tilman Pfau. Ultracold chromium atoms: from feshbach resonances to a dipolar boseeinsteinstein condensate. *Journal of Modern Optics*, 54(5):647–660, 2007. doi:[10.1080/09500340600677088](https://doi.org/10.1080/09500340600677088).
- William C. Stwalley. Stability of spin-aligned hydrogen at low temperatures and high magnetic fields: New field-dependent scattering resonances and predissociations. *Phys. Rev. Lett.*, 37: 1628–1631, Dec 1976. doi:[10.1103/PhysRevLett.37.1628](https://doi.org/10.1103/PhysRevLett.37.1628).
- William C. Stwalley and He Wang. Photoassociation of ultracold atoms: A new spectroscopic technique. *J. Mol. Spectrosc.*, 195(2):194 – 228, 1999. doi:[10.1006/jmsp.1999.7838](https://doi.org/10.1006/jmsp.1999.7838).
- William C. Stwalley, Yea-Hwang Uang, and Goran Pichler. Pure long-range molecules. *Phys. Rev. Lett.*, 41:1164–1167, Oct 1978. doi:[10.1103/PhysRevLett.41.1164](https://doi.org/10.1103/PhysRevLett.41.1164).
- Seiji Sugawa, Kensuke Inaba, Shintaro Taie, Rekishi Yamazaki, Makoto Yamashita, and Yoshiro Takahashi. Interaction and filling-induced quantum phases of dual mott insulators of bosons and fermions. *Nature Physics*, 7(8):642–648, 2011. doi:[10.1038/nphys2028](https://doi.org/10.1038/nphys2028).
- Sune Svanberg. *Atomic and Molecular Spectroscopy*. Springer, 2004.
- M Taglieber. *Quantum Degeneracy in an Atomic Fermi-Fermi-Bose Mixture*. PhD thesis, LMU, 2008.
- M. Taglieber, A.-C. Voigt, F. Henkel, S. Fray, T. W. Hänsch, and K. Dieckmann. Simultaneous magneto-optical trapping of three atomic species. *Phys. Rev. A*, 73:011402, Jan 2006. doi:[10.1103/PhysRevA.73.011402](https://doi.org/10.1103/PhysRevA.73.011402).
- M. Taglieber, A.-C. Voigt, T. Aoki, T. W. Hänsch, and K. Dieckmann. Quantum Degenerate Two-Species Fermi-Fermi Mixture Coexisting with a Bose-Einstein Condensate. *Phys. Rev. Lett.*, 100:010401, Jan 2008. doi:[10.1103/PhysRevLett.100.010401](https://doi.org/10.1103/PhysRevLett.100.010401).

Tetsu Takekoshi, Markus Debatin, Raffael Rameshan, Francesca Ferlaino, Rudolf Grimm, Hanns-Christoph Nägerl, C. Ruth Le Sueur, Jeremy M. Hutson, Paul S. Julienne, Svetlana Kotochigova, and Eberhard Tiemann. Towards the production of ultracold ground-state rbcs molecules: Feshbach resonances, weakly bound states, and the coupled-channel model. *Phys. Rev. A*, 85:032506, Mar 2012. doi:[10.1103/PhysRevA.85.032506](https://doi.org/10.1103/PhysRevA.85.032506).

Tetsu Takekoshi, Lukas Reichsöllner, Andreas Schindewolf, Jeremy M. Hutson, C. Ruth Le Sueur, Olivier Dulieu, Francesca Ferlaino, Rudolf Grimm, and Hanns-Christoph Nägerl. Ultracold dense samples of dipolar rbcs molecules in the rovibrational and hyperfine ground state. *Phys. Rev. Lett.*, 113:205301, Nov 2014. doi:[10.1103/PhysRevLett.113.205301](https://doi.org/10.1103/PhysRevLett.113.205301).

Yijun Tang, Andrew Sykes, Nathaniel Q. Burdick, John L. Bohn, and Benjamin L. Lev. *s*-wave scattering lengths of the strongly dipolar bosons ^{162}Dy and ^{164}Dy . *Phys. Rev. A*, 92:022703, Aug 2015. doi:[10.1103/PhysRevA.92.022703](https://doi.org/10.1103/PhysRevA.92.022703).

H. R. Telle. *Frequency Control of Semiconductor Lasers*, chapter 5, pages 138–167. Wiley-Interscience, 1996.

Harald R Telle, G Steinmeyer, Amy E Dunlop, Joern Stenger, Dirk H Sutter, and Ursula Keller. Carrier-envelope offset phase control: A novel concept for absolute optical frequency measurement and ultrashort pulse generation. *Applied Physics B*, 69(4):327–332, 1999. doi:[10.1007/s003400050813](https://doi.org/10.1007/s003400050813).

Tiago Quevedo Teodoro, Roberto Luiz Andrade Haiduke, and Lucas Visscher. Nuclear electric quadrupole moment of potassium from the molecular method. *Phys. Rev. A*, 91:032516, Mar 2015. doi:[10.1103/PhysRevA.91.032516](https://doi.org/10.1103/PhysRevA.91.032516).

J. D. Thompson, T. G. Tiecke, A. S. Zibrov, V. Vuletić, and M. D. Lukin. Coherence and raman sideband cooling of a single atom in an optical tweezer. *Phys. Rev. Lett.*, 110:133001, Mar 2013. doi:[10.1103/PhysRevLett.110.133001](https://doi.org/10.1103/PhysRevLett.110.133001).

H. R. Thorsheim, J. Weiner, and P. S. Julienne. Laser-induced photoassociation of ultracold sodium atoms. *Phys. Rev. Lett.*, 58(23):2420–2423, June 1987. doi:[10.1103/PhysRevLett.58.2420](https://doi.org/10.1103/PhysRevLett.58.2420).

T. G. Tiecke, M. R. Goosen, A. Ludewig, S. D. Gensemer, S. Kraft, S. J. J. M. F. Kokkelmans, and J. T. M. Walraven. Broad feshbach resonance in the $^6\text{Li}^{40}\text{K}$ mixture. *Phys. Rev. Lett.*, 104:053202, Feb 2010a. doi:[10.1103/PhysRevLett.104.053202](https://doi.org/10.1103/PhysRevLett.104.053202).

T. G. Tiecke, M. R. Goosen, J. T. M. Walraven, and S. J. J. M. F. Kokkelmans. Asymptotic-bound-state model for feshbach resonances. *Phys. Rev. A*, 82:042712, Oct 2010b. doi:[10.1103/PhysRevA.82.042712](https://doi.org/10.1103/PhysRevA.82.042712).

TG Tiecke. Properties of potassium.

E. Tiemann, H. Knöckel, P. Kowalczyk, W. Jastrzebski, A. Pashov, H. Salami, and A. J. Ross. Coupled system $a\ ^3\Sigma^+$ and $X^1\Sigma^+$ of kli: Feshbach resonances and corrections to the born-oppenheimer approximation. *Phys. Rev. A*, 79:042716, Apr 2009. doi:[10.1103/PhysRevA.79.042716](https://doi.org/10.1103/PhysRevA.79.042716).

E. Tiesinga, B. J. Verhaar, and H. T. C. Stoof. Threshold and resonance phenomena in ultracold ground-state collisions. *Phys. Rev. A*, 47(5):4114–4122, May 1993. doi:[10.1103/PhysRevA.47.4114](https://doi.org/10.1103/PhysRevA.47.4114).

- E. Torrontegui, S. Ibáñez, Xi Chen, A. Ruschhaupt, D. Guéry-Odelin, and J. G. Muga. Fast atomic transport without vibrational heating. *Phys. Rev. A*, 83:013415, Jan 2011. doi:[10.1103/PhysRevA.83.013415](https://doi.org/10.1103/PhysRevA.83.013415).
- C. H. Townes and A. L. Schawlow. *Microwave Spectroscopy*, chapter 8, pages 195–196. McGraw-Hill Book Company, Inc, 1955.
- C. G. Townsend, N. H. Edwards, C. J. Cooper, K. P. Zetie, C. J. Foot, A. M. Steane, P. Sriftgiser, H. Perrin, and J. Dalibard. Phase-space density in the magneto-optical trap. *Phys. Rev. A*, 52:1423–1440, Aug 1995. doi:[10.1103/PhysRevA.52.1423](https://doi.org/10.1103/PhysRevA.52.1423).
- A. Trautmann, P. Ilzhöfer, G. Durastante, C. Politi, M. Sohmen, M. J. Mark, and F. Ferlaino. Dipolar quantum mixtures of erbium and dysprosium atoms. *Phys. Rev. Lett.*, 121:213601, Nov 2018. doi:[10.1103/PhysRevLett.121.213601](https://doi.org/10.1103/PhysRevLett.121.213601).
- C Trefzger, C Menotti, B Capogrosso-Sansone, and M Lewenstein. Ultracold dipolar gases in optical lattices. *Journal of Physics B: Atomic, Molecular and Optical Physics*, 44(19):193001, sep 2011. doi:[10.1088/0953-4075/44/19/193001](https://doi.org/10.1088/0953-4075/44/19/193001).
- JW Tromp and RJ LeRoy. Near-dissociation expansion representation of large spectroscopic data sets - the $b(^3\pi_{0u})the b(3 - pi - ou+)[- x(1 - sigma - g+)system of i - 2$. *J. Mol. Spectrosc.*, 109(2) : 352 – – 367, 1985. doi : [10.1016/0022-2852\(85\)90318-2](https://doi.org/10.1016/0022-2852(85)90318-2).
- Andrew G. Truscott, Kevin E. Strecker, William I. McAlexander, Guthrie B. Partridge, and Randall G. Hulet. Observation of fermi pressure in a gas of trapped atoms. *Science*, 291(5513):2570–2572, 2001. doi:[10.1126/science.1059318](https://doi.org/10.1126/science.1059318).
- Ieva Čepaitė. LiKab initio Calculations. *Internship Report*, 2018.
- Juris Ulmanis, Johannes Deiglmayr, Marc Repp, Roland Wester, and Matthias Weidmüller. Ultracold molecules formed by photoassociation: Heteronuclear dimers, inelastic collisions, and interactions with ultrashort laser pulses. *Chem. Rev.*, 112(9):4890–4927, 2012. doi:[10.1021/cr300215h](https://doi.org/10.1021/cr300215h).
- P. J. Ungar, D. S. Weiss, E. Riis, and Steven Chu. Optical molasses and multilevel atoms: theory. *J. Opt. Soc. Am. B*, 6(11):2058–2071, November 1989. doi:[10.1364/JOSAB.6.002058](https://doi.org/10.1364/JOSAB.6.002058).
- Giacomo Valtolina, Kyle Matsuda, William G Tobias, Jun-Ru Li, Luigi De Marco, and Jun Ye. Dipolar evaporation of reactive molecules to below the fermi temperature. *Nature*, 588(7837): 239–243, 2020. doi:[10.1038/s41586-020-2980-7](https://doi.org/10.1038/s41586-020-2980-7).
- J. Van Dongen, C. Zhu, D. Clement, G. Dufour, J. L. Booth, and K. W. Madison. Trap-depth determination from residual gas collisions. *Phys. Rev. A*, 84:022708, Aug 2011. doi:[10.1103/PhysRevA.84.022708](https://doi.org/10.1103/PhysRevA.84.022708).
- R. Vexiau, D. Borsalino, M. Lepers, A. Orbán, M. Aymar, O. Dulieu, and N. Boulofa Maafa. Dynamic dipole polarizabilities of heteronuclear alkali dimers: optical response, trapping and control of ultracold molecules. *International Reviews in Physical Chemistry*, 36(4):709–750, 2017. doi:[10.1080/0144235X.2017.1351821](https://doi.org/10.1080/0144235X.2017.1351821).
- John R. Vig, Eva. S. Ferre-Pikal, J. C. Camparo, L. S. Cutler, L. Maleki, W. J. Riley, S. R. Stein, C. Thomas, F. L. Walls, and J. D White. Ieee standard definitions of physical quantities for fundamental frequency and time metrology-random instabilities. *IEEE Std 1139-1999*, pages 1–40, 1999. doi:[10.1109/IEEESTD.1999.90575](https://doi.org/10.1109/IEEESTD.1999.90575).

- Nathaniel B. Vilas, Christian Hallas, Loic Anderegg, Paige Robichaud, Andrew Winnicki, De-bayan Mitra, and John M. Doyle. Magneto-optical trapping and sub-doppler cooling of a polyatomic molecule. *Nature*, 606(7912):70, 06 2022. doi:[10.1038/s41586-022-04620-5](https://doi.org/10.1038/s41586-022-04620-5).
- N. V. Vitanov and S. Stenholm. Analytic properties and effective two-level problems in stimulated raman adiabatic passage. *Phys. Rev. A*, 55:648–660, Jan 1997. doi:[10.1103/PhysRevA.55.648](https://doi.org/10.1103/PhysRevA.55.648).
- Nikolay V. Vitanov, Andon A. Rangelov, Bruce W. Shore, and Klaas Bergmann. Stimulated raman adiabatic passage in physics, chemistry, and beyond. *Rev. Mod. Phys.*, 89:015006, Mar 2017. doi:[10.1103/RevModPhys.89.015006](https://doi.org/10.1103/RevModPhys.89.015006).
- NV Vitanov and S Stenholm. Adiabatic population transfer via multiple intermediate states. *Phys. Rev. A*, 60(5):3820–3832, NOV 1999. doi:[10.1103/PhysRevA.60.3820](https://doi.org/10.1103/PhysRevA.60.3820).
- K. K. Voges, P. Gersema, M. M. Z. Borgloh, T. A. Schulze, T. Hartmann, A. Zenesini, and S. Ospelkaus. Ultracold gas of bosonic (nak)-na-23-k-39 ground-state molecules. *Phys. Rev. Lett.*, 125(8):083401, August 2020a.
- Kai K Voges, Philipp Gersema, Torsten Hartmann, Torben A Schulze, Alessandro Zenesini, and Silke Ospelkaus. A pathway to ultracold bosonic $\text{\AA}^2\text{Na}^3\text{K}$ ground state molecules. *New Journal of Physics*, 21(12):123034, dec 2019. doi:[10.1088/1367-2630/ab5f31](https://doi.org/10.1088/1367-2630/ab5f31).
- Kai K. Voges, Philipp Gersema, Mara Meyer zum Alten Borgloh, Torben A. Schulze, Torsten Hartmann, Alessandro Zenesini, and Silke Ospelkaus. Ultracold gas of bosonic $^{23}\text{Na}^{39}\text{K}$ ground-state molecules. *Phys. Rev. Lett.*, 125:083401, Aug 2020b. doi:[10.1103/PhysRevLett.125.083401](https://doi.org/10.1103/PhysRevLett.125.083401).
- A.-C. Voigt. *Heteronuclear Molecules from a Quantum Degenerate Fermi-Fermi Mixture*. PhD thesis, Ludwig-Maximilians Universität at München, 2009.
- A.-C. Voigt, M. Taglieber, L. Costa, T. Aoki, W. Wieser, T. W. Hänsch, and K. Dieckmann. Ultracold heteronuclear fermi-fermi molecules. *Phys. Rev. Lett.*, 102:020405, Jan 2009. doi:[10.1103/PhysRevLett.102.020405](https://doi.org/10.1103/PhysRevLett.102.020405).
- Arne-Christian Voigt. *Simultanes Fangen von drei Atomsorten in einer magnetooptischen Falle*. PhD thesis, Technische Universität München, 2004.
- Vladan Vuletić, Cheng Chin, Andrew J. Kerman, and Steven Chu. Degenerate raman sideband cooling of trapped cesium atoms at very high atomic densities. *Phys. Rev. Lett.*, 81:5768–5771, Dec 1998. doi:[10.1103/PhysRevLett.81.5768](https://doi.org/10.1103/PhysRevLett.81.5768).
- J. Walls, R. Ashby, J.J. Clarke, B. Lu, and W.A. van Wijngaarden. Measurement of isotope shifts, fine and hyperfine structure splittings of the lithium d lines. *The European Physical Journal D - Atomic, Molecular, Optical and Plasma Physics*, 22(2):159–162, 2003. doi:[10.1140/epjd/e2003-00001-5](https://doi.org/10.1140/epjd/e2003-00001-5).
- J.T.M. Walraven. Quantum gases - statistics and interactions, 2014.
- D. Wang, B. Neyenhuis, M. H. G. de Miranda, K.-K. Ni, S. Ospelkaus, D. S. Jin, and J. Ye. Direct absorption imaging of ultracold polar molecules. *Phys. Rev. A*, 81:061404, Jun 2010. doi:[10.1103/PhysRevA.81.061404](https://doi.org/10.1103/PhysRevA.81.061404).
- Fudong Wang, Xiaodong He, Xiaoke Li, Bing Zhu, Jun Chen, and Dajun Wang. Formation of ultracold NaRb feshbach molecules. *New Journal of Physics*, 17(3):035003, mar 2015. doi:[10.1088/1367-2630/17/3/035003](https://doi.org/10.1088/1367-2630/17/3/035003).

- Fudong Wang, Xin Ye, Mingyang Guo, D Blume, and Dajun Wang. Observation of resonant scattering between ultracold heteronuclear feshbach molecules. *Physical Review A*, 100(4):042706, 2019. doi:doi.org/10.1103/PhysRevA.100.042706.
- C. Weber, G. Barontini, J. Catani, G. Thalhammer, M. Inguscio, and F. Minardi. Association of ultracold double-species bosonic molecules. *Phys. Rev. A*, 78:061601(R), Dec 2008. doi:[10.1103/PhysRevA.78.061601](https://doi.org/10.1103/PhysRevA.78.061601).
- M. Weidemüller, T. Esslinger, M. A. Ol'shanii, A. Hemmerich, and T. W. Hänsch. A novel scheme for efficient cooling below the photon recoil limit. *EPL (Europhysics Letters)*, 27(2):109, 1994. doi:[10.1209/0295-5075/27/2/006](https://doi.org/10.1209/0295-5075/27/2/006).
- Wolf Weimer, Kai Morgener, Vijay Pal Singh, Jonas Siegl, Klaus Hueck, Niclas Luick, Ludwig Mathey, and Henning Moritz. Critical velocity in the bec-bcs crossover. *Phys. Rev. Lett.*, 114:095301, Mar 2015. doi:[10.1103/PhysRevLett.114.095301](https://doi.org/10.1103/PhysRevLett.114.095301).
- John Weiner, Vanderlei S. Bagnato, Sergio Zilio, and Paul S. Julienne. Experiments and theory in cold and ultracold collisions. *Rev. Mod. Phys.*, 71(1):1–85, January 1999. doi:[10.1103/RevModPhys.71.1](https://doi.org/10.1103/RevModPhys.71.1).
- Jonathan D. Weinstein, Robert deCarvalho, Thierry Guillet, Bretislav Friedrich, and John M. Doyle. Magnetic trapping of calcium monohydride molecules at millikelvin temperatures. *Nature*, 395(6698):148–150, 1998. doi:[10.1038/25949](https://doi.org/10.1038/25949).
- David S. Weiss, Erling Riis, Yaakov Shevy, P. Jeffrey Ungar, and Steven Chu. Optical molasses and multilevel atoms: experiment. *J. Opt. Soc. Am. B*, 6(11):2072–2083, Nov 1989. doi:[10.1364/JOSAB.6.002072](https://doi.org/10.1364/JOSAB.6.002072).
- H.-J. Werner and Peter J. Knowles. An Efficient Internally Contracted Multiconfiguration Reference CI Method. *J. Chem. Phys.*, 89:5803–5814, 1988a. doi:[10.1063/1.455556](https://doi.org/10.1063/1.455556).
- H.-J. Werner and Peter J. Knowles. An Efficient Internally Contracted Multiconfiguration Reference CI Method. *J. Chem. Phys.*, 89:5803–5814, 1988b. doi:[10.1063/1.455556](https://doi.org/10.1063/1.455556).
- Hans-Joachim Werner, Peter J. Knowles, Gerald Knizia, Frederick R. Manby, and Martin Schuetz. Molpro: a general-purpose quantum chemistry program package. *Wiley Interdiscip. Rev.: Comput. Mol. Sci.*, 2(2):242–253, MAR-APR 2012. doi:[10.1002/wcms.82](https://doi.org/10.1002/wcms.82).
- Lennard Wharton, L. Peter Gold, and William Klemperer. Quadrupole moment of Li^6 . *Phys. Rev.*, 133:B270–B272, Jan 1964. doi:[10.1103/PhysRev.133.B270](https://doi.org/10.1103/PhysRev.133.B270).
- Martyn D. Wheeler, Stuart M. Newman, Andrew J. Orr-Ewing, and Michael N. R. Ashfold. Cavity ring-down spectroscopy. *J. Chem. Soc., Faraday Trans.*, 94:337–351, 1998. doi:[10.1039/A707686J](https://doi.org/10.1039/A707686J).
- PO Widmark, PA Malmqvist, and BO Roos. Density-Matrix Averaged Atomic Natural Orbital (ANO) Basis-Sets for Correlated Molecular Wave-Functions .1. 1st Row Atoms. *Theor. Chim. Acta.*, 77(5):291–306, JUL 1990. doi:[10.1007/BF01120130](https://doi.org/10.1007/BF01120130).
- Wolfgang Wieser. An optical dipole trap for ultracold bosons and fermions. Diploma Thesis, 2006.
- Sebastian A. Will, Jee Woo Park, Zoe Z. Yan, Huanqian Loh, and Martin W. Zwierlein. Coherent microwave control of ultracold $^{23}\text{Na}^{40}\text{K}$ molecules. *Phys. Rev. Lett.*, 116:225306, Jun 2016. doi:[10.1103/PhysRevLett.116.225306](https://doi.org/10.1103/PhysRevLett.116.225306).

- E. Wille, F. M. Spiegelhalder, G. Kerner, D. Naik, A. Trenkwalder, G. Hendl, F. Schreck, R. Grimm, T. G. Tiecke, J. T. M. Walraven, S. J. J. M. F. Kokkelmans, E. Tiesinga, and P. S. Julienne. Exploring an ultracold fermi-fermi mixture: Interspecies feshbach resonances and scattering properties of ^6Li and ^{40}K . *Phys. Rev. Lett.*, 100:053201, Feb 2008. doi:[10.1103/PhysRevLett.100.053201](https://doi.org/10.1103/PhysRevLett.100.053201).
- F. Egan William. *Practical RF System Design*, chapter 9, page 246. Wiley, 2003.
- D. J. Wineland, R. E. Drullinger, and F. L. Walls. Radiation-pressure cooling of bound resonant absorbers. *Phys. Rev. Lett.*, 40:1639–1642, Jun 1978. doi:[10.1103/PhysRevLett.40.1639](https://doi.org/10.1103/PhysRevLett.40.1639).
- D. J. Wineland, M. Barrett, J. Britton, J. Chiaverini, B. DeMarco, W. M. Itano, B. Ježenković, C. Langer, D. Leibfried, V. Meyer, T. Rosenband, and T. Schätz. Quantum information processing with trapped ions. *Philosophical Transactions of the Royal Society of London. Series A: Mathematical, Physical and Engineering Sciences*, 361(1808):1349–1361, 2003. doi:[10.1098/rsta.2003.1205](https://doi.org/10.1098/rsta.2003.1205).
- K. Winkler, G. Thalhammer, F. Lang, R. Grimm, J. Hecker Denschlag, A. J. Daley, A. Kantian, H. P. Böhm, and P. Zoller. Repulsively bound atom pairs in an optical lattice. *Nature*, 441(7095):853–856, 2006. doi:[10.1038/nature04918](https://doi.org/10.1038/nature04918).
- K. Winkler, F. Lang, G. Thalhammer, P. v. d. Straten, R. Grimm, and J. Hecker Denschlag. Coherent optical transfer of feshbach molecules to a lower vibrational state. *Phys. Rev. Lett.*, 98:043201, Jan 2007. doi:[10.1103/PhysRevLett.98.043201](https://doi.org/10.1103/PhysRevLett.98.043201).
- Cheng-Hsun Wu, Ibon Santiago, Jee Woo Park, Peyman Ahmadi, and Martin W. Zwierlein. Strongly interacting isotopic bose-fermi mixture immersed in a fermi sea. *Phys. Rev. A*, 84:011601, Jul 2011. doi:[10.1103/PhysRevA.84.011601](https://doi.org/10.1103/PhysRevA.84.011601).
- Cheng-Hsun Wu, Jee Woo Park, Peyman Ahmadi, Sebastian Will, and Martin W. Zwierlein. Ultracold fermionic feshbach molecules of $^{23}\text{Na}^{40}\text{K}$. *Phys. Rev. Lett.*, 109:085301, Aug 2012. doi:[10.1103/PhysRevLett.109.085301](https://doi.org/10.1103/PhysRevLett.109.085301).
- Xing Wu, Thomas Gantner, Manuel Koller, Martin Zeppenfeld, Sotir Chervenkov, and Gerhard Rempe. A cryofuge for cold-collision experiments with slow polar molecules. *Science*, 358(6363):645–648, 10 2017. doi:[10.1126/science.aan3029](https://doi.org/10.1126/science.aan3029).
- Nie Xiaoyu. *This PhD thesis is expected to be completed under the supervision of Prof. Kai Dieckmann by Xiaoyu, Nie at a later date.* PhD thesis, National University of Singapore, Expected 2026.
- Xinye Xu, Thomas H. Loftus, Josh W. Dunn, Chris H. Greene, John L. Hall, Alan Gallagher, and Jun Ye. Single-stage sub-Doppler cooling of alkaline earth atoms. *Phys. Rev. Lett.*, 90(19):193002–, May 2003. doi:[10.1103/PhysRevLett.90.193002](https://doi.org/10.1103/PhysRevLett.90.193002).
- Bo Yan, Steven A Moses, Bryce Gadway, Jacob P Covey, Kaden RA Hazzard, Ana Maria Rey, Deborah S Jin, and Jun Ye. Observation of dipolar spin-exchange interactions with lattice-confined polar molecules. *Nature*, 501(7468):521–525, 2013. doi:[10.1038/nature12483](https://doi.org/10.1038/nature12483).
- Zoe Z. Yan, Jee Woo Park, Yiqi Ni, Huanqian Loh, Sebastian Will, Tijs Karman, and Martin Zwierlein. Resonant dipolar collisions of ultracold molecules induced by microwave dressing. *Phys. Rev. Lett.*, 125:063401, Aug 2020. doi:[10.1103/PhysRevLett.125.063401](https://doi.org/10.1103/PhysRevLett.125.063401).
- Zong-Chao Yan, James F. Babb, A. Dalgarno, and G. W. F. Drake. Variational calculations of dispersion coefficients for interactions among h, he, and li atoms. *Phys. Rev. A*, 54:2824–2833, Oct 1996. doi:[10.1103/PhysRevA.54.2824](https://doi.org/10.1103/PhysRevA.54.2824).

- A. Yang, S. Botsi, S. Kumar, S. B. Pal, M. M. Lam, I. Čepaitė, A. Laugharn, and K. Dieckmann. Singlet pathway to the ground state of ultracold polar molecules. *Phys. Rev. Lett.*, 124:133203, Apr 2020. doi:[10.1103/PhysRevLett.124.133203](https://doi.org/10.1103/PhysRevLett.124.133203).
- A. Yang, C. He, X. Nie, V. Avalos, S. Botsi, S. Kumar, and K. Dieckmann. Improving stirap efficiency for ultracold ground state ^6Li - ^{40}K molecules. *preprint*, 2025.
- Anbang Yang. *Singlet Pathway to the Dipolar Ground State of Ultracold ^6Li - ^{40}K Molecules*. PhD thesis, National University of Singapore, 2021a.
- Anbang Yang. *Singlet Pathway to the Dipolar Ground State of Ultracold ^6Li - ^{40}K Molecules*. PhD thesis, National University of Singapore, 2021b.
- Huan Yang, De-Chao Zhang, Lan Liu, Ya-Xiong Liu, Jue Nan, Bo Zhao, and Jian-Wei Pan. Observation of magnetically tunable feshbach resonances in ultracold (nak)-na-23-k-40+k-40 collisions. *Science*, 363(6424):261, JAN 18 2019. doi:[10.1126/science.aau5322](https://doi.org/10.1126/science.aau5322).
- Huan Yang, Jin Cao, Zhen Su, Jun Rui, Bo Zhao, and Jian-Wei Pan. Creation of an ultracold gas of triatomic molecules from an atom-diatom mixture. *Science*, 378(6623):1009–1013, 2022a. doi:[10.1126/science.adf6307](https://doi.org/10.1126/science.adf6307).
- Huan Yang, Xin-Yao Wang, Zhen Su, Jin Cao, De-Chao Zhang, Jun Rui, Bo Zhao, Chun-Li Bai, and Jian-Wei Pan. Evidence for the association of triatomic molecules in ultracold 23na40k+40k mixtures. *Nature*, 602(7896):229–233, 2022b. doi:doi.org/10.1038/s41586-021-04297-2.
- N. Y. Yao, M. P. Zaletel, D. M. Stamper-Kurn, and A. Vishwanath. A quantum dipolar spin liquid. *Nat. Phys.*, 14(4):405–410, April 2018.
- L. P. Yatsenko, V. I. Romanenko, B. W. Shore, and K. Bergmann. Stimulated raman adiabatic passage with partially coherent laser fields. *Phys. Rev. A*, 65:043409, Apr 2002. doi:[10.1103/PhysRevA.65.043409](https://doi.org/10.1103/PhysRevA.65.043409).
- L. P. Yatsenko, B. W. Shore, and K. Bergmann. Detrimental consequences of small rapid laser fluctuations on stimulated raman adiabatic passage. *Phys. Rev. A*, 89:013831, Jan 2014. doi:[10.1103/PhysRevA.89.013831](https://doi.org/10.1103/PhysRevA.89.013831).
- Jun Ye. *Ultrasensitive high resolution laser spectroscopy and its application to optical frequency standards*. PhD thesis, University of Colorado at Boulder, 1997.
- Jun Ye and Steven T Cundiff. *Femtosecond optical frequency comb: principle, operation and applications*. Springer Science & Business Media, 2005.
- Xin Ye, Mingyang Guo, Maykel L González-Martínez, Goulven Quéméner, and Dajun Wang. Collisions of ultracold 23na87rb molecules with controlled chemical reactivities. *Science advances*, 4(1):eaaq0083, 2018. doi:[10.1126/sciadv.aaq0083](https://doi.org/10.1126/sciadv.aaq0083).
- S. F. Yelin, K. Kirby, and Robin Côté. Schemes for robust quantum computation with polar molecules. *Phys. Rev. A*, 74:050301, Nov 2006. doi:[10.1103/PhysRevA.74.050301](https://doi.org/10.1103/PhysRevA.74.050301).
- Yu Yichao. *Coherent creation of single molecules from single atoms*. PhD thesis, Harvard University, 2020.
- P. Zabawa, A. Wakim, M. Haruza, and N. P. Bigelow. Formation of ultracold $\text{X}^1\sigma^+(v = 0)$ nacs molecules via coupled photoassociation channels. *Phys. Rev. A*, 84:061401, Dec 2011. doi:[10.1103/PhysRevA.84.061401](https://doi.org/10.1103/PhysRevA.84.061401).

M. Zaccanti, B. Deissler, C. D'Errico, M. Fattori, M. Jona-Lasinio, S. Mller, G. Roati, M. Inguscio, and G. Modugno. Observation of an efimov spectrum in an atomicsystem. *Nature Physics*, 5(8):586–591, 2009. doi:[10.1038/nphys1334](https://doi.org/10.1038/nphys1334).

Ren Zhang, Yanting Cheng, Hui Zhai, and Peng Zhang. Orbital feshbach resonance in alkali-earth atoms. *Phys. Rev. Lett.*, 115:135301, Sep 2015. doi:[10.1103/PhysRevLett.115.135301](https://doi.org/10.1103/PhysRevLett.115.135301).

Bing Zhu, Xiaoke Li, Xiaodong He, Mingyang Guo, Fudong Wang, Romain Vexiau, Nadia Bouloufa-Maafa, Olivier Dulieu, and Dajun Wang. Long-range states of the narb molecule near the na(3 s-2(1/2))+rb(5 p-2(3/2)) asymptote. *Phys. Rev. A*, 93(1):012508, JAN 14 2016. doi:[10.1103/PhysRevA.93.012508](https://doi.org/10.1103/PhysRevA.93.012508).

Shi-Liang Zhu, Baigeng Wang, and L.-M. Duan. Simulation and detection of dirac fermions with cold atoms in an optical lattice. *Phys. Rev. Lett.*, 98(26):260402–, June 2007. doi:[10.1103/PhysRevLett.98.260402](https://doi.org/10.1103/PhysRevLett.98.260402).

B Zimmermann, T Müller, J Meineke, T Esslinger, and H Moritz. High-resolution imaging of ultracold fermions in microscopically tailored optical potentials. *New J. Phys.*, 13(4):043007–, 2011. doi:[10.1088/1367-2630/13/4/043007](https://doi.org/10.1088/1367-2630/13/4/043007).

Bruno Zimmermann. *Microscopy of ultra-cold fermionic lithium*. PhD thesis, ETH Zurich, 2010.

J. J. Zirbel, K.-K. Ni, S. Ospelkaus, T. L. Nicholson, M. L. Olsen, P. S. Julienne, C. E. Wieman, J. Ye, and D. S. Jin. Heteronuclear molecules in an optical dipole trap. *Phys. Rev. A*, 78: 013416, Jul 2008. doi:[10.1103/PhysRevA.78.013416](https://doi.org/10.1103/PhysRevA.78.013416).

G. Zürn, T. Lompe, A. N. Wenz, S. Jochim, P. S. Julienne, and J. M. Hutson. Precise characterization of ${}^6\text{Li}$ feshbach resonances using trap-sideband-resolved RF spectroscopy of weakly bound molecules. *Phys. Rev. Lett.*, 110:135301, Mar 2013. doi:[10.1103/PhysRevLett.110.135301](https://doi.org/10.1103/PhysRevLett.110.135301).

M. W. Zwierlein, C. A. Stan, C. H. Schunck, S. M. F. Raupach, S. Gupta, Z. Hadzibabic, and W. Ketterle. Observation of Bose-Einstein condensation of molecules. *Phys. Rev. Lett.*, 91 (25):250401–, December 2003. doi:[10.1103/PhysRevLett.91.250401](https://doi.org/10.1103/PhysRevLett.91.250401).

M. W. Zwierlein, J. R. Abo-Shaeer, A. Schirotzek, C. H. Schunck, and W. Ketterle. Vortices and superfluidity in a strongly interacting fermi gas. *Nature*, 435(7045):1047–1051, June 2005. doi:[10.1038/nature03858](https://doi.org/10.1038/nature03858).

A. Fundamental Physical Constants

The CODATA recommended values for the fundamental physical constants are taken from the NIST Physics Laboratory Web site ([CODATA2018](#)).

quantity	symbol	unit	value
speed of light	c	299792458	ms^{-1}
Boltzmann constant	k_B	1.380649×10^{-23}	JK^{-1}
Planck's constant	h	$6.62607015 \times 10^{-34}$	JHz^{-1}
vacuum permittivity	ϵ_0	$8.8541878128(13) \times 10^{-12}$	Fm^{-1}
vacuum permeability	μ_0	$1.25663706212(19) \times 10^{-6}$	NA^{-2}
Bohr radius	a_0	$5.29177210903(80) \times 10^{-11}$	m
Bohr magneton	μ_B	$9.2740100783(28) \times 10^{-24}$	JT^{-1}
electron charge	e	$1.602176634 \times 10^{-19}$	C
electron mass	m_e	$9.1093837015(28) \times 10^{-31}$	kg
atomic mass unit	u	$1.66053906660(50) \times 10^{-27}$	kg
inversed fine structure constant	$1/\alpha$	$137.035999084(21)$	

B. STIRAP Summary Table

Species	Excited State	η	$\Gamma/2\pi$ (MHz)	K_0 (Theory) ($\text{cm}^3 \text{s}^{-1}$)	K_0 (Exp.) ($\text{cm}^3 \text{s}^{-1}$)	τ	reference
${}^6\text{Li}{}^{40}\text{K}$	$\text{A}^1\Sigma$	96(4)%	6.6(1.3)	7.9×10^{-10}	$3.8(1.9) \times 10^{-10}$	$5.0(3)$ ms	This work
${}^{23}\text{Na}{}^{40}\text{K}$	$\text{c}^3\Sigma^+ \sim \text{B}^1\Pi$	75 – 80%	9 – 11(1)	6×10^{-11}	1.4×10^{-11}	2.5(5)&2.7(8) s	Bause et al. (2021); Liu et al. (2019); Park et al. (2015a)
${}^{23}\text{Na}{}^{40}\text{K}$	$\text{d}^3\Pi \sim \text{D}^1\Pi$	50%	20	/	/	/	Seeßelberg et al. (2018a)
${}^{23}\text{Na}{}^{39}\text{K}$	$\text{c}^3\Sigma^+ \sim \text{B}^1\Pi$	70%	6	6.5×10^{-10}	$4.49(1.18) \times 10^{-10}$	/	Voges et al. (2020b)
${}^{23}\text{Na}{}^{87}\text{Rb}$	$\text{A}^1\Sigma^+ \sim \text{b}^3\Pi$	93%	0.67	3.5×10^{-10}	$2.5(9) \times 10^{-10}$	0.2 s	Guo et al. (2016); Ye et al. (2018)
${}^{23}\text{Na}{}^{133}\text{Cs}$	$\text{B}^1\Pi$	55(3)%	15(3)	8×10^{-10}	$7(3) \times 10^{-10}$	10(1) ms	Stevenson et al. (2023)
${}^{40}\text{K}{}^{87}\text{Rb}$	$2^3\Sigma^+ \sim 1^1\Pi$	89(4)%	/	1.5×10^{-12}	$3.3(7) \times 10^{-12}$	$170(20)$ μs	Ni et al. (2008)
${}^{87}\text{Rb}{}^{133}\text{Cs}$	$\text{A}^1\Sigma^+ \sim \text{b}^3\Pi$	98.7(1)%	0.135(10)	1.1×10^{-10}	$5.4(9) \times 10^{-11}$	0.53(6) ms	Maddox et al. (2024); Molony et al. (2014); Takekoshi et al. (2014)
${}^{23}\text{Na}{}^6\text{Li}$	$\text{c}^3\Sigma^+$	86%	6	3×10^{-12}	$1.6(1.2) \times 10^{-11}$	4.6 s	Rvachov et al. (2017)

Table B.1: Collection of the STIRAP results for different species.

